Hard X-ray Synchrotron Beamline Instrumentation for Millisecond Quick Extended X-ray Absorption Spectroscopy

A dissertation in fulfillment of the
requirements for the degree of doctor in the faculty of
mathematics and natural science

submitted to the department of physics
of the
Bergische Universität Wuppertal

by
Dipl.-Phys. Oliver Müller

Wuppertal, 2016

Die Dissertation kann wie folgt zitiert werden:

urn:nbn:de:hbz:468-20160926-113328-5
[http://nbn-resolving.de/urn/resolver.pl?urn=urn%3Anbn%3Ade%3Ahbz%3A468-20160926-113328-5]

Table of Contents

1 Introduction

X-ray absorption spectroscopy (XAS) is a powerful experimental method to probe the atomic short range order of crystalline and non-crystalline condensed matter. The distinct fine structure of the energy dependent X-ray absorption coefficient found above an absorption edge contains element specific information about the local atomic and electronic structure. Experimental advances and the high X-ray intensity over a broad continuous spectral range available synchrotron radiation sources led to the development of Quick scanning EXAFS (QEXAFS), which progressively pushed the acquisition time of a single X-ray absorption spectrum from tens of minutes down to the sub-second regime [**1**,**2**,**3**,**4**]. By means of this method, the X-ray absorption near edge structure (XANES) and the extended X-ray absorption fine structure (EXAFS) can be acquired continuously with a high repetition rate. Not only does QEXAFS boost techniques which require a large number of spectra, such as XANES mapping or tomographic XAS [**5**,**6**], it also, and more importantly, adds time resolution to XAS on a very useful scale. This unique combination of element sensitivity, time resolution and the high penetration depth of hard X-rays makes QEXAFS an invaluable tool for in-situ investigations of chemical reactions. Applications originate from a broad field of various disciplines including catalysis research, energy research including e.g. batteries and solar cells, material science, corrosion science, environmental science and more [**7**,**8**,**9**,**10**,**11**,**12**,**13**].

The main concept of QEXAFS is to record the absorption spectrum on-the-fly while the monochromator performs uninterrupted successive energy scans. In contrast to conventional XAS, which executes a scan in a repetitive start stop procedure at discrete energy values, dead times are completely eliminated leading to a significant reduction of the acquisition time per spectrum. QEXAFS with conventional monochromators typically reach the sub-minute time scale and is widely available at synchrotron radiation facilities worldwide. However, when aiming at the sub-second time regime highly specialized monochromators, detectors and data acquisition systems are required.

A hard X-ray monochromator used in XAS applications essentially exploits Bragg's law of X-ray diffraction. Energy scans are performed by rotating a single crystal thus altering the Bragg angle which defines the reflected photon energy. To obtain absorption spectra using the QEXAFS method, the Bragg angle, from which the photon energy is derived afterwards, is measured synchronously with the

absorption of the sample, while the monochromator crystal is in continuous oscillatory motion [**14**,**15**]. Following this concept, in particular the monochromator and the data acquisition system need to be optimized for this specific task. A dedicated QEXAFS monochromator therefore incorporates specialized drive mechanics to enable the oscillatory motion of the monochromator crystal. As part of this work a new concept of a QEXAFS monochromator based on a direct drive torque motor was developed and two monochromators have been realized [**16**]. The first device was installed at the SuperXAS beamline at the SLS (PSI, Switzerland) in January 2015 [**4**]. It is in user operation since then. The second device was build for the P64 beamline at PETRA III (DESY, Germany). Both beamlines are discussed in section 2.2.2. The new drive mechanics allow oscillation frequencies of up to 50 Hz, which corresponds to 100 spectra per second. Also owing to the capabilities of the new drive, the build monochromators are the first dedicated QEXAFS monochromators, which are equipped with two different channel cut crystals to extend the accessible photon energy from about 4 keV to 44 keV. The monochromator, the direct drive and the capabilities are discussed in Chapter 3.

The time resolution of a measurement is defined by the oscillation frequency of the monochromator crystals. The QEXAFS data acquisition system is required to synchronously record the detector signal outputs and the Bragg angle with a sufficient sampling frequency up to the MHz regime, in order not to undersample the absorption spectra. In Chapter 4 the implemented data acquisition system is discussed and an estimation of the minimal required sampling frequency based on the energy resolution of monochromator is derived. In the same chapter an elaborate software program, called *JAQ*, is presented. It was written to allow XAFS data evaluation of large QEXAFS data sets. Since these can contain up to more than hundred thousand of individual absorption spectra, specialized software is necessary to fully exploit the benefits of QEXAFS. Furthermore, the access to sophisticated software tools supporting QEXAFS data evaluation, is still a critical issue to promote QEXAFS to a larger user community. The development of JAQ is also intended to improve the situation in this regard.

Using the QEXAFS method, the bandwidth of the detectors, which are used to determine the absorption of the sample is a critical characteristic and has to match the sampling frequency of the DAQ. In conventional XAFS as well as with the QEXAFS method, the X-ray absorption of a sample is usually determined by measuring the incident and transmitted X-ray intensities with gas filled ionization chambers. However, the bandwidth of conventional planar parallel plate ionization chambers is limited by the ion drift velocity and can severely impair fast QEXAFS measurements. Although the ion drift velocity can be increased, for instance by applying higher voltages or choosing lighter gases, the dielectric strength of the filling gas leads to an absolute upper limit. The major breakthrough was achieved by the development of the gridded ionization chambers, which are not limited by the ion drift velocity [**17**]. As a consequence the frequency bandwidth is significantly increased and the step response is reduced by typically two orders of magnitude. The gridded ionization chamber is one of the major improvements to enable time resolutions below 100 ms. Chapter 5 is dedicated to the discussion of the basic principles of planar parallel plate and gridded ionization chambers. Extensive investigations of the

step response behavior of both types of ionization chambers have been performed and are discussed in this chapter.

The potential of the new QEXAFS setup installed at the SuperXAS beamline is demonstrated in Chapter 6. Besides fast static measurements which intend to characterize the capabilities of the setup, the nucleation and growth of Cu_2ZnSnS_4 (CZTS) nanocrystals are investigated in-situ and the kinetics are analyzed. CZTS is a promising candidate for the photon absorbing layer in future solar cells. This material was synthesized in an one-pot hot-injection process, which represents an entire class of synthesizing processes which are ideally suited for in-situ investigation with the QEXAFS method.

The presented work extensively covers the import aspects of synchrotron beamline instrumentation to facilitate hard X-ray sub-second QEXAFS experiment. The required components are reviewed with respect to their influence on data quality and their temporal response behavior to enable fastest measurements. All critical components (monochromator, ionization chambers, current amplifiers, data acquisition system, data acquisition and data evaluation software) have been newly developed and improved in their characteristics and functional range. These developments enable investigations on shorter time scales with higher precision than it was feasible before.

2 X-ray Absorption Spectroscopy

X-ray absorption spectroscopy (XAS) is a commonly used method at synchrotron radiation facilities to study the atomic and electronic structure of many classes of condensed matter. The fine structure of the energy dependent X-ray absorption coefficient just above an absorption edge depends sensitively on the local atomic arrangement and electronic properties of the material [**18**]. XAS probes the local short range order of individual atomic species and thus enables studies of crystalline and non-crystalline materials as well. The Quick EXAFS (QEXAFS) method adds time resolution to XAS and allows to follow dynamic structural changes [**1**,**2**,**3**,**4**,**19**,**20**]. By this means, the X-ray Absorption Near Edge Structure (XANES) and the Extended Absorption Fine Structure (EXAFS), which are adjacent regions of an X-ray absorption spectrum can be measured with high repetition rates in real time.

XAS is well covered in the literature and comprehensive discussions can be found in [**15**,**18**,**21**,**22**,**23**,**24**]. The following section 2.1 summarizes the theoretical background of XAS. In section 2.1.2 general experimental requirements of XAS at synchrotron radiation sources are discussed. In this section the two beamlines, SuperXAS (SLS, PSI Switzerland) and P64 (PETRA III, DESY Germany) are described. The new QEXAFS setup which is presented throughout chapters 3 to 5 has been installed at these beamlines.

2.1 Introduction to X-ray Absorption Spectroscopy

X-rays which pass through matter are attenuated due to various photon-matter interactions. The attenuation of the incident intensity is described by the Lambert-Beer law [**25**]:

$$I_1 = I_0 e^{-\mu(E)d}. \tag{2.1}$$

The quantities I_0 and I_1 are measures of the incident and transmitted intensities. The argument of the exponential function, which can be determined experimentally, contains the product of the penetrated thickness d and the energy dependent X-ray absorption coefficient μ. This quantity includes the cross sections of photon-matter interactions and is essentially responsible for the energy dependency of the Lambert-Beer law. X-ray absorption spectroscopy intends to measure the X-ray absorption coefficient

as a function of energy. Its distinct structure is unique for the probed material and sensitive to the electronic and atomic structure of the absorbing atom [**18**].

The Energy Dependency of the Absorption Coefficient and its Fine Structure

Within the considered hard X-ray regime, which ranges from a few keV to about 40 keV, elastic or inelastic scattering occur but only take a minor share and the attenuation, i.e. the absorption coefficient, is dominated by the photoelectric effect [**26**,**27**]. As a result of this interaction, energy and angular momentum of the incident photon are entirely transferred to a bound electron. If the incident photon energy exceeds its binding energy, the electron is emitted from the atom creating a photoelectron. The interaction probability, which is measured by the photoelectric cross section, is a monotonously decreasing function of energy. Only if the incident photon energy becomes high enough to ionize the next tighter bound electron, the monotonic behavior is interrupted by an abrupt increase of the interaction probability. Since the X-ray absorption increases likewise, these energetic positions are termed absorption edges [**28**]. For photon energies below this threshold, the absorbing electron can also be excited to higher unoccupied bound states, if this transition is not suppressed by dipole selection rules.

Far away from absorption edges the decreasing trend of the X-ray absorption is well described by the empirical Victoreen function [**29**]:

$$\mu(E) \sim C_{III} E^{-3} - C_{IV} E^{-4}. \tag{2.2}$$

The coefficients C_{III} and C_{IV} depend on the absorbing material and are constant between consecutive absorption edges. The specific values can be determined by linear least squares fitting of the Victoreen function to experimental data (see section 4.3.2). This is routinely performed to remove the background absorption, which is a necessary step towards normalization of spectra or extraction of its fine structure.

X-ray Absorption Fine Structure

The X-ray absorption shows a remarkable structure in the vicinity of an absorption edge. This structure can extend to over more than 2000 eV beyond the absorption edge and is termed the X-ray absorption fine structure (XAFS) [**30**,**31**,**32**,**33**,**34**,**35**,**36**]. Figure 2.1 shows an X-ray absorption spectrum of metallic copper measured at the Cu K-edge. Based on the underlying physical processes, which dominate the XAFS, absorption spectra are separated into two different regions. The region followed by the absorption edge is referred to as the X-ray absorption near edge structure (XANES). This part of the XAFS extends to about 20 eV to 50 eV above the absorption edge and is sensitive to the electronic structure and the local spatial arrangement and symmetry around the absorbing atom. The XANES smoothly merges into a region termed extended X-ray absorption fine structure (EXAFS). Detailed information about local interatomic distances and coordination numbers around the absorbing atom can be retrieved from the EXAFS.

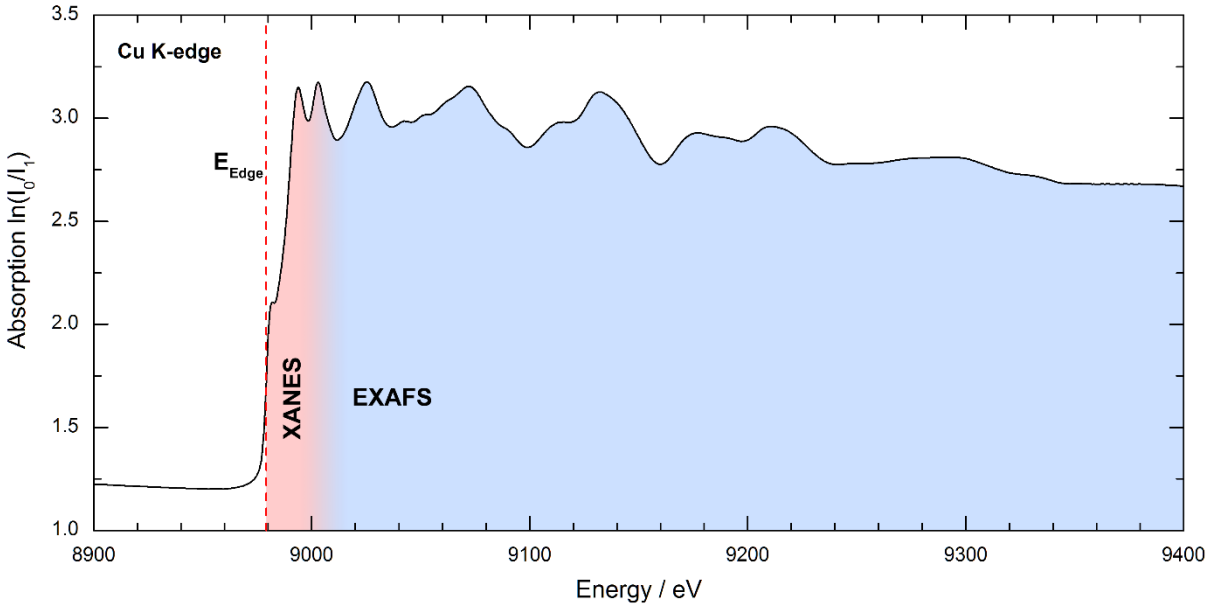

Figure 2.1: X-ray absorption spectrum of copper around the K absorption edge at E_{Edge} = 8979 eV. The transition between the XANES and EXAFS region is not clearly defined.

2.1.1 EXAFS

The extended X-ray absorption fine structure (EXAFS) starts about 20 eV to 50 eV above the absorption edge (see Figure 2.1). The relative modulation of the X-ray absorption within the EXAFS regime is defined by

$$\chi(E) = \frac{\mu(E) - \mu_0(E)}{\mu_0(E)} \tag{2.3}$$

where $\mu_0(E)$ refers to a smoothly varying atomic-like background. Since all information is contained in this function, $\chi(E)$ is often synonymously called 'fine structure' or 'EXAFS' of the absorption spectrum. Extraction of $\chi(E)$ from experimental data and the problem of finding a proper background $\mu_0(E)$ is described in section 4.3.2.

The oscillatory modulation of the X-ray absorption can be interpreted as an interference effect involving the outgoing photoelectron wave which is (back) scattered at neighboring atoms. This is schematically depicted in Figure 2.2. The probability of an X-ray photon being absorbed by a localized core electron is proportional to the amplitude of the final state of the emitted photoelectron at the absorbing atom. This state is given by the superposition of the outgoing and all backscattered electron waves. Consequently, the modulation of the absorption depends on the relative phase of the electron waves, which in turn depends on the wave number $k = 2\pi/\lambda$ and the distances between the absorbing and backscattering atoms. For instance, in the case of straight backscattering by a neighboring atom the phase difference amounts to approximately $2kr$, where r is the interatomic distance and k is the wave number of the electron as given by equation (2.4).

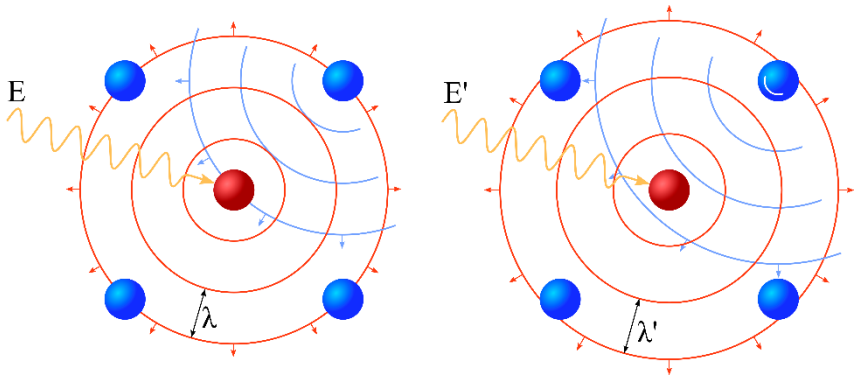

Figure 2.2: Schematic representation of the origin of the EXAFS. The central atom (red) is ionized by absorption of a photon (orange wave). The emitted photoelectron is shown as an outgoing spherical wave (red circles). The outgoing photoelectron wave is backscattered (blue circle segments) at the top right atom (blue), to illustrate a single straight backscattering process. The two pictures show the situation for different electron wavelengths leading to constructive (left) and destructive (right) interference of the electron waves.

$$k = \frac{1}{\hbar}\sqrt{2m_e\left(E - E_{Edge}\right)} \tag{2.4}$$

The energy of the absorbed photon is denoted by E, whereas E_{Edge} refers to the binding energy of the core electron. Thus, the wave number increases as the photon energy is increased which leads to alternating constructive and destructive interference between the electron waves. This gives rise to the oscillatory modulation of the X-ray absorption. In this respect, the EXAFS oscillations as a whole can be interpreted as a superposition of individual scattering paths [**37**]. A common parametrization is given by the so-called EXAFS equation [**18**,**37**]:

$$\chi(k) = \sum_j S_0^2 N_j \frac{\left|f_j(k)\right|}{kr_j^2} e^{-\frac{2r_j}{\lambda_j(k)}} e^{-2\sigma_j^2 k^2} sin\left(2kr_j + \Phi_{ij}(k)\right). \tag{2.5}$$

The sine function of this equation accounts for the interference effect and reflects the oscillatory behavior of the fine structure. The argument of the sine function contains the oscillation frequency $2kr_j$ and a phase $\Phi_{ij}(k)$, which accounts for the total phase shift experienced by the electron wave as it perceives the potentials of the central atom and the neighboring atom. The other parameters in front of the sine function define the amplitude of the particular scattering path and include the coordination number N_j, the backscattering amplitude $f_j(k)$, a correction factor S_0^2, and two dampening exponential functions. S_0^2 accounts for multi-excitations and losses at the absorbing atom by reducing the total amplitude. The first exponential function, $exp\left(-2r_j/\lambda_j(k)\right)$, depends on the mean free path of the photoelectron λ_j, which arises from the decay of the electron wave due to its finite lifetime. The second exponential, $exp\left(-2\sigma_j^2 k^2\right)$, introduces the Debye-Waller factor representing structural disorder and thermal vibrations of the atoms. The quantity σ_j^2 is the root mean square deviation from the average interatomic distance and is mainly responsible for temperature dependency of the EXAFS.

Since EXAFS arises from an interference effect, the interatomic distances correlate with the frequencies contained within the fine structure. In the EXAFS equation this connection is captured by the sine function. Thus, the Fourier transform of the fine structure $\chi(k)$, which has been corrected for the induced phase shift $\Phi_{ij}(k)$, directly correlates with the radial distribution function of surrounding atoms. Further information about the theory of EXAFS is available in the literature [**18**,**24**,**23**,**21**].

2.1.2 XANES

The X-ray absorption near edge structure (XANES) extends to about 40 eV above an absorption edge (see Figure 2.1). In contrast to EXAFS, the mean free path of the emitted photoelectron is substantially longer within the XANES regime. In addition, scattering of the electron wave at surrounding atoms is more efficient. Consequently, XANES is strongly dominated by multiple scattering involving several atoms making it very sensitive to the local symmetry around the absorbing atom [**24**,**22**,**38**,**39**,**40**]. Excitations of the core electron to unoccupied bound states near the absorption edge are very likely and also affect the XANES [**41**]. Since these transitions depend sensitively on the electronic structure of the material, XANES provides information about the local chemical environment as well. This property is of great interest in many fields, in particular regarding in-situ investigations of chemical reactions, such as in catalysis research.

Due to the complexity of XANES, a quantitative interpretation is very difficult and ab initio calculations are still an ongoing field of research [**42**,**43**]. XANES is therefore often qualitatively interpreted. The rich and distinct near edge structure allows it to be used as a ‘fingerprint’ [**18**,**24**]. Linear combination analysis (LCA) and suitable reference XANES spectra from known materials enable to determine the composition of the probed sample. The theoretical background and software implementation of LCA is discussed in section 4.3.3. The application of LCA, performed on a time resolved XAFS measurement, can be found in section 6.2.1.

2.2 Experimental Requirements of hard X-ray Absorption Spectroscopy

Today, EXAFS and XANES measurements are almost exclusively performed at synchrotron radiation facilities. This is due to two main properties: high photon flux and wide spectral bandwidth. The EXAFS signal is comparably weak and the modulation of the background absorption is found to be in the order of 10^{-2} to 10^{-3} at the far end of the spectrum. Consequently, a signal-to-noise ratio of better than 10^{-3} is required to properly resolve the fine structure. Considering the uncertainty of intensity measurements, which is typically given by the square root of the number of involved photons, and the demand of acquisition times of several minutes to a few milliseconds, intensities of 10^{6} photons per second to more than 10^{12} photons per second are required. This flux needs to be provided over a broad and continuous energy band. To enable access to the absorption edges of different elements a total spectral bandwidth of several 10 keV is required. For instance, the K-edges of the important 3d transition

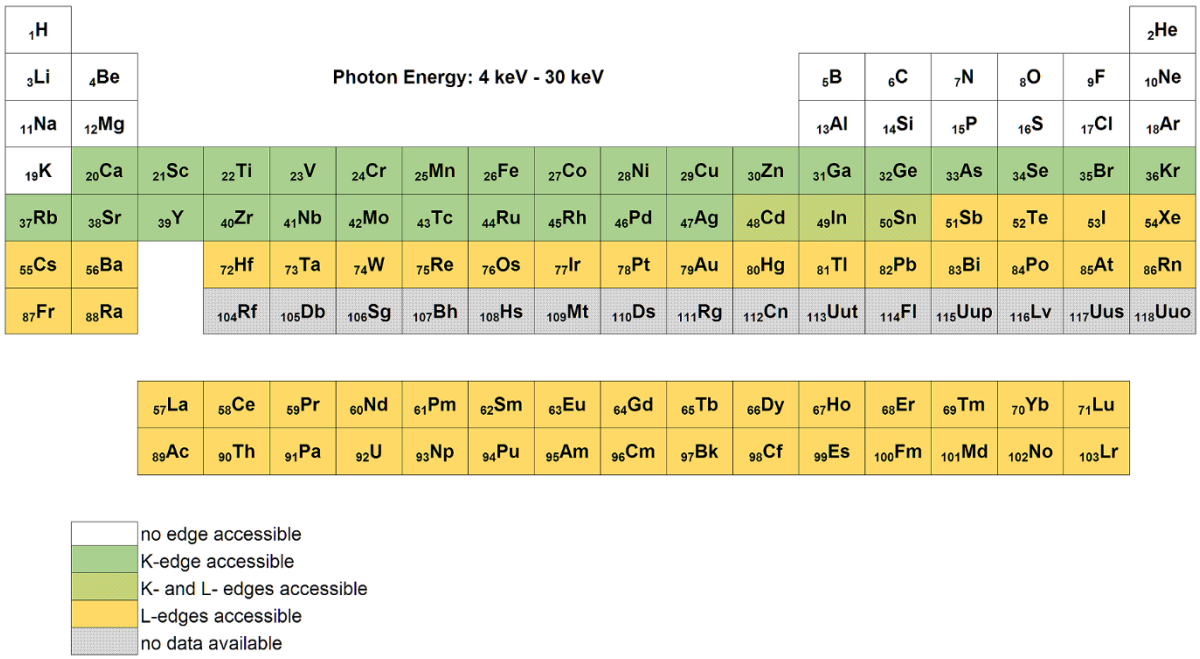

Figure 2.3: Periodic table of the elements indicating the accessible K- and L-edges within the energy band of 4 keV to 30 keV. Data based on [**146**].

metals range between 4 keV and 10 keV (e.g. Ti to Zn: 4966 eV – 9659 eV). The K-edges of the 4d transition metals fall within 17 keV and 27 keV (e.g. Zr to Sn: 17998 eV – 29200 eV). In between, from about 10 keV to 15 keV, many L-edges of the 5d elements are found (e.g. Ta to Au: 9881 eV – 14353 eV). This makes the energy band of 4 keV – 30 keV the most versatile in hard X-ray absorption spectroscopy and should be covered by dedicated beamlines. Figure 2.3 shows the accessible K- and L-edges of the elements in this energy band.

A further fundamental requirement to measure X-ray absorption spectra is a tunable monochromator with an appropriate energy resolution to resolve the fine structure. The EXAFS contains rather low frequency components and does not issue very high demands on the energy resolution. The XANES on the other hand can definitely benefit from a good energy resolution but is inevitably broadened by the finite lifetime of the core hole [**44**]. A reasonable energy resolution of 1 eV – 2 eV is typically sufficient for highly accurate XAFS measurements [**45**,**46**]. More important properties of monochromators used in XAS, are stability and reproducibility. Furthermore the monochromator should cover the entire provided bandwidth of the synchrotron radiation source. Since this is technically not always possible to facilitate in one device, often two or more monochromators (or crystals) are necessary.

Experimental Setup

With a tunable monochromatic X-ray beam provided, the experimental setup for XAFS measurements can be quite simple and the basic layout is shown in Figure 2.4. The idea is to probe Lambert-Beers law (see equation (2.1)) by measuring the incident and transmitted intensities I_0 and I_1. The natural logarithm of the ratio of both intensities yields the absorption of the sample. Optionally

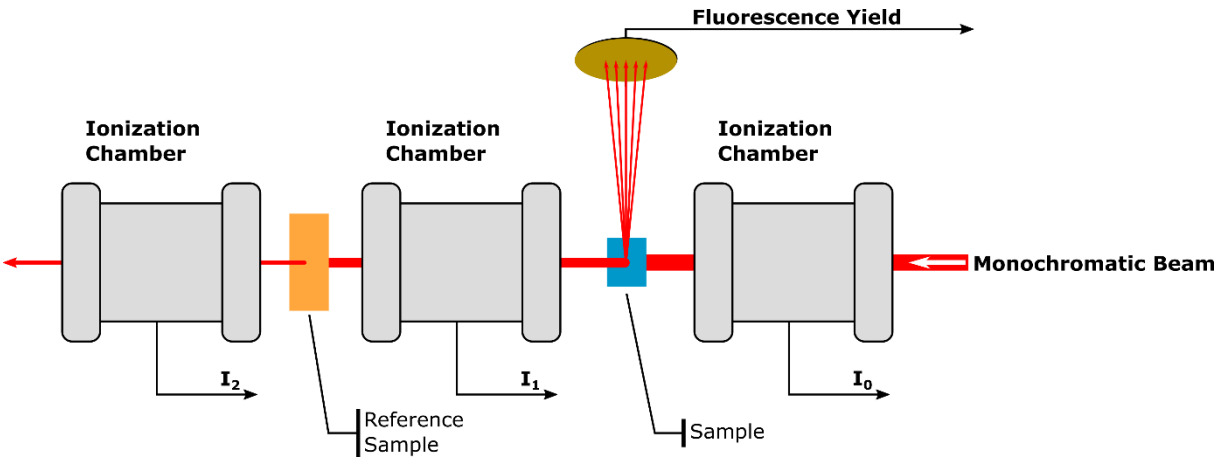

Figure 2.4: Schematic layout of a typical XAFS experiment. The incident and transmitted intensities of the sample and of the reference sample are measured by ionization chambers in transmission geometry. Optionally the fluorescence yield can be measured instead of the transmitted intensity.

secondary processes which are physically linked to the absorption, such as the fluorescence yield can also be measured to determine this value. With an additional intensity measurement behind a reference sample, the energy calibration of the measurement can be verified and corrected if necessary.

The X-ray intensities I_0, I_1 need to be measured with detectors which exhibit a reasonable low self-absorption. Furthermore, these detectors should not interfere with the direction of the beam or its optical properties. These are the reasons why ionization chambers are still the most important detectors for hard X-ray XAFS measurements. In contrast to solid state detectors such as PIN diodes, ionization chambers also allow to be optimized to operate at almost any photon energy by adjusting its gas filling and its pressure.

Sub-Second and Time Resolved X-ray Absorption Spectroscopy - QEXAFS

A way to obtain time resolution is to rapidly and continuously change the incident photon energy back and forth. The absorption spectra are then acquired sequentially by recording the time functions of the intensities I_0 and I_1 while the photon energy is periodically changed. This is the basic principle of the QEXAFS technique [**3**,**4**,**19**,**20**]. Within one oscillation period of the photon energy, two spectra are measured, one with increasing and one with decreasing energy. Hence the spectra acquisition rate is twice the energy oscillation frequency of the monochromator and the acquired spectra are referred to as *up* or *down* depending on the energy scan direction. To enable fast scans specialized monochromators are required. These dedicated QEXAFS monochromators are optimized in regard to fast repetitive energy changes, which require specialized mechanics and drives. Different implementations which have been realized in the past and the design of the new drive are discussed in section 3.2.

Due to the high scan rates (10 keV/s to 50 keV/s) achievable with modern QEXAFS monochromators, the synchrotron radiation source can not be scanned synchronously with the monochromator and thus needs to deliver a continuous spectrum covering at least the scan range. This in particular, leads to restrictions concerning undulator sources, which typically emit a narrow line-type

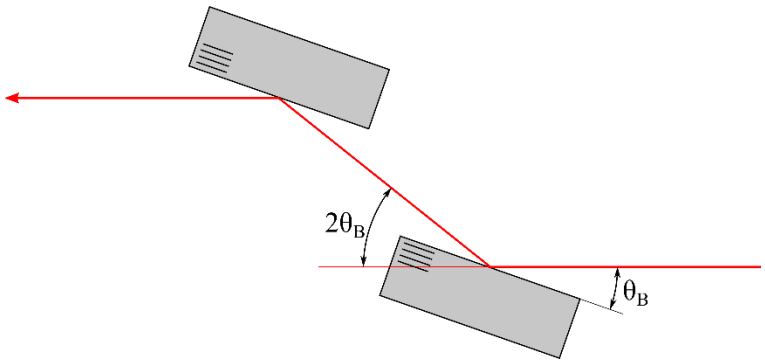

Figure 2.5: Principle of a double crystal monochromator using symmetric Bragg diffraction at two parallel crystals. By tuning the Bragg angle θ_B the transmitted photon energy is set.

spectrum [**47**,**48**]. Tapering of undulators is a possibility to broaden the width of its harmonics. However, the spatial homogeneity and especially the energy dependency of the spatial radiation distribution need to be considered since it might affect the XAFS measurements [**49**].

Since the time functions of the quantities I_0 and I_1 are measured, there are severe requirements on the frequency bandwidth of the detectors and data acquisition system. If not sufficient their finite response blur the XAFS and therefore limit the actual time resolution. Especially energy dispersive detectors which are based on single photon counting have only limited application due to their comparable low saturation count rate. Also large area photo diodes often exhibit large capacities that can lead to electronic oscillations in the signal path and are therefore not suited for fast measurements [**50**]. Best results are obtained using gaseous ionization chambers. Their response time has been pushed to the low microsecond regime, which now allows EXAFS and XANES measurements on the millisecond time scale [**17**]. The development and performance of fast ionization chambers are discussed in detail in Chapter 5.

2.2.1 X-ray Monochromators

X-ray monochromators are essential for XAFS measurements at synchrotron radiation facilities. The monochromator is used to select a narrow energy band out of the broad spectrum emitted by the synchrotron radiation source. By repeatedly changing of the selected energy, an X-ray absorption spectrum can be sampled.

Hard X-ray monochromators rely on X-ray diffraction at perfect single crystals. By adjusting the incident Bragg θ_B angle, the reflected wavelength $\lambda = hc/E$ can be selected. This is well described by Bragg's equation:

$$E = m\frac{hc}{2d_{hkl}}\frac{1}{sin(\theta_B)} \tag{2.6}$$

where m is a natural number to include higher order reflections and d_{hkl} is the normal distance between two consecutive lattice planes, which are defined by the Miller indices h, k, l. As shown in Figure 2.5, typically two Bragg reflections at two parallel single crystals are used to compensate the angular

deflection, thus obtaining a monochromatic beam which is again parallel to the incident one. The two crystal surfaces do not necessarily need to belong to two physically separated crystals but can also be machined from one large crystal by sharing a common backplane. These monolithic crystals are termed channel cut crystals and are due to their importance for QEXAFS monochromators discussed in more detail in section 3.1.2.

Energy Resolution

The achievable energy resolution of crystal monochromators is fundamentally limited by the divergence of the incident beam and the intrinsic Darwin width. The beam divergence is a property of the source and can be manipulated by optical components. At modern beamlines (e.g. SuperXAS, see section 2.2.2) a collimating mirror is typically used to reduce the vertical divergence. The Darwin width refers to the angular range at which Bragg reflection occurs. This is a result of the dynamical diffraction theory and caused by the large number of parallel lattice planes involved in the diffraction at thick perfect crystals [**25**,**51**,**52**]. Given the Darwin width ω_D, the intrinsic energy resolution $\Delta E/E$ can be determined by means of the differential form of the Bragg equation (2.6), leading to equations (2.7) and (2.8) [**25**,**45**].

$$\frac{\Delta E}{E} = cot(\theta_B)\omega_D \tag{2.7}$$

$$= \frac{4 r_e d_{hkl}^2 |F_{hkl}|}{\pi V} \tag{2.8}$$

Here r_e is the classic electron radius, F_{hkl} denotes the structure factor of the unit cell for scattering from a plane (*hkl*) and V is the volume of the unit cell. Using silicon crystals with (111) or (311) cuts, the intrinsic Darwin widths limit the energy resolution according to the equation (2.8) to about $\Delta E/E|_{Si(111)} \sim 1.3 \times 10^{-4}$ and $\Delta E/E|_{Si(311)} \sim 0.4 \times 10^{-4}$. This resolution is well suited for XAFS applications. Furthermore, these specific cuts suppress the second order harmonic, since the structure factors F_{222} and F_{622} vanish. The actual energy resolution is also affected by internal stress within the crystals, which might be caused by mounting forces or thermal deformation. The latter is a critical issue due to the high heat load of synchrotron radiation sources and requires the monochromator crystals to be cooled [**53**,**54**,**55**,**56**].

2.2.2 Synchrotron Radiation Beamlines for X-ray Absorption Spectroscopy

The intense X-ray radiation available at synchrotron radiation facilities is an essential prerequisite for time resolved XAFS measurements. In synchrotron radiation facilities electrons (or positrons) are stored at relativistic energies of several GeV circulating within a storage ring. The synchrotron radiation is generated in sources at the storage ring. By means of specialized magnetic structures the source exert external forces on the electron beam. This causes the electron beam to emit electromagnetic radiation. The Lorentz transformation of the emitted radiation in the electron system to

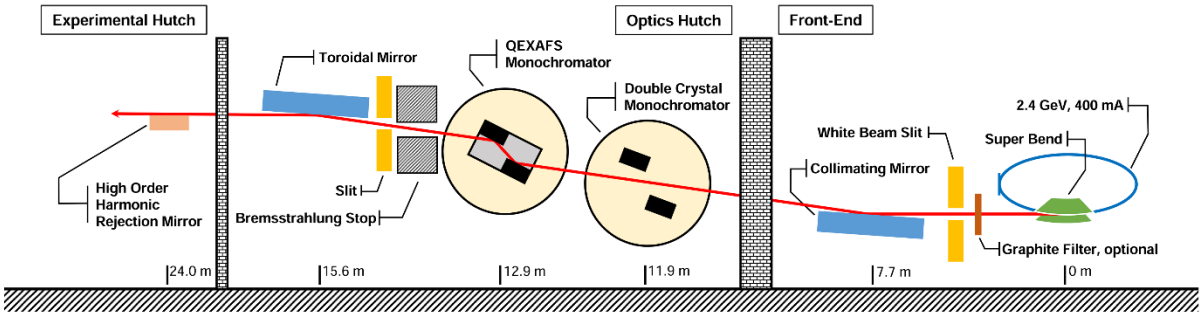

Figure 2.6: Schematic view of the main optical components installed at the SuperXAS (SLS, Switzerland) beamline [**4**].

the experimental system of rest gives rise to the unique properties of synchrotron radiation. The principles and properties of synchrotron radiation facilities and sources are discussed in more detail elsewhere [**25**,**45**,**57**]. The radiation is guided in vacuum to the experiment and the section from the source to the experiment is called a beamline and is usually designed for a specific scientific purpose. In the following two beamlines are described which both enable time resolved X-absorption spectroscopy and at which the new developed QEXAFS monochromators have been installed.

SuperXAS (SLS, Paul-Scherrer-Institut, Switzerland)

The SuperXAS beamline is dedicated to time resolved XAS and X-ray emission spectroscopy (XES). It is located at the Swiss Light Source (SLS) at the Paul-Scherrer-Institute (PSI, Switzerland). The synchrotron radiation facility is operated in top-up mode with 400 mA at 2.4 GeV electron energy. Figure 2.6 shows a schematic overview of the optical components of the beamline. A SuperBend magnet with a critical energy of 11.1 keV delivers X-rays with a flux ranging from about 10^{11} photons per second to 10^{12} photons per second over a spectral range covering roughly 4 keV to 32 keV. The first optical component after the synchrotron radiation source is a collimating mirror, which collects the radiation of the bending magnet and shifts its apparent source point to infinity, thus eliminating the beam divergence in vertical direction. This preserves the intrinsic energy resolution of the monochromator (see section 2.2.1). The mirror also cuts off the high energy part of the emitted spectrum, which reduces the total heat load onto the first monochromator crystal and the amount of higher harmonics in the monochromatic beam. The suppression of higher order harmonics can be further improved by a dedicated mirror downstream in the experimental hutch. The low energy part of the emitted spectrum is removed by graphite filters of various thicknesses. The collimating mirror is followed by a conventional fixed-exit double crystal monochromator and QEXAFS monochromator. This QEXAFS monochromator was new developed and is described in detail in Chapter 3. It has been installed and commissioned in January 2015 [**4**] and replaces the former QEXAFS monochromator [**58**]. The second mirror downstream is used to focus the monochromatic X-ray beam onto the sample, down to a diameter of typically 100 µm. Different coatings allow to change the cut-off energy and to alter the reflective properties of the mirrors. Both mirrors have stripes of platinum and rhodium next to each other. The

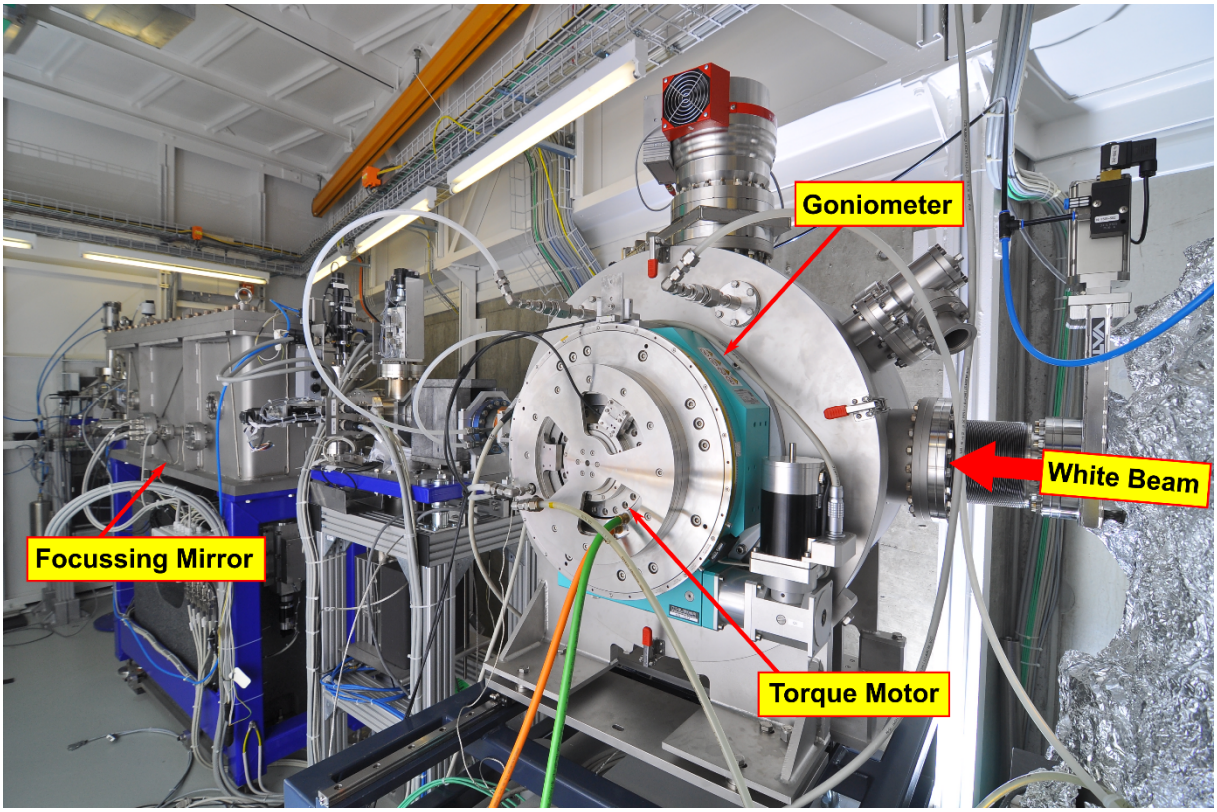

Figure 2.7: Photograph of the interior of the optics hutch of the SuperXAS beamline. The collimated beam enters from the right. The QEXAFS monochromator is recognizable by the turquois goniometer in front of the vacuum chamber of the monochromator.

collimating mirror also offers the bare polished silicon surface. The view of the interior of the optics hutch including the new QEXAFS monochromator is shown in Figure 2.7.

P64 (PETRA III, Deutsches Elektronen Synchrotron, Germany)

The P64 beamline is located at the PETRA III storage ring at the Deutsches Elektronen Synchrotron (DESY, Germany). P64 is dedicated to high-flux XAS experiments and methods, such as QEXAFS on the sub-second time regime, EXAFS of highly diluted systems and X-ray emission spectroscopy (XES). Commissioning of the beamlines started in 2015 and user operation is expected for 2016.

The PETRA III storage ring is operated in top-up mode with 100 mA at 6 GeV. P64 is equipped with a 2 m long undulator which will provide a monochromatic flux of 10^{12} photons per second to 10^{13} photons per second. The accessible photon energy ranges from 4 keV to 40 keV. This undulator can be tapered to enable QEXAFS measurements. In Figure 2.8 the schematic overview of the main optical components are shown. To cope with the high heat-load of the undulator, the monochromators are liquid nitrogen cooled and placed in front of both mirrors. Hence the mirrors are subject to the monochromatic beam only and do not need cooling. The first mirror downstream is a fixed cylinder used for horizontal focusing. The second mirror is flat but can be bent to focus the beam in the vertical direction. A spot size of about 100 µm in diameter will be possible to achieve. Figure 2.9 shows the P64

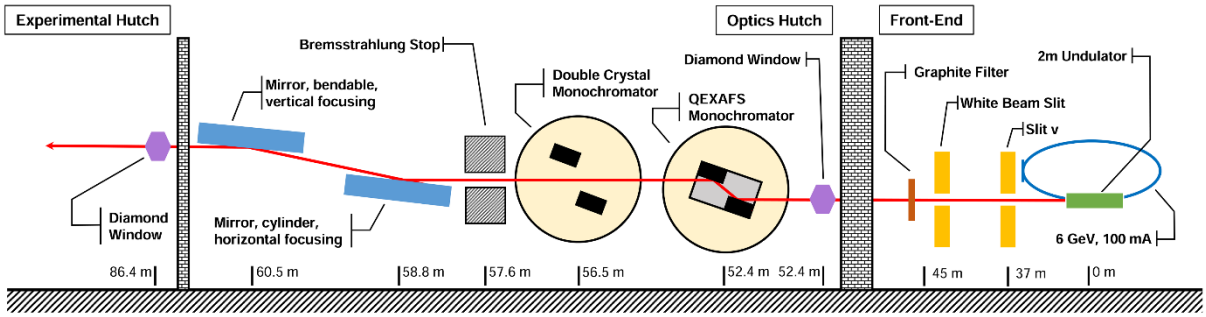

Figure 2.8: Schematic view of the main optical components installed at the P64 (PETRA III, Germany) beamline.

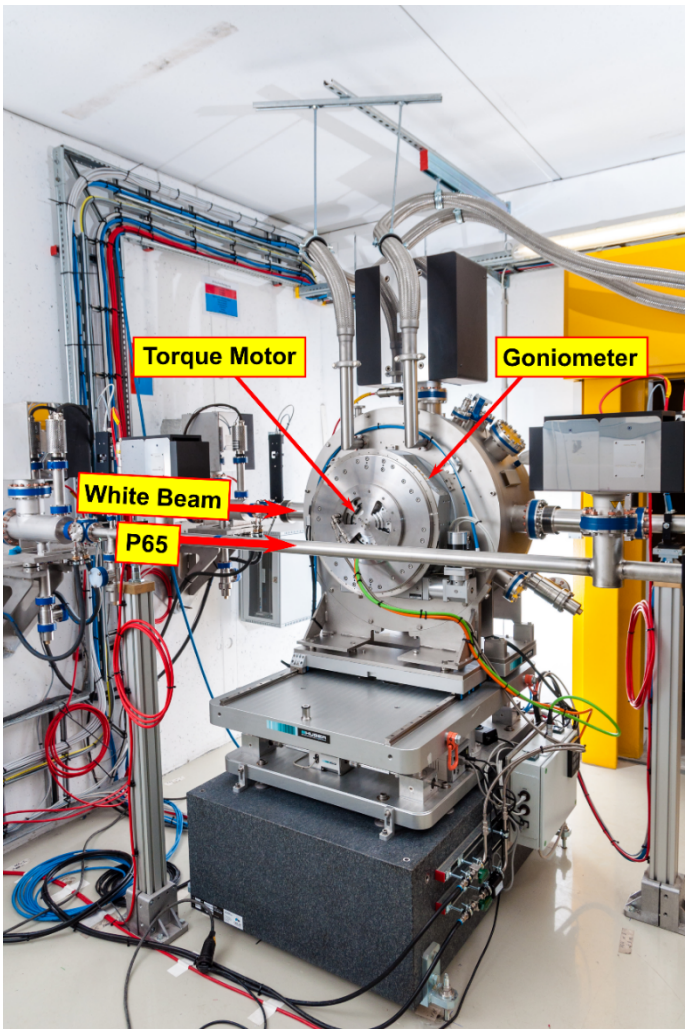

Figure 2.9: Photograph of the QEXAFS monochromator installed in the optics hutch of the beamlines P64 and P65. The white beam enters from the left side. In front of the monochromator the beam tube of P65 is visible.

QEXAFS monochromator installed in the optics hutch. Like the QEXAFS monochromator installed at the SuperXAS, this device was newly developed and is described in detail in Chapter 3.

3 The Dedicated QEXAFS Monochromator

The power of QEXAFS as a structural tool with real time resolution is in particular dependent on the performance of the QEXAFS monochromator. Achievable time resolution, scan range and accessible photon energy define the usability of the monochromator and its value for the user community. High stability and reproducibility of the fast energy scans and special features such as interchangeable crystals define a properly working device and are technically very demanding.

An entirely new design of a QEXAFS monochromator, which meets the experimental demands raised by current research and the requirements and restrictions at modern XAS beamlines, has been developed [**16**]. Two complete monochromators have been manufactured in-house based on this design. The first completed monochromator has been installed at the SuperXAS beamline at the SLS in January 2015 (see section 2.2.2) and is available for user operation since then [**4**]. The successor has been installed in August 2015 at the newly built beamline P64 at PETRA III (see section 2.2.2). Here, user operation is expected to start in the second quarter of 2016 after commissioning. A 3D CAD rendering of both monochromators is shown in Figure 3.1.

This chapter is dedicated to the discussion of the design and concept of the new QEXAFS monochromator. Section 3 covers the mechanical design and section 3.2 presents the novel oscillatory drive of the monochromator. The chapter concludes with an overview of the capabilities and performance of the monochromator. X-ray absorption measurements are presented in Chapter 6.

3.1 Mechanical Design and Concept of the Monochromator

The Bragg axis of the crystal stage is driven by a direct drive torque motor and a goniometer. The torque motor is used to drive the oscillatory movement of the crystals during QEXAFS operation, while the goniometer facilitates precise alignment of the center angle of the oscillation. It also enables conventional step-scanning capabilities when the torque motor is halted. This is a key function towards a one monochromator solution for X-ray spectroscopic beamlines, offering both QEXAFS measurements and conventional scans.

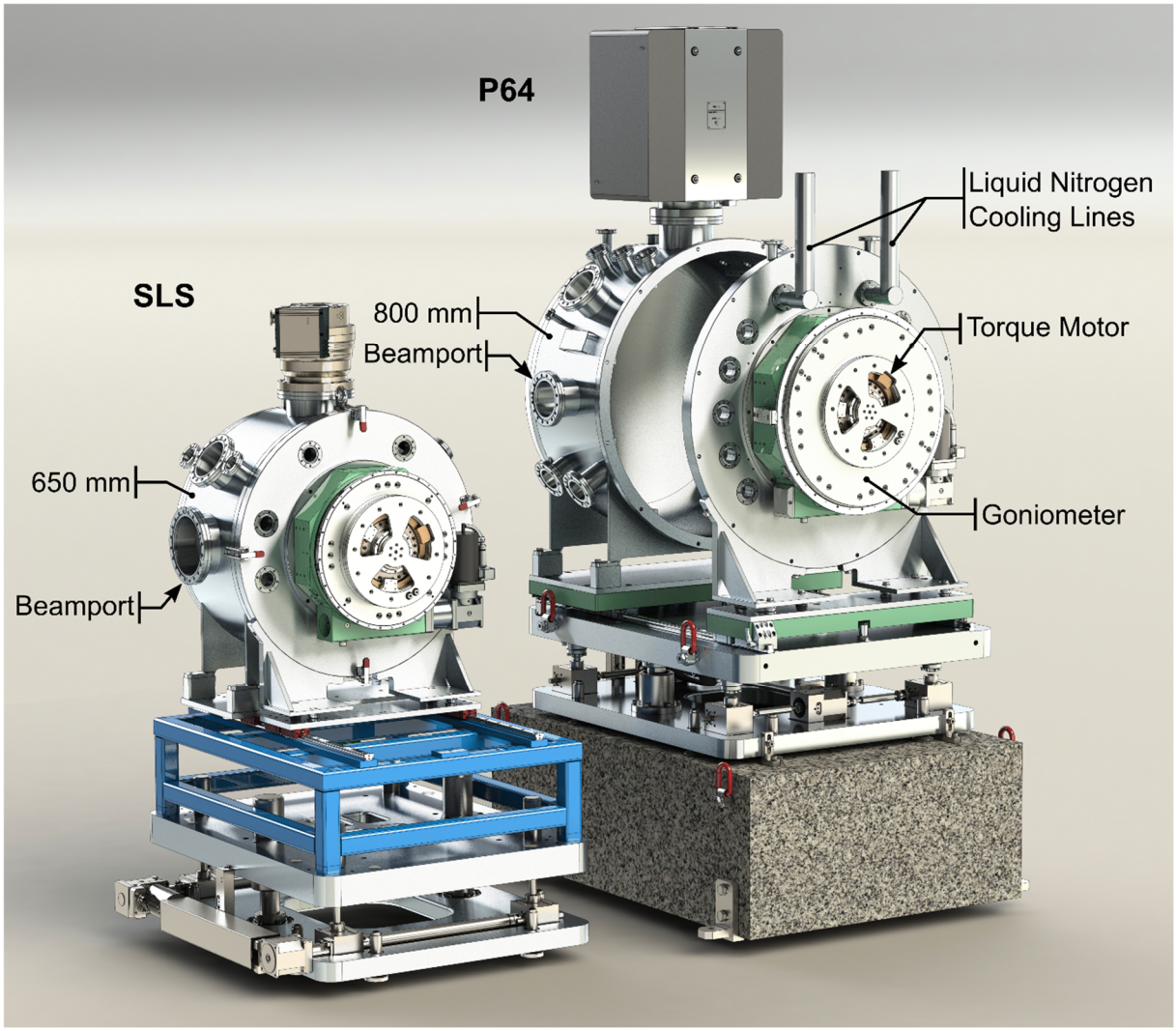

Figure 3.1: 3D rendering of the two QEXAFS monochromators build for the SuperXAS (left) and P64 (right) beamlines.

The entire drive mechanics are installed on the atmospheric side of the monochromator. They consist of a water cooled torque motor (Siemens SIMOTICS 1FW6), which is mounted coaxially to a goniometer. The SLS monochromator uses a Huber 430, the P64 monochromator a larger Huber 440 goniometer. When the rotor of the torque motor oscillates the crystals with a given amplitude and frequency, the goniometer facilitates the adjustment of the mean Bragg angle θ_0. In this way, the movement of the crystal stage θ_{Bragg} is completely mechanically decoupled into a constant and a time-dependent part $\theta_{Osc}(t)$:

$$\theta_{Bragg}(t) = \theta_0 + \theta_{Osc}(t). \tag{3.1}$$

Both axes of rotation are fed independently of each other into the vacuum chamber by means of a single ferrofluidic sealed coaxial rotary feedthrough (VacSol GmbH). This coaxial design considerably simplifies the construction of the drive mechanics, since the exterior components do not need to comply with any vacuum requirements. In addition, maintenance is much easier due to improved accessibility. Mechanical vacuum feedthroughs based on a ferrofluidic seal are known to occasionally cause sharp

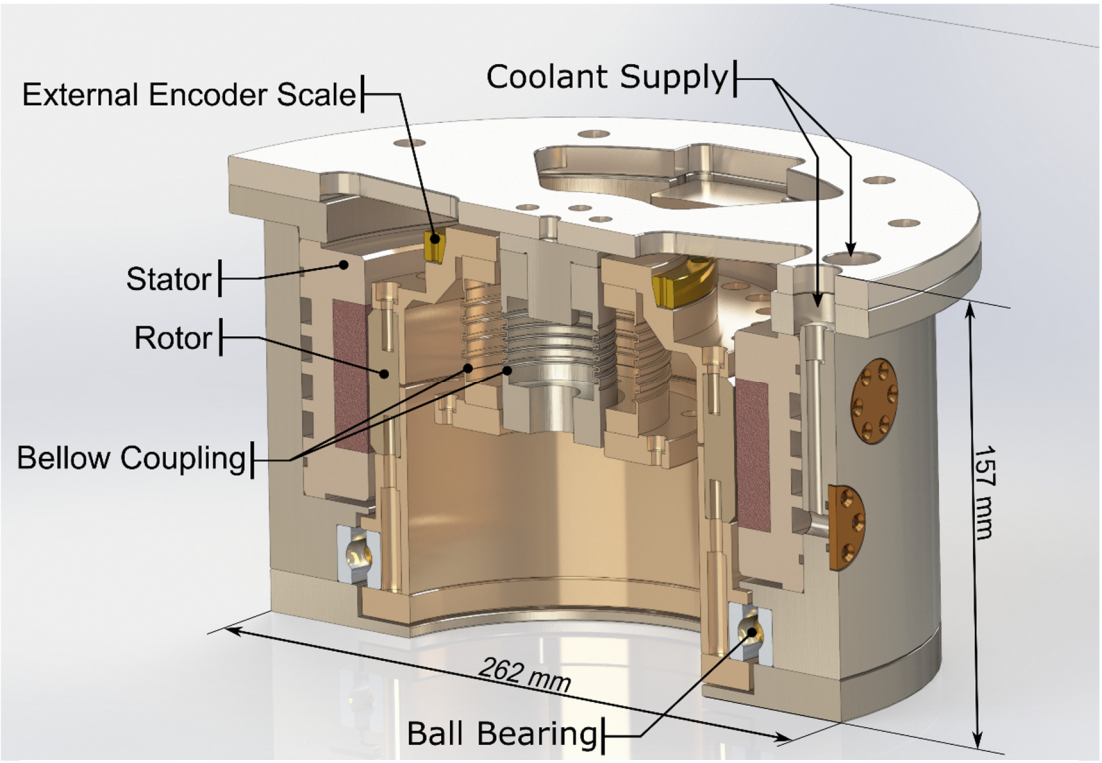

Figure 3.2: Sectional view of the direct drive torque motor. The external encoder is not used for QEXAFS measurements, but can be used to monitor the motion of the rotor. Both bellow couplings are mounted to a single coaxial rotary feedthrough.

pressure spikes caused by microscopic gas bubbles diffusing through the ferrofluid towards the ultra high vacuum side. These pressure spikes were also observed with the employed model, however, no alteration of the frequency of occurrence correlated to the motion of any of the two axes could be noticed. Furthermore, the base pressure of the SLS monochromator of around 5×10^{-8} mbar was stable even at the highest oscillation frequencies of 50 Hz, proving the suitability of ferrofluidic sealed feedthroughs for fast oscillating motions.

A sectional view of the assembled direct drive is given in Figure 3.2. The entire device is mounted coaxially to the goniometer by means of the protruding rim at the top (see Figure 3.1). The hollow orifice of the motor at the bottom fits around the rotary feedthrough (not shown). The interconnection between motor and feedthrough is provided by two metal bellow couplings to compensate for small alignment errors and manufacturing tolerances such as eccentricities, tilt angles and overall length errors. The inner bellow coupling transfers the static motion from the goniometer, while the outer bellow also transfers the oscillatory motion of the rotor. Its transfer torque is rated 100 Nm. Stator and rotor are the actual components of the torque motor. Its working principle and electrical connection is discussed in section 3.2.1.

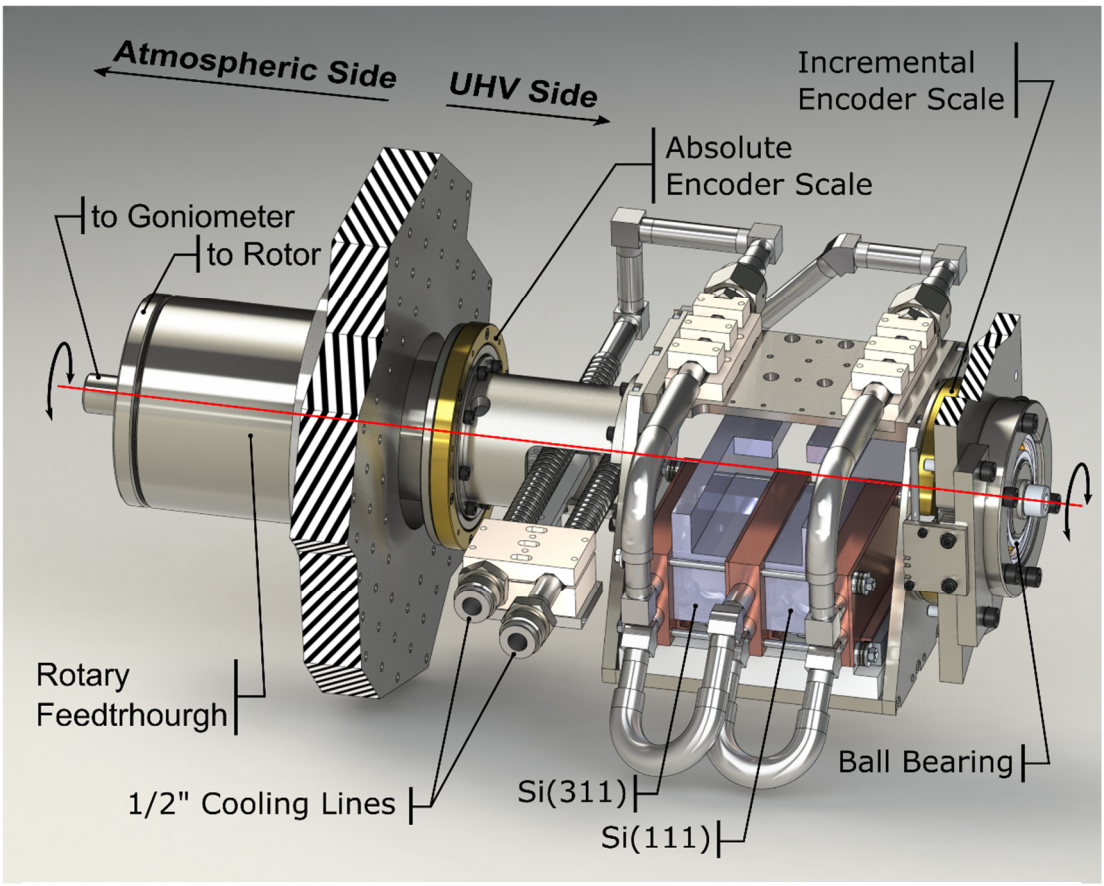

Figure 3.3: Drawing of the in-vacuum crystal stage. The flat front flange of the monochromator vacuum chamber is broken to allow a view onto the atmospheric part of the rotary feedthrough. Cut faces are shaded black and white.

3.1.1 Crystal Stage

The crystal stage is mounted to the outer axis which connects the rotor of the torque motor and is stabilized in vacuum by a lubrication-free ZrO_2 ceramic ball-bearing. The crystal stage holds the monochromator crystals, the crystal cooling unit and the angular encoder scales. Since the entire crystal stage is oscillating during QEXAFS operation, it is optimized with regard to a low mass moment of inertia and high rigidity. A 3D CAD rendering showing the in-vacuum mechanics, the crystal stage and the rotary feedthrough is given in Figure 3.3.

Inside of the vacuum chamber the cooling lines are mounted to a cantilever which is directly driven by the outside goniometer. In this way the mechanical load, which is caused by the static bending of the cooling lines at different Bragg angles, is completely taken by the goniometer instead of the torque motor. Only a short section of the cooling lines of about 20 cm length is bent due to the deflection of the crystal stage.

The crystal stage hosts two channel cut crystals, mounted side by side. A combination of Si(111) and Si(311) crystals allows to cover a wide spectral bandwidth ranging from about 4 keV to 40 keV. The active crystal is selected by a horizontal movement of the monochromator perpendicular to the direction of the X-ray beam. To enable this movement, the monochromator is mounted on support rails

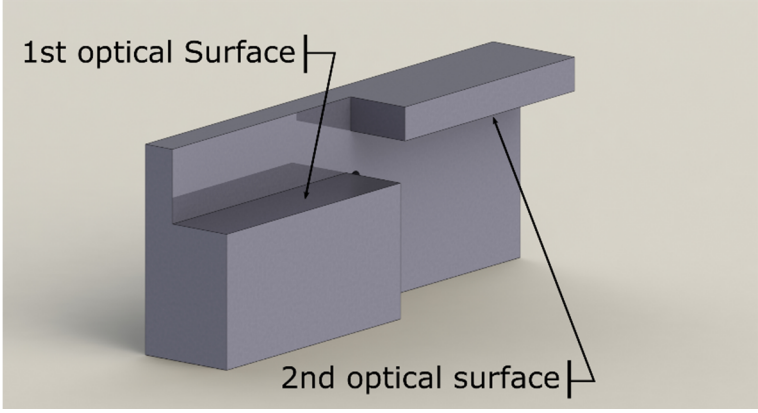

Figure 3.4: 3D image of a generic channel cut crystal. The incident white beam impinges on the 1st optical surface.

and is connected via flexible bellows to the beamline. A remote change of the crystals can be performed without breaking the vacuum within less than one minute. This concept is new to QEXAFS monochromators. At current facilities the QEXAFS monochromators only carry one crystal at a time. To still cover an extended energy range, two separate identical monochromators, equipped with different crystals, are often installed in a row at a beamline [**19**,**20**]. This implementation obviously requires twice the acquisition cost for two complete monochromator and space in the optics hutch.

3.1.2 Channel Cut Crystals

Channel cut crystals are made of one large single crystal (see Figure 3.4). Due to the common backplane and compact dimensions they give ultimate intrinsic strength against distortions or deformations and allow for highest displacement velocities. Channel cut crystals are therefore ideally suited for QEXAFS monochromators. Furthermore, the lattice planes of the optical surfaces are already perfectly parallel to each other, making any degree of freedom and potentially weak spots, which otherwise require alignment, needless. Thus by omitting these actuators the vulnerability of exciting unwanted vibrations are significantly reduced. However, there are two major drawbacks of channel cut crystals, which need to be considered in X-ray monochromator applications. Both shortcomings, which are outlined in the next paragraphs, can be adequately compensated for by using coated and focusing mirrors [**25**,**45**].

The first undesirable property is a direct consequence of the parallelism of the optical surfaces. The lattice planes of these surfaces of a stress-free well manufactured channel cut crystal are perfectly parallel to each other yielding the optimum reflectivity of the fundamental wavelength. However, according to Bragg's law, equation (2.6), higher harmonic wavelengths are also reflected with high efficiency and contaminate the monochromatic beam. Since a generic channel cut crystal cannot be detuned easily, the harmonic content needs to be rejected with additional optical components along the beamline. Coated mirrors are well suited to perform this task by exploiting their properties of reflectivity around the critical angle [**25**,**45**]. Currently there are also intentions to develop tunable channel cut

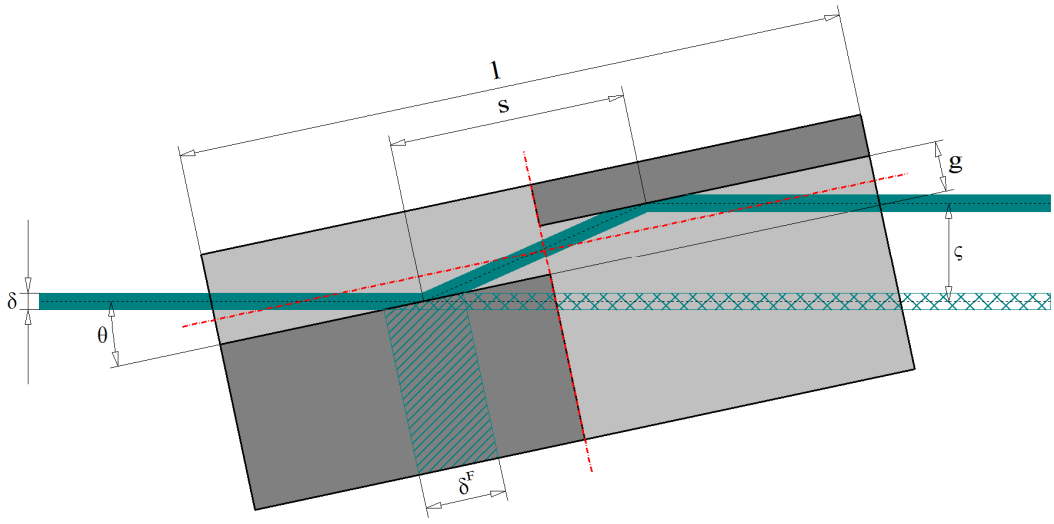

Figure 3.5: Shown is the lateral view of a generic channel cut crystal with total length l and crystal gap g. Here, the axis of rotation is perpendicular to the plane of projection and goes through the intersection of the red dashed cross lines. The shaded area beneath the 1st optical surface illustrates the width of the footprint δ^F of the incident beam whose width is δ. The distance of the two points of impact is denoted by s and the vertical displacement of the beam is denoted by ζ.

crystals for QEXAFS monochromators [**59**]. However, building a tunable and yet stable crystal unit is quite challenging due to the strong alternating acting forces caused by the rapid oscillations.

The second unwanted property is a result of the geometry, which leads to a change of the beam height of the outgoing monochromatic beam during an energy scan. This displacement ζ between the inbound and outbound beam is a function of the Bragg angle θ and the gap width between the optical surfaces, which is denoted as g according to the drawing of Figure 3.5. The total displacement ζ and the actual variation during an energy scan $\Delta\zeta$ are given by equations (3.2) and (3.3). The latter is a function of the start energy E_1 and the scan range $\Delta E = E_2 - E_1$ and is evaluated in Figure 3.6 for a Si(111) and Si(311) channel cut crystal with a gap width of 12 mm.

$$\zeta = 2g\cos(\theta) \tag{3.2}$$

$$\Delta\zeta(E_1, \Delta E) = 2g\left(\sqrt{1-\left(\frac{hc}{2d}\right)^2\left(\frac{1}{E_1+\Delta E}\right)^2} - \sqrt{1-\left(\frac{hc}{2d}\right)^2\left(\frac{1}{E_1}\right)^2}\right) \tag{3.3}$$

Typically these vertical movements are in the order of a few 100 µm. For instance, measuring the EXAFS of the Cu K-edge from 8.8 keV to 9.9 keV causes a vertical shift of about 130 µm using the Si(111) crystal. Measuring the Pd K-edge from 24.2 keV to 25.3 keV using a Si(311) crystal results in a beam movement of about 25 µm. However, the actual beam movement on the sample can be efficiently reduced if focusing optics such as mirrors or lenses are used downstream of the monochromator.

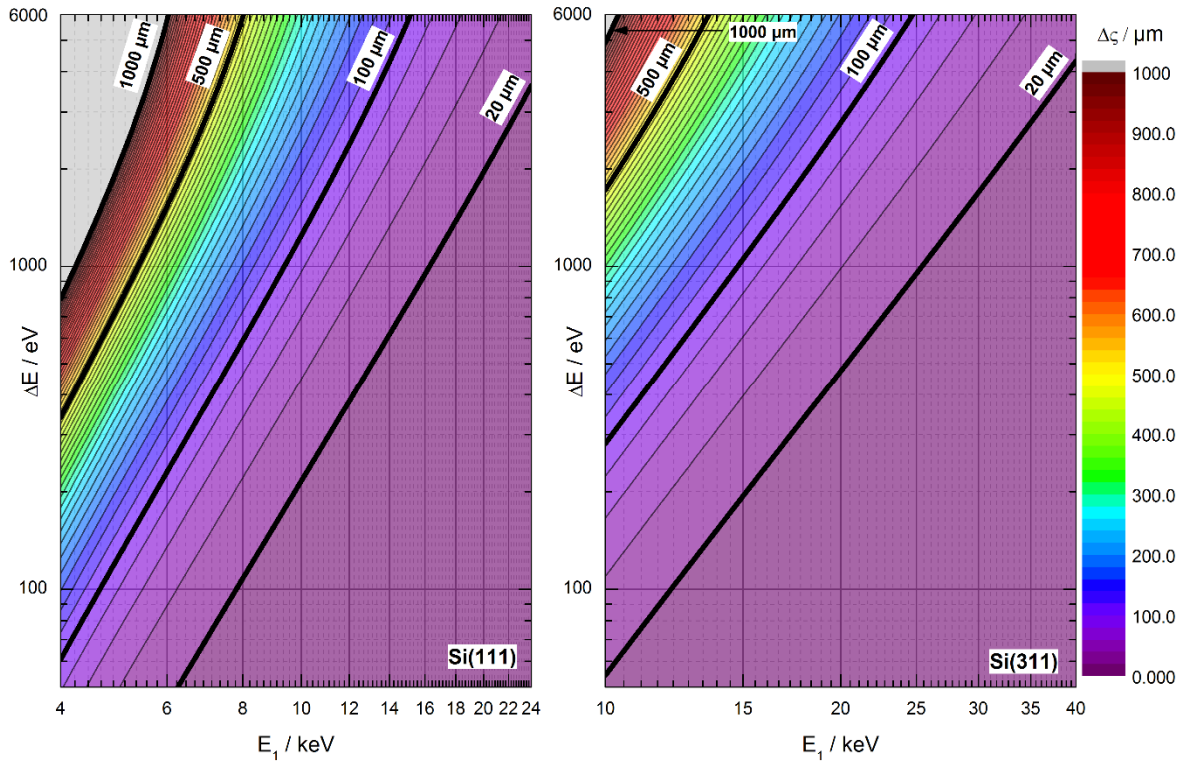

Figure 3.6: The colors indicate the variation of the beam height ζ after the monochromator during an energy scan using a channel cut crystal with a gap width of 12 mm. The data is based on equation (3.3). The black solid lines are equally spaced (20 µm).

Observations at the SLS with a focused beam of 100 µm cross section showed rarely a vertical beam movement larger than 50 µm during QEXAFS measurements.

Boundary Conditions and Crystal Dimensions

The design of a channel cut crystal is usually subject to some boundary conditions. Besides the need to cover the desired energy range, radiation safety issues may also influence the design. At PETRA III it is required that the vertical distance between the inbound white beam, which is within the orbit plane of the storage ring, and the outbound monochromatic beam is larger than 20 mm. At the same time, this distance may not be larger than 24 mm. These restrictions are due to radiation safety specifications and an aperture with these dimension is installed downstream in the optics hutch of the beamline (see Figure 2.8) in order to block bremsstrahlung and arbitrary scattered photons.

The design parameters as well as the actual properties which were realized in the final design of the channel cut crystals are listed in Table 3.1. To cover the complete desired energy range from 4 keV to 40 keV and to avoid too shallow Bragg angles it was decided to use two different channel cut crystals. Therefore, the monochromators are equipped with Si(111) and Si(311) channel cut crystals, which are mirror images of each other. The required Bragg angle to reach the lowest target energy E^*_{min} with a Si(111) crystal and equation (3.2) dictate the minimum permitted gap width. The minimum length $l = s + \delta^F$ of the crystal is given by the distance $s = g/tan(\theta)$ between the two points of incidence on the

Target Values				Actual Values			
Crystal	**Variable**	**Value**	**Unit**	**Crystal**	**Variable**	**Value**	**Unit**
Si(111)	E^*_{min}	4	keV		θ_{min}	5	°
Si(311)	E^*_{max}	40	keV		θ_{max}	30	°
	ζ^*_{min}	20	mm		g	12	mm
	ζ^*_{max}	24	mm		l	160	mm
	δ^*_{Beam}	1.5	mm		δ_{Beam}	1.5	mm
	$\theta(E^*_{min})$	5.4	°	Si(111)	E_{min}	3.95	keV
	$\theta(E^*_{max})$	29.6	°	Si(111)	E_{max}	22.68	keV
	$g(E^*_{min})$	11.50	mm	Si(311)	E_{min}	7.57	keV
	$s(E^*_{max})$	121.7	mm	Si(311)	E_{max}	43.44	keV
	$\delta^F(E^*_{max})$	15.9	mm		ζ_{min}	20.8	mm
					ζ_{max}	23.9	mm
					s_{min}	20.8	mm
					s_{max}	137.2	mm
					δ^F_{min}	3.0	mm
					δ^F_{max}	17.2	mm

Table 3.1: The design of the QEXAFS monochromator for P64 is based on the target values.

optical surfaces at the highest target energy E^*_{max} using a Si(311) and the beam footprint $\delta^F = \delta/sin(\theta)$ at this Bragg angle.

The dimensions listed in Table 3.1 do not yet define the crystal entirely. The point through which the Bragg axis is placed needs to be defined, as it determines the length of each optical surface. The final design is a compromise between a minimized mass moment of inertia and an optimized contact area for indirect lateral cooling. Figure 3.7 shows two different possible designs of this crystal. The top crystal A) is a solution which places the Bragg axis centric within the 1st optical surface while the Bragg axis of the bottom crystal B) is placed symmetrically midway between the two optical surfaces. The latter design B) holds a much larger contact area as compared to the other option. In addition, the outer regions of the crystal are subject to smaller tangential velocities during oscillation, which improves stability. This particular design was chosen for the QEXAFS monochromator. However, due to its symmetry and in contrast to crystal A), different areas of the 1st optical surface are illuminated at different Bragg angles. In order to keep the beam on the crystal, as shown in the drawing, its height relative to the incident white beam needs to be adjusted if large energy changes are made. The required vertical movement of the crystal due to a change of the Bragg angle is given by equation (3.4) and amounts to 1.56 mm at most, considering the full Bragg angle range from 5° to 30°. During typical QEXAFS energy scans the required movements are so small that they can be entirely neglected.

$$\zeta_{Crystal} = g(cos\theta_1 - cos\theta_2) \tag{3.4}$$

The final crystal, bottom drawing of Figure 3.7, is 160 mm long and has a gap width of 12 mm. In compliance with the PETRA III radiation safety specifications, the Bragg angle range is from 5° to 30°. This allows to access photon energies between 4 keV and 22 keV with a Si(111) and 8 keV to more

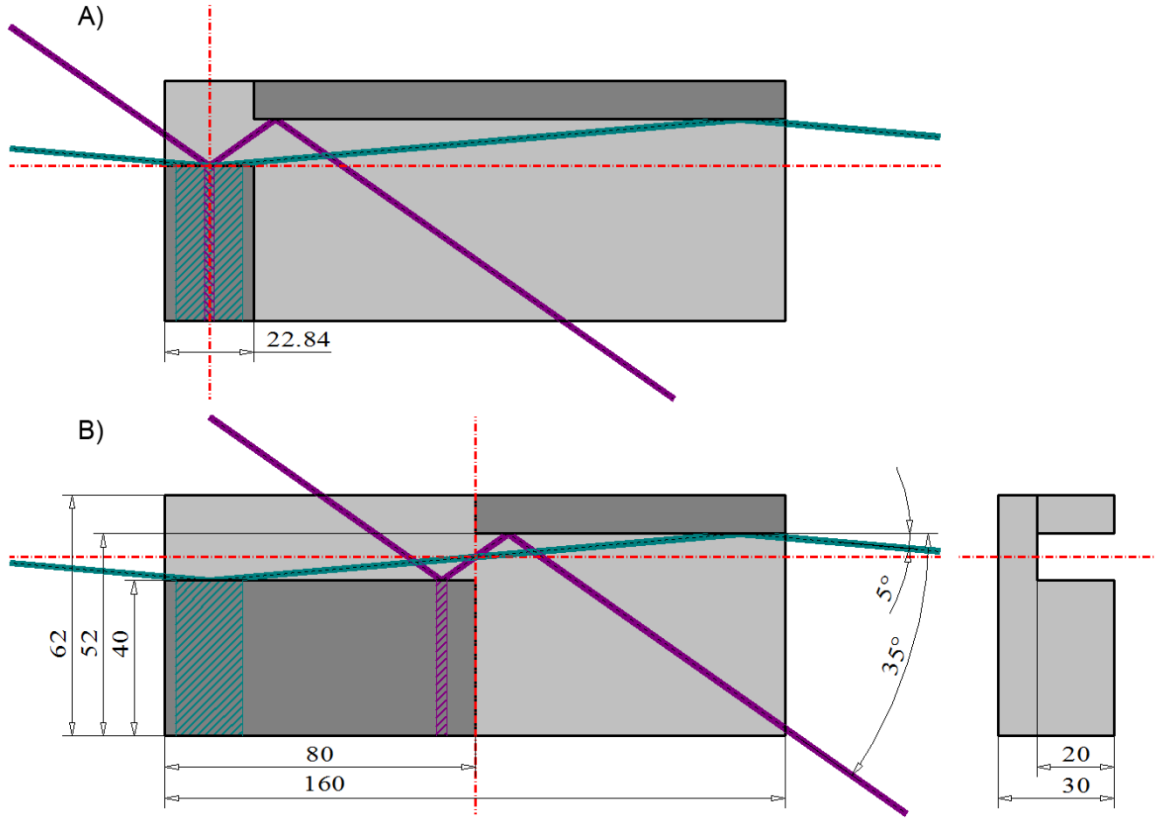

Figure 3.7: Drawing of two different channel cut crystal with the same outer dimensions according to Table 4.1. The Bragg axis of rotation is perpendicular to the plane of projection and goes through the intersection of the red dashed cross lines. The shaded areas beneath the 1st optical surface illustrate the width of the footprint of the incident beam. Crystal B) is used for the PETRA III and SLS QEXAFS monochromators.

than 40 keV with a Si(311) crystal. Due to different radiation safety regulations at the SLS, the Bragg angle can be increased to over 35° using the same crystal there. This enables to reach the Fe K-edge at 7111 eV with a Si(311) crystal.

3.2 Oscillatory Drive

The main task of a QEXAFS monochromator is to facilitate fast and continuous energy scans. In order to extend the scan rate into the sub-second time regime, dedicated monochromators with specialized mechanics are required. The accuracy and stability of the involved motions are of utmost importance especially at higher scan rates. To minimize mechanical stress and vibrations on the mechanics and crystals, energy scans are preferably realized by a smooth sinusoidal-like oscillation of the Bragg axis. This oscillatory motion is realized by means of a specialized drive, which meets the required accuracies and can be operated continuously for hours without interruptions.

The oscillatory drive is that mechanical component which puts the monochromator crystals into oscillatory motion. There are different approaches to realize this motion and the majority of dedicated QEXAFS monochromators, which are in operation today, are either based on a cam shaft [**19**,**60**] or a

direct drive [**4**,**20**]. All modern implementations facilitate continuous sub-second resolution and remote control of the scan rate and range.

Cam Shaft Drives

At present the most often used drive for QEXAFS monochromators is based on a mechanical cam shaft originally developed in 2005 [**61**]. The rotation of an eccentric disk or shaft is transferred into an oscillatory motion, which deflects a tilt table. The crystal assembly is mounted on top of that tilt table and follows its motion. The mechanics are very elaborate in order to achieve a reproducible oscillatory motion and is quite complex, involving multiple gears and flexible hinges. The entire mechanical construction is often placed inside the vacuum chamber of the monochromator, which puts restrictions on the overall size and hence attainable torque, as well as on applicable materials, in particular with regard to lubricants required for built-in gears. The most important representatives of synchrotron beamlines using a cam shaft driven QEXAFS monochromator today are the ROCK beamline (Soleil, France) [**19**] and until recently the SuperXAS beamline (SLS, Switzerland) [**58**]. In January 2015, the QEXAFS monochromator at the SuperXAS was replaced in favor of the newly build monochromator, which uses a direct drive.

Direct Drives

The fundamental idea behind a direct drive is to achieve a fully electronically controlled motion. The oscillation frequency and amplitude or even the actual trajectory of the oscillatory motion should be remotely controllable without involving mechanical parts. This is typically realized by means of a gearless servo motor and a direct mount of the monochromator crystals to the shaft of the motor. Since this requires significantly less mechanical components, especially moving parts, such as gears, bearings or hinges, the mechanical complexity is considerably reduced. This simplifies the design of the drive and improves the overall stability, durability and vacuum compatibility. The modern direct drive concept is a very young trend even for conventional X-ray monochromators and a more recent development for QEXAFS monochromators. Apart from the two newly build QEXAFS monochromators, there is only one other direct driven QEXAFS monochromator system in operation at present. This device is part of beamline BL33XU (SPring-8, Japan) [**20**].

Piezo Drives

In terms of a pure electronically controlled motion, a piezo drive can be regarded as a special variation of a direct drive. The crystal assembly of a piezo driven QEXAFS monochromator is mounted on top of a piezo tilt table [**62**,**63**,**64**,**65**]. An applied sinusoidal voltage excites oscillations of the tilt table and thus the crystal assembly. Due to the high dynamics of piezo actuators, very high oscillation frequencies can be achieved and frequencies of up to 111 Hz have been reported [**62**]. However, the angular range of the tilt tables used so far were very limited prohibiting in most cases full EXAFS

measurements. The hysteresis of the piezo elements and their durability in UHV environments and upon exposure to the radiation background are still problems which need to be solved. Despite this promising approach and suitability for instance for quick XANES 2D mapping of surfaces or 3D XANES tomography [**5**,**6**], there is no piezo drive based QEXAFS monochromator in operation today.

3.2.1 The Direct Drive Torque Motor of the QEXAFS Monochromator

The oscillation of the monochromator crystals is driven by a direct drive torque motor (Siemens SIMOTICS 1FW6). This type of motor is a special layout of a three-phase synchronous machine, featuring a brushless design and improved capability of creating and maintaining a high torque at low or even zero speed. Therefore, the motor holds a high number of magnetic poles on a comparatively large diameter. A sectional view of the bare torque motor is given in Figure 3.8 and a summary of its properties are listed in Table 3.2.

The electromagnet of the motor contains three internally starlike connected coils which each has 44 magnetic poles distributed alternating along the inner circumference of the stator. The magnetic field composed of these coils causes a torque on the rotor until it has reached its equilibrium position by rotation into a potential minimum. Due to the arrangement of the electromagnet the potential minimum can be placed anywhere on the circumference by proper current feeding of the three coils. In this way positioning can be realized. In typical applications a dedicated controller unit constantly monitors the angular position of the rotor with respect to the magnetic field and regulates the required currents in a closed-loop feedback. This scheme allows to realize nearly arbitrary trajectories of the rotor but is limited by the time constant of the control loop, which often amounts to a few milliseconds. The actually employed concept to drive the torque motor in an oscillatory motion differs distinctly from this general scheme. Instead of the common closed-loop technique an unique open-loop scheme was developed to overcome the restrictions of a finite time constant. This scheme is described in section 3.2.2.

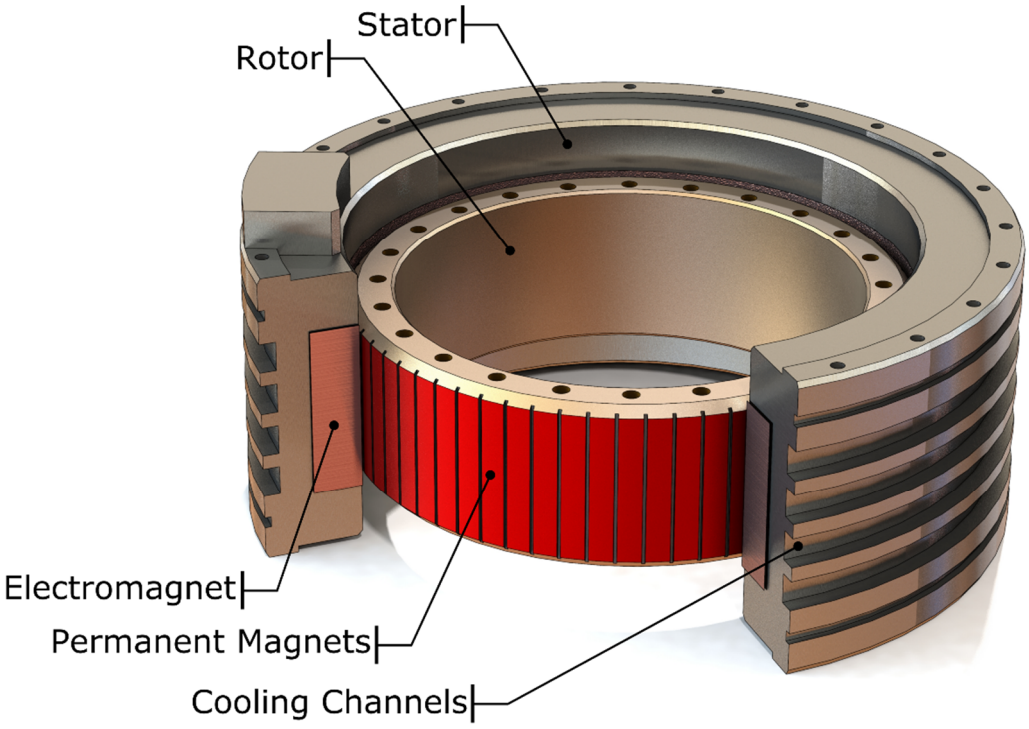

Figure 3.8: Sectional view of the used torque motor (Siemens SIMOTICS 1FW6). The open diameter of the rotor amounts to 140 mm. The grooves on the outer surface of the stator provide efficient water cooling to remove heat from the electromagnet.

Siemens SIMOTICS 1FW6

Parameter	Value	Unit
Rated Torque	113	Nm
Maximum Torque	179	Nm
Thermal Stall Torque	84.1	Nm
Rated Current	5.6	A
Maximum Current	9.5	A
Thermal Stall Current	4.1	A
Number of Pole Pairs	22	
Torque Constant	20.8	Nm/A
Voltage Constant	1258	Vmin/1000
Rotor Mass	2.6	kg
Rotor Mass Moment of Inertia	1.52	$10^{-2}kgm^2$
Phase Resistance	14.9	Ω
Phase Inductivity	47.1	mH

Table 3.2: Summary of the torque motors data sheet showing the significant properties.

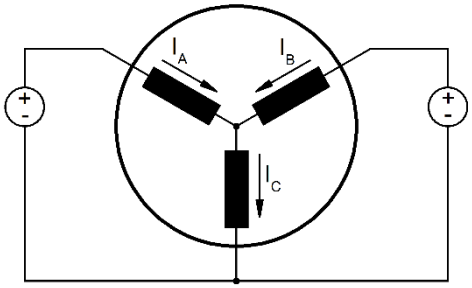

Figure 3.9: Schematic of the external connections of the torque motor. The quantities I_A and I_B refer to the electrical currents driven by the two power supplies shown on the sides. The electrical current I_C results due to the internal and external connections of the three coils.

3.2.2 The Open Loop Drive

Instead of controlling the magnetic field continuously in order to position the rotor in a closed-loop scheme, the open-loop concept exploits the periodic structure of the magnetic field. In total the motor holds 22 pole pairs per coil distributed around its circumference, giving rise to a sinusoidal magnetic field with a periodic length of about 16.4°. The field of a single coil is used as a static background potential and oscillations of the rotor are excited by induced perturbations to this potential by means of the remaining two coils (see Figure 3.9). This implementation facilitates free oscillations around the equilibrium position which is the potential minimum of the background potential. Since no control loop is involved, this drive concept is not restricted by any time constant or propagation delay. The achievable oscillation frequencies and amplitudes are only limited by the maximum attainable torque of the motor, the mass moment of inertia of the moving parts and the control speed of the used power supplies, which deliver the coil currents. Realized frequencies and amplitudes of this drive, as well as the accuracy and repeatability of the oscillatory motion, are discussed in the next section 3.3.

Two power supplies (Elektro-Automatik PSI8720-152U-HS) are used to feed sinusoidal currents through two arbitrary coils. The third coil and the power supplies are drawn to the same ground, as depicted in Figure 3.9. If the currents, I_A and I_B are of the form of equations (3.5) and (3.6) the current through the third coil is static and equals 2β. The DC components of these currents determine the background potential, whereas the AC components cause a deflection of the rotor leading to an oscillation around the potential minimum.

$$I_A(t) = \alpha \cdot \sin(2\pi f_{Osc} t) + \beta \tag{3.5}$$

$$I_B(t) = \alpha \cdot \sin(2\pi f_{Osc} t + \pi) + \beta \tag{3.6}$$

The properties of the rotor oscillation, i.e. amplitude and frequency, depend on the parameters α, β and f_{Osc} of equations (3.5) and (3.6). The frequency of the mechanical oscillation is controlled by the parameter f_{Osc}. The scaling factor α influences the strength of the deflection and is thus positively correlated to the amplitude of the oscillation. The parameter β controls the shape of the potential, which

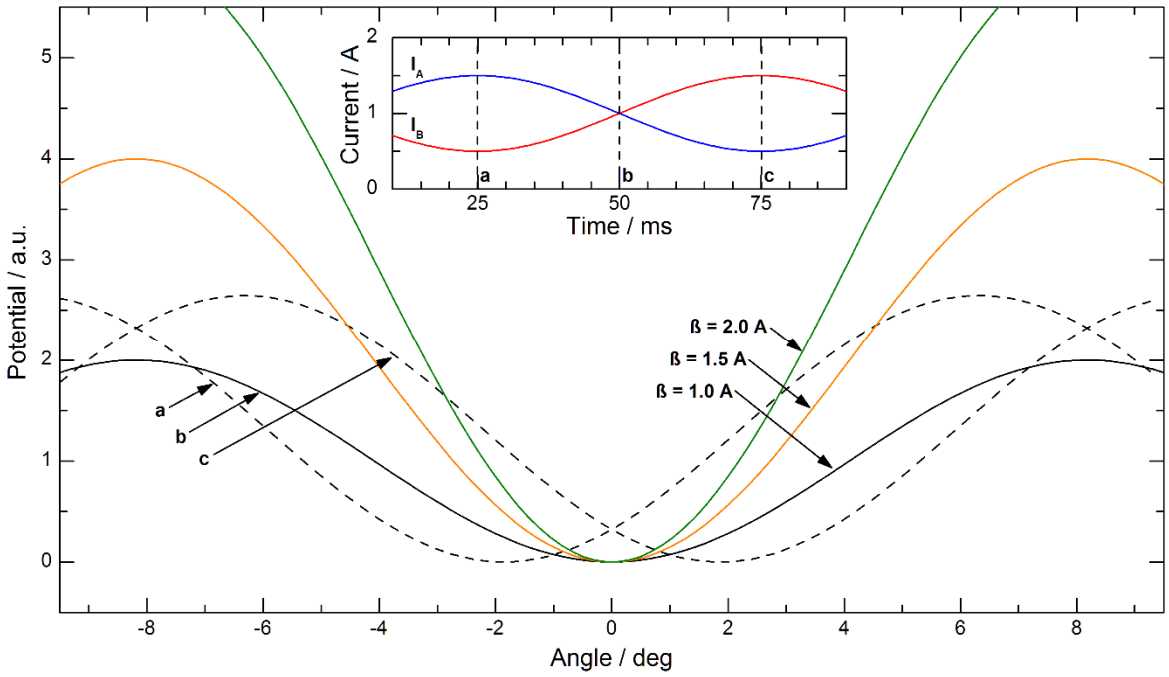

Figure 3.10: The solid lines show the magnetic potential experienced by the rotor for α = 0.5 A and different values of β. The dashed lines show the perturbed potential at two different points in time, as indicated by the vertical lines a and c in the inset, which shows the time dependent current according to equations (3.5) and (3.6) with α = 0.5 A, β = 1.0 A and f_{osc} = 10 Hz.

is shown in Figure 3.10. Since a change of β shifts the resonance frequency of the system inevitably, the oscillation amplitude is altered mutually. It therefore depends on the actual oscillation frequency whether a change of β correlates positive or negative with the oscillation amplitude.

3.3 Capabilities and Mechanical Performance

In the following sections, the capabilities and the mechanical performance of the new QEXAFS monochromator are investigated and discussed. First the achievable scan rate and scan range, i.e. oscillation frequency and amplitude, using the described open loop drive are reviewed. The actual accuracy and repeatability of the oscillation are examined, based on angular encoder measurements during QEXAFS operation. Finally the long term stability is tested, which is an important property for non-QEXAFS applications.

3.3.1 Scan Rate and Range

The attainable angular amplitude ε of the oscillating rotor dependents strongly on its oscillation frequency f_{Osc}. This is consistent with the assumption of a constant maximal kinetic energy, which is proportional to $\varepsilon^2 f_{Osc}^2$ in the case of a pure sinusoidal movement. In a simple mechanical model, where the rotor follows a sinusoidal trajectory and drag and friction emerging from the mechanics and bearings are neglected, the attainable amplitude can be estimated from equation (3.7).

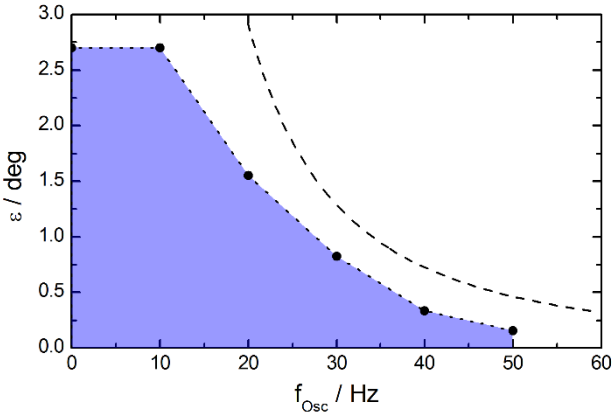

Figure 3.11: The data points of the dotted line show the observed maximum angular amplitudes of the oscillatory drive installed at the fully assembled SLS monochromator. The blue area beneath this line represents the accessible parameter range for QEXAFS operation. The dashed line displays the theoretical expectation based on equation (3.7) with τ = 80 Nm and J = 0.1 kgm^2.

$$\varepsilon = \frac{1}{4\pi^2 f_{Osc}^2}\frac{\tau}{J} \tag{3.7}$$

Here τ is the torque of the motor and J the mass moment of inertia of all the moving parts. The largest experimentally obtained amplitude of the fully assembled monochromator and the theoretical expectation according to this equation as a function of the oscillation frequency are shown in Figure 3.11. The usable parameter space of the oscillatory drive is given by the blue colored area beneath the dotted line. Angular amplitudes larger than 2.7° may be technically possible at low frequencies, but were not investigated in detail, in order to avoid too much load on the mechanics. Frequencies greater than 50 Hz result in very small impractical amplitudes. Besides the limited strength of the torque motor, this limitation is also caused by the employed power supplies which are not able to fully regulate the sinusoidal currents at high frequencies. As a consequence the offset current β increases inevitably at these frequencies and dampens the angular amplitude.

Energy Scan Range

As in conventional XAS measurements, the scan range of QEXAFS spectra is given by the Bragg angle range. It is therefore defined by the amplitude and center position of the crystal oscillation. The maximum amplitude is limited by the torque of the direct drive motor and decreases with higher oscillation frequencies as observed above. The two plots of Figure 3.12 indicate the attainable spectral range $\Delta E = E_2 - E_1$ as a function of the start energy E_1 based on the largest possible amplitude at a given oscillation frequency (see Figure 3.11). Consequently, the gray colored areas below any solid curve represent the accessible spectral range at this oscillation frequency. The plots indicate that the total scan range can be made quite large, which can be well exploited in order to acquire several

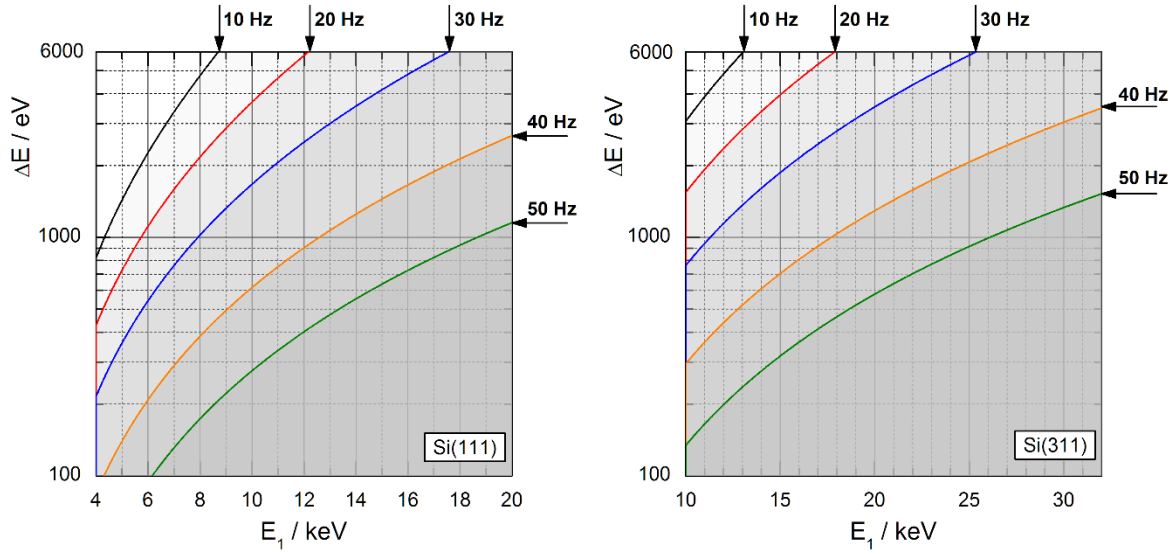

Figure 3.12: The solid curves show the accessible spectral range from E_1 to $E_1 + \Delta E$ of a QEXAFS measurement at constant oscillation frequencies using Si(111) and Si(311) crystals. QEXAFS measurements are possible within the grey areas beneath the solid curves.

absorption edges simultaneously. An example which nicely demonstrates the advantage of having timely correlated measurements at two absorption edges is given in section 6.2.1.

3.3.2 Accuracy of the Crystal Oscillation

The crystal motion is measured with high accuracy using the angular encoder during QEXAFS scans. It is therefore, that its actual trajectory does not need to be known precisely in advance. However, the trajectory can severely influence the mechanical stability of the monochromator, especially if it deviates from a pure sinusoidal motion and is hence likely to excite unwanted vibrations of the mechanics. The crystal oscillations were analyzed for various oscillation frequencies and amplitudes. The evaluated angular encoder data are based on the QEXAFS measurements at the Yb L_{III}-edge which will be discussed in section 6.1.1.

Raw encoder signals with gradually increasing angular deflection from 0.61° to 2.56° at a constant oscillation frequency of 10 Hz are shown in the left plot of Figure 3.13. The right plot of this figure shows the deviation of the raw encoder data from a sinusoidal fit performed over 100 successive oscillation periods. The maximum deviations are in the range of 25 arcsec to 119 arcsec. The increase of the deviations generally correlate with the increase of the angular deflection. This observation agrees well with the principles of the open-loop drive as discussed in section 3.2.2, according to which the rotor oscillates in the minimum of a sinusoidal potential. For small angular deflections the experienced potential is nearly harmonic, resulting in a motion close to a perfect sine curve. As the amplitude increases, the experienced potential becomes more anharmonic, resulting in increased deviations from a pure sinusoidal movement.

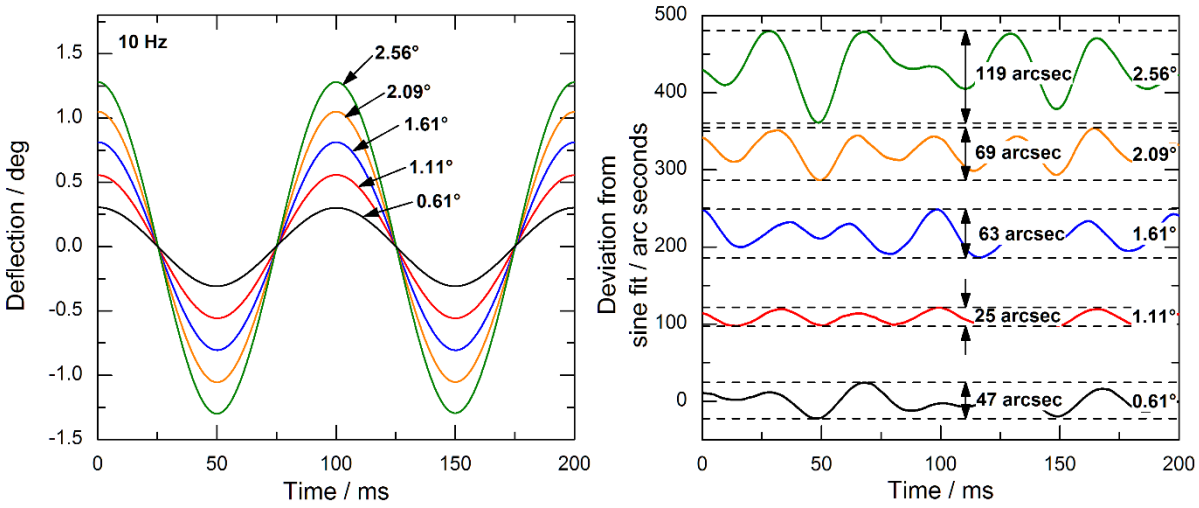

Figure 3.13: Trajectory at 10 Hz oscillation frequency and various amplitudes [**16**]. Given are the total angular ranges of the oscillation. The right plot shows the difference of the actual movement to sinusoidal fits.

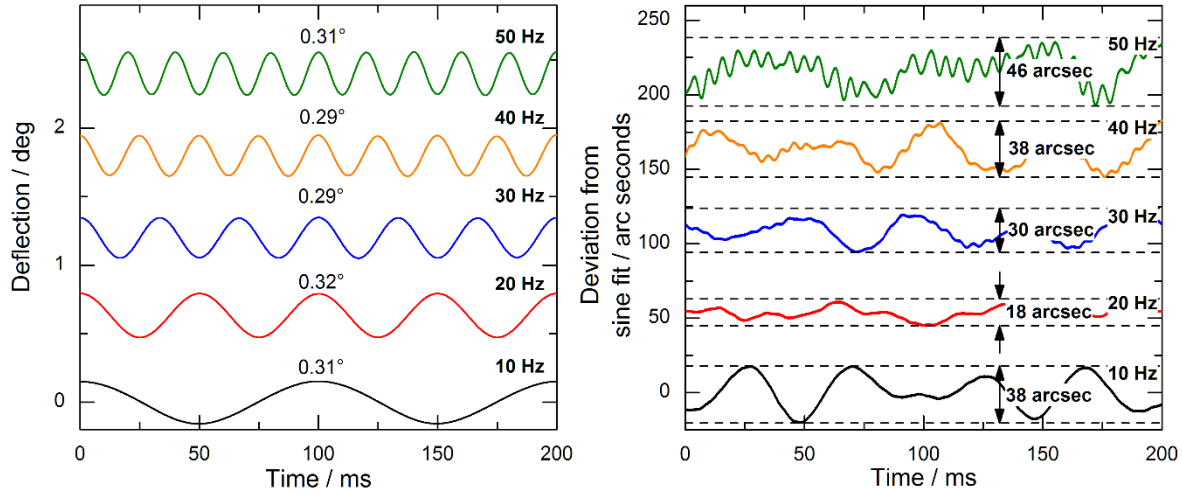

Figure 3.14: Trajectory at different oscillation frequencies [**16**]. Given are the total angular ranges of the oscillations. The right plot shows the difference of the actual movement to sinusoidal fits.

Crystal movements at a nearly constant angular deflection of 0.3° and increasing oscillation frequencies from 10 Hz to 50 Hz were also analyzed. The corresponding raw encoder signals are shown on the left side of Figure 3.14. Again, the right plot shows the deviations of the raw encoder values from a sinusoidal fit performed over 100 oscillation periods. The observed deviations stay within 46 arcsec and do not increase significantly with higher oscillation frequencies, which is again in agreement with the principles of the open-loop drive, since the magnetic potential is nearly harmonic throughout the measurements.

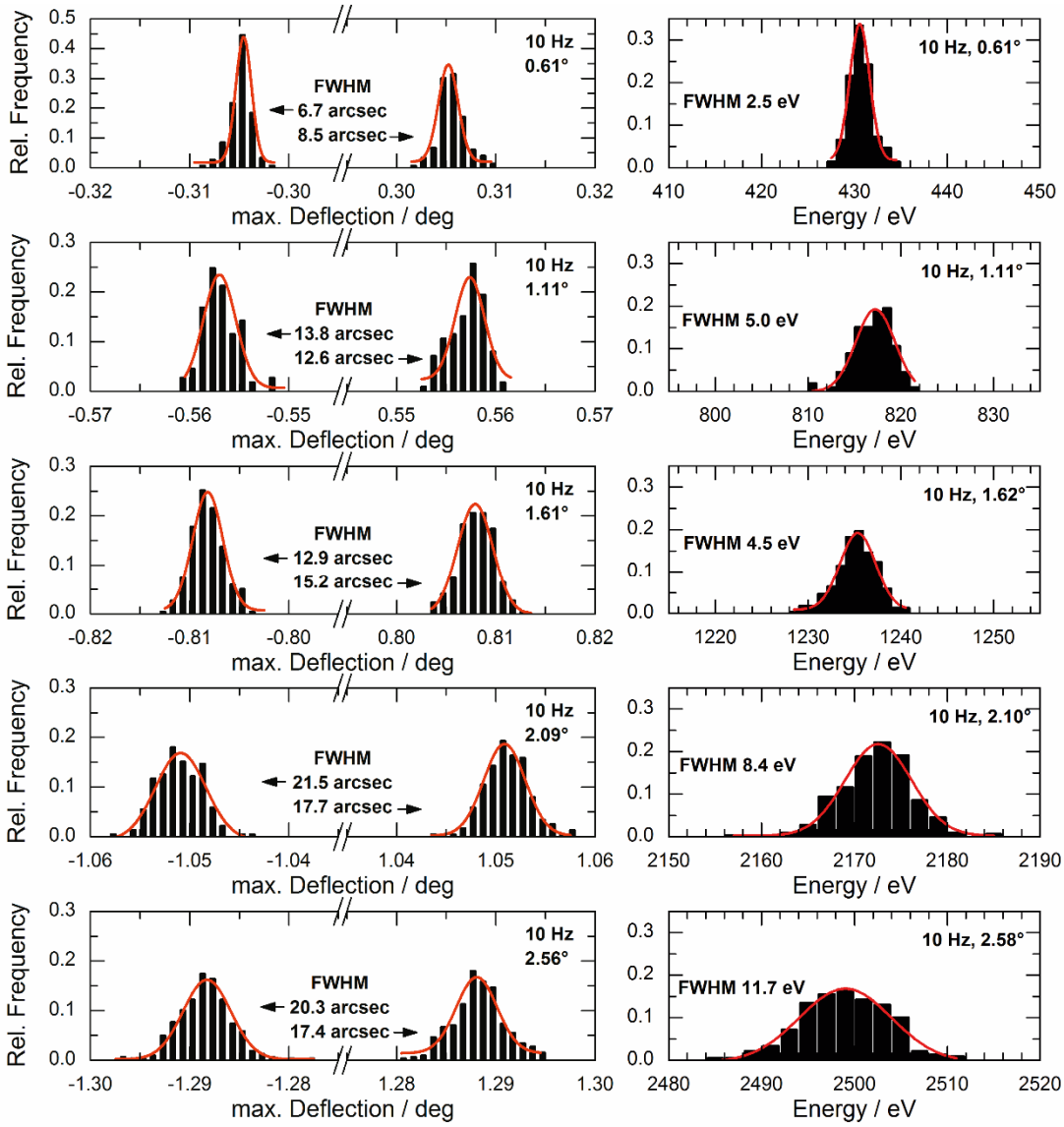

Figure 3.15: Relative frequency of the crystals angular deflection at its reversal points during oscillation and resulting energy jitter [**16**]. The red curves represent Gaussian fits to the data.

3.3.3 Repeatability of the Crystal Motion

The stability of the scan range was investigated by evaluating the maximum angular deflection at the reversal points of the movement. The analyzed data are based on the same QEXAFS measurements already evaluated in Figures 3.13 and 3.14 and again cover 100 oscillation periods. Figures 3.15 and 3.16 show the jitter of the maximum angular deflection as well as the resulting energy jitter of the scans. A Gaussian is fitted to each distribution to compare and quantify the variations. The mean jitter increases for larger angular deflections and higher oscillation frequencies and is found to be within 8 arcsec and 30 arcsec throughout the measurements. This jitter corresponds to a variation of the total scan range of

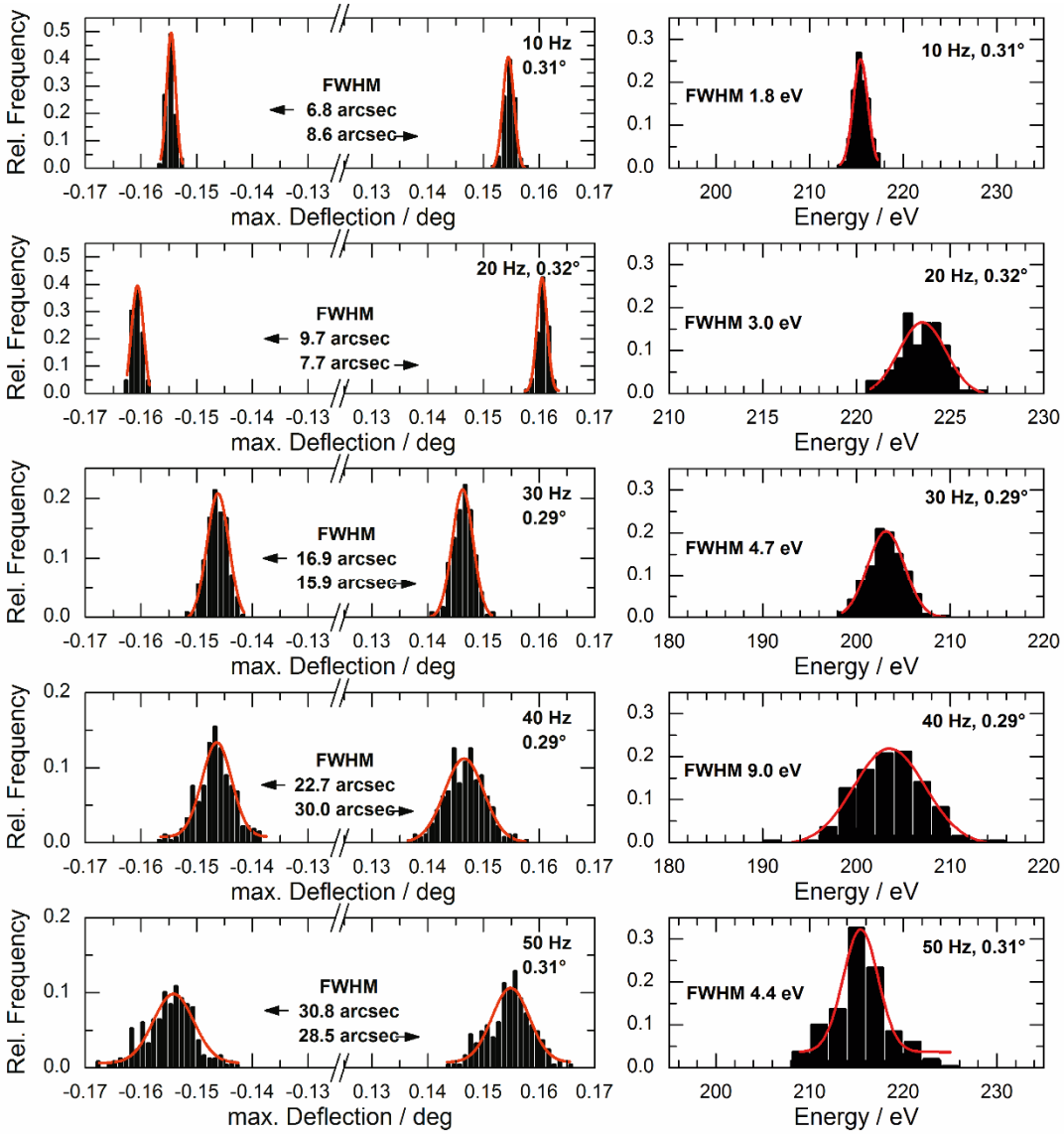

Figure 3.16: Relative frequency of the crystals angular deflection at its reversal points during oscillation and resulting energy jitter [**16**]. The red curves represent Gaussian fits to the data.

a few eV. This minor jitter of less than 5% of the total scan range is in general of no significance for QEXAFS measurements.

3.3.4 Long Term Stability

The standstill stability of the Bragg angle is of particular importance in the non-QEXAFS or conventional step scanning mode. This mode is required for step-scanning techniques, such as conventional XAS or X-ray emission spectroscopy (XES) methods and fixed energy experiments, such as HEROS [**66**,**67**] or laser pump X-ray probe experiments. To realize best stability, the rotor of the torque motor can be mechanically locked from the atmospheric side by means of a metal clamp. In this case, the goniometer still facilitates rotations of the crystals over the entire angular range and the in-vacuum angular encoder can still be used to read the Bragg angle. The stability was verified by continuous sampling of the in-vacuum encoder output at 10 kHz over 65 hours. Over the entire

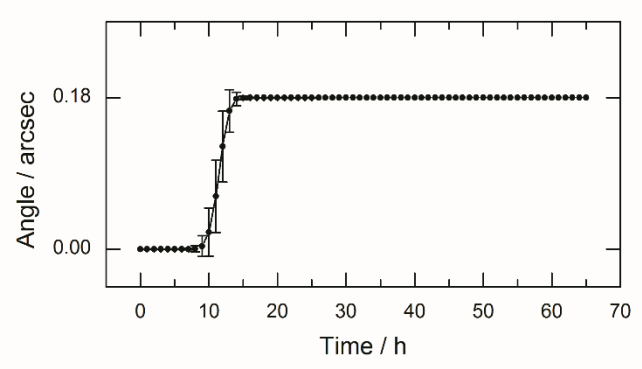

Figure 3.17: Deflection of the Bragg angle in the standstill non-QEXAFS mode recorded over 65 hours [**4**]. The black dots display the mean angular position averaged over one hour and the error bars indicate their standard deviation.

observation time, the encoder readings toggled only between two adjacent discrete values separated by its angular resolution of 0.18 arc seconds. The mean angular position averaged over one hour is plotted over time in Figure 3.17. The angular position is static within adjacent values and there is no real drift. Taking into account a typical Darwin width (FWHM) of e.g. 6.6 arc seconds at 9 keV for Si(111) or 1.5 arcsec at 16 keV for Si(311), the Bragg angle is absolute stable within a fraction of the Darwin width over the full observation period. This is fully sufficient for any practical application.

4 Data Acquisition and Evaluation

QEXAFS is a real time method. As such, the sample is probed continuously, while the changes, which are in focus of the investigation, occur. This puts essential requirements towards a data acquisition system (DAQ), since the experimental data need to be acquired and stored in real time as well. Furthermore, all relevant signals, such as the detector signals of ionization chambers and the Bragg angle, have to be sampled absolutely simultaneously in order to calculate the correct absorption at defined X-ray energies. The DAQ build for the SLS QEXAFS experiment meets these requirements and is presented in section 4.1. The DAQ employed at P64 differs only in a few aspects, which are specifically highlighted, if necessary.

QEXAFS experiments, which run for several minutes to a few hours, typically accumulate tens of thousands to over hundreds of thousand individual spectra, leading to datasets in the double digit GB range. Sections 4.2 and 4.3 explain the data evaluation software JAQ, which was developed to facilitate access to the huge amount of data acquired during QEXAFS measurements.

4.1 DAQ Hard- and Software

The data acquisition system (DAQ) is based on the industry standard PXI (PCI eXtension for Instrumentation) platform. This platform is an extension of the PCI and PCIe architecture known from personal computers with additional timing and trigger channels to facilitate synchronization among bus subscribers. The bus provides high bandwidth, low latency and is physically distributed via a backplane in an external chassis. Multiple backplanes, i.e. chassis, and a bus master can be linked by means of bridges utilizing copper or glass fiber interconnections. The DAQ configured for QEXAFS utilizes a National Instruments PXIe-6366 multifunctional data acquisition board. This module provides multiple analog-to-digital-converters (ADCs), digital-to-analog-converters (DACs) and general purpose digital input output pins (GPIOs). It is used to acquire spectra and to control the oscillation of the monochromator. The module is installed in a chassis (NI PXIe-1073 at SLS, NI PXIe-1082 at P64) next to a MXI glass fiber bridge (NI PXIe-PCIe8375) which connects to an external bus master, a Windows based host PC located in the control hutch. The glass fiber connection ensures a fully electrical isolated and interference free connection. The chassis is small enough to be placed on the experimental table

NI PXIe-6366		
Analog Input – ADC		
Number of Channels	8	
Resolution	16	bits
Sample Rate per Channel	2	MS/s
Bandwidth	1	MHz
max. Input Range	±10	V
Input Impedance	>100	GΩ
Timing Resolution	10	ns
Timing Accuracy	50	ppm
Analog Output - DAC		
Number of Channels	2	
Resolution	16	bits
Sample Rate per Channel	3.3	MS/s
max. Output Range	±10	V
Timing Resolution	10	ns
Timing Accuracy	50	ppm
Counter		
Number of Channels	4	
Number of Encoder Inputs	2	
Resolution	32	bits
max. Internal Base Clock	100	MHz
Base Clock Accuracy	50	ppm

Table 4.1: Summary of the relevant specifications of the PXIe multifunctional data acquisition board.

close to the detectors. This keeps the length of sensitive signal cables as short as possible. The digital encoder signals are less susceptible to electronic noise or interference and are directly transmitted from the monochromator to the chassis. The output voltages of the detectors are digitized simultaneously by the ADCs provided by the DAQ. Sinusoidal voltages, which are required to drive the power supplies of the torque motor, are generated with DAC channels and the digital counters of the DAQ are used to read the incremental quadrature output of the angular encoder. An overview of the layout is shown in Figure 4.1 and a summary of the important features is given in Table 4.1.

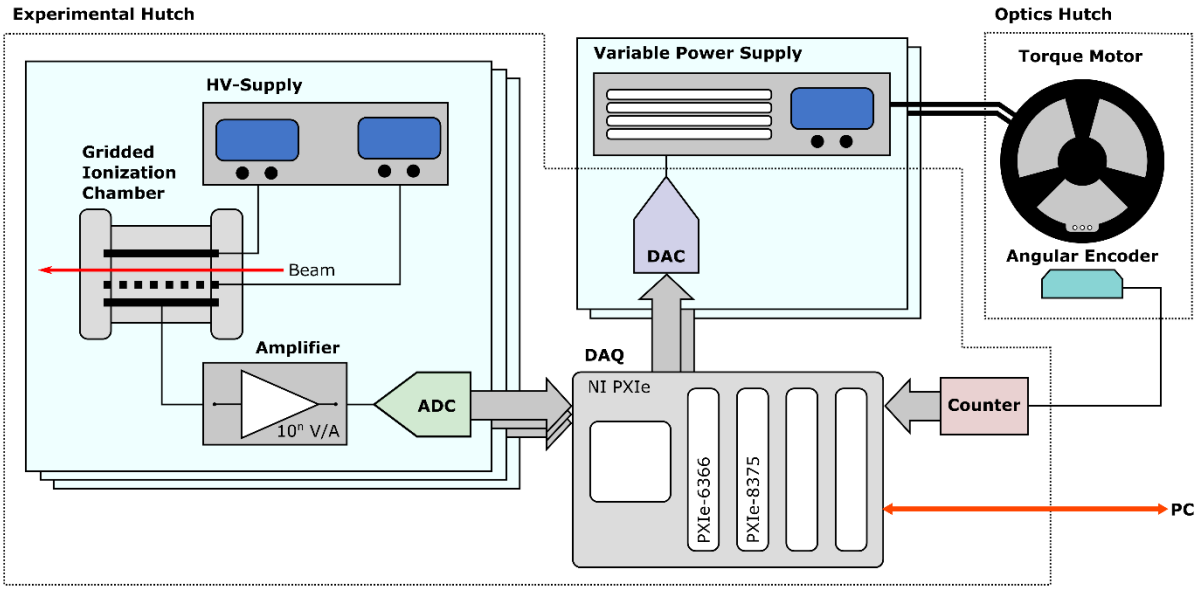

Figure 4.1: Layout of the data acquisition system used for QEXAFS measurements. Depending on the experimental setup and sample chamber, unused analog or digital inputs may be used to simultaneously acquire additional sensor readings, such as temperatures, pressures or valve switching states.

Sampling Frequency

A master clock running at 100 MHz is passed through a prescaler and is distributed among the ADCs. This ensures that the conversion of all channels is triggered at exactly the same moment in time. The sampling frequency f_S, which is defined by the settings of the prescaler, needs to be high enough, in order to avoid loss of information due to undersampling. A lower limit of f_S can be determined by equation (4.1), which considers the active crystals intrinsic energy resolution δE and the maximum scan rate $|dE/dt|_{max}$.

$$f_S^{min} = \frac{1}{\delta E}\left|\frac{dE}{dt}\right|_{max} \tag{4.1}$$

Assuming a sinusoidal crystal oscillation, following the form $\phi_{Bragg}(t) = \varepsilon\, sin(2\pi f_{Osc} t) + \phi_0$, which is in good agreement with the true motion of the crystals (see section 3.3.2), the maximum scan rate $|dE/dt|_{max}$ can be estimated by the following inequality

$$\left|\frac{dE}{dt}\right|_{max} < \langle \frac{dE}{dt}\Big|_{max} \rangle := \frac{hc}{2d} 2\pi\varepsilon f_{Osc} \frac{cos(\phi_0 - \varepsilon)}{sin(\phi_0 - \varepsilon)^2}, \tag{4.2}$$[i]

which leads to the final estimation of the minimal necessary sampling frequency f_S^{min}:

$$f_S^{min} < \frac{1}{\delta E} \langle \frac{dE}{dt}\Big|_{max} \rangle. \tag{4.3}$$

The right term of this estimate can be evaluated as a function of the scan start energy E_1, the scan range ΔE and the oscillation frequency f_{Osc}. Lower limits of f_S can be found, by taking the capabilities of the

[i] The derivation of this inequality is carried out in the Appendix A.

oscillatory drive, i.e. the dependency between f_{Osc} and ε (see section 3.3.1) into account. The results are shown in the plots of Figure 4.2 for various oscillation frequencies between 10 Hz and 50 Hz for both available monochromator crystals. The blue area limited by the dotted black line represents the capabilities of the drive, i.e. the allowed operating conditions of the monochromator, while the solid curves solve $1/\delta E \, \langle dE/dt|_{max} \rangle$ for constant scan ranges ΔE typically used in experiments. Required sampling frequencies are found on the solid curves within the blue area. Accordingly, sampling frequencies of a few 100 kHz not exceeding 200 kHz for the Si(111) crystal or 500 kHz in the case of the Si(311) crystal are sufficient in any practical scenario. This demand is well matched by the analog inputs of the employed DAQ, which provides an input bandwidth of 1 MHz and a maximum sampling frequency of 2 MHz per channel.

The acquisition software, presented in the next section 4.1.2, was developed to be operated by the users during experiments and allows to set the sampling frequency. However, a maxed out sampling frequency of 2 MHz is generally preferable and exclusively used for the XAS measurements shown and discussed throughout this work. At this sampling frequency the QEXAFS measurements are almost in any case oversampled, which allows to resolve higher frequency components of the noise spectrum originating from the detection system and the ADC itself [**68**]. Subsequent digital low pass filtering can be performed to remove these components and to improve the signal-to-noise ratio.

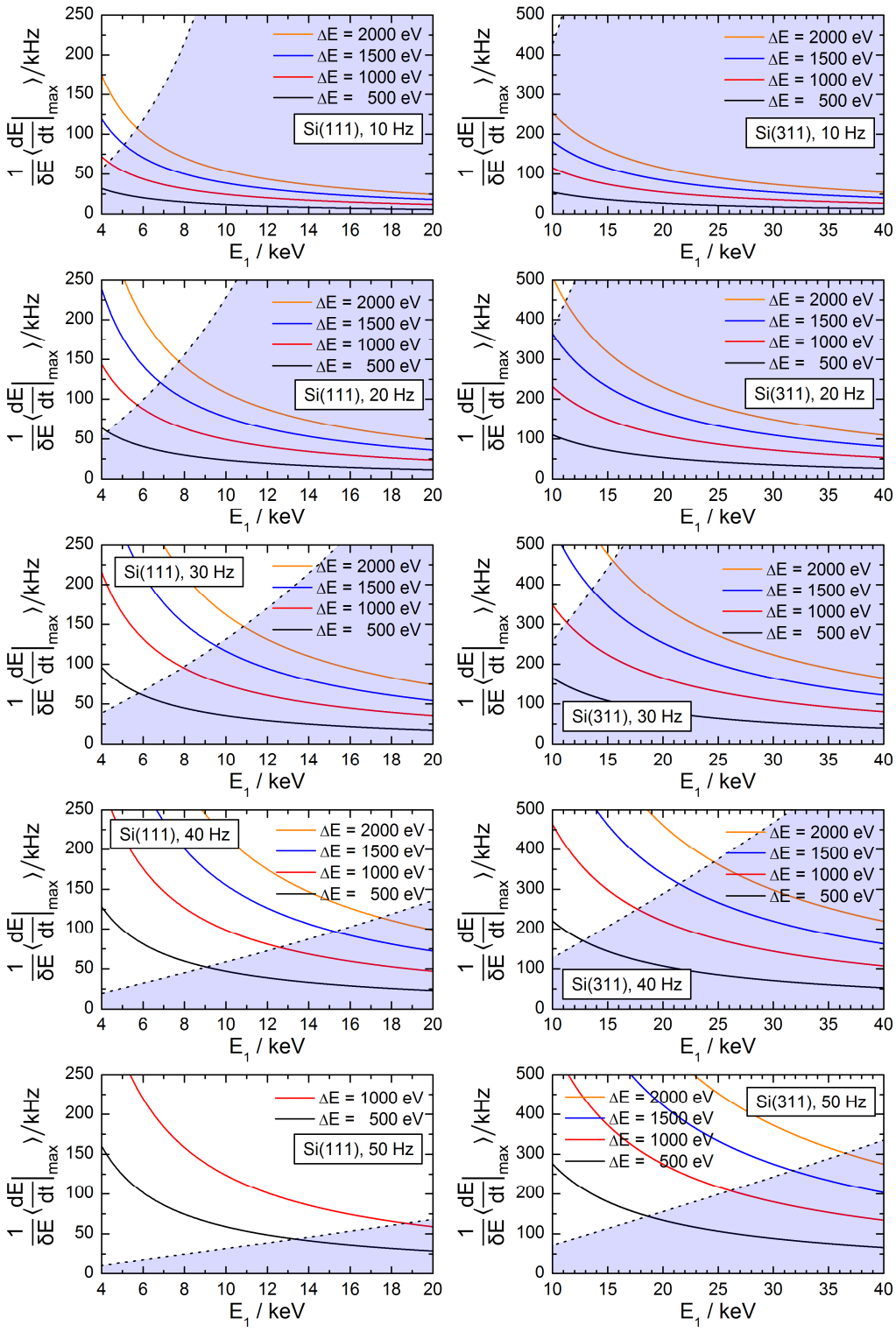

Figure 4.2: The function $\frac{1}{\delta E}\langle\frac{dE}{dt}\big|_{max}\rangle$ serves as an estimate of the required sampling frequency. Here it is given as a function of the scan start energy E_1 and represented by the solid curves. The blue area indicates the operational range of the monochromator as observed in section 3.3.1.

Electronic Noise

The frequency distribution of single bits occurring in an unfiltered raw measurement is shown in Figure 4.3. For that purpose, the dark current of a gridded ionization chamber, installed at a beamline

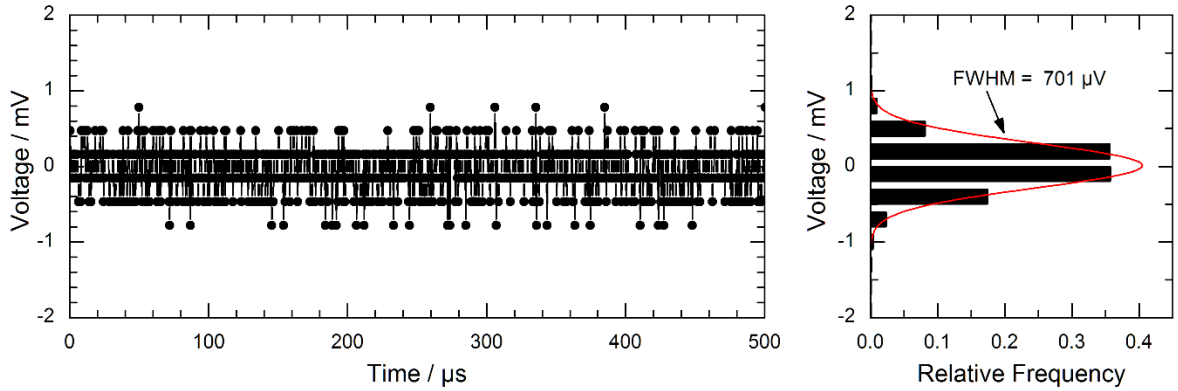

Figure 4.3: Noise level sampled at 2 MHz with powered ionization chambers and current amplifiers at a gain of 10^6 V/A, without X-ray beam. The left plot shows the first 500 µs of the acquired raw values, the right plot displays the frequency distribution of 5×10^6 samples. The Gaussian (red curve) fitted to the distribution reveals a FWHM of 701 µV.

on the experimental table and connected through a current amplifier with a gain of 10^6 V/A, was sampled for 2.5 s at 2 MHz. A two channel table-top high voltage power supply (ISEG, THQ DPS 30-405-24-5) was specifically chosen to operate the ionization chambers, due to its low ripple of less than 3 mV at 3 keV output voltage. This is a crucial property for minimizing noise in the output signals of ionization chambers. A Gaussian fitted to the frequency distribution shows a FWHM of the measured background noise of 0.701 mV. Assuming a typical signal level of a few Volts during a real QEXAFS measurements, this noise level results in a signal-to-noise ratio of higher than 10^3.

4.1.1 Angular Encoder

Determining the accurate Bragg angle of the used monochromator crystal in real time is of crucial importance in QEXAFS experiments. This angle defines the energy scale of each spectrum and imprecise measurements would severely affect the quality and significance of the measured spectra. Due to the high displacement velocity of the crystals during QEXAFS operation and the required angular resolution in the sub arc second regime, utmost care is needed to realize a fast and valid angular measurement.

The Bragg angle is resolved by two optical angular encoders. An incremental encoder (Renishaw: Tonic T2611-30M, RESM20USA115) is used for fast on-the-fly measurements during QEXAFS operation, while an additional absolute encoder (Renishaw: Resolute RA32BVA115B30V, RESA30USA115B) is available for calibration purposes. Each encoder read head uses its own circular scale, which is mounted to the crystal stage in-vacuum (see Figure 3.3). The read heads are mounted to the main front flange of the vacuum chamber by means of rigid frames. Consequently, these encoders read the real Bragg angle with respect to the vacuum chamber, which is according to equation (3.1) the sum of the goniometer and the torque motor angles. This arrangement eliminates incorrect measurements of the Bragg angle due to possible backlash or mechanical play in the mechanics of the goniometer.

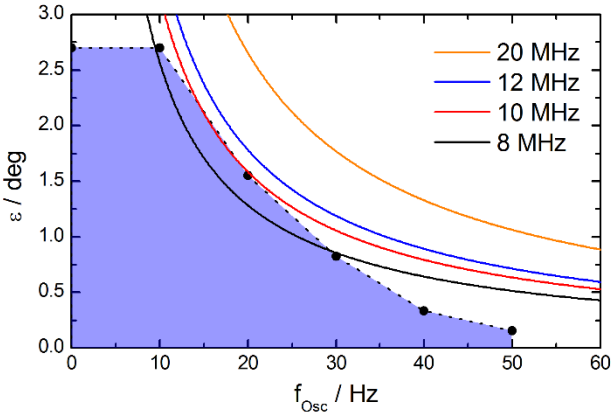

Figure 4.4: The areas beneath the solid curves indicate sinusoidal oscillations, which do not exceed the maximum radial velocity measurable with the employed angular encoder at a given output frequency. The solid lines represent the limit of the measurable oscillations. The blue area restricted by the black dotted line shows the feasible oscillation parameter field of the SLS monochromator.

Incremental Encoder

The incremental encoder is particularly important for QEXAFS measurements, since it provides real time angular information with the required high resolution. The analog output of the read head is electronically interpolated and converted into a digital quadrature signal, which is transmitted to the DAQ. A quadrature signal contains two phase shifted high frequency digital square waves. The output frequency $f_{Encoder}$, typically in the MHz regime, is limited by the employed interpolator and defines the highest measurable angular velocity of the Bragg axis and the radial velocity $v_{Encoder}^{max}$ of the circular scale. Assuming a sinusoidal oscillation of the Bragg axis and considering the highest angular velocity of this motion, the dependency of the maximum usable oscillation amplitude ε on the oscillation frequency f_{Osc} can be determined by

$$\varepsilon = \frac{v_{Encoder}^{max}(f_{Encoder})}{2\pi f_{Osc} r_{Scale}}. \tag{4.4}$$

This dependency is plotted in Figure 4.4 for different commercially available encoder output frequencies. The blue area in the background represents the experimentally observed oscillation capabilities of the SLS monochromator, which is discussed in section 3.3. From this plot it can be deduced that the output frequency must be larger than 10 MHz. Considering a margin for future upgrades and improvements an interpolator with a higher output frequency should be chosen. However, transmitting high frequency square waves over a long distance, typically on the order of 30 m to 100 m, without distorting its phase relationship is critical and should therefore be avoided by minimizing the frequency as far as possible. The interpolator used with the SLS monochromator (Renishaw DOP0400A50A) features an output frequency of 50 MHz.

The angular resolution of the incremental encoder using a x400 interpolator amounts to 0.18 arc seconds, which for instance corresponds to an energy resolution of about 0.05 eV at 10 keV using the Si(311) crystal and 0.09 eV at 20 keV using the Si(311) crystal.

Absolute Encoder

The absolute encoder divides the circumference of its scale into 2^{32} equidistant ticks and reaches a total accuracy of ±2.44 arc seconds. This is sufficient to pre-align the Si(111) crystals within 1 eV and the Si(311) within 2 eV. The major advantage of the absolute encoder is an immediate accurate reading of the absolute angular position at any time even after restart or power down of the data acquisition system. This is different from the incremental encoder which is reset to zero every time it is initialized. However, the absolute encoder alone is not suited for fast QEXAFS measurement since its readout frequency is too low.

Implementation of the Angular Encoder

The incremental angular encoder provides an analog sine/cosine signal and if connected to an interpolator, a digital quadrature signal as well. In principle both signals can be recorded by the DAQ and used for QEXAFS measurements, but there are distinct differences concerning their implementations and consequences due to their sensitivity towards electronic interference.

The analog signal can be directly fed into free ADC channels of the DAQ. In this way the encoder signal is intrinsically synchronized with the analog data of the detectors. Moreover, this procedure offers the advantage of setting the final angular resolution after the measurement was taken. However, this implementation is sensitive to electronic noise, which could limit the achievable angular resolution in the end, especially since the encoder signal has to be transmitted over a long distance from the monochromator to the DAQ. This scheme is therefore not implemented at the SuperXAS nor at the P64 beamlines. Instead, in both cases the digital quadrature signal is used. This signal is obtained by hardware interpolation within the interpolators electronics and does not need further processing. It is fed into two digital counter inputs capable of interpreting quadrature signals. However, in this case proper synchronization of the ADCs and counters has to be established. It is not only essential to have both devices triggering simultaneously but it is also required to start on the same clock edge. With respect to the fact that both devices can only be configured and initialized one after another and that both devices need a different number of clock cycles to actually activate, the implementation of a synchronous start is a critical task.

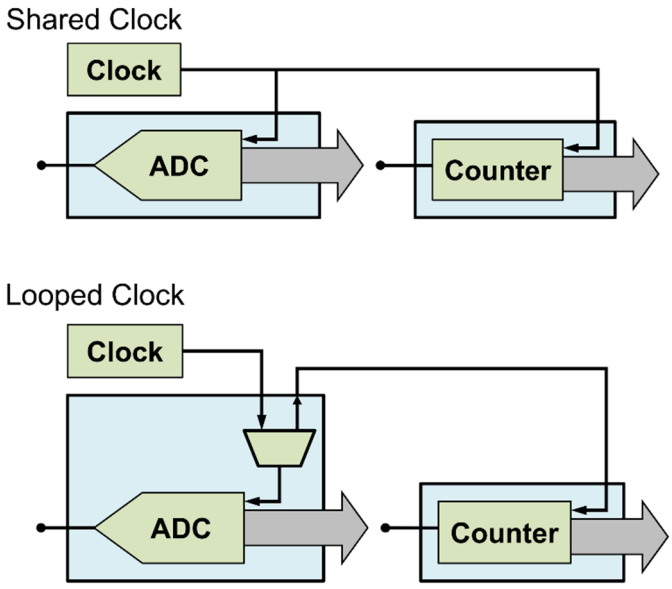

Figure 4.5: Two different implementations of clock distribution among devices of the DAQ. The devices receive the same clock in both schemes, however only the 'Looped Clock' scheme enables a synchronous start of both devices on the same clock edge.

To achieve accurate synchronization, the clock is looped through one of the devices to the other, instead of a parallel distribution (see Figure 4.5). By doing so, the last device, here the digital counter, can be first configured, initialized and left armed, waiting for the first clock cycle. Then the other device is configured and initialized. At the moment when the latter becomes active, the clock is immediately passed through and both devices start acquiring data on the same clock edge. Not doing so results in a constant time shift between the acquired angular and analog data streams.

Correct synchronization was verified by simultaneous sampling of both, the analog sine/cosine and the digital quadrature signals provided by the angular encoder. Figure 4.6 shows random angular noise which was recorded during relaxation after the crystal stage of the monochromator has been slightly displaced. The top plot makes use of the shared clock scheme. The clear shift between both signals prove an unsynchronized start of the acquisition. The lower plot is based on a measurement with a looped clock. Here the analog and digital signals overlap without a noticeable phase-shift, which confirms the accurate synchronization.

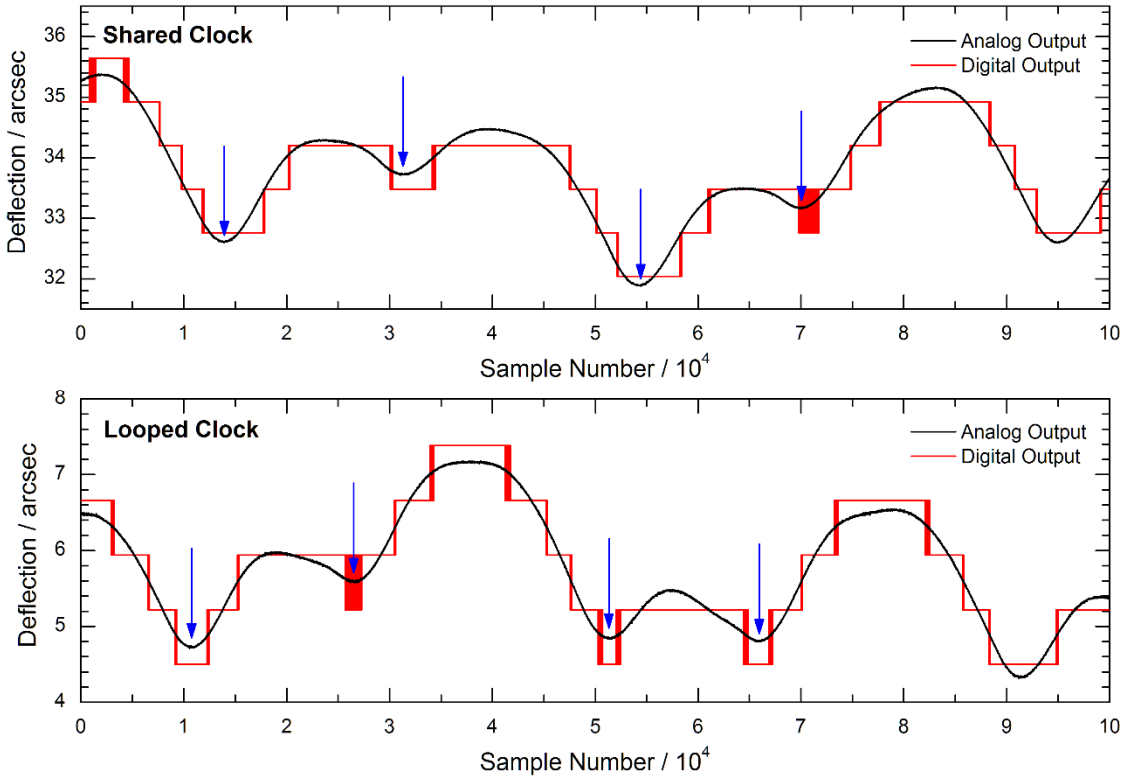

Figure 4.6: Shown are the digital and analog incremental encoder outputs of random angular noise, which have been simultaneously sampled at 2 MHz to verify the synchronization of the analog and digital part of the data acquisition system. The top plot exhibits a clear shift between the analog and digital signals indicating an incorrect synchronization. The blue arrows point to regions at which the phase relationship is particular obvious.

4.1.2 DAQ Software

All data acquired by the DAQ is transmitted by means of a glass fiber bridge to a computer in the control hutch. A software program, written in C# .net 4.5 and running on this computer under the operating system Microsoft Windows 7, was developed to operate the DAQ. It was designed to be used by the experimentalists and external user groups at the beamline. The program enables to configure and operate the DAQ. It further displays the current input signals as a function of time with an adjustable refresh rate of up to 10 Hz. To facilitate these functions, the program handles all the relevant data streams, going to and originating from the DAQ, as well as the write-to-disk data stream.

In a typical QEXAFS experiment 4 channels are acquired, three analog signals of detectors and one angular encoder signal. If sampled with 2 MHz and transmitted in double precision (8 Bytes), this yields a continuous data rate of approximately 61 MB per second. Incoming data is distributed among buffers temporarily stored in the main memory. The size of each buffer matches the refresh rate of the displayed data multiplied by the sampling frequency. If a buffer is filled the raw unedited data is written to disk and the buffer is discarded. Two files are created, one containing all analog signals, the other

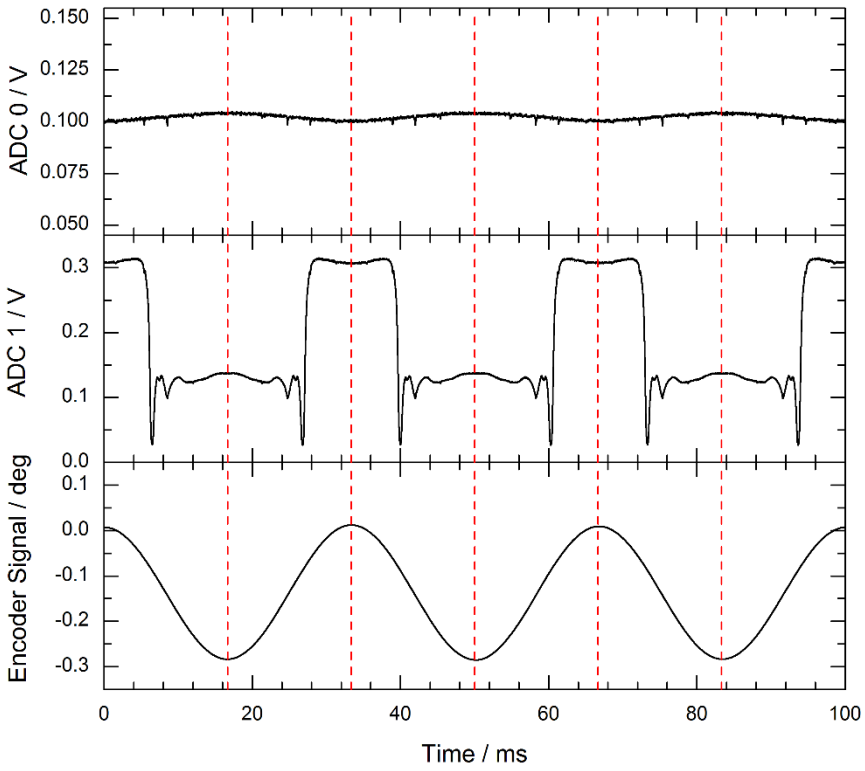

Figure 4.7: Example of a QEXAFS measurement of Yb_2O_3 at the L_{III}-edge showing the acquired raw data of each channel. ADC 0 refers to the first, ADC 1 to the second output of current amplifiers connected to gridded ionization chambers. The red dashed lines indicate the beginning and ending of single spectra contained in the data streams.

containing angular encoder data. To lessen the actual file sizes on disk, data is stored binary with single precision (4 Bytes). A detailed description of the data structure can be found in the Appendix B.

Figure 4.7 shows typical raw data of a QEXAFS experiment acquired by the DAQ. A Yb_2O_3 powder sample was measured in transmission at the Yb L_{III}-edge with a repetition rate of 60 spectra per second. The signals ADC 0 and ADC 1 refer to the measured output voltages of current amplifiers connected to corresponding gridded ionization chambers. ADC 0 is proportional to the incident photon flux and ADC 1 is proportional to the transmitted photon flux. The encoder signal shows the sinusoidal crystal deflection around an unknown Bragg angle offset. It is an essential task of a dedicated evaluation software to determine this offset and to isolate each spectrum in the data stream. The program JAQ was developed to fulfill this task and is presented in the next section.

4.2 Data Evaluation with JAQ – Preprocessing

A comprehensive software program was developed, that allows to edit, process, evaluate and export QEXAFS datasets. This program is named JAQ [ʤæk], which is the recursive acronym for JAQ Analyzes QEXAFS. It was specifically developed to be capable of processing time resolved XAS measurements comprising of more than hundred thousands of individual XAS spectra. This feature in particular distinguishes JAQ from other well established XAS evaluation programs, such as WinXAS

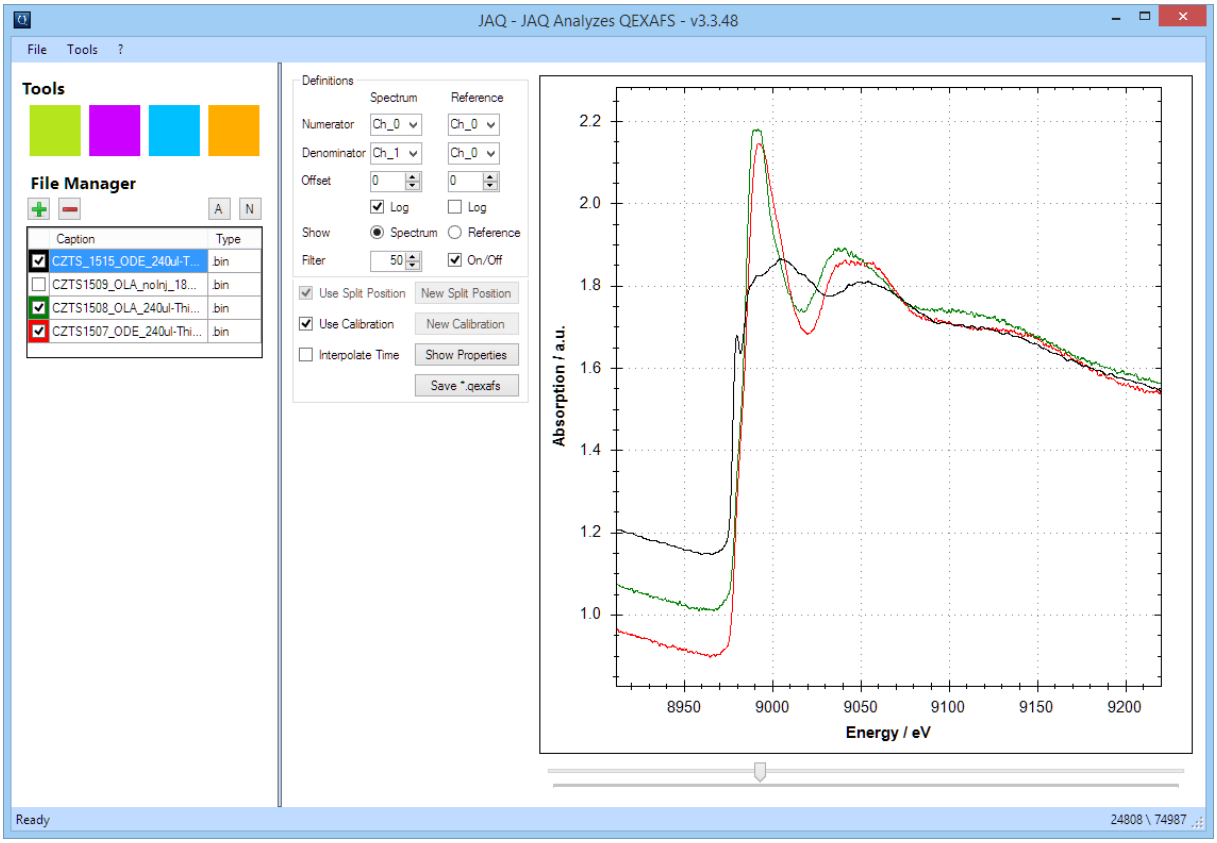

Figure 4.8: Main window of JAQ. The File Manager on the left lists all loaded files. These can be of different type, such as binary QEXAFS data sets, single spectra in ASCII and more. The scrollbar below the plot window enables the user to browse through the spectra of the active data set.

[**69**], Ifeffit [**70**,**71**] or Viper [**72**], which lack the ability to process significantly more than 20 to 50 individual spectra at once. JAQ is also the only program available, which makes use of the precise time information between recorded spectra and the comprised data points. For instance, this is crucial for the time correction interpolation (TCI) and digital filtering as discussed in sections 4.2.3 and 4.3.1. The graphical user interface (GUI) of the main window of JAQ is shown in Figure 4.8.

JAQ is written in the object oriented programming language C# using Microsoft's .Net environment. Basic algorithms, for instance used for linear least-squares fitting of numerical data are based on [**73**] and have been translated from Fortran, ANSI C or C++ into C#. The only external library incorporated is the ZedGraph class library which is available under the GNU LGPLv2 license [**74**] and used for the plot plane.

The QEXAFS Workflow

The typical workflow of QEXAFS data evaluation differs in a few steps from conventional XAFS analysis. To retrieve an arbitrary spectrum from a data set preprocessing is required. All necessary working steps are implemented in JAQ. An overview indicating the workflow is given in Figure 4.9. The algorithms behind the functions *Splitting* and *Energy Calibration* are described in sections 4.2.1 and 4.2.2. Once single spectra can be addressed and retrieved from the data set the measurement can be

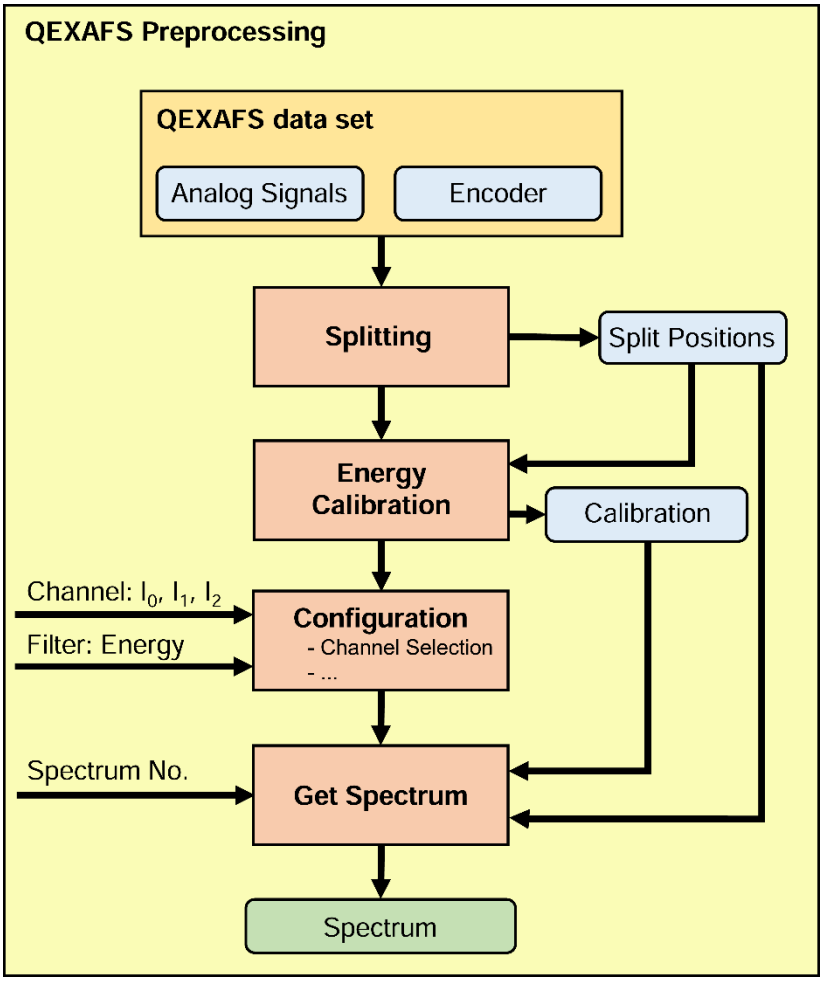

Figure 4.9: Schematic of the initial workflow in JAQ. Once the files *Split Positions* and *Calibration* are created the associated steps *Splitting* and *Energy Calibration* can be skipped.

evaluated using the implemented features of JAQ. These are described in section 4.3. Alternatively all or individual spectra can be converted to ASCII for further processing with 3rd party software programs.

4.2.1 Splitting

The very first step in QEXAFS data evaluation requires to isolate each single spectrum in the data set. This step is performed in the *Splitting* feature of JAQ by processing the encoder data. The major aim, at this stage, is to get a list of pointers, which refer to the beginning of each spectrum in the stream. By means of this list any spectrum can be accessed by reading data between two consecutive pointers. In JAQ, these pointers are called *Split Positions*, and are stored in an additional file (see Appendix B) using the suffix '*_SplitPositions.bin*'. The relevant steps of the splitting algorithm is schematically shown in Figure 4.10.

During a measurement the monochromator crystals follow a sinusoidal trajectory which is monitored by the angular encoder. The reversal points of this motion define the needed split positions between two successive spectra. Determining these positions reliable is more challenging than it appears at a first glance. The angular speed near the reversal points is very low and eventually vanishes. Due to

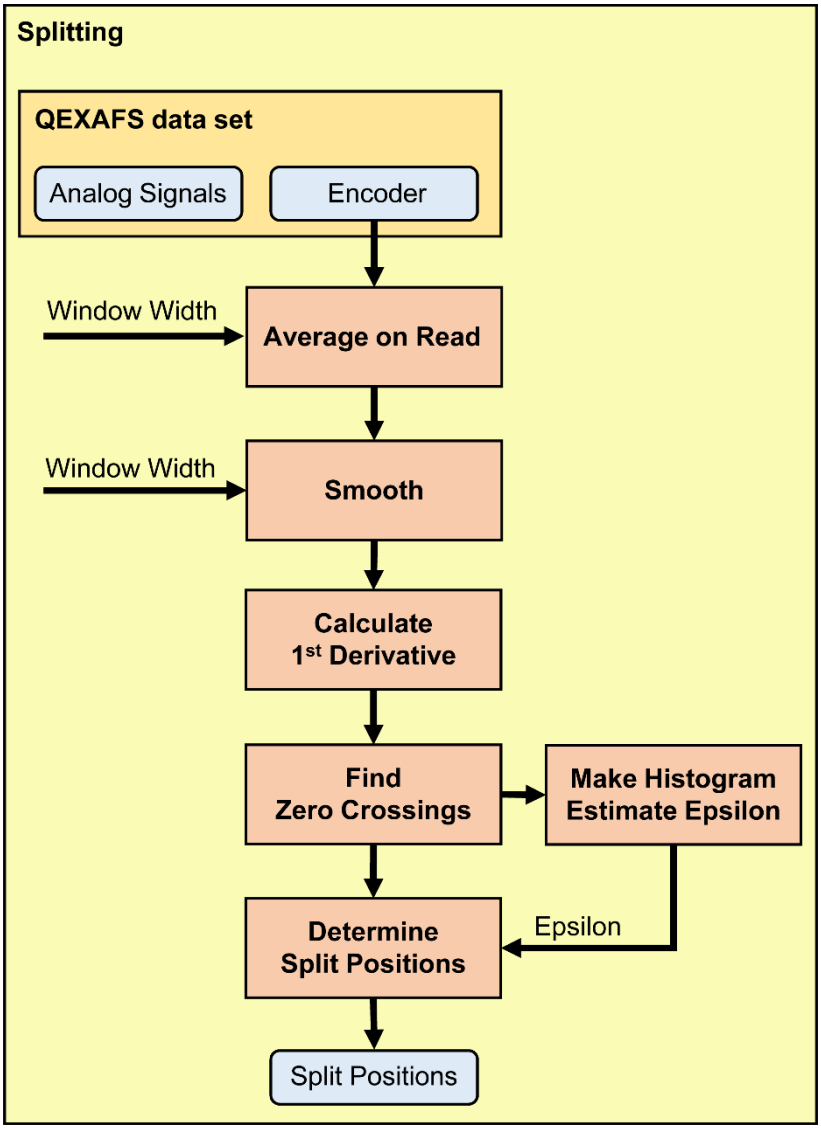

Figure 4.10: Schematic of the Splitting algorithm implemented in JAQ. The algorithm is used to determine a list of *Split Positions* which indicate the beginning and end of each spectrum in the QEXAFS data set.

the discrete nature of the encoder values, the actual values around this region might not change over a certain number of samples. In addition, the angular values are subject to a number of uncertainties, which complicate the problem. Typical characteristics of the movement such as offset, amplitude and frequency may not be known in advance and might also jitter to a certain amount. A further obstacle is that the size of the encoder data only may be larger than the available space in the main memory of the processing computer. File sizes of encoder data of the order of 10 GB are not uncommon and thus it might not be possible to store the entire encoder stream in one large array.

The Split Algorithm

The split algorithm implemented in JAQ solves several of the mentioned problems within its first two working steps. Instead of locating the extreme values of the recorded motion directly, zero crossings of the 1st derivate are tracked. These can be easily detected by a change of sign or a value

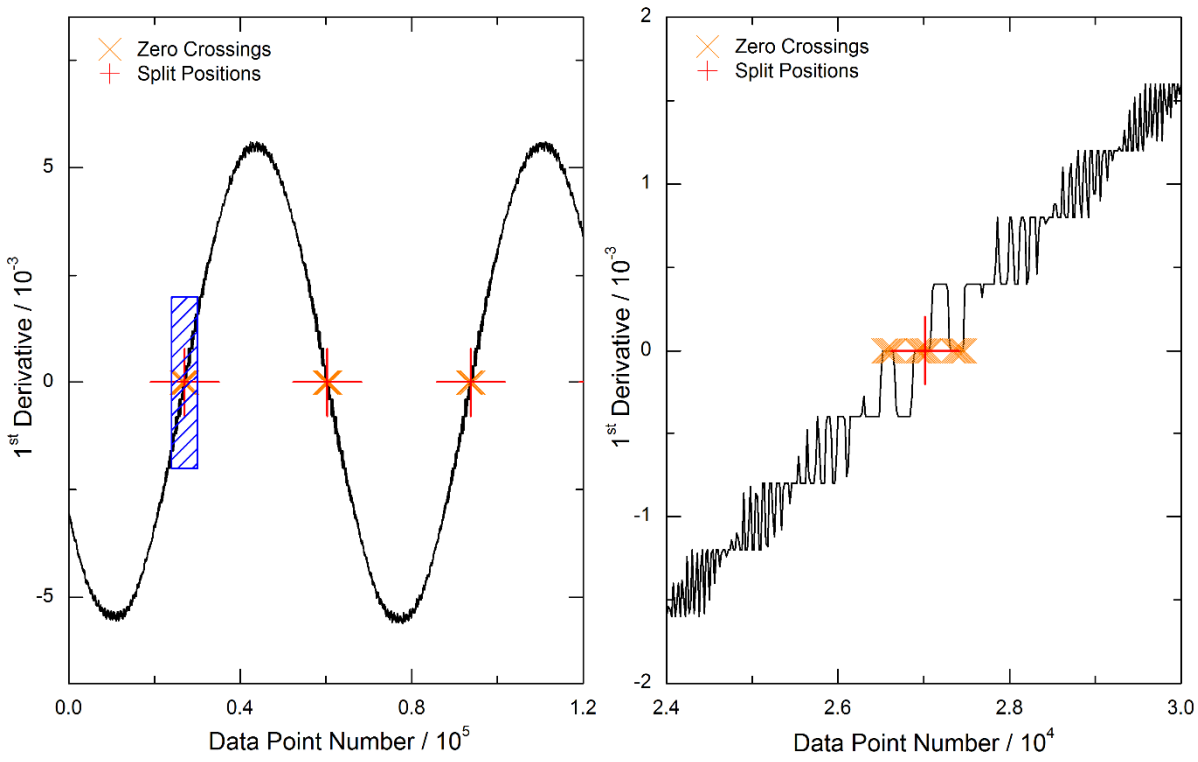

Figure 4.11: Derivative of a 30 Hz sinusoidal crystal trajectory after initial averaging and smoothing. The right plot shows the blue shaded area around a reversal point of motion more closely.

equal to zero. Furthermore, by differentiating the encoder date, the arbitrary offset and the unknown amplitude is lost. However, a straightforward numeric derivation, following the simple instruction

$$x'_i := x_{i+1} - x_i \tag{4.5}$$

does not always yield a meaningful derivative. The reason is that the angular encoder is often oversampled (see section 4.1) and due to the quantized encoder values, there are always a few consecutive samples x_i, x_{i+1}, ... which do not differ from each other. As a consequence, the simple approach based on equation (4.5) would yield a derivative which is zero everywhere but for single positions where the samples actually change, obscuring the underlying sinusoidal movement completely. Efficient smoothing of the encoder data first is therefore an essential step in the algorithm.

The initial smoothing, following equation (4.6), is performed when the file is accessed for the first time. By averaging over a given number of samples and keeping only the averaged values, the number of samples is reduced to a length which can fit in the main memory. In addition, the encoder data stream is sufficiently smooth to be differentiated.

$$\bar{x}_j := \frac{1}{n}\sum_{i=0}^{n-1} x_{i+jn} \tag{4.6}$$

The smoothed and derived encoder function of a 30 Hz QEXAFS measurement is shown in the plots of Figure 4.11. The encoder signal was sampled with 2 MHz and initially averaged over 14 samples. This pre-smoothed function was further smoothed by means of a moving window with a width of 10 samples before its derivative was calculated. The right plot of this figure shows a closer look to a section near a

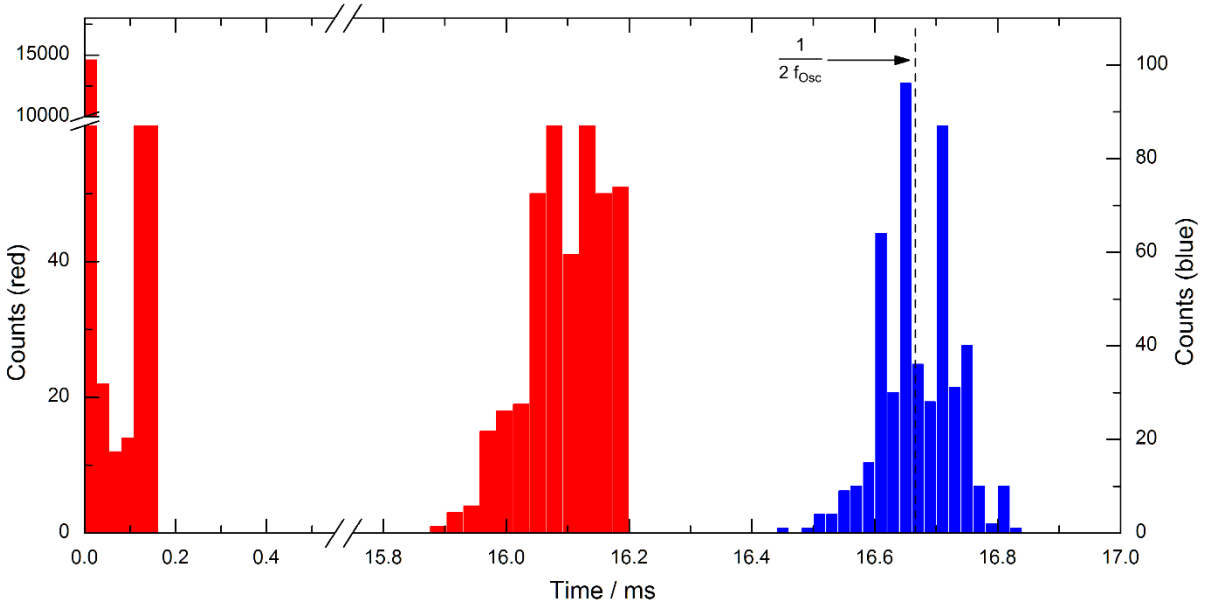

Figure 4.12: Red histogram: Frequency distribution of next neighbor distances between all zero crossings of a 30 Hz sinusoidal crystal trajectory. This histogram is used to define a reasonable ϵ-surrounding. Blue histogram: Frequency distribution of next neighbor distances between all split positions which have been determined based on an ϵ-surrounding of 7.96 ms.

reversal point. There are still multiple zero crossings found indicating that the performed smoothing was not too strong but adequate. To get reasonable split positions from a list of zero crossings, the algorithm makes use of ϵ-surroundings. Each zero crossing laying within a surrounding ϵ is assumed to belong to a single unique reversal point. The final split positions are then determined as the center of gravity of all zero crossings found within the ϵ-surrounding.

To help to determine a reasonable width of an ϵ-surrounding, the algorithm calculates the distances of each zero crossing to its next right neighbor and computes their frequency distribution, which is then displayed in a histogram, as shown in the red plot of Figure 4.12. The distribution typically separates into two disjoint fairly sharp bounded blocks. At the left side all distances which amount to only a few data points are displayed. On the right side the long distances accumulate. These are only found between the last and the first zero crossing of two adjacent reversal points. A good value for the width of an ϵ-surrounding is therefore found anywhere in between these two sets.

By choosing an appropriate ϵ-surrounding a list of *split positons* can be determined. This list can be similarly analyzed in a histogram. The blue histogram of Figure 4.12 shows the frequency distribution of distances between adjacent split positions. This distribution is now centered around the expected value of $1/2f_{osc}$. Since the sampling rate is known this distribution can be used to precisely determine the oscillation frequency of the monochromator and its jitter. Also corrupt measurements caused by unstable oscillations can be quickly identified by these histograms.

In extremely rare cases it was observed that the oscillatory motion of the crystals has been disturbed, supposably due to a delayed buffer reload of the DAC. An example is given in Figure 4.13,

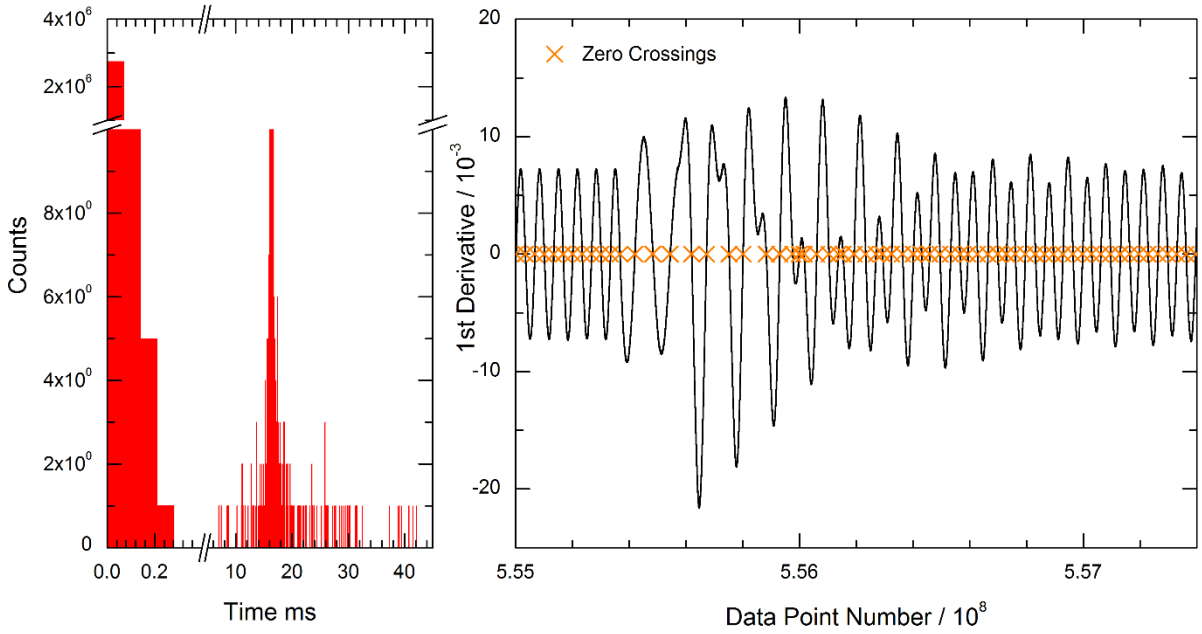

Figure 4.13: Histogram and encoder signal of a corrupt QEXAFS measurement. The histogram displays the frequency distribution of next neighbor distances between all zero crossings. The right plot shows a section of the encoder signal around the imperfection. The affected part amounts to about one second. By removing this region from the data set, the rest of the measurement can be saved and still be analyzed.

which shows the encoder signal and the frequency distribution of zero crossings of an impaired measurement. In this case the histogram differs distinctly from that shown in Figure 4.12. The accumulation of long time gaps is not as sharp as in typical measurements and shows lot of individual spikes. JAQ provides various tools to identify problems of the measurement, to locate the position of the imperfection and to restore the measurement.

The GUI of the Splitting Module in JAQ

The GUI (Graphical User Interface) of the split module is shown in Figure 4.14. The right plot shows the smoothed derivative of the encoder signal. Zero crossings (orange x-crosses) and *split positions* (red diamonds) are plotted on top of this graph. The frequency distribution of the time distance between consecutive zero crossings is shown as a histogram in the left plot. This plot window also shows a cursor which can be moved by the track bar below. By means of this cursor the width of the ϵ-surrounding can be set by the user.

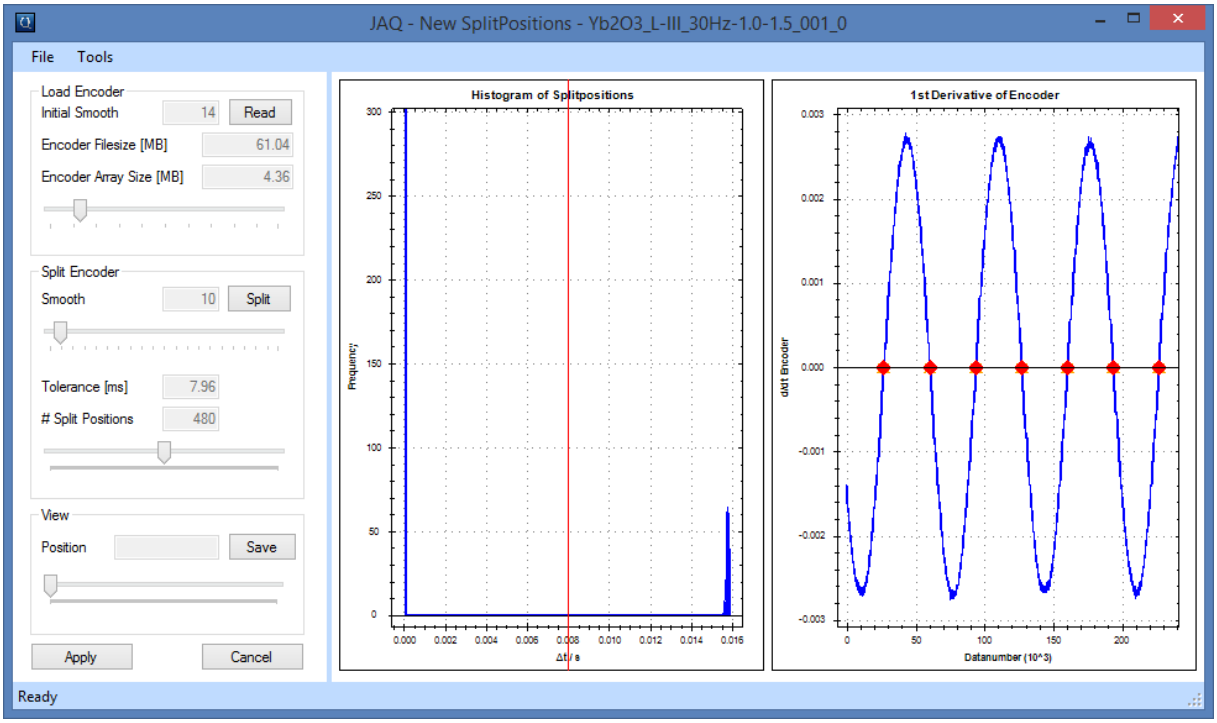

Figure 4.14: GUI of the Splitting module in JAQ. The left plot shows the frequency distribution of the calculated distances between zero crossings, whereas the right plot displays the first derivative of the smoothed encoder signal. The red diamond symbols indicate the determined *Split Positions* based on the ϵ-surrounding defined by the red cursor in the left histogram plot.

4.2.2 Energy Calibration

The energy scale is determined from the angular measurement of the monochromator crystals. This measurement is not necessarily calibrated and the Bragg angle may be measured relative to an unknown static offset θ_0. JAQ can determine this offset if the correct energy at an arbitrary position within the measurement is known. Typically the absorption edge position of the sample or of a reference material and the corresponding electron binding energy E_{Edge} are well suited for this purpose. The offset is determined according to equation (4.7), where $\theta(t)|_{Edge}$ is the local encoder value at the position of the absorption edge.

$$\theta_0 = asin\left(\frac{hc}{2d_{hkl}}\frac{1}{E_{Edge}}\right) - \theta(t)|_{Edge} \tag{4.7}$$

The determined offset is stored together with other parameters, such as the lattice constant d_{hkl} and the binding energy, in an additional file (see Appendix B) with the suffix "_C*alibrations.bin*". The encoder values of a spectrum can then be transformed into energy by means of equation (4.8).

$$E = \frac{hc}{2d_{hkl}}\frac{1}{sin\big(\theta_0 + \theta(t)\big)} \tag{4.8}$$

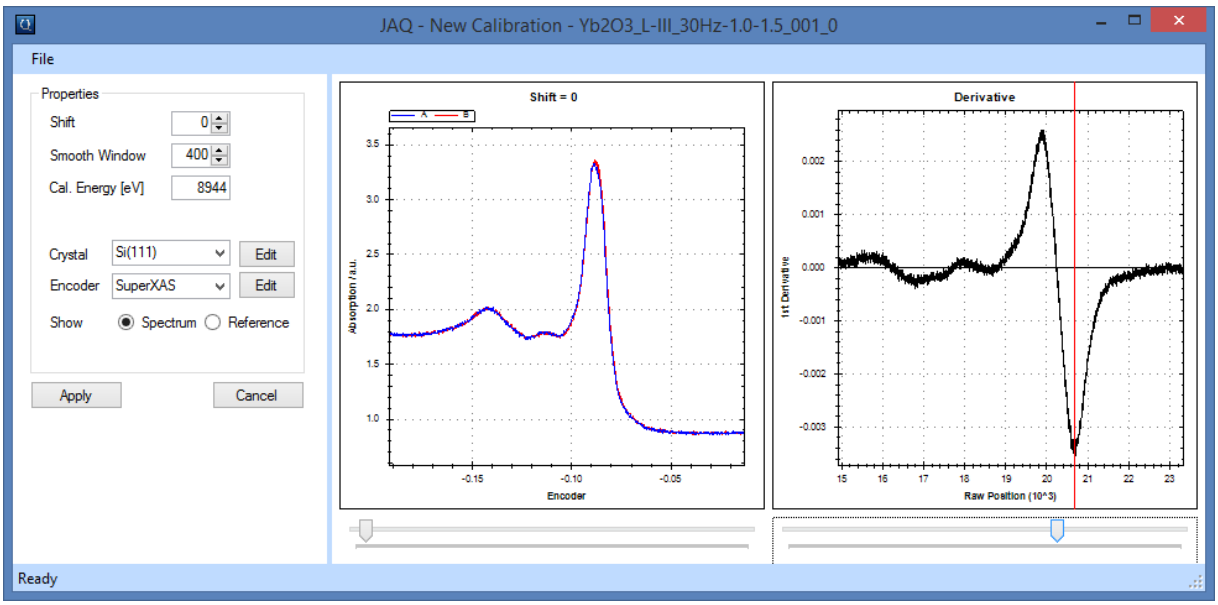

Figure 4.15: GUI of the Calibration module in JAQ. The left plot displays single consecutive *up* and *down* spectra on top of each other. The right plot shows the first derivative of a selected spectrum and displays a cursor to define the edge position. The spectra shown are still a function of encoder values or sample number.

The GUI of the Calibration Module in JAQ

Figure 4.15 shows the GUI of the calibration module in JAQ. All required steps to transform the encoder signal into photon energy can be performed in this window.

The left plot shows two consecutive spectra plotted on top of each other. These are not yet calibrated but plotted as a function of encoder value. Since one of these spectra is measured with increasing energy and the other with decreasing energy, any differences between these spectra indicate an impaired measurement, most likely due to an insufficient bandwidth of the detector system, imprecise Bragg angle measurements or a false synchronization between the detector inputs and the encoder signals. The latter can be corrected in some cases by adding a constant time shift to the encoder signal.

The right plot is used to calibrate the energy scale of the measurements. The absorption edge is usually defined by a local extreme value of the first derivative of the absorption spectrum. To help the user locate this position, this plot window shows the first derivative of the blue spectrum. The red cursor can then be placed manually to define the edge position.

4.2.3 Get Spectra and Time Correction Interpolation

By using the information obtained in the two previous steps, *Splitting* and *Energy Calibration*, real absorption spectra can finally be retrieved from the dataset. This is performed by the function *Get Spectra* (see Figure 4.9). Furthermore, this function also maps all measured data onto a single equidistant energy grid, which is a necessary step towards enabling batch processing. This energy grid is defined by the highest start energy and the lowest end energy of all scans. To accomplish this, the spectra are

cropped to equal length in order to remove the jitter of the oscillation amplitude. In a next step multiple analog samples which are acquired at the same encoder value are averaged. Thus, the resulting number of data points in a spectrum is rather given by the resolution of the angular encoder than the sampling frequency, meaning that increasing the sampling frequency improves the average but keeps the final number of data points in a spectrum untouched.

Time Base

A straightforward time reference based on the fixed oscillation frequency f_{Osc} and the sequential numbering of all m spectra in the dataset can be constructed. The center time t_i and period Δt_i of a given spectrum is then defined by

$$t_i = \frac{2i+1}{4f_{Osc}} + t_0 \tag{4.9}$$

$$\Delta t_i = \frac{1}{4f_{Osc}} \tag{4.10}$$

where the index i runs from 0 to $m-1$ and t_0 is a constant time offset to account for the -1^{th} spectrum which is only partially acquired and therefore rejected. The time frame during which a specific spectrum has been recorded is then given by $t_i \pm \Delta t_i$.

Time Correction Interpolation

The period Δt_i (see Equation (4.10)) reflects the fact that QEXAFS spectra are sequentially acquired and although, in a strict sense, it is not possible to attribute a single point in time to a given spectrum, QEXAFS data is often treated in this way. This can be justified by the basic assumption made for most QEXAFS experiments, that any change of the sample which would lead to a measureable change of its absorption spectrum is negligible within the acquisition time of one spectrum. In other words: The oscillation frequency is chosen high enough to oversample the measurement in the time domain. The Time Correction Interpolation (TCI) was developed to improve the situation if this can not be ensured and hence single spectra can not be regarded as quasi static. Applied to the entire QEXAFS data set, the TCI yields a new set of X-ray absorption coefficients $\mu(E,t)$ which are equally spaced in the energy as well as in the time domain. As a consequence, the new interpolated absorption coefficients belonging to an individual spectrum are virtually measured simultaneously at one specific point in time. A theoretical example on how this improves the linear combination analysis of QEXAFS measurements is given at the end of this section, while the principles of the linear combination analysis are explained in section 4.3.3. Moreover, an equidistant dataset is also an important requirement for the application of digital filters. These are discussed in section 4.3.1.

The TCI maps the measured data onto an equidistant time grid by linear interpolating along the time direction. This is illustrated in the two plots of Figure 4.16. The dotted black sinusoidal line drawn in the left plot approximates the scanning behavior of the monochromator. The black dots on top of this

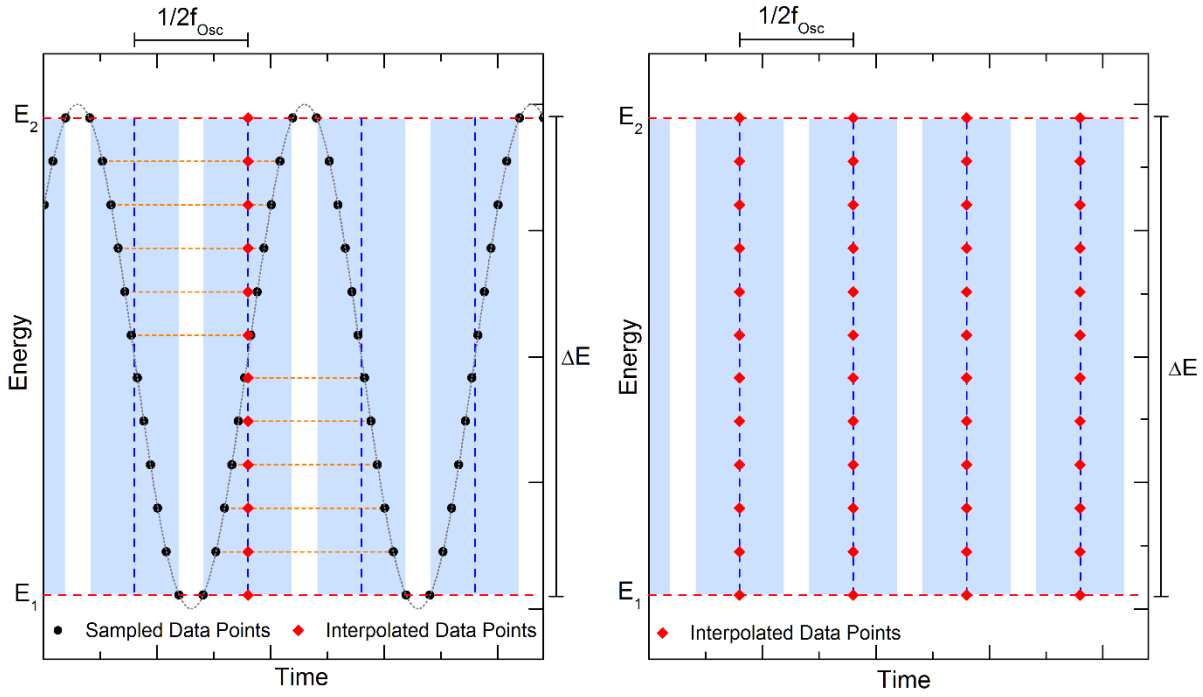

Figure 4.16: The black dots of the left plot schematically indicate where the X-ray absorption coefficient $\mu(E,t)$ is determined by the QEXAFS measurement. These points are not equally spaced along the time direction. The TCI determines new data points by linear interpolation along the horizontal orange lines. The right plot illustrates the result, showing equidistant data points.

line indicate where the X-ray absorption coefficient is known in the time-energy plane. The blue areas depict the time period during which the individual spectra are measured. The TCI determines new data points, shown as red diamonds in the plot, by linear interpolation between two successive samples of μ, which have been measured at the same energy but actually belong to different spectra. The interpolation is then evaluated at the center time of the individual spectra. This procedure is illustrated by the dashed orange lines, which connect the two samples of μ used for the interpolation. The final result is depicted in the right plot, showing a regular array of interpolated samples equidistant in energy and time.

The time corrected spectra can now be attributed to single points in time. Similar to the idea of equation (4.9) the center time of the time corrected spectra can be computed by equation (4.11) where the oscillation frequency and the time offset have been substituted with their means in order to account for jitter in oscillation frequency and amplitude.

$$t_i^c = \frac{2i+1}{4\langle f_{osc}\rangle} + \langle t_0\rangle \tag{4.11}$$

Based on the *split positions* s_i (see section 4.2.3), these means can be computed according to equations (4.12) and (4.13), which are derived in Appendix C.

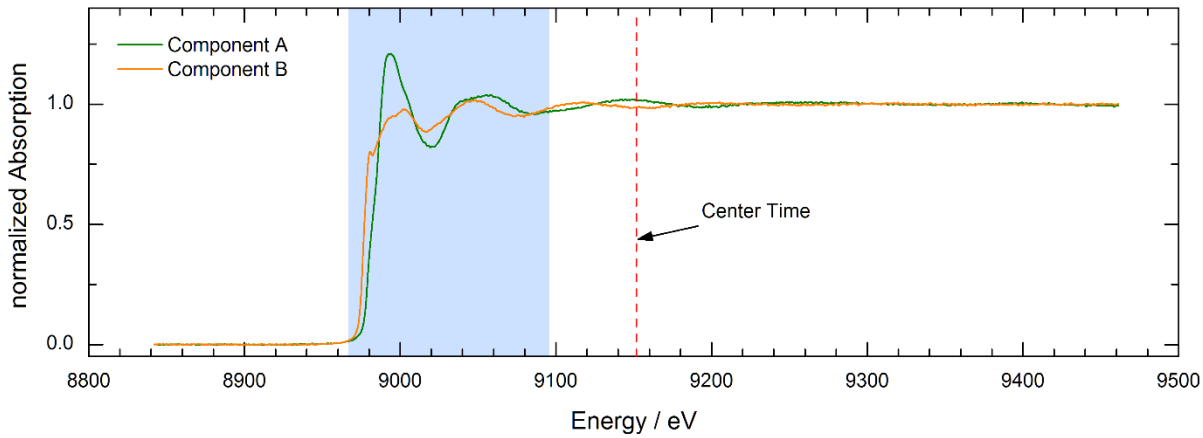

Figure 4.17: Normalized XAS spectra used for the demonstration of the time corrected linear combination analysis feature of JAQ. The blue area indicates the fitting region. The spectra have been extracted from a real QEXAFS measurement of copper zinc tin sulfide (CZTS) formation during steady state conditions of the sample.

$$\langle f_{Osc} \rangle = \frac{1}{2} \frac{m-1}{s_{m-1} - s_0} \tag{4.12}$$

$$\langle t_0 \rangle = \frac{s_0 + s_{m-1}}{2(m-1)} - \frac{1}{2}(s_{m-1} - s_0) + \frac{1}{m-1} \sum_{i=1}^{m-2} s_i \tag{4.13}$$

Example of the Time Correction Interpolation using linear combination analysis

A brief example of the benefits of using the TCI when performing a linear combination analysis (LCA) is given here. The underlying principles of the LCA and their implementation in JAQ are discussed in section 4.3.3. For this example, two single X-ray absorption spectra have been extracted from a real QEXAFS measurement of copper zinc tin sulfide (CZTS) formation taken at Cu K-edge. The two extracted spectra represent the initial and final state of a chemical reaction and are here used to model a hypothetical transition with a well-defined kinetic. Given the normalized static spectra, μ^A_{norm} and μ^B_{norm} the model can be expressed as:

$$\mu_{norm}(E,t) = \big(1 - c(t)\big)\mu^A_{norm}(E) + c(t)\mu^B_{norm}(E) \tag{4.14}$$

with an appropriate transition function $c(t)$. The transition used in this example is defined by equations (4.15) and (4.16). It is based on a smooth symmetric step function $f_{Step}(t)$ defining the transition between the components A and B.

$$c(t) = \begin{cases} 0 & 0 \le t \le t_1 \\ f_{Step}\left(\dfrac{t - t_1}{t_2 - t_1}\right) & t_1 \le t \le t_2 \\ 1 & t_2 \le t \end{cases} \tag{4.15}$$

$$f_{Step}(t) = 6t^5 - 15t^4 + 10t^3 \tag{4.16}$$

The input spectra, μ^A_{norm} and μ^B_{norm} are shown in Figure 4.17. These are also used as the reference spectra in the analysis. Hence, the LCA should yield the known coefficients $1 - c(t)$ and $c(t)$. However, since these are not static within the fitting range, which is indicated by the blue area, errors

are to be expected. To evaluate the influence of the TCI, the LCA is performed firstly according to the conventional approach, i.e. by using the spectra as is, and secondly with time corrected spectra.

The plots of Figure 4.18 display the results of the LCA. In the upper plots the transition was chosen to complete within 5 spectra and in the lower plots the transition was chosen to complete within 10 spectra. The upper plots of both evaluations show the values of the coefficients, found with a conventional approach, the time corrected approach and the expectation values based on the models input. The lower plots evaluate the quality of the LCA fits by calculating its coefficient of determination R^2. This error estimate is defined by equations (4.17) and (4.18), where the y_i's are the dependent variables, i.e. the measured data points and the $\hat{y}_i$'s are the results of the fit.

$$R^2 = 1 - \frac{\sum_{i=0}^{n-1}(y_i - \hat{y}_i)^2}{\sum_{i=0}^{n-1}(y_i - \langle y \rangle)^2} \tag{4.17}$$

$$\langle y \rangle = \frac{1}{n}\sum_{i=0}^{n-1} y_i \tag{4.18}$$

The examples show that in both cases the time corrected approach using the TCI yield the better fit and coefficients with smaller errors. The actual improvement is more pronounced for the faster transition, which is shown in the top plot. Within the static regions, before and after the transition, both methods yield the same correct coefficients. Thus, for slow transitions approaching the limit of quasi static changes, the differences between the results of both methods vanishes and using the time corrected approach becomes optional. However, in the case of very fast sample changes the TCI is a valid and promising approach to improve the analysis of time resolved QEXAFS measurements.

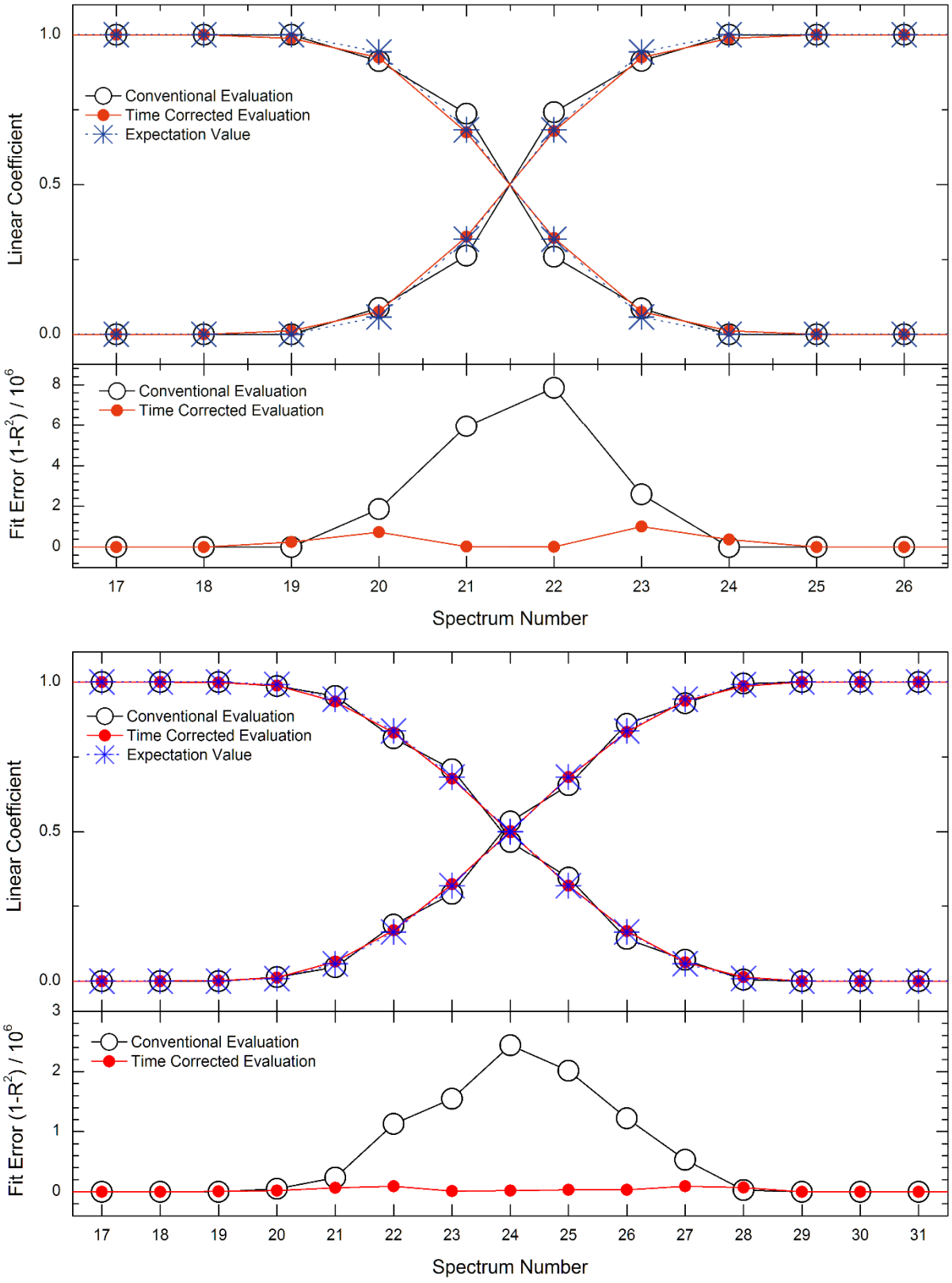

Figure 4.18: Results of a LCA using unmodified spectra in the conventional evaluation and time corrected spectra using the TCI. The analysis is based on a hypothetical model, providing a smooth and complete transition between two pure states. The transition completes within 5 (upper plots) or 10 (lower plots) successive spectra.

4.3 Data Evaluation with JAQ - Features of JAQ

Once preprocessing of the QEXAFS dataset is completed and individual spectra are accessible, the actual measurement can be evaluated. For that purpose JAQ provides various tools of which the most important ones within the scope of this work will be discussed in the following sections.

The implementation of digital filers to improve the signal-to-noise ratio are discussed in section 4.3.1. Section 4.3.2 deals with all common functions which are needed in typical XAS data processing, such as background subtraction, normalization and the extraction of the fine structure $\chi(k)$. Fourier transformation of the $\chi(k)$, based on the FFT (Fast Fourier Transform) and the FFTW (Fastest Fourier Transform of the West) [**75**] algorithms was implemented by Becker [**76**]. This will therefore not be discussed in this text. Linear combination analysis is a powerful method to determine time constants of reaction kinetics and hence probably one of the most often used evaluation methods of QEXAFS measurements. This tool is described in section 4.3.3.

4.3.1 Digital Filtering

One strength of QEXAFS is certainly its possibility of averaging consecutive spectra in order to improve the signal-to-noise ratio after the measurement has been acquired. Of course, this comes with a cost and is always a trade-off between time resolution and signal-to-noise ratio. Averaging is therefore always admissible if the time resolution, which is given by the acquisition rate of spectra, is higher than the time constants of the kinetics, which are in focus of the investigation, or in other words, if the measurement is oversampled in the time domain. The same is also valid for averaging within a spectrum along the energy scale. Since QEXAFS measurements are almost always oversampled in the energy domain and quite often in the time domain as well, averaging or more sophisticated digital filtering techniques are a relevant part of the QEXAFS data preparation and analysis.

Savitzky-Golay Filter

JAQ provides one dimensional Savitzky–Golay filters, which can be independently applied to the time or the energy direction of QEXAFS measurements. In contrast to an ordinary moving window average filter, which essentially is the lowest order of a Savitzky-Golay filter, this type of filter can preserve higher order moments. It is thus better suited to represent absorption spectra especially with respect to the steepness of the edge jump or peaks in the XANES region. The implementation of the filter module in JAQ is shown in Figure 4.19. The idea behind the Savitzky-Golay of filter is simple. Basically, as the filter moves along the data set, least squares fits of a polynomial over a given interval are performed and the value of the input function at the current position of the filter is replaced by the function value of the polynomial. This procedure results in low pass filtering of the input function and is equivalent to a discrete convolution with a finite impulse response [**77**,**78**]. Hence, the filter can be computed by a linear combination of the input values μ_i using a proper set of filter coefficients c_k as shown in equation (4.19).

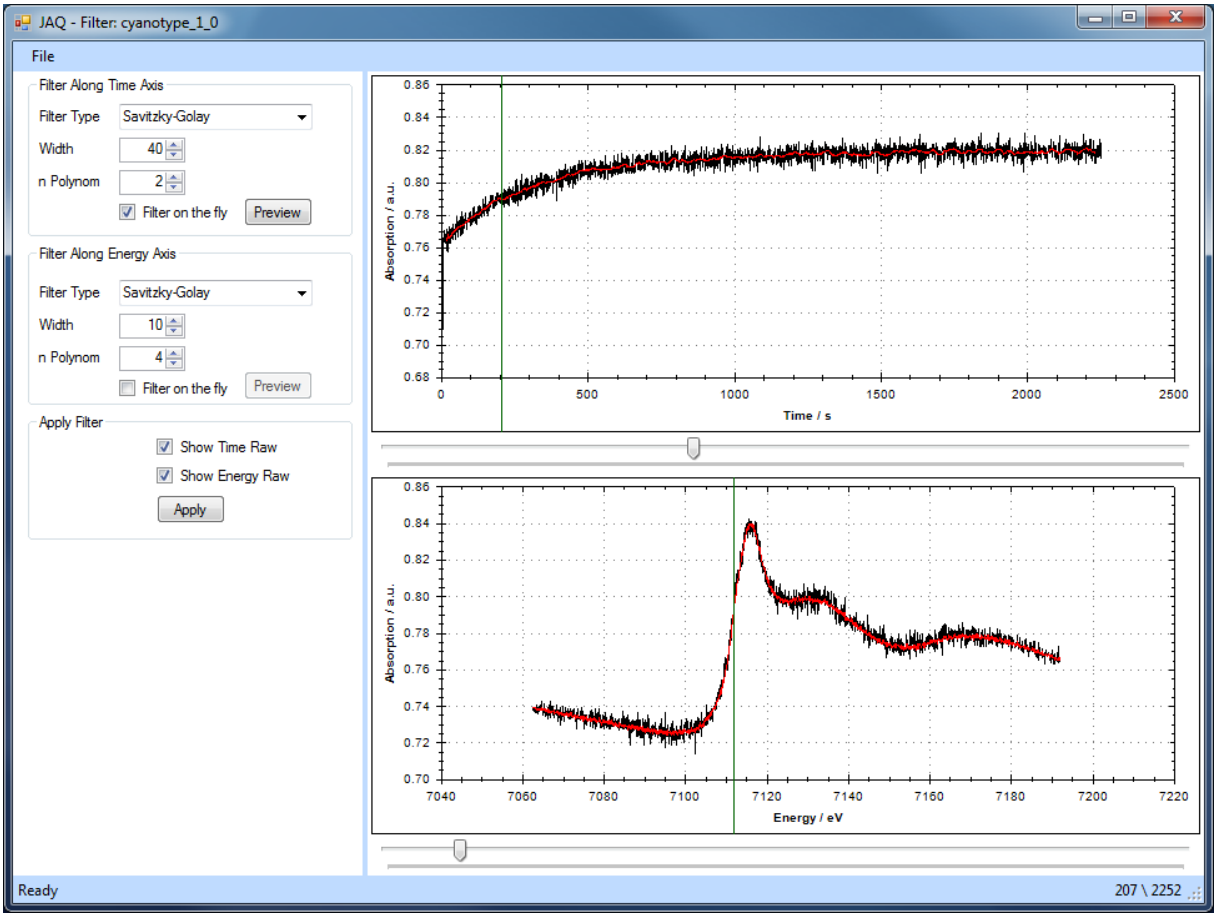

Figure 4.19: GUI of the digital filter module in JAQ. Shown is a XANES measurement at the iron K-edge of Cyanotype. The top plot displays the absorption of the sample at a constant energy as a function of time. The bottom plot displays the absorption of the sample at a selected time as a function of energy. The green vertical cursers can be moved by the track bars below and indicate the energy and time values, which are kept constant in the respective plots. The black curves show the raw data and the red curves the filtered data. Here, only the results of one filter along the time direction is shown.

$$\mu_{i,j}^{Filtered} = \sum_{k=-n_L}^{n_R} c_k \, \mu_{i+k,j} \tag{4.19}$$

The index i runs along the direction, which is intended to be filtered, thus corresponds to either energy or time. Consequently, the index j corresponds to the other one. To obtain filtered absorption spectra (which are obviously functions of energy) equation (4.19) is repeated for all energies in the dataset.

The filter and consequently the filter coefficients c_k of equation (4.19) are defined by the polynomial degree and the window width, which is the length of the interval used in the local fitting. In general, the window, defined by the left and the right length, n_L and n_R, may be asymmetric but in JAQ is implemented to be symmetric, thus forcing $n_L = n_R$. This ensures, that no unwanted shift or delay is introduced. However, to allow this, the first and last n_L values are not processed by the filter. The filter coefficients c_k are computed by an algorithm outlined in [**73**].

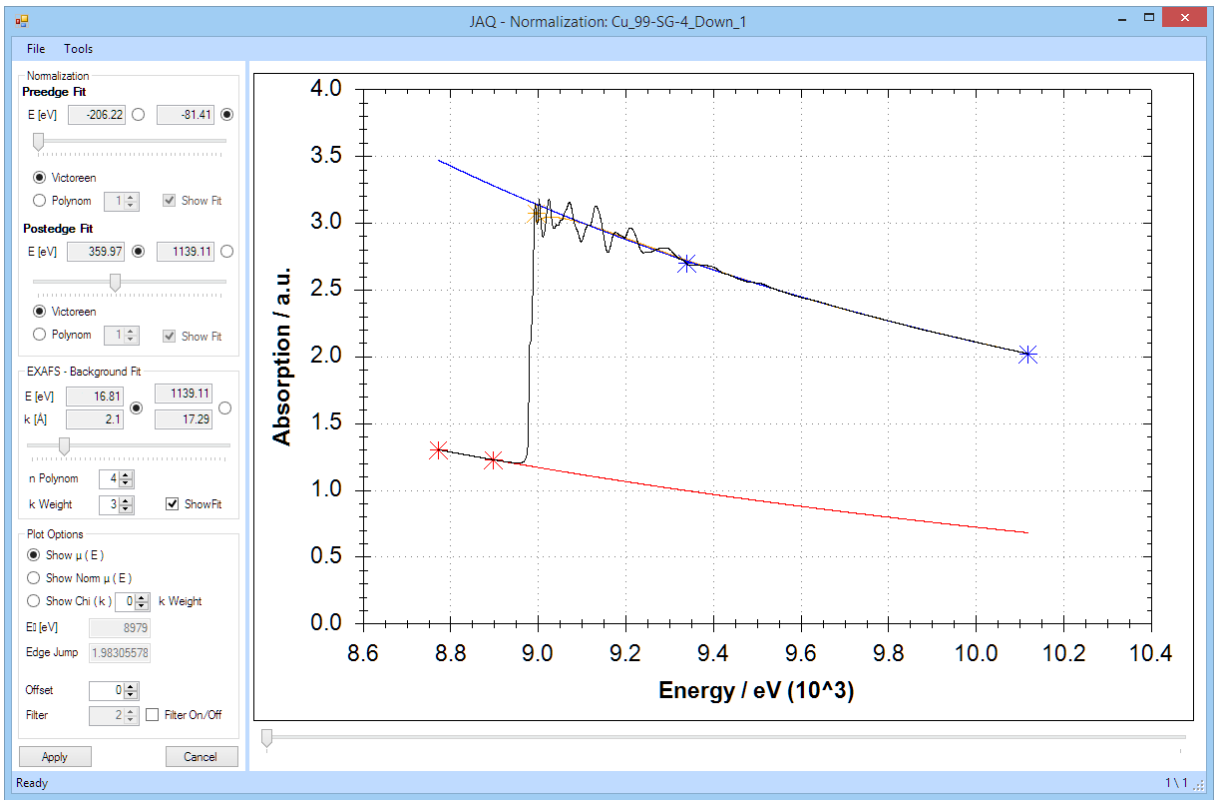

Figure 4.20: GUI of the normalization module in JAQ. Shown is a measured X-ray absorption spectrum of a metallic copper foil at the K-edge. The pre- and post-edge fits (red and blue) are based on a Victoreen function. A k^3 weighted polynomial of degree 4 (orange) is used to fit the atomic background. The colored asterisks indicate the regions used for the particular fits. The second blue and orange asterisks overlay at the end of the spectrum.

4.3.2 Background Subtraction

To obtain the sample's normalized X-ray absorption coefficient $\mu_{norm}(E)$ or its fine structure $\chi(k)$ the background absorption needs to be removed. This is attained by fitting the pre-edge and post-edge region with suitable functions. JAQ provides a dedicated GUI to setup and perform all required steps. The GUI is shown in Figure 4.20 displaying an absorption spectrum of a metallic copper foil and the corresponding fits. Adjusting a fit parameter or browsing through the data set invokes an almost instant visual response to the change.

Normalization

In the case of obtaining $\mu_{norm}(E)$ the procedure is comparable simple, since the overall trend of the X-ray absorption is known. Far away from absorption edges, the X-ray absorption coefficient follows the empiric Victoreen function which can be fitted to the pre- and post-edge regions of the spectrum. If $\mu_{Pre}(E)$ and $\mu_{Post}(E)$ are the wanted background functions the normalized or flattened spectrum can be calculated according to equations (4.20) or (4.21).

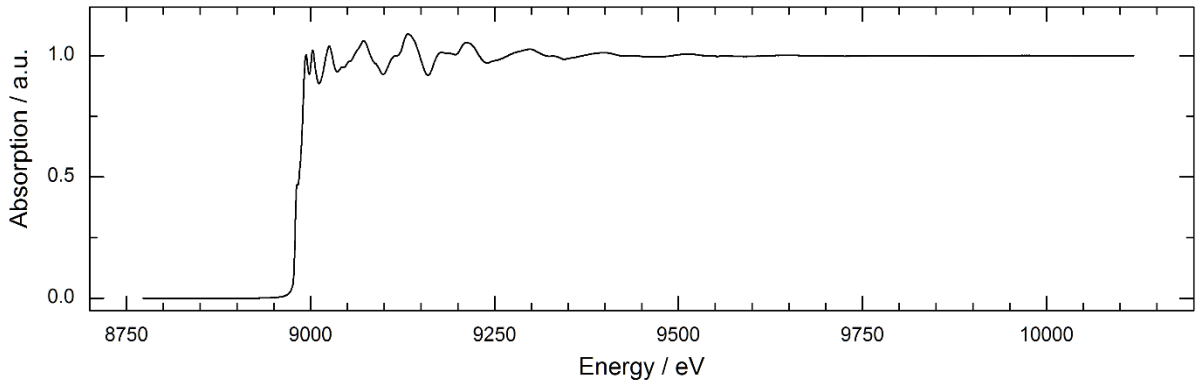

Figure 4.21: Normalized and flattened X-ray absorption spectrum of copper at the K-edge. The raw spectrum which is shown in **Figure 4.20**.

$$\mu^*_{norm}(E) = \frac{\mu(E) - \mu_{Pre}(E)}{\mu_{Post}(E_{Edge}) - \mu_{Pre}(E_{Edge})} \tag{4.20}$$

$$\mu_{norm}(E) = \frac{\mu(E) - \mu_{Pre}(E)}{\mu_{Post}(E) - \mu_{Pre}(E)} \tag{4.21}$$

The difference is found in the denominators. The constant value of the denominator of equation (4.20) is called the edge step of the absorption spectrum:

$$\Delta\mu_0 = \mu_{Post}(E_{Edge}) - \mu_{Pre}(E_{Edge}) \tag{4.22}$$

While equation (4.20) normalizes the edge jump to unity, equation (4.21) also raises the entire post-edge part of the spectrum to have the fine structure oscillating around unity, as shown in the plot of Figure 4.21. In literature, often no differentiation between these two functions are made and both are named *normalized*. However, the flattened spectrum is more frequently used to display and compare XANES measurements and is therefore often used for evaluation methods, such as linear combination analysis (see section 4.3.3).

For normalization purposes, JAQ provides a Victoreen and a polynomial function of adjustable degree to fit the pre- and post-edge regions. The Victoreen function implemented in JAQ, given by equation (4.23), has been extended by a constant variable c_0 to account for offsets, which for instance may originate from the arbitrariness of the gain settings of current amplifiers or of the absorption strength of ionization chambers.

$$\mu_{Victoreen}(E) = c_{III}E^{-3} - c_{IV}E^{-4} + c_0 \tag{4.23}$$

Since the Victoreen function is linear in its coefficients, JAQ can use the same linear least-squares algorithm as used for the polynomial fit. Computing the fit in this way is significantly faster than using iterative algorithms such as Levenberg-Marquardt.

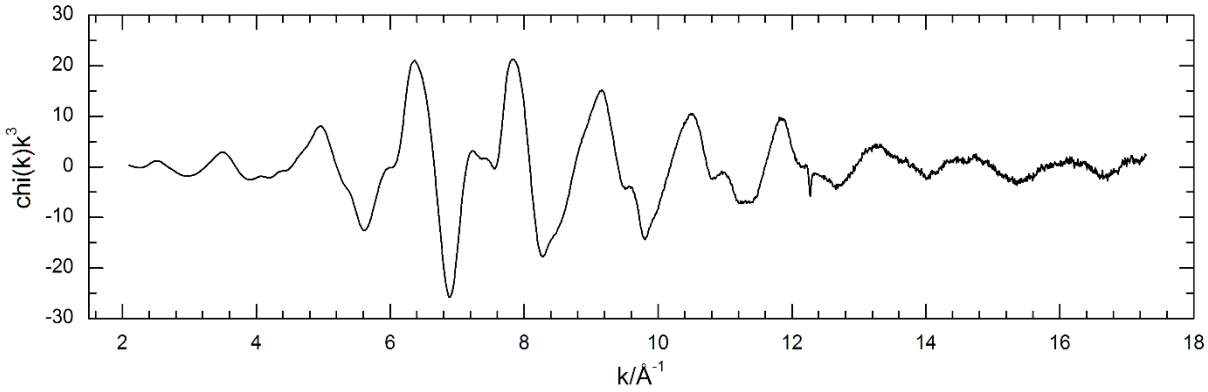

Figure 4.22: Extracted and k^3 weighted K-edge X-ray absorption fine structure of copper.

Fine structure

Retrieving the fine structure $\chi(k)$ is a more complex problem. Since the specific background function is in general not known exactly, neither through experimental measurements nor through theoretical calculations [**72**], this function needs to be guessed and approximated in some way.

All recognized and commonly used approaches assume a slow varying background beneath the faster oscillating fine structure [**21**,**32**,**70**,**72**]. They differ mainly in the assumption about smoothness and magnitude of low frequency components and require a different amount of computational effort. In the current version, JAQ employs a low degree k^n-weighted polynomial fit performed in k space. The polynomial degree can be adjusted by the user and appropriate values are typically found between 3 and 5. This gives a function which is flexible enough to follow the trend but not too flexible to mimic the fine structure and dampen its oscillations. The weighting in k space compensates the natural damping of the oscillations and ensures that the fit stays close to the mean of the absorption spectrum at high energies and is not distracted by the very strong oscillations near the absorption edge. Considering the computational effort, this approach is very efficient, and uses the same linear least-squares solver, which is used for the normalization fits.

Giving the fitted background function $\mu_{Atom}(E)$ and the previously determined edge step $\Delta\mu_0$, the fine structure, still as a function of energy, is defined by equation (4.24).

$$\chi(E) = \frac{1}{\Delta\mu_0}\big(\mu(E) - \mu_{Atom}(E)\big) \tag{4.24}$$

In a next step the photon energy E is converted to the photoelectron wave number k by means of equation (4.25).

$$k = \frac{1}{\hbar}\sqrt{2m_e\big(E - E_{Edge}\big)} \tag{4.25}$$

To compensate the dampening of the fine structure at increasing wave numbers, the fine structure $\chi(k)$ can be weighted by a factor k^n, where n is an integer number between 1 and 3. The final result is shown in Figure 4.22.

4.3.3 Linear Combination Analysis

Probably one of the most powerful and basic tools of QEXAFS data analysis is given with linear combination analysis (LCA), also called linear combination fitting (LCF). The aim of this method is to describe the current state of the sample as a linear combination of well-known states, often called references or basis functions. The current state is given by a measured and normalized X-ray absorption spectrum $\boldsymbol{\mu} = [\cdots, \quad \mu(E_j), \quad \cdots]^T$. Providing appropriate reference spectra $\hat{\boldsymbol{\mu}}_l$ as input, the LCA yields linear coefficients c_l which satisfy equation (4.26) with an error $\boldsymbol{\varepsilon}$ as small as possible.

$$\boldsymbol{\mu} = \sum_{l=0}^{k-1} c_l \hat{\boldsymbol{\mu}}_l + \boldsymbol{\varepsilon} \tag{4.26}$$

If multiple or even all spectra of a QEXAFS measurement are analyzed the coefficients can be determined as a function of time. The gained information is often utterly important and invaluable for the determination of reaction kinetics and the verification of theoretical models which describe the underlying chemical reactions.

In practical applications, however, the required references or even the right number of different linearly independent references to properly model the measurement, might be unknown a priori. To support the LCA, various auxiliary methods are available with 3rd party software. Two of the more important ones are the principal component analysis (PCA) which helps to determine the number of pure states contained in a measurement [**79**,**80**] and multivariate chemometric methods which try to identify the pure states [**81**,**82**].

Singular Value Decomposition

The LCA can be expressed as a linear least squares problem by calling to minimize the absolute square of the error vector $\boldsymbol{\varepsilon}$. This leads to the governing equation (4.27) and the task to minimize $\chi^2_{(i)}$, which may not be mistaken for the fine structure $\chi(k)$. Here, the outer index i denotes the different spectra of the QEXAFS dataset and the corresponding coefficient vectors.

$$\chi^2_{(i)} = \left| \begin{bmatrix} \vdots & \vdots & & \vdots \\ \hat{\mu}_0(E_j) & \hat{\mu}_1(E_j) & \cdots & \hat{\mu}_{k-1}(E_j) \\ \vdots & \vdots & & \vdots \end{bmatrix} \begin{bmatrix} c_0 \\ c_1 \\ \vdots \\ c_{k-1} \end{bmatrix}_{(i)} - \begin{bmatrix} \vdots \\ \mu(E_j) \\ \vdots \end{bmatrix}_{(i)} \right|^2 \tag{4.27}$$

$$= \left| \boldsymbol{D} \cdot \boldsymbol{c}_{(i)} - \boldsymbol{\mu}_{(i)} \right|^2 \tag{4.28}$$

The columns of the matrix $\boldsymbol{D}$ contain the reference spectra and is usually referred to as the design matrix of this problem. When performing the LCA on a large QEXAFS dataset, this matrix stays unaltered and only the current state $\boldsymbol{\mu}_{(i)}$, which is to be analyzed, is successively replaced in each cycle of a batch processing loop. Thus, all necessary transformations of $\boldsymbol{D}$ only need to be computed once, initially before entering the loop. To find the best coefficient vector $\boldsymbol{c}_{(i)}$ which minimizes $\chi^2_{(i)}$ JAQ uses a

singular value decomposition (SVD) of the design matrix. In general the SVD yields three matrices, which together satisfy equation (4.29).

$$\boldsymbol{D} = \boldsymbol{U} \cdot \begin{bmatrix} \ddots & & \\ & w_l & \\ & & \ddots \end{bmatrix} \cdot \boldsymbol{V}^T \tag{4.29}$$

The matrix $\boldsymbol{U}$ is column-orthogonal, $\boldsymbol{V}$ is orthogonal and the matrix in the middle contains only the singular values w_l of $\boldsymbol{D}$ on its diagonal. With the Moore-Penrose pseudoinverse of this matrix, equation (4.28) can be rearranged and the coefficient vector can be calculated according to equation (4.30).

$$\boldsymbol{c}_{(i)} = \left\{ \boldsymbol{V} \cdot \begin{bmatrix} \ddots & & \\ & {}^{1}/_{w_l} & \\ & & \ddots \end{bmatrix} \cdot \boldsymbol{U}^T \right\} \cdot \boldsymbol{\mu}_{(i)} \tag{4.30}$$

As already mentioned, the computation of the entire decomposition and of all matrix multiplications within the braces of equation (4.30), is required only once. After that it is only one matrix vector multiplication per spectrum to determine the coefficients. On today's conventional office computers the presented procedure allows to analyze tens of thousands of spectra within a couple of minutes.

The GUI

JAQ implements a dedicated module to enable LCA. All loaded QEXAFS files and absorption spectra which have been normalized in a previous step are available within the LCA GUI. This is shown in Figure 4.23. From two tables the user can define the source function, i.e. the data set which is to be analyzed, and the basis functions. The fitting range in the energy domain can be set by the user to specify a region of interest. On command all spectra within the data set are analyzed and the coefficients of each reference spectrum are plotted as a function of the source spectrum number. The error estimate R^2, as defined by equation (4.17), is as well displayed as a function of the source spectrum number. A horizontal scrollbar enables to browse through all source spectra. Simultaneously a vertical cursor is drawn in the coefficient's plot indicating the current position within the data set. Thus, distinctive regions and changes of the coefficients can be readily followed in the spectra's plot. Furthermore, all input and output functions can be converted and exported to ASCII to enable post processing with 3rd party programs.

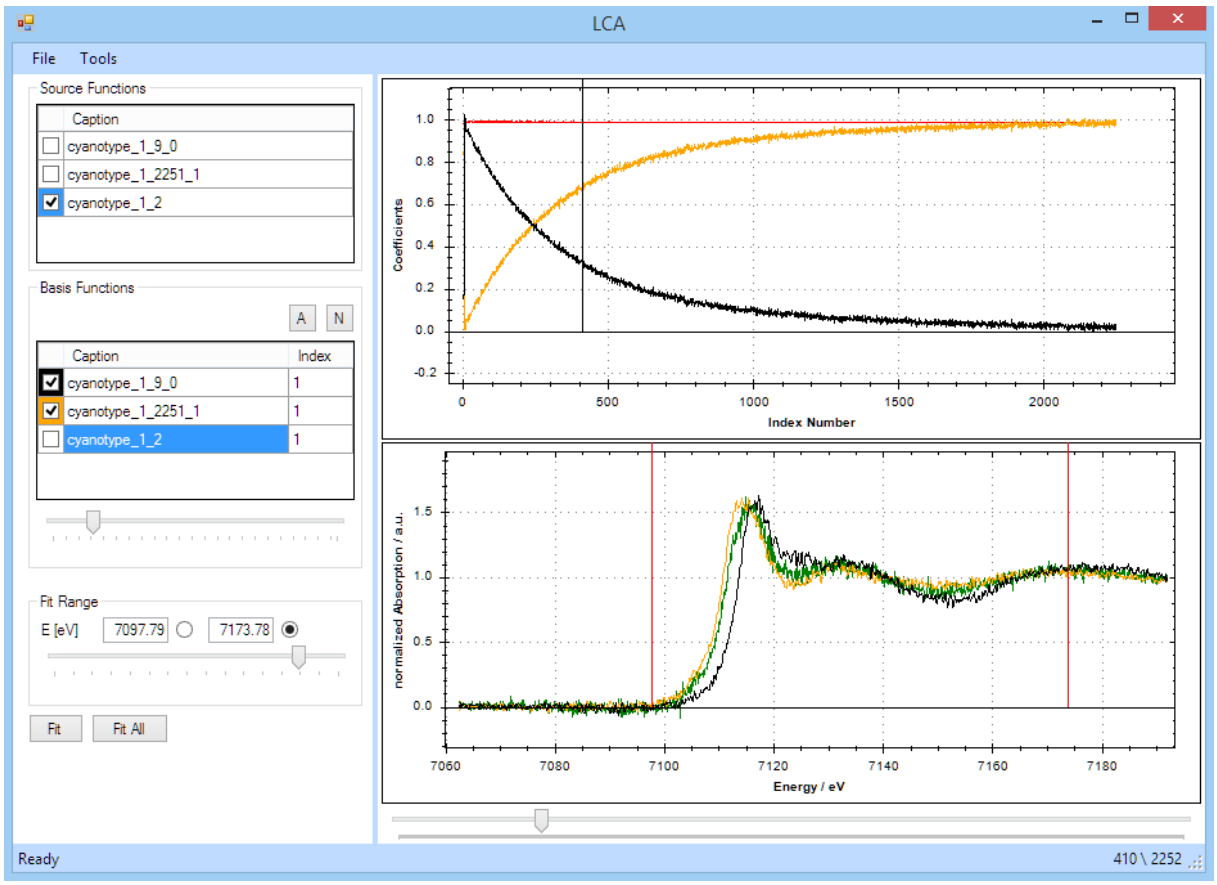

Figure 4.23: GUI of the LCA module in JAQ. The bottom plot shows all input spectra and indicates the fitting range with vertical red cursors. The top plot displays the evolution of the found linear coefficients and R^2 (see equation (4.17)) as a function of spectrum number. Shown is the aging process of Cyanotype due to radiation damage. The XANES spectra were recorded with 1 Hz oscillation frequency.

5 Planar Parallel Plate and Gridded Ionization Chambers

The gridded ionization chamber is a much more sophisticated design of the well-known planar parallel plate ionization chamber. A conductive grid, placed above the electron sensitive electrode, screens the slow drift motion of positive ions [**83**,**84**]. Without their influence the response time can be significantly improved by typically two orders of magnitude down to a few microseconds [**17**]. This allows to further expand into the sub-second time regime of QEXAFS measurements and is therefore one of the major breakthroughs in QEXAFS instrumentation [**4**,**15**]. Furthermore it is probably the most important development of ionization chambers at synchrotron radiation sources during the last two decades.

Historically, a grid electrode was first added to ionization chambers by O. R. Frisch in the 1950s [**83**,**84**,**85**] and hence is also often called a Frisch-Grid. At that time, the grid was required to enable precise energy measurements of α-particles emitted from radioactive samples. The application of a grid electrode to improve the bandwidth of ionization chambers, however, is new.

This chapter deals with the gridded and planar parallel plate ionization chamber in detail. Section 5.1 reviews the underlying principles of gaseous ionization chambers in general. It closes with a discussion of the fundamental processes which lead to the output ionization current and define the dynamic behavior. Built devices, which have been used for the QEXAFS measurements presented in this text, are investigated in particular with respect to their step response. The prerequisites to perform these measurements and their results are discussed in section 5.2.

5.1 Principles of Ionization Chambers

Ionization chambers are gas based X-ray detectors. Incident X-rays interact with the filling gas and are converted into ions and electrons which are then electronically detected as an electric current. Under proper operational conditions the measurable output current is proportional to the incident X-ray flux. The basic principles have been investigated and discussed over many years [**85**,**86**,**87**,**88**]. A brief

overview, emphasizing the relevant parts and differences of gridded ionization chambers is given in this section.

Within the considered hard X-ray regime, ranging from a few keV to about 40 keV photon energy, the photo electric effect is by far the strongest photon-matter interaction [**27**,**89**]. As a result of this process the entire energy of the incident photon is transferred to the atom or molecule, which immediately causes the ejection of a single photoelectron. After the photoelectron is released the atom is left in an excited state with a hole in the ionized shell. This hole propagates to the outer shells via a combination of Auger and fluorescence transitions. The emitted Auger electrons, fluorescence photons and the primary photoelectron can in turn also ionize the gas giving rise to a cascade, creating more free ions and electrons. Within the linear regime of the ionization chamber this cascade dies out eventually and the released electrons and ions thermalize quickly [**90**].

The generic ionization chamber consist of two separated plane parallel electrodes. The X-ray beam passes between these electrodes and ionizes the filling gas. An electric field caused by an applied voltage across these electrodes draws the free charge carriers apart towards the oppositely charged electrodes. This charge drift generates an electric current which is proportional to the ionization rate, especially if recombination is small or negligible. This current is thus a measure of the incident photon flux.

5.1.1 Electron and Ion Interaction in Gases

The ionization processes create singly and multiply charged positive ions and free electrons. With electronegative gases present, such as oxygen or water vapor, also negative ions can be formed through electron attachment [**90**]. To benefit from a gridded ionization chamber it is required to prevent the formation of negative ions, since they are able to bypass the grid and thereby render it ineffective. Therefore only gases with zero electron attachment cross sections, such as the rare gases or nitrogen are used and considered in the following sections.

The measurable output ionization current is caused by the movement of the charge carriers. Their behavior determine the properties of the ionization chamber including the response time and are therefore of great interest. Free ions and electrons in a gaseous environment are in constant thermal motion. The electric field of the ionization chamber gives rise to a superimposed velocity component along the field lines. Since the electric field is constant in time and spatially homogenous, this leads to a constant drift velocity. The equilibrium drift velocities of the different charge carriers are one of the most important properties which determine the response behavior of ionization chambers.

Ion Drift Velocity

The drift velocity of ions, u^+, in a gaseous environment depends on the electric field strength $\mathcal{E}$ and the gas pressure p. It has been observed that the drift velocity follows equation (5.1) over a wide range of the quotient $\mathcal{E}/p$ [**91**,**92**,**93**,**94**,**95**].

$$u^+ = \mu^+ \frac{\mathcal{E}}{p} \tag{5.1}$$

The proportional factor μ^+ is called the ion mobility. As long as the energy gain between two collisions is small compared to the thermal energy, the ion mobility can be assumed to be constant and independent of the field strength and pressure [**85**,**87**]. Tabulated values of the reduced ion mobility are listed in tables 5.1 to 5.3 for various species of nitrogen, argon and neon ions in their parent gases.

The expression of the reduced ion mobility is generally accepted in order to enable comparison between measurements which have been performed under different conditions, such as gas temperature T and gas pressure p. The ion mobility μ^+ is therefore corrected to standard conditions by means of equation (5.2) yielding the reduced ion mobility μ_0^+.

$$\mu_0^+ = \mu^+ \frac{273.15\ \mathrm{K}}{T} \frac{p}{101325\ \mathrm{Pa}} \tag{5.2}$$

The usual field strength of a planar parallel plate ionization chamber is on the order of some thousand Volts per centimeter. This results in a typical ion drift velocity of about 10 mm/ms. Since the ions have to travel at least a few millimeters to arrive at an electrode, the ion transient time is of the order of some tenth of a millisecond. At this point it is clear that solely due to the ion transient time variations of the ionization rate, which occur on a shorter time scale, can not be measured without distortions.

Nitrogen

N^+	N_2^+	N_3^+	N_4^+	Ref.	Year of Publication
			2.6	[**96**]	(1965)
2.47	1.44		1.84	[**97**]	(1965)
2.54	1.7	1.9	2.34	[**98**]	(1965)
2.97	1.87	2.26	2.33	[**99**]	(1969)
3.01	1.9	2.26	2.31	[**91**]	(1976)
			2.37	[**100**]	(2012)

Reduced mobilities in cm^2/Vs.

Table 5.1: Reduced mobilities of nitrogen ions in nitrogen.

Argon

Ar^+	Ar^{++}		Ar_2^+	Ar_3^+	Ar_{13}^+	Ar_{33}^+	Ref.	Year of Publication
	^3P	^1D						
1.63							[**101**]	(1952)
1.6	2.65*)						[**102**]	(1954)
1.6			1.9				[**103**]	(1963)
1.54	2.6		1.83				[**104**]	(1967)
1.4	2.4		1.95				[**105**]	(1967)
1.55						0.82	[**106**]	(1969)
1.56			1.84		1.23	0.82	[**107**]	(1975)
1.53	2.49		1.83				[**91**]	(1976)
	2.7	2.2					[**108**]	(1978)
2.1			1.8	1.65			[**109**]	(1978)
1.5			1.85				[**110**]	(2010)

Reduced mobilities in cm^2/Vs.

*) Value attributed to Ar^{++} ion based on ref [**108**].

Table 5.2: Reduced mobilities of argon ions in argon.

Neon

Ne^+	Ne^{++}		Ne_2^+	Ne_3^+	Ne_{13}^+	Ne_{33}^+	Ref.	Year of Publication
	^3P	^1D						
4.4							[**101**]	(1952)
4.0			6.5				[**102**]	(1954)
4.1			6.5				[**103**]	(1963)
					3.1	2.25	[**107**]	(1975)
4.07			6.16				[**91**]	(1976)
	7.0	6.5					[**108**]	(1978)
			5.4	5.4			[**109**]	(1978)
4.4			6.2				[**111**]	(2011)

Reduced mobilities in cm^2/Vs.

Table 5.3: Reduced mobilities of neon ions in neon.

Electron Drift Velocity

Free electrons are created in various ways. Besides the high energy photoelectron, secondary electrons of lower energy are released during numerous relaxation processes. These electrons thermalize rapidly as a result of elastic and inelastic scattering at the surrounding gas [**90**]. Due to the large difference in mass only small amounts of energy are transferred in electron-atom or electron-molecule collisions. At the same time the energy gain from the electric field is very effective. As a consequence the mean energy of the free electrons, which are subject to an electric field can be easily in excess of the thermal energy. The energy distribution as well as the drift velocity of the thermalized electrons are determined by the momentum transfer cross sections (see Appendix E) of the involved gas species and the present electric field strength [**112**]. Classical theories, which calculate theses quantities, are based on the Boltzmann transport equation [**113**]. Its solution yields information about the electron transport including diffusion coefficients, drift velocity and energy distribution [**90**,**114**,**115**]. There are several approaches in order to solve the Boltzmann transport equation. The data of figures 5.1 to 5.4 are based on calculations performed with the MAGBOLTZ 2 code [**116**], which employs a Monte Carlo integration technique to solve the problem [**117**,**118**].

The plots of figures 5.1 to 5.4 show the drift velocity and mean energy of the electron swarm in Ar / N_2, Ar / CO_2, Ar / NH_3 and Ar / CH_4 mixtures at typical gas pressures, slightly above ambient pressure. The gases are added to the argon in order to modify the free electron energies and to increase the dielectric strength of the filling gas. This allows to work at a higher electric field strength and prevents electric break down of the gas [**119**,**120**]. The alteration of the total X-ray absorption of the filling gas raised by the additives is typically negligible due to their relative small amount and the comparable high atomic number of argon. As such N_2, CO_2, NH_3 and CH_4 act as efficient quenching gases which can be added in almost any case without any concern. At the same time the electron drift velocity is substantially increased, sometimes even further than the drift velocity of the pure gases. This effect was observed very early [**86**,**121**,**122**] and is caused by the dominant Ramsauer-Townsend resonance of argon (see Appendix E). By adding a small amount of molecular gasses such as N_2, CO_2, NH_3 or CH_4, the free electrons can lower their energy in small amounts by exciting vibrations and rotations of the additive, limiting the possibility to gain higher energies. As a consequence the energy distribution is considerably shifted to lower energies at which the momentum transfer cross section of Argon exhibits a pronounced minimum, i.e. the Ramsauer-Townsend resonance. Due to the reduced frequency of electron-Argon collisions, the main share of the filling gas (the Argon) becomes basically transparent for low energetic electrons and the drift velocity increases. The drift velocity of thermalized electrons is strongly dependent on the actual gas mixture. Even small impurities for instance from outgassing components can affect the drift velocity. However, based on the calculations shown in figures 5.1 to 5.4 the drift velocity of thermalized electrons is on the order of some 10 mm/µs, which is roughly three orders of magnitude higher than the drift velocity of ions.

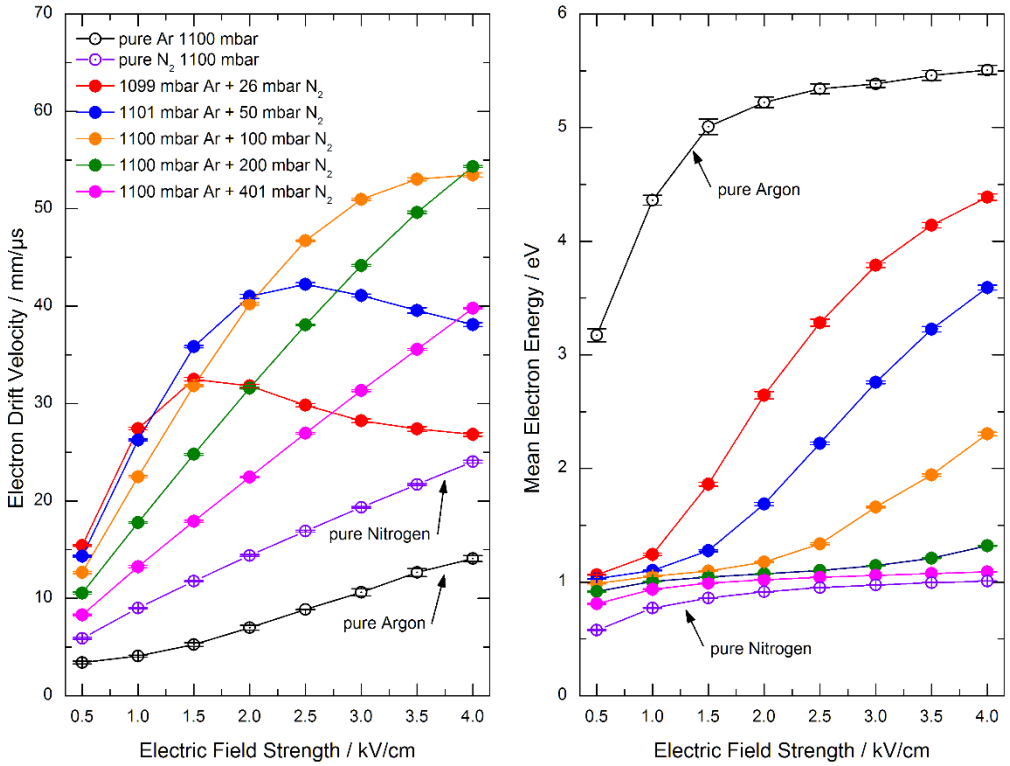

Figure 5.1: Electron drift velocity and electron mean energy in argon / nitrogen mixtures as a function of the electric field strength.

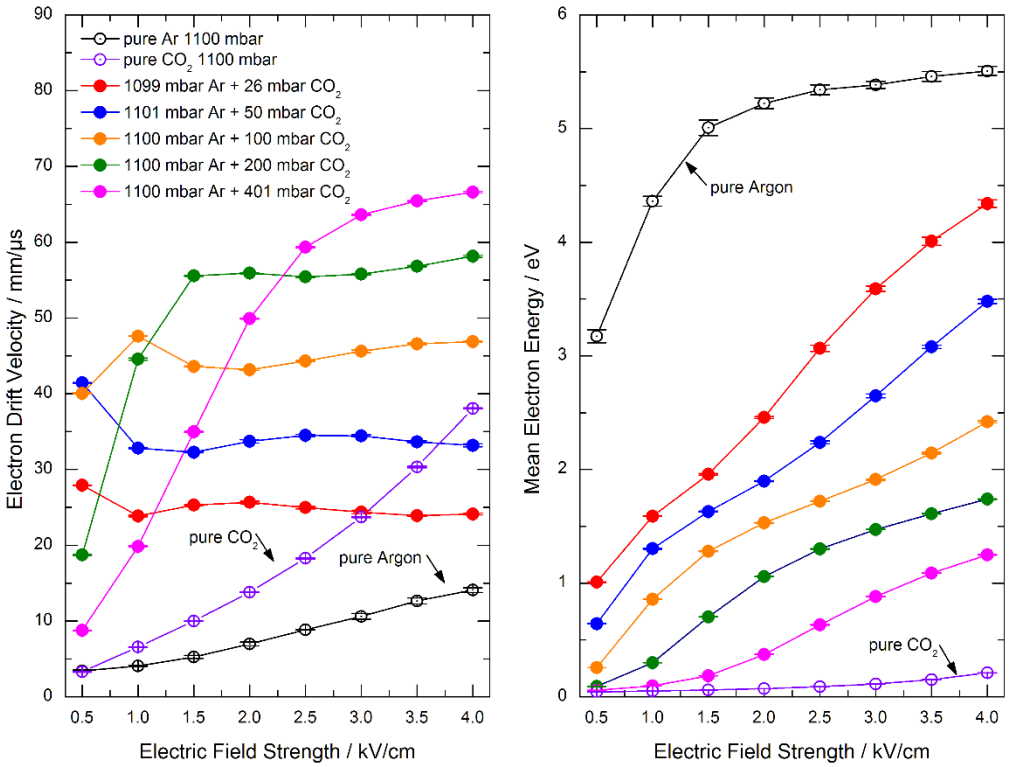

Figure 5.2: Electron drift velocity and electron mean energy in argon / carbon dioxide mixtures as a function of the electric field strength.

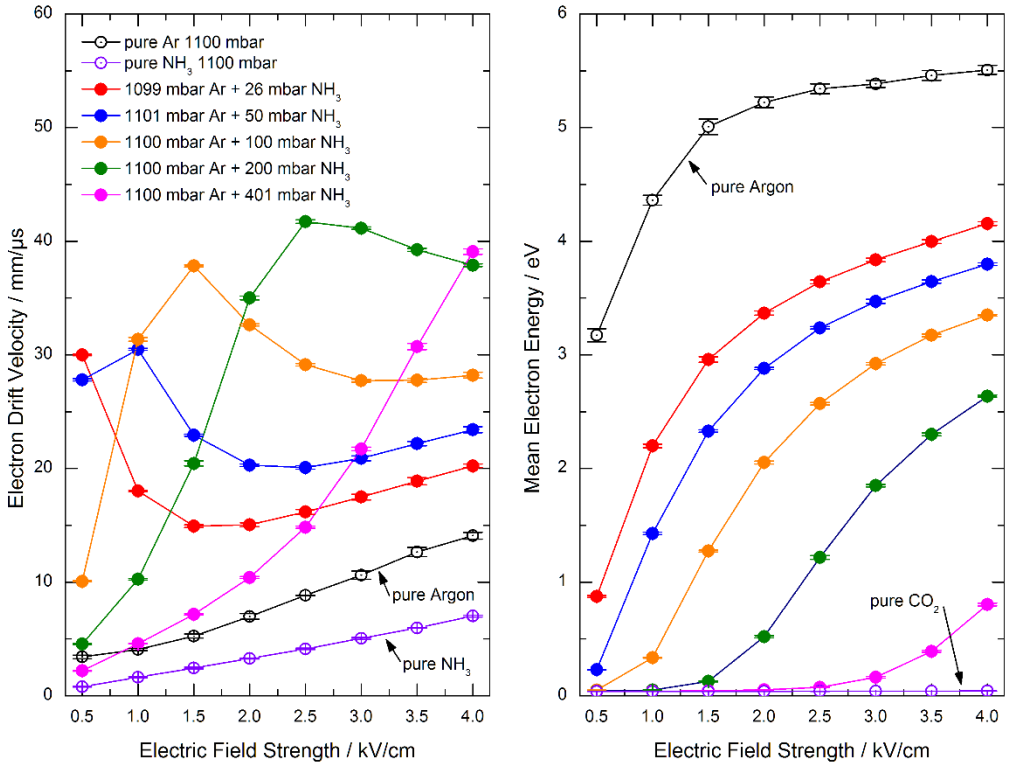

Figure 5.3: Electron drift velocity and electron mean energy in argon / ammonia mixtures as a function of the electric field strength.

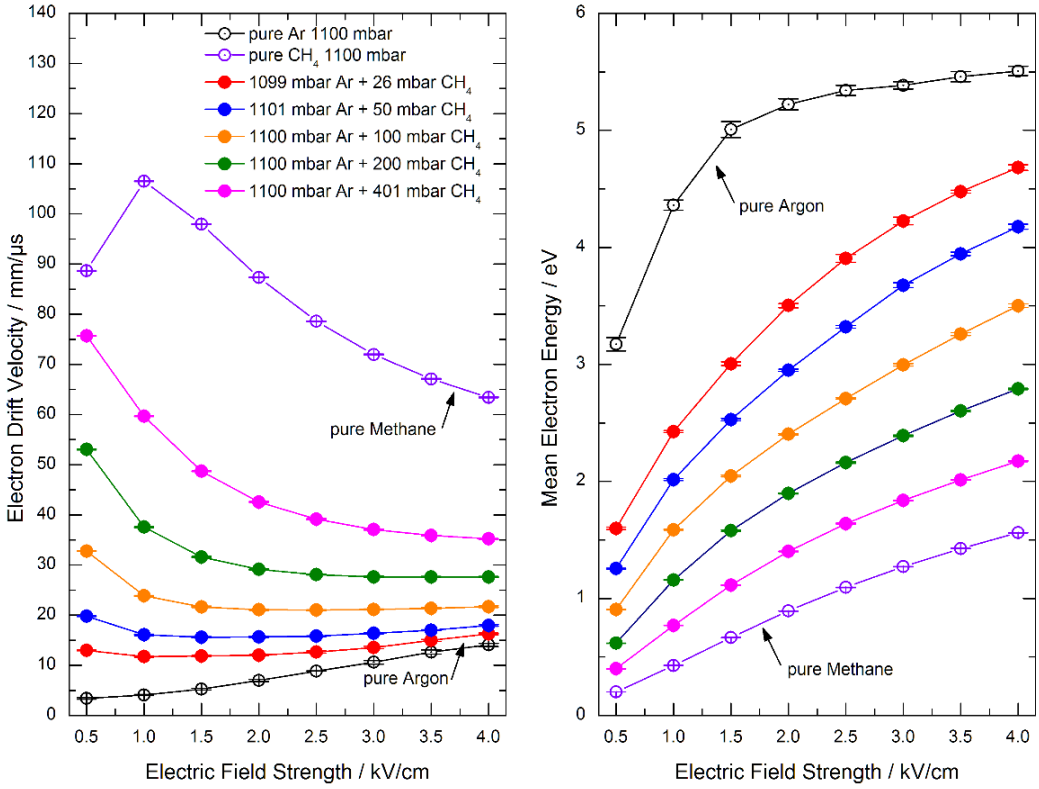

Figure 5.4: Electron drift velocity and electron mean energy in argon / methane mixtures as a function of the electric field strength.

5.1.2 Pulse and Step Response

The pulse response of an ionization chamber is the time dependent output current caused by a single ionization event. It can be derived by considering the surface charges, which are induced by the released charge carriers. Here, the single ionization event is considered as an instant transformation of a neutral atom or molecule into single already thermalized positive and negative point charges, each carrying a total charge of $\pm q$. This approach is obviously not able to resolve the effects during the thermalization itself. However, this process takes place on the nanosecond time scale [**90**], which is much faster than the transient time of the charge carriers within the ionization chamber and is therefore not relevant to the overall dynamic behavior. In this way, the derived pulse response is basically the idealized convolution kernel of an ionization chamber and hence can be used to calculate the step response by means of a mathematic convolution.

A single point charge q placed somewhere between the electrodes of an ionization chamber induces a surface charge on these electrodes. The strength of the charge induction depends on the location of the point charge. Assuming two planar parallel infinitely large electrodes, this function becomes dependent on the perpendicular height, z, of the charge only. Having electrode ***I*** at the origin of a coordinate system and electrode ***II*** at the distance d_{Gap} the induced surface charge follows equations (5.3) and (5.4).

$$q_{\boldsymbol{I}}(z) = -q\left(1 - \frac{z}{d_{Gap}}\right) \tag{5.3}$$[ii]

$$q_{\boldsymbol{II}}(z) = -q\frac{z}{d_{Gap}} \tag{5.4}$$

Since the point charge is drifting towards the oppositely charged electrode due to the action of the electric field, the induced surface charge changes with time. If electrode ***I*** is electrically grounded and electrode ***II*** is on a negative electric potential as depicted in Figure 5.5, a negative charge would drift downwards towards electrode ***I*** and a positive charge upwards towards electrode ***II***. Giving the point of origin of the ionization event, z_0, the drift motion of a negative and a positive charge carrier can be described by equations (5.5) and (5.6).

$$z^- = z_0 - u^- t \tag{5.5}$$

$$z^+ = z_0 + u^+ t \tag{5.6}$$

[ii] The derivation of this equation can be found in Appendix D.

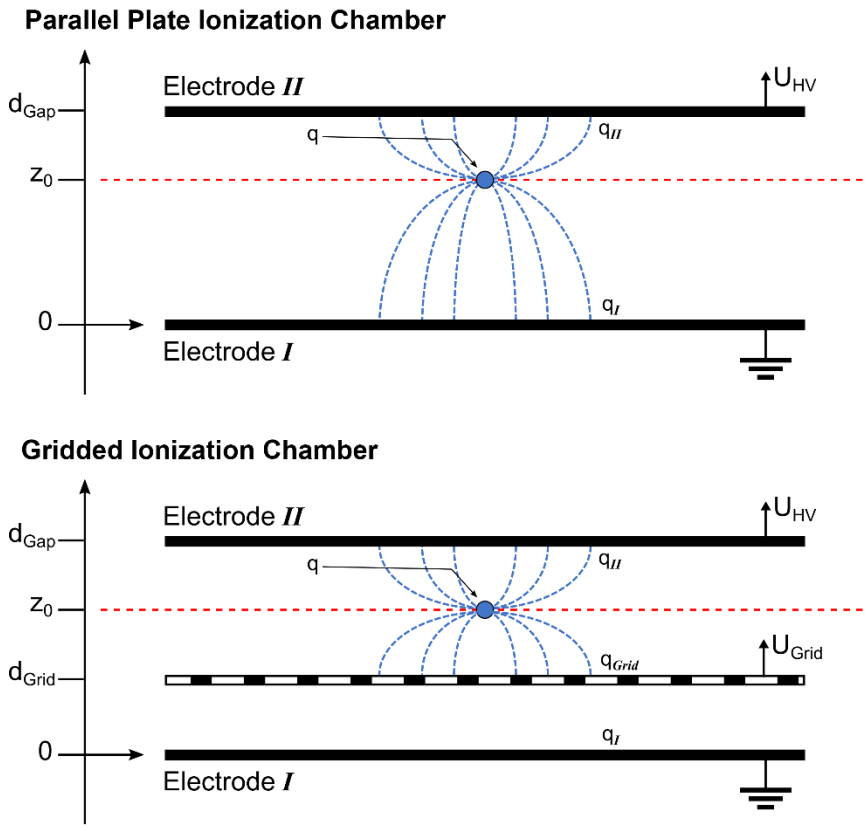

Figure 5.5: Schematic representation of a parallel plate and gridded ionization chamber indicating the surface charge induced by a point charge q. The grid acts as an electric shield and prevents the point charge of inducing surface charges on electrode ***I***. At the same time it is penetrable for negative charge carriers only.

Since an ion pair is created during the considered ionization event, the actually induced surface charge is given by the superposition of both point charges. Expanding equations (5.3) and (5.4) and substituting the drift motion leads to the time dependent surface charge of the electrodes ***I*** and ***II***:

$$q_I\ (t) = \frac{q}{d_{Gap}}(u^- + u^+)t \tag{5.7}$$

$$q_{II}(t) = -\frac{q}{d_{Gap}}(u^- + u^+)t \tag{5.8}$$

These surface charges are drained by external components in order to keep the electric potentials of the electrodes constant. To achieve that, charges of the same magnitude are moved. Thus, the time derivative of these functions yield the electric current which can be measured flowing between the electrodes and the external components. Accordingly, it does not matter, except for the sign, if the current is measured at the grounded or at the high voltage electrode. However, in almost all practical scenarios it is easier and safer to measure the current at the grounded electrode.

Pulse Shape and Step Response of a Planar Parallel Plate Ionization Chamber

The charge carriers eventually arrive at the electrodes. From that moment on the particular charge carriers are not contributing to the surface charges any longer. Referring to those points in time

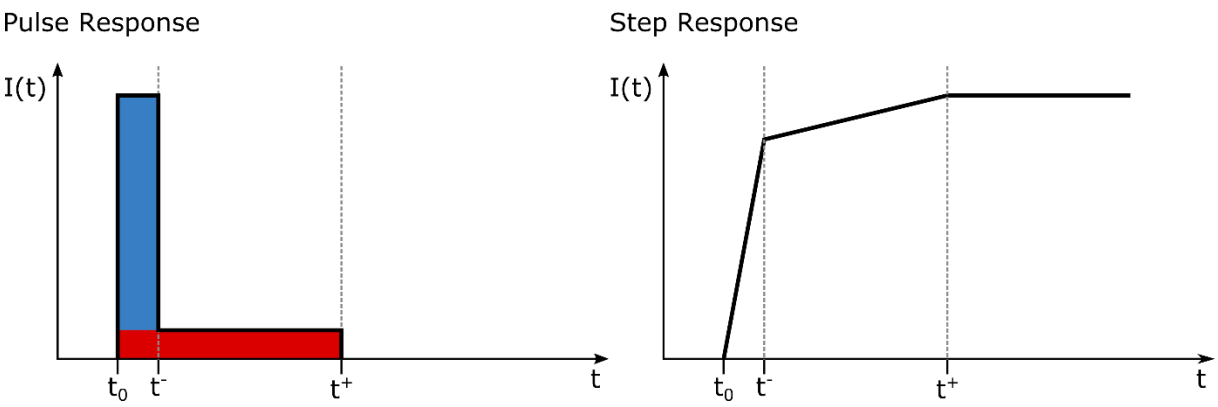

Figure 5.6: Schematic illustration of the pulse and step response of a parallel plate ionization chamber. The colored regions of the left plot indicate the contribution of different charge carriers. The fast electron is represented by the blue area and the much slower ion is represented by the red area. The left plot, i.e. the step response, is obtained by a convolution of the pulse response with step function.

as t^-, t^+ and letting the ionization event occur at $t = 0$, the entire output current pulse from a single ionization event follows equation (5.9).

$$I(t) = \begin{cases} \frac{q}{d_{Gap}}(u^- + u^+) & : \quad 0 < t < t_- \\ \frac{q}{d_{Gap}}u^+ & : \quad t_- < t < t_+ \\ 0 & : \quad \text{otherwise} \end{cases} \tag{5.9}$$

$$t^- = \frac{z_0}{u^-} \tag{5.10}$$

$$t^+ = \frac{d_{Gap} - z_0}{u^+} \tag{5.11}$$

Here it is assumed that the positive charge carrier, i.e. the ion, reaches its electrode at last. When both charge carriers have arrived at their electrodes the ionization event is completed and the current pulse ends. This obviously infers that the pulse length and as such the response time of the ionization chamber is dominated by the slowest charge carrier, which contributes to the output signal.

The pulse and step response according to the equations above are schematically depicted in Figure 5.6. The step response is obtained by a convolution of the pulse response with a step function. It is recognizable that the two contributions of the pulse response, blue for fast electrons and red for slower ions, lead to two different slopes in the step response.

From the equations (5.10) and (5.11) four significant parameters which determine the response time can be identified. These are the electrode spacing d_{Gap}, the point of origin z_0 and the drift velocities u^- and u^+. The latter are functions of the electric field strength and gas species and was discussed in the previous section 5.1.1. The geometric quantity d_{Gap} is a parameter which needs to be considered during the construction of the ionization chamber, since it typically can not be altered at a later time.

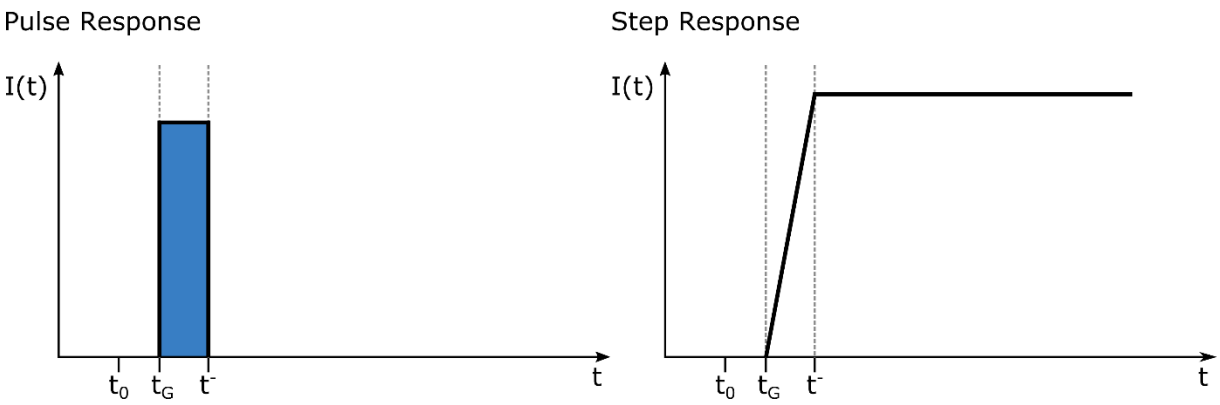

Figure 5.7: Schematic illustration of the pulse and step response of a gridded plate ionization chamber. The blue region of the left plot indicates the sole electron contribution. The left plot, i.e. the step response, is obtained by a convolution of the pulse response with a step function.

Trying to improve the response time by adjusting these parameters is technically limited by various factors. Most important, the dielectric strength of the filling gas prevents the operation at very high electric field strength. This limits both, the achievable drift velocity of the ions and the minimal electrode spacing d_{Gap}, which defines the drift length. Furthermore the intense X-ray beam should be kept at a minimum distance from any electrode or surface to prevent high energetic, not yet fully thermalized, electrons from hitting them. This also dictates a minimum electrode gap as well as a minimum distance z_0. In conclusion, the time response of conventional parallel plate ionization chambers is always limited by the ion drift. An adequate solution to this problem is given by the gridded ionization chamber which screens the ionic contribution almost completely and relies on the electron motion only.

Pulse Shape and Step Response of a Gridded Ionization Chamber

The grid, as shown in Figure 5.5, separates the space between the electrodes in two regions, which will be called the ionization and drift region. In a device, X-rays pass between the electrode ***II*** and the grid electrode, thus creating ion pairs within the ionization region. If the grid is at an intermediate negative potential the drift directions are not altered and the positive charge still drifts upwards while the negative charge drifts downwards towards the grid electrode. These movements, again, generate currents due to charge induction. However, the electrode ***I*** is now shielded by the grid and is therefore not affected by the charge drift motion within the ionization region. Negative charge carriers are able to pass the grid and enter the drift region. From this point on, surface charges are induced on the electrode ***I*** and generate a current while the charge carrier is drifting towards it. As a consequence, all terms of equation (5.9) which refer to the positive charge carrier vanish and the equation reduces to

$$I(t) = \begin{cases} \frac{q}{d_{Grid}} u^- & : \quad t_G < t < t_- \\ 0 & : \quad \text{otherwise} \end{cases} \tag{5.12}$$

$$t_{Grid} = \frac{z_0 - d_{Grid}}{u^-} \tag{5.13}$$

$$t^- = \frac{d_{Grid}}{u^-} \tag{5.14}$$

where t_{Grid} denotes the point in time at which the negative charge carrier passes the grid electrode. The resulting pulse and step response are schematically shown in Figure 5.7. Compared to the response behavior of a conventional parallel plate ionization chamber, the ionic contribution is suppressed leaving only the electrons. Since these have to bypass the grid first to be measured, a short delay t_{Grid} appears. Accordingly, the step response is slightly shifted by the delay and broadened by electron transient time t^-.

Owing to the high electron drift velocity, t_{Grid} and t^- amount to usually less than a few hundred nanoseconds. Hence, the total step response is typically shorter than one microsecond. To observe the delay or to investigate the influence of the electron drift velocity, extremely fast electronics including amplifiers and ADCs with a combined bandwidth in the 100 MHz regime would be required.

5.2 Step Response Measurements of Ionization Chambers

In QEXAFS experiments, ionization chambers are used to measure incident X-ray intensities as a function of time. The intensities may change rapidly, in particular in the regions around the absorption edges. For the experiment it is crucial that the output signal of the ionization chambers are proportional to the incident intensity and are not distorted by their finite response time. In section 4.1 a lower limit of the required DAQ's sampling frequency in a QEXAFS experiment was derived. This limit was found based on the requirement, not to loose any information of the spectrum and the assumption that the spectrum can not be better resolved than enabled by the energy resolution of the monochromator. In this sense, the derived minimum sampling frequency ensures that any two consecutive sampled data points are not further distant than the given energy resolution. These considerations can be expanded for the entire measurement chain, especially including the ionization chambers and current amplifiers. As a consequence the bandwidth, or in other terms the response time, of these devices have to match or better exceed the minimum sampling frequency. Considering the results of Figure 4.2 a bandwidth on the order of a couple of 100 kHz or response time below 10 µs are required. It will be shown in this section that this demand is satisfied by the use of gridded ionization chambers.

In order to determine the response time of conventional and gridded ionization chambers, the step response function has been measured. This function gives a detailed insight in the underlying physical principles which govern the dynamic behavior and lead to the finite response. Finally, the step response functions allow to determine the convolution kernels of these detectors.

The Convolution Kernel and the Step Response Function

Since ionization chambers belong to the class of linear time invariant systems, their response behavior can be described mathematically by an individual convolution kernel $h(t)$. Based on this function, the response $g(t)$ to an arbitrary input $s(t)$, i.e. a time dependent incident X-ray flux, can be calculated by means of a convolution:

$$g(t) = \int_{-\infty}^{+\infty} s(\tau)h(t-\tau)d\tau. \tag{5.15}$$

To determine the convolution kernel experimentally, a well-known fast changing X-ray pulse is necessary. Obviously, a sufficiently short input pulse, which approaches the Dirac delta function would directly yield the wanted convolution kernel. However, the accuracy of this method is limited by the actual finite width of the input pulse. Furthermore, the integral intensity of such a pulse is often extremely low making this approach exceedingly challenging in practice.

A simpler method to obtain the convolution kernel is to measure the step response function of the ionization chamber. This is the time dependent output response, which is caused by a sudden change of the incident X-ray flux. If noise is negligible, the convolution kernel can be determined by a time derivative of the measured step response function. This is expressed in equation (5.16), where $\Theta(t)$ is the Heaviside step-function.

$$h(t) = \frac{d}{dt}\int_{-\infty}^{+\infty} \Theta(t)h(t-\tau)d\tau \tag{5.16}$$

With this method the accuracy of the convolution kernel is mainly dependent on the edge sharpness of the step function $\Theta(t)$.

Experimental Setup

The step response was measured at the SuperXAS beamline. A fast X-ray chopper was built to generate defined X-pulses and to enable the measurements [**50**]. This device is presented in the next section 5.2.1. The measurements were conducted using a monochromatic beam of 8979 eV. The beam was focused to a vertical height of 120 µm and the chopper was placed in the focal plane between two ionization chambers, as illustrated in Figure 5.8. The ionization chamber under test was mounted electrically isolated on a translational stage to allow vertical scans and step response measurements at different positions within the ionization region. An additional ionization chamber in front of the X-ray chopper was dedicated to monitor the incident X-ray flux and to allow normalization of the step response measurements.

The outputs of both ionization chambers were amplified with fast current-to-voltage amplifiers and sampled at 2 MHz with the 16 bit ADCs of the QEXAFS DAQ (c.f. section 4). The amplifiers were specifically build with regard to short rise times in the low microsecond regime. The design and properties of the employed current amplifiers are presented in section 5.2.2. In addition to the output

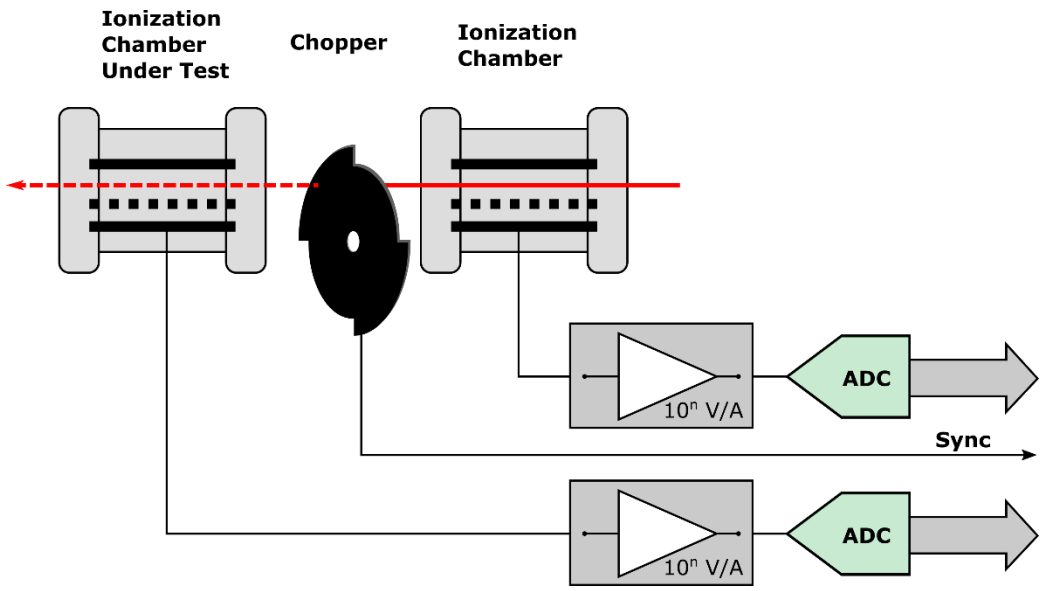

Figure 5.8: Experimental setup to measure the step response of ionization chambers. The ionization chamber on the right is used to normalize the response to the incident intensity.

signals a synchronization signal from the chopper generated by means of a photoelectric light barrier was sampled as well. The absolute gas pressure of the ionization chambers were measured during the filling procedures. For this purpose, each ionization chamber was equipped with a piezo resistive pressure transducer (Newport Omega PAA33X-C-3). Using its digital output, this device provides a precision of 0.05% at its full scale of 3000 mbar, thus yielding an error of ±1.5 mbar. During all measurements the valves were closed gas-proof in order to avoid pressure fluctuations.

5.2.1 X-ray Chopper

The indented step response measurements require sharp, well-defined, X-ray pulses. These can be generated with shutters or spinning disk choppers. Although shutters are fairly flexible to create arbitrary pulse patterns it is very difficult to reach fast opening or closing times in the microsecond regime [**123**]. Using choppers, however, extremely short opening and closing times in the microsecond regime and even well below have been realized [**124**]. Hence, a rotating disk chopper with its rotational axis perpendicular to the direction of the X-ray beam was built. A picture of the chopper revealing the geometry of the disc is shown in Figure 5.9. The chopper is capable of producing X-ray pulses with a typical rise time of a few microseconds and a period length of about 2 ms. The pulse width is long enough to allow the output current of the ionization chamber to settle before the next intensity jump occurs. This assures the applicability of equation (5.16), which retrieves the convolution kernel from the step response function.

The chopper uses the brushless DC motor and the drive electronics of a common hard disk drive (HDD). The platters of the HDD were replaced by a single 2 mm thick aluminum disk with a diameter of 140 mm. These match the mass moment of inertia of the original platters, which allows to use the drive electronics of the HDD. The driver embeds a closed feedback loop in order to maintain a constant

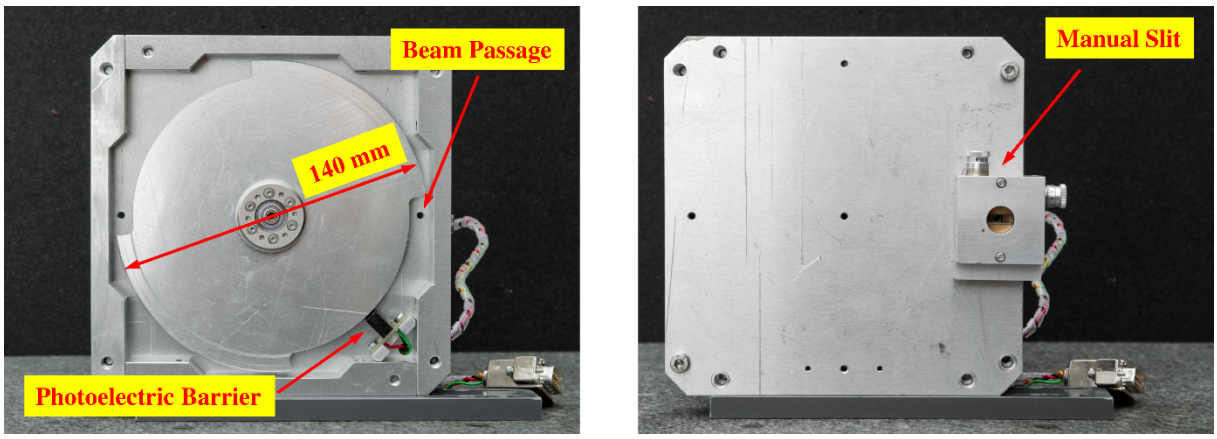

Figure 5.9: Left: Opened X-ray chopper, showing the notched disk and the forked photoelectric barrier in the bottom right corner. This is used to generate a reference signal, which can be used to synchronize multiple measurements. Right: Closed X-ray chopper, showing a manual horizontal and vertical slit system mounted in front of the beam passage to cut the beam halo. This figure was partly published in [**50**].

angular frequency. A photoelectric light barrier (Vishay TCST1300) was integrated to monitor the rotation and to provide a means to synchronize multiple measurements. Observations of the angular frequency over 1 h by means of this light barrier, showed a mean angular frequency of 120.9000 Hz ± 0.8 mHz. The small jitter results in a rise time stability in the picosecond regime.

Rise Time and Pulse Width

The chopper uses a symmetrically notched disk to periodically interrupt the X-ray beam. Each of the two notches cover one quarter of the circumference. This geometry creates a symmetric rectangular pulse pattern. Given the angular frequency of the disk, the pulse width t_{Period} defined by equation (5.17) amounts to 2.07 ms. The rise time of the created pulses is approximated by equation (5.18). Here, δ denotes the width of the beam's cross section and r is the distance of the center of beam measured from the axis of rotation. This distance amounts to 68 mm.

$$t_{Period} = \frac{1}{4f} \tag{5.17}$$

$$t_{Rise} \approx \frac{\delta}{2\pi f r} \tag{5.18}$$

All parameters but the width of the beam are fixed with this chopper. Thus the beam size is important and should be kept small, ideally by focusing. According to the equation above, a beam width of 120 µm, results in a rise time of to 2.3 µs.

5.2.2 Current Amplifier

The output signals of ionization chambers are usually very small. Even with a reasonable high flux of 10^{11} photons per second to 10^{12} photons per second, an ionization chamber which absorbs 10% of the incident X-rays, will yield an ionization current of around one microampere only. The second

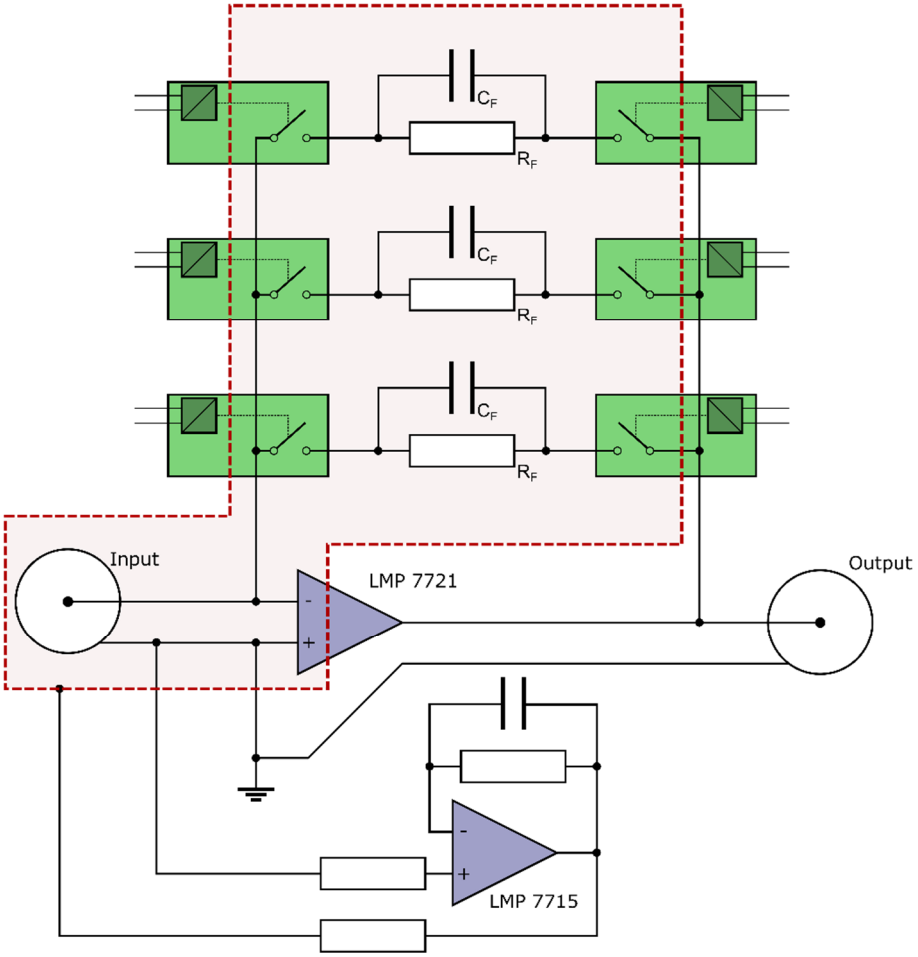

Figure 5.10: Schematic view of the newly developed current-to-voltage amplifier. The red dashed line illustrates the guard ring which frames the sensitive traces to prevent leakage currents. Each of the three feedback resistors R_F define a specific gain and are remotely activated by relays.

ionization chamber, behind the sample in a QEXAFS experiment, is subject to an even lower incident intensity. Although the intrinsic absorption of it can be set higher, for instance to about 80%, the output current is typically one to two orders of magnitude lower. In order to measure these small currents precisely, they need to be amplified and converted into macroscopic voltages first. Hence, gains between 10^5 VA^{-1} and 10^9 VA^{-1} are very common for these applications. At synchrotron radiation facilities, the *Keithley 428 Programmable Current Amplifier* is widely spread and very often used in conventional EXAFS and QEXAFS experiments. This device incorporates an inverting current-to-voltage amplifier with adjustable gain and a low pass output filter stage. However, even with the filter disabled the provided bandwidth at the required gain is not high enough for fast QEXAFS measurements in the millisecond regime. In fact, by employing the new gridded ionization the current amplifier becomes the bandwidth limiting device. Due to this limitation a new current amplifier was developed and finally used for all QEXAFS and step response measurements presented throughout this text.

Properties of the LMP Current Amplifier

A transimpedance amplifier based on the voltage-to-voltage operational amplifier LMP7721 manufactured by Texas Instruments (formerly National Semiconductor) was built. This chip was

specifically chosen based on the extremely low input bias current of typically ±20 fA and the comparatively high gain bandwidth product (GBW) of 17 MHz. The amplifier was designed to address the two most often required gain settings at modern QEXAFS beamlines, which are 10^6 VA^{-1} and 10^7 VA^{-1}. A schematic circuit diagram is shown in Figure 5.10. The feedback resistors R_F match and define the gain and can be remotely interchanged by electro mechanical latching relays. During operation only one feedback resistor is active at a time.

The achievable bandwidth of this transimpedance amplifier depends on the total input capacitance. Considering the ionization chamber, cables, connectors and electrical feedthroughs the total input capacitance estimates to about 30 pF to 60 pF. By using a simplified single pole approximation of the gain transfer function and maintaining a minimum phase margin of 45°, the maximum bandwidth can be determined by equation (5.19) [**125**].

$$f_{BW}^{max} = \sqrt{\frac{f_U}{2\pi R_F C_I}} \tag{5.19}$$

Here, f_u is the unity gain bandwidth, i.e. the GBW of 17 MHz, and C_I the input capacitance. With the estimated input capacitance a bandwidth of 212 kHz to 300 kHz at a gain of 10^6 VA^{-1} and 67 kHz to 95 kHz at a gain of 10^7 VA^{-1} is the absolute maximum with this chip. This already shows that due to its high slew rate of greater than 9 $V\mu s^{-1}$, it is unlikely that the amplifier will become slew rate limited. However, the bandwidth determined in this way can only be realized with a matched feedback capacitance C_F, which can be calculated by equation (5.20).

$$C_F^{opt} = \sqrt{\frac{C_I}{2\pi R_F f_U}} \tag{5.20}$$

According to this equation the feedback capacitors at both gains need to be less than 1 pF. Since parasitic capacitances originating from traces on the circuit board (PCB) and the package of the feedback resistors and the capacitors can already be in excess of the targeted value, careful PCB layout is required. Direct measurements of the bandwidth of the built amplifier reveal 196 kHz at 10^6 VA^{-1} and 93 kHz at 10^7 VA^{-1}. These results can be used to deduce the actual feedback capacitance by means of equation (5.21).

$$C_F = \frac{1}{2\pi R_F f_{BW}} \tag{5.21}$$

The measured and calculated properties are summarized in Table 5.4. It shows that the amplifier at a gain of 10^7 VA^{-1} is already near its optimum, whereas at a gain of 10^6 VA^{-1} the feedback capacity could still be improved. However, at both gains the LMP based amplifier exhibits a bandwidth which is roughly 3 times higher than that of the Keithley (see Table 5.5).

Transimpedance Amplifier - LMP7721						
Paramter	**Symbol**	**Unit**	**Value**			
Unity Gain Bandwidth	f_U	MHz	17			
Gain		VA^{-1}	10^6		10^7	
Feedback Resistance	R_F	MΩ	1		10	
Estimated Total Input Capacitance	C_I	pF	30	60	30	60
Maxiumum Bandwidth	f_{BW}^{max}	kHz	300	212	95	67
Optimal Feedback Capacitance	C_F^{opt}	pF	0.53	0.75	0.17	0.24
Measured Bandwidth	f_{BW}	kHz	196		93	
Actual Feedback Capacitance	C_F	pF	0.81		0.17	

Table 5.4: Expected and experimentally determined properties of the transimpendance amplifier based on the LMP7721 chip.

	Keithley 428		**LMP**	
Gain	10^6	10^7	10^6	10^7
Rise Time	5.6 µs	9.3 µs	1.8 µs	4.2 µs
Bandwidth	58 kHz	35 kHz	196 kHz	93 kHz
Noise RMS	3 nA_{pp}	0.6 nA_{pp}	3 nA_{pp}	1.1 nA_{pp}

Table 5.5: Comparison between the Keithley 428 Programmable Current Amplifier and the new developed LMP based amplifier. The noise was sampled with an Agilent DSO 7100B at 15.625 MS/s.

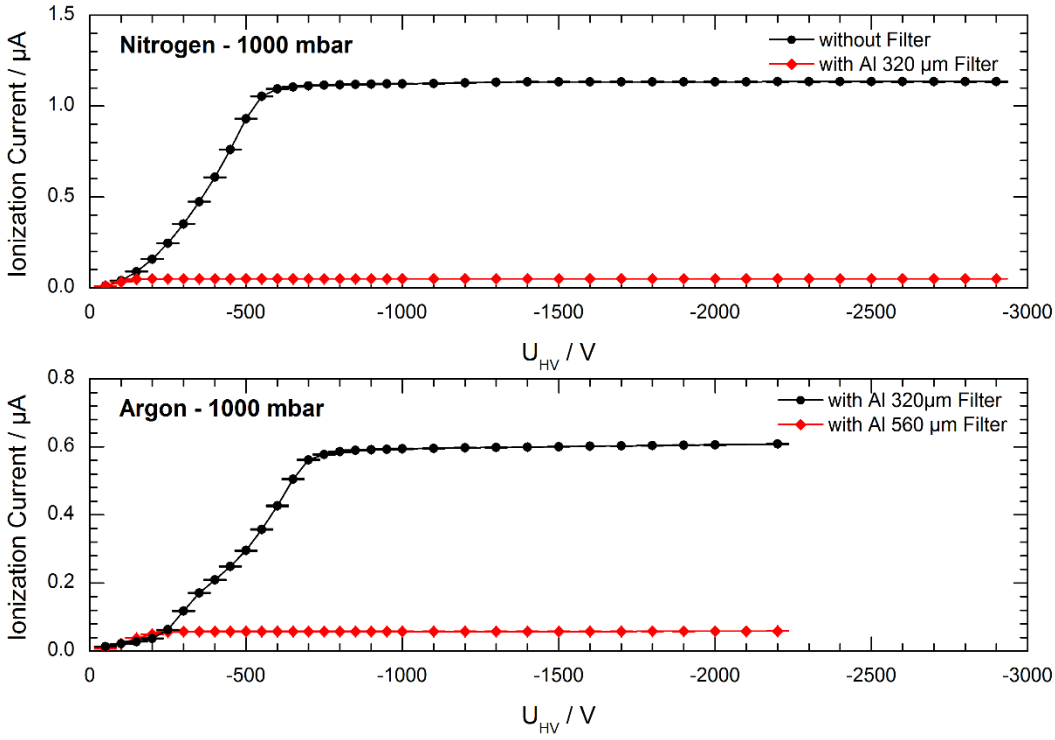

Figure 5.11: Voltage scans of a planar parallel plate ionization chamber filled with nitrogen (top) and argon (bottom) measured with an incident X-ray energy of 8979 eV. The red curves are measured with a lower incident intensity, which was attained by using aluminum filters of various thicknesses.

5.2.3 Response of Parallel Plate Ionization Chambers

The step response of a conventional planar parallel plate ionization chamber was investigated. The electrodes inside of the gastight housing were mounted 13.5 mm apart. The entrance and exit windows featured a circular aperture of 12 mm in diameter, which gives enough space to investigate the vertical dependency of the step response. The bottom electrode was grounded through the current-to-voltage amplifier, whereas the upper electrode was connected to a negative voltage provided by a stable high voltage power supply (ISEG, THQ DPS 30-405-24-5). All measurements were conducted with a focused beam (~120 µm) at 8979 eV.

Voltage Scan

To ensure an operation within the linear regime of the ionization chamber, voltage scans were performed prior to the step response measurements, as shown in Figure 5.11. Increasing the electric field strength within the ionization region by adjusting the applied voltage, results in a likewise increase of the output current at the beginning. This behavior is due to an increase of free charge carriers caused by an actual reduction of charge carrier loss due to recombination [**88**,**126**]. This rise is monotonic until the output current saturates. At this point recombination becomes negligible and the output current becomes independent of the applied voltage. This is where the linear regime of the ionization chamber begins and where the output current becomes an actual measure of the ionization rate, i.e. of the incident X-ray flux.

Thus the linear regime is reached earlier if the ionization chamber is subject to a lower incident flux, as shown by the red curves of Figure 5.11.

Step Response

As discussed in section 5.1.2 the output current of an ionization chamber is caused by the motion of the released charge carriers. With a homogenous and constant electric field present, this motion is entirely defined by just two parameters, the drift velocity and the drift length. This is also stated by the equations (5.9) to (5.11), which describe the pulse response. Since the drift length depends on the origin of the created charge carriers, the response time is expected to be dependent on the actual beam position relative to the electrodes. This dependency was investigated by the step response measurement shown in Figure 5.12. Here the beam position was varied in steps of 2 mm around the center position midway between the electrodes. The coordinate z_0 defines the beam position above the bottom, electron collecting, electrode. The step response was recorded for each position. By moving the X-ray beam closer to the negative high voltage electrode, i.e. by increasing z, the total drift length of the positive ions is reduced and the overall response time decreases. The very steep immediate rise of the step response originates from the fast electrons and is smoothed by the bandwidth of the current amplifier. It is independent on the beam height. The first derivatives of the step response functions, shown in the center plot of Figure 5.12, represent the convolution kernels of the ionization chamber (c.f. section 5.2). It clearly shows that the dominant slope of the step response, which is proportional to the ion mobility μ^+, is constant throughout the measurement and that the duration of this region correlates proportionally with the beam position z. The bottom plot displays the value $\hat{\mu}_0^+$ which is defined and calculated according to equations (5.22), (5.23) and (5.2).

$$\hat{\mu}^+ \coloneqq \frac{e}{I_{eq}} \sum_i \eta_i \mu_i \tag{5.22}$$[iii]

$$= \frac{d_{Gap}}{I_{eq} \mathcal{E}} \frac{d}{dt} I(t) \tag{5.23}$$

The value $\hat{\mu}^+$ is of the same unit [cm²/Vs] as the general ion mobility μ and will therefore be called *effective mobility* and $\hat{\mu}_0^+$ *reduced effective mobility* correspondingly. This quantity is used to describe the observable ion drift motion if multiple ion species with different mobilities μ_i are present. The coefficients η_i refer to the constant creation rates of the ith ion species. This coefficient may also incorporate the corresponding charge state which is created. The current I_{eq} is the equilibrium current, which settles when the ionization current $I(t)$ becomes stable. If only one ion species is present, this current, I_{eq} , equals ηe and the effective mobility becomes the actual ion mobility.

Based on the nature of the measurement, the effective ion mobility can not be determined within the first few microseconds during which the electron movement (and the current amplifiers bandwidth)

[iii] This equation is derived in Appendix F.

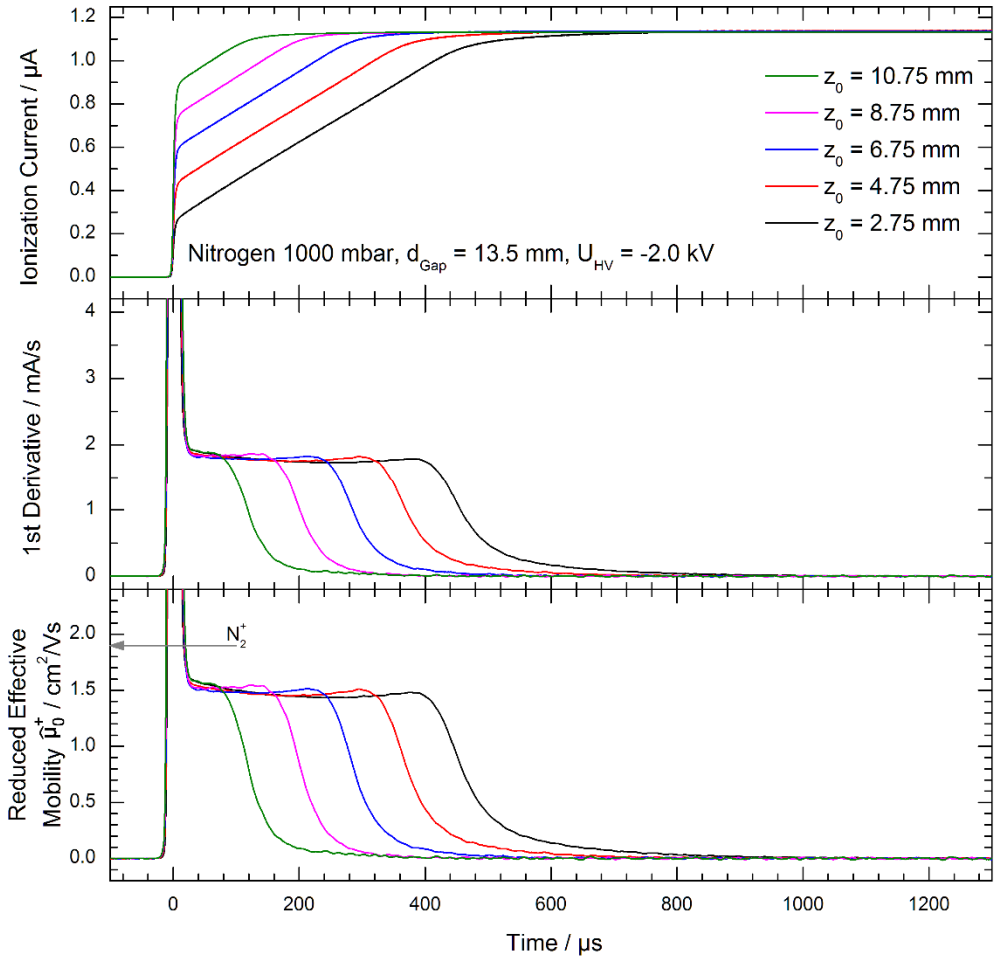

Figure 5.12: Top: Step response function of a nitrogen filled planar parallel plate ionization chamber measured at different vertical beam positions. The coordinate *z* defines the height of the beam above the electron collecting electrode. Center: The first derivative of the step response function, representing the convolution kernel of the ionization chamber. Bottom: Effective mobility according to equation (5.23). The grey arrow indicates the real mobility of the N_2^+ ion based on **Table 5.1**.

dominates the curve progression. Therefore the relevant part of the curve with respect to the effective ion mobility begins not until the first steep descend sets in. In this region, the observed effective ion mobility is nearly the same for all measurements and varies only weakly between 1.26 cm²/Vs and 1.36 cm²/Vs during the measurement. Detailed investigations and discussions of this behavior are discussed in the next subsection.

The dependency of the step response on the drift velocity of the ions was investigated by altering the applied voltage. In this way the electric field strength within the ionization region is altered causing different drift velocities. According to equation (5.1) the drift velocity correlates linearly with the applied voltage, which was increased in steps of 400 V starting at -1200 V up to -2800 V. The step responses, the first derivatives and the effective ion mobilities are shown in Figure 5.13. These measurements confirm the expected behavior: The drift velocity increases and the response time reduces at higher field strengths. Furthermore, the observed effective ion mobility shows to be independent of the field strength.

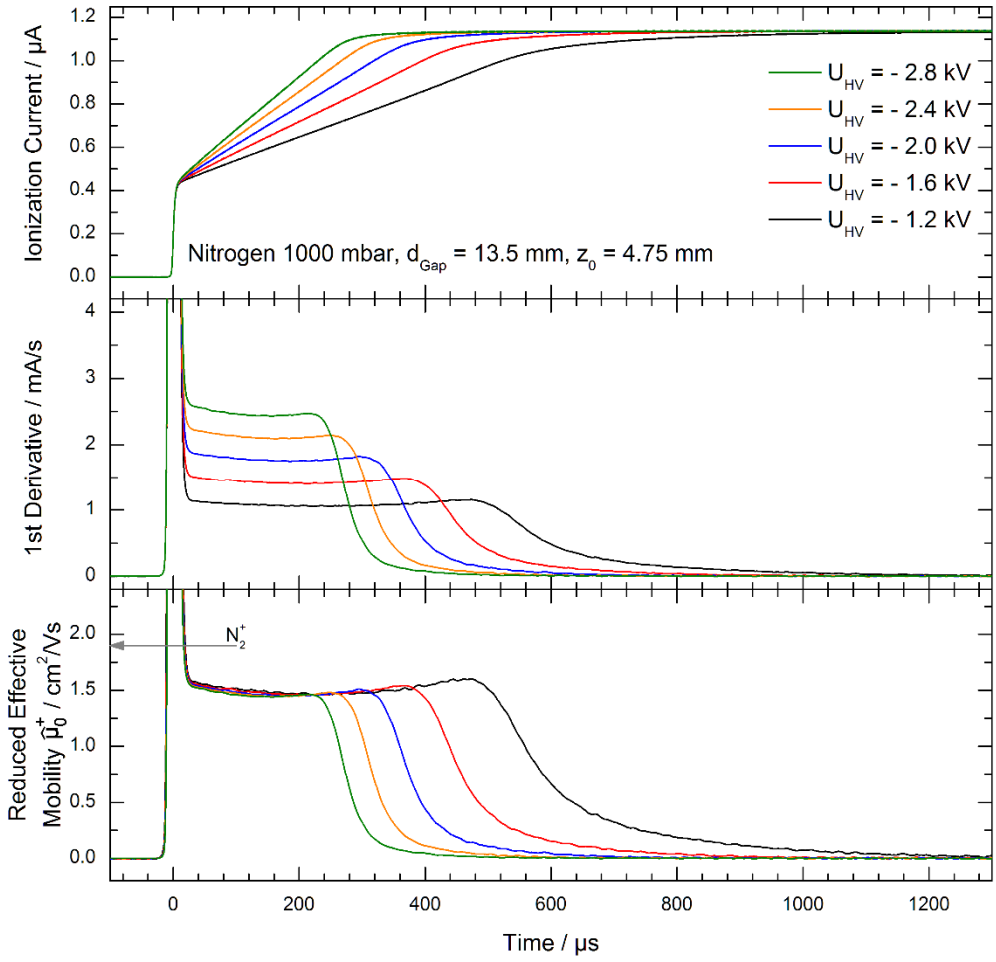

Figure 5.13: Top: Step response function of a nitrogen filled planar parallel plate ionization chamber measured with different applied voltages. Center: The first time derivative of the step response function, representing the convolution kernel of the ionization chamber. Bottom: Effective mobility according to equation (5.23). The grey arrow indicates the mobility of the N_2^+ ion based on **Table 5.1**.

According to these measurements the response time of planar parallel plate ionization chambers is clearly dominated by the ion movement. Increasing the applied voltage or reducing the drift length by aligning the ionization chamber in a way that the X-ray beam passes closer to the high voltage electrode improves the response time. However, the response times stay in the order of some 100 µs. The steep initial rise has not been altered during the entire series of step response measurements. This implies that the transient time of the electrons was always substantially shorter than the convolved combination of the rise times of the current amplifier (~1.8 µs) and the X-ray chopper (~2.3 µs). In fact, based on the theoretical drift velocity calculations (see Figure 5.1), the transient time for electrons at z_0 = 4.75 mm and -1200 V amounts to 1.2 µs in pure argon or 0.6 µs in pure nitrogen.

The Ion Drift Velocity

The dominant slope of the step response function is proportional to the ion drift velocity. If multiple ion species with different mobilities μ_i are created during the operation of the ionization

chamber their contribution to the slope depends on their specific creation rate η_i. With these rates unknown the actual ion mobilities are not directly accessible through these measurements and instead the effective ion mobility $\hat{\mu}^+$ is used to analyze, compare and quantify the step response. Equation (5.23) calculates the effective ion mobility by evaluating the slope and the plateau region of the step response function. In order to facilitate comparison between the referenced data given in the Tables 5.1 to 5.3 and the experimentally found values by means of this method, the effective mobility $\hat{\mu}^+$ is converted into the reduced effective ion mobility $\hat{\mu}_0^+$ which is defined by equation (5.2).

Nitrogen

Considering the step response measurements with Nitrogen (see Figures 5.12 and 5.13), the fact that the slopes after the kink are actually more or less constant over the entire rest of the response, suggest a single or at least very similar positive ion drift velocity or velocities. Otherwise, if ions with various drift velocities which differ distinctly from each other were present, multiple regions with different slopes should be identifiable in the step response measurements. In that case the derivatives are expected to show multiple plateaus. Since this was not observed in any of the step response measurements of the nitrogen filled ionization chamber, it can be assumed, that an equilibrium ion distribution is reached quite shortly within the first few microseconds [**127**]. Furthermore the present ion distribution seems to be independent of the applied electric field strength.

The effective ion mobility is constant within the range between 1.26 cm^2/Vs and 1.36 cm^2/Vs over a wide region. The observed effective mobility is lower than the mobility of any of the ions (N^+, N_2^+, N_3^+, N_4^+) given in Table 5.1. It seems therefore not possible to attribute a specific ion or a certain distribution of these ions to be accountable for the step response behavior. Instead the measurements suggest larger ionic nitrogen clusters with lower mobilities to be present.

Argon

The step response of an Argon filled planar parallel plate ionization chamber has been investigated as well. The situation here is more complex as shown by the measurements given in Figure 5.14. Both plots display the step response at different beam positions, while the electric field strength was kept constant. The left plots show the response behavior with -700 V, the right plots with -1400 V applied across the electrodes. Although, the ionization chamber was always operated within its linear regime (see Figure 5.11), the dependency of the step response on the beam position is quite different. While the measurements at -700 V strongly resemble the behavior of the nitrogen filled ionization chamber, the measured responses at -1400 V clearly deviate.

The lower plots, which show the effective ion mobility, give a more detailed insight. At -700 V the effective ion mobility decays weakly within the first 500 µs from about 1.8 cm^2/Vs to a value of 1.1 $cm^2/Vs \pm 0.1$ cm^2/Vs and keeps constant there. There is almost no noticeable dependency on the beam height. The same measurements at -1400 V show a different picture. The observable effective ion

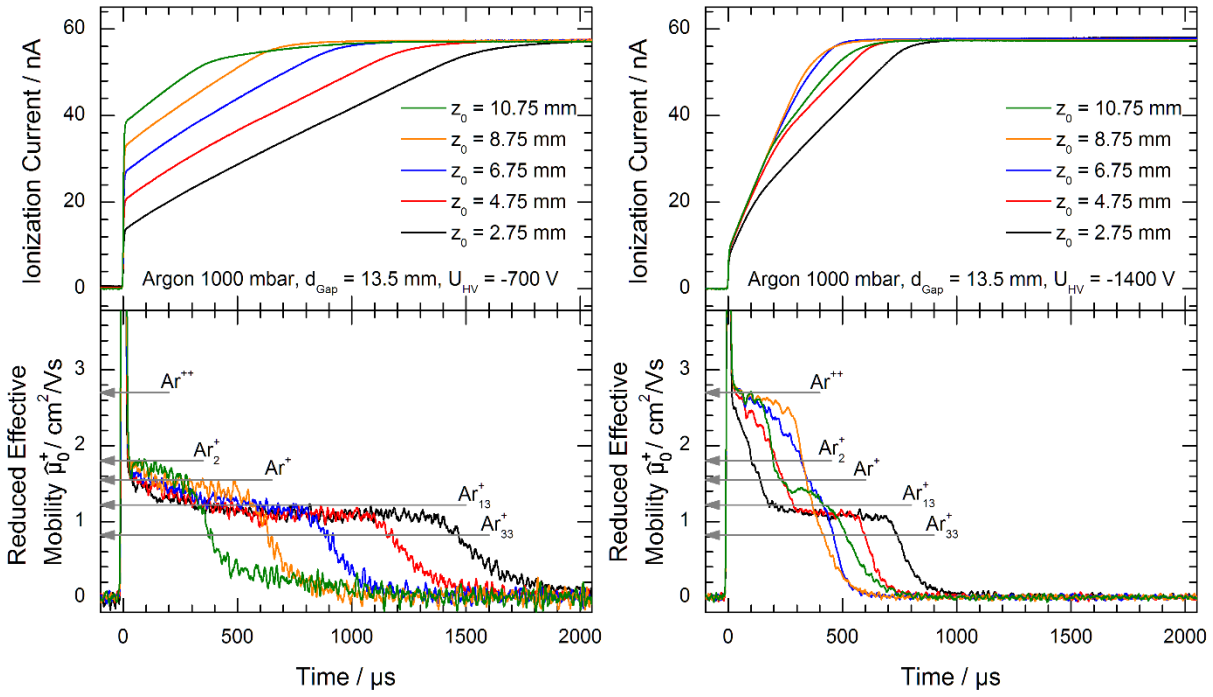

Figure 5.14: Step response functions and effective ion mobility of an argon filled planar parallel plate ionization chamber measured at different X-ray beam positions. The grey arrows represent the specific argon ion mobilities based on Table 5.2.

mobility starts at 2.6 $cm^2/Vs \pm 0.1$ cm^2/Vs and immediately begins to drop. The black and red curves, which belong to the long ion drift lengths of 10.75 mm and 8.75 mm, both show a distinct plateau around 1.1 cm^2/Vs. These plateaus are fairly stable over several hundred microseconds, until the effective mobility drops to zero, which happens when the ions ultimately reach the electrode. Following the progression of the blue and orange curves a plateau does not develop. While the blue curve smoothly falls without any pronounced structure, the orange curve drops abruptly after around 250 µs. At this point in time the ions reach the electrode with a still high, almost unchanged effective mobility.

The obvious dependency on the electric field strength is investigated in more detail in the plots of Figure 5.15. Here the step response is shown for different applied voltages between -700 V and -2200 V. The left and right plots display the response measured with a fixed beam position of 8.75 mm and 4.75 mm, above the electron collecting electrode. There are solid and dashed curves, which differentiate between a low, 519 V/cm to 740 V/cm (dashed curves) and a high 890 V/cm to 1630 V/cm (solid curves) electric field strength. The partitioning is not arbitrary, but should reflect the overall behavior of the step responses. The solid curves show a very similar progression among themselves, while the dashed curves are very sensitive to a variation of the applied voltage. Looking upon the high field dashed curves, the observed effective ion mobilities start at around 2.6 $cm^2/Vs \pm 0.1$ cm^2/Vs. Depending on the beam position, the effective mobilities drop either abruptly to zero (short drift length) or develop an intermediate plateau around 1.1 cm^2/Vs (long drift length) before decaying to zero.

The difference between the low and high field behavior can possibly be explained by means of the thermalized mean energy of the free electrons (see Figure 5.1) which are released during the

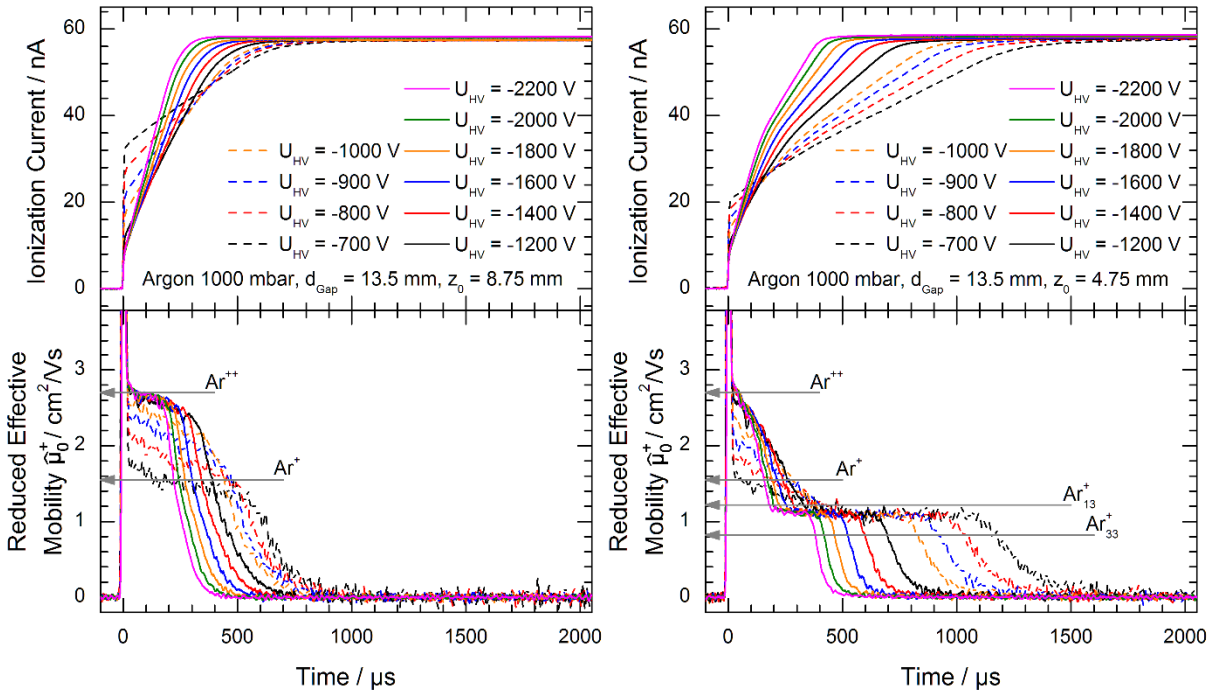

Figure 5.15: Step response functions and effective ion mobility of an argon filled planar parallel plate ionization chamber. The dashed curves indicate an electric field strength ≤ 740 V/cm and are given in increments of 100 V. The solid curves indicate a higher electric field strength ≥ 890 V/cm and are successively incremented by 200 V. The grey arrows represent the specific argon ion mobilities based on Table 5.2.

ionization events. This function is as well quite sensitive in beginning, before the mean energy asymptotically saturates. In fact the mean energy is altered between 3.1 eV and 3.8 eV within the 300 V variation of the dashed curves and between 4 eV and 5 eV within the 1000 V variation of the solid curves.

A dependency on the applied voltage is clearly noticeable. In contrast to the measurements with nitrogen, the electric field strength not only affects the drift velocity but also seems to modify the present ion distribution. This is suggested by the observed effective ion mobility. By comparing the ion mobilities (see Table 5.2) of Ar^{++}, Ar^{+} and singly charged ion clusters Ar_n^{+}, with the discussed measurements assumptions about the involved ions can be made. Following this idea, Ar^{++} ions can be present, however only if the field strength is high enough. The effective mobility is never truly constant around the Ar^{++} value but decreases towards lower values. If the drift length is short, this decrease is weak and it seems that a significant amount of Ar^{++} ions actually reach the high voltage electrode. However with a longer drift length the measurements show a more pronounced decrease which eventually becomes stable again (i.e. the plateau) around a low value which could be attributed to clustered argon ions. Thus it seems, that in this case the initial amount of Ar^{++} ions decays before the electrode is reached and less mobile cluster ions are formed. Ion clustering is not atypically especially not at high gas pressures, as it was used in the presented measurements [**106**,**107**,**127**,**128**,**129**,**130**,**131**,**132**,**133**]. The single charged Ar^{+} ion is hardly visible. The effective

mobility does not exhibit a distinct feature around the Ar^+ value. However, it seems possible that the Ar^+ ion is present as a share of a distribution of Ar^{++} or Ar_n^+ ions.

5.2.4 Response of Gridded Ionization Chambers

The step response of the gridded ionization chamber was measured in the same way as the planar parallel plate ionization chamber discussed in the previous section. The bottom electrode was grounded through the current-to-voltage amplifier, whereas the top electrode and the grid were connected to two independent negative voltages provided by stable high voltage power supplies (ISEG, THQ DPS 30-405-24-5). The X-ray beam entered midway between the high voltage electrode and the grid. The working aperture defined by the high voltage electrode to grid distance amounts to 6 mm.

Voltage Scans and Step Response

Since the gridded ionization chamber requires two high voltages, the parameter space of operation is larger than that of a conventional ionization chamber. The two voltages must be chosen depending on each other since the electric field strengths within the ionization and drift regions influence the efficiency and linearity of the gridded ionization chamber. To investigate the static behavior of the ionization chamber on the applied voltages, scans were performed. The grid voltage U_{Grid} was varied in steps of 500 V starting at -500 V up to -2000 V. With the grid voltage set, the electric potential of the top electrode was scanned from 100 V below the grid voltage up to -3000 V. The normalized ionization current as a function of these scans is shown in the top plot of Figure 5.16. Similar to the voltage scans of the planar plate ionization chamber (see Figure 5.11) the ionization current increases at the beginning. Here this behavior is due to two reasons: The increase of the electric field strength within the ionization region leads to a reduction of recombination losses and secondly the grid becomes more and more transparent for the released electrons. Both effects increase the rate of electrons entering the drift region beyond the grid. This course ceases eventually and the ionization current saturates. Within the beginning plateau region recombination is suppressed to a negligible amount and the transparency of the grid is almost independent of U_{HV}. This changes at higher values of U_{HV}. While the recombination loss remains negligible, the grids transparency diminishes, and the ionization current slowly drops again. Thus, the voltage scans can be divided into three different regions: Pre Plateau, Plateau and Post Plateau. However, the first scan with U_{Grid} = -500 V, does not reach the plateau region at all. Here recombination dominates until the applied voltage is high enough to already cause electron collection by the grid. With a reduced incident flux the plateau could probably be accessible, since a lower voltage is required to prevent recombination. As a consequence a minimum grid voltage, which is obviously dependent on the incident flux, is always required to operate the gridded ionization chamber.

The step response was measured at each data point of the voltage scans. The bottom plots of Figure 5.16 shows the step response in the case of the orange curve with U_{Grid} = -2000 V. According to the three identified regions of the voltage scans, the step response measurements are gathered in groups.

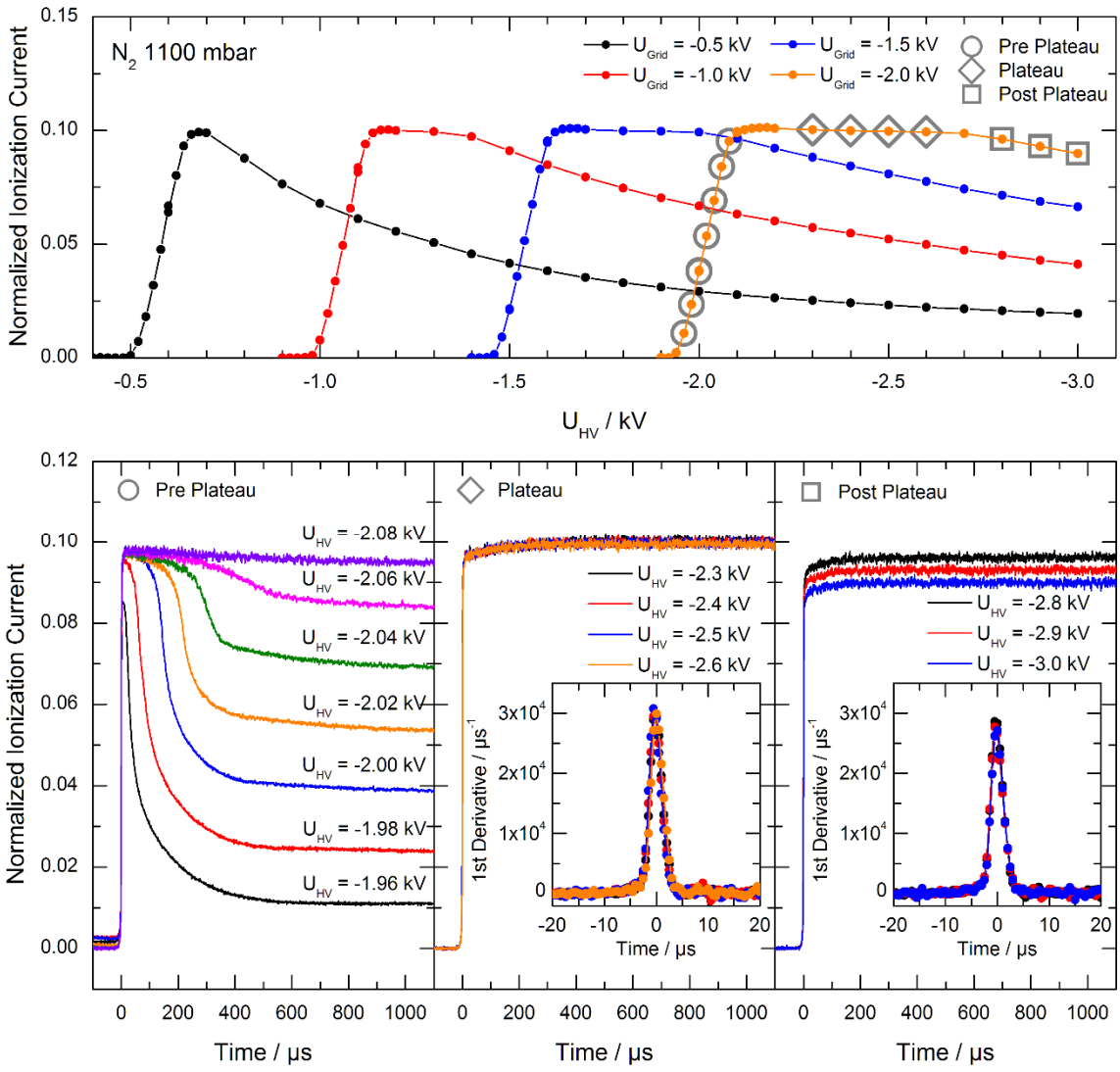

Figure 5.16: Top: U_{HV} scan of the gridded ionization chamber at various grid voltages. Bottom: Shown are the step responses at a fixed grid voltage of U_{Grid} = -2 kV and different values of U_{HV}. The measurements are grouped according to the three regions apparent in the voltage scan (top) and indicated by the symbols ○, ◇ and □. The insets of the middle and right bottom plot display the first derivatives of the corresponding step response.

Within each of these groups the step response functions are very similar to each other, owing to the governing effects.

For QEXAFS measurements the plateau region is the most important one. The corresponding step response is almost ideal. It is independent of the actual voltage U_{HV} and does not exhibit the distinct kink, which was observable with the planar parallel plate ionization chamber. This is a clear indication that no ions actually contribute to the output signal. As a consequence the total response time is significantly shorter and the rise time amounts to 3.5 µs ± 0.5µs. This is hardly broader than the combined response times of the current amplifier (~1.8 µs) and of the X-ray chopper (~2.3 µs). The inset of this plot shows the first derivative of the step response. The shape is close to a Gaussian, which makes it a near perfect real-world convolution kernel.

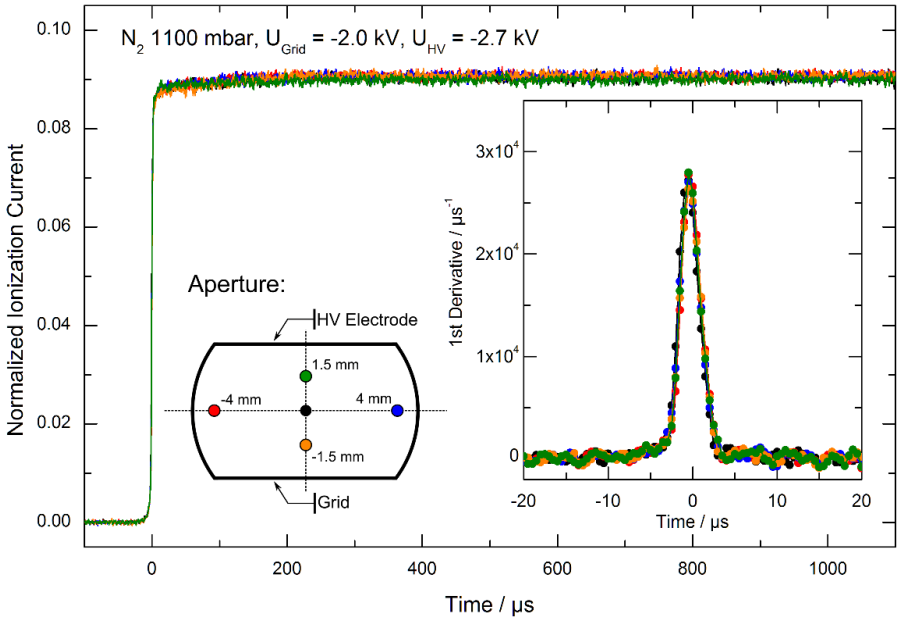

Figure 5.17: Verification of the spatial dependency of the step response of the gridded ionization chamber. The drawing shows the aperture of the ionization chamber and the color coded beam positions chosen within.

The adjacent post plateau region shows a similar step response. The rise time is as short as it is within the plateau region, however the amplitude of the function is reduced due to the diminished electron transparency of the grid. Although this causes a deteriorated efficiency of gridded ionization chamber, this region is still suitable for fast QEXAFS measurements. And again, the convolution kernel given by the first derivative is still close to a Gaussian.

Due to the lack of linearity caused by the high rate of recombination, the gridded ionization chamber is not suited to be operated within the pre plateau region. The step response under these conditions is very different from the behavior at the other regions. Interestingly, a fast rise at the beginning is still observable at any voltage. However, this immediate rise is followed by a decay of variable speed and after a few hundred microseconds the output current becomes static at a lower level. This observation can be explained by the accumulating of a positive space charge which decreases the present electric field and favors recombination when it has reached a certain magnitude.

Spatial Dependency of the Step Response

The step response was also investigated with respect to the beam position. The gridded ionization chamber was operated within its plateau region with U_{HV} = -2.7 kV and U_{Grid} = -2.0 kV. The step response was acquired at five different positions within the aperture of the ionization chamber. Figure 5.17 shows the corresponding measurements and a schematic drawing of the tested beam positions. The enclosed plot of this figure displays the first derivatives and proves that there is no noticeable dependency. The step response is the same at all positions and the derivatives are sharp Gaussians as it is expected within the plateau region.

6 QEXAFS Applications and Measurements

The QEXAFS system discussed throughout the last three chapters has been installed at the SuperXAS beamline at the SLS [**4**]. The beamline layout and infrastructure available there (see. Figure 2.6) facilitate QEXAFS measurements with optimal conditions. Since January 2015, when the system was installed, it is available for external user groups and has been in operation since then.

This chapter is dedicated to measurements performed with the presented QEXAFS system at the SuperXAS beamline to demonstrate its performance. In section 6.1 measurements of static samples are discussed. Metallic foils and powder samples of various materials have been measured to verify stability and reproducibility of the system as well as to identify its capabilities. An example of a dynamic sample system is given in section 6.2. The nucleation and growth of nano crystals is investigated and the observed kinetics are analyzed by means of LCA (see section 4.3.3).

6.1 Quick XANES and Quick EXAFS measurements of static samples

Static samples have been measured extensively at various oscillation frequencies and amplitudes in order to investigate the performance of the entire QEXAFS system. It is clear that with static samples each acquired absorption spectrum should match each other, independent on the scan rate or scan direction. Deviations, however, would indicate an insufficient bandwidth of the detectors, mechanical instabilities of the monochromator or inaccurate angular measurements. The measurements are therefore in particularly examined with respect to their reproducibility.

The shown absorption spectra are processed either entirely with JAQ (see sections 4.2 and 4.3) or with supplementary use of Athena [**71**]. Digital filter and interpolation techniques have been used along the energy direction only. No averaging nor filtering have been performed over consecutive spectra. Thus, the shown data reflect the achievable quality within the stated acquisition time of $(2f_{Osc})^{-1}$.

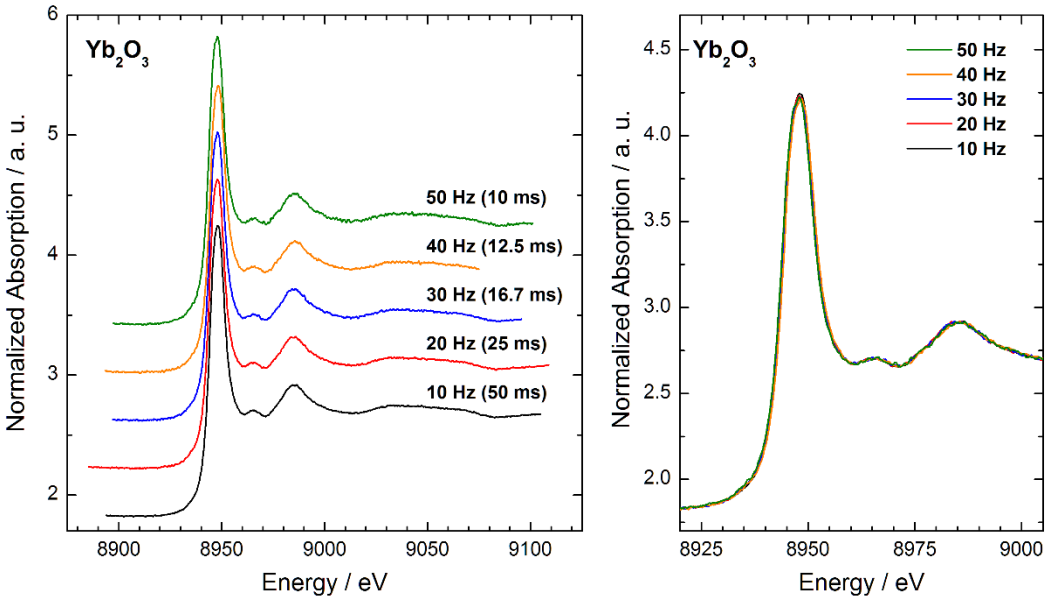

Figure 6.1: Single *down* XANES spectra as measured at the Yb L_{III}-edge of a Yb_2O_3 powder sample at various oscillation frequencies ranging from 10 Hz to 50 Hz.

6.1.1 Yb L_{III}-edge

The Yb L_{III}-edge at 8944 eV of Yb_2O_3 shows a strong whiteline. Due its sharpness this feature is well suited to benchmark the capabilities of the QEXAFS setup in terms of stability, time resolution and reproducibility.

The XANES of a powder sample was measured with acquisition rates ranging from 20 spectra per second to 100 spectra per second, which corresponds to oscillation frequencies between 10 Hz and 50 Hz. Acquired *down* spectra are shown in Figure 6.1. The right plot gives a closer look of the whiteline of the same spectra. Without the vertical shift the excellent match among one another at all oscillation frequencies becomes apparent.

The whiteline of consecutive spectra are compared in the plots of Figure 6.2. The acquired spectra are indistinguishable for oscillation frequencies of up to 30 Hz. Minor deviations appear to be noticeable at 40 Hz but are still insignificant for data evaluation. The 50 Hz measurements show an evident deviation, seemingly in form of a slight energy shift. This shift-like deviation amounts to approximately 0.3 eV at the edge positon. Although, the observable deviation is not constant throughout the spectrum it is the same for each pair of consecutive spectra. Since the shift depends locally on the rate of change of the measured intensities it most probably originates from an insufficient bandwidth of the detector system. However, since within an absorption spectrum the absorption edge or the whiteline exhibit the greatest rate of change, the strongest shifts only occur around these regions. The remaining parts of the spectra are therefore less disturbed, which essentially leads to unaffected measurements in the EXAFS region.

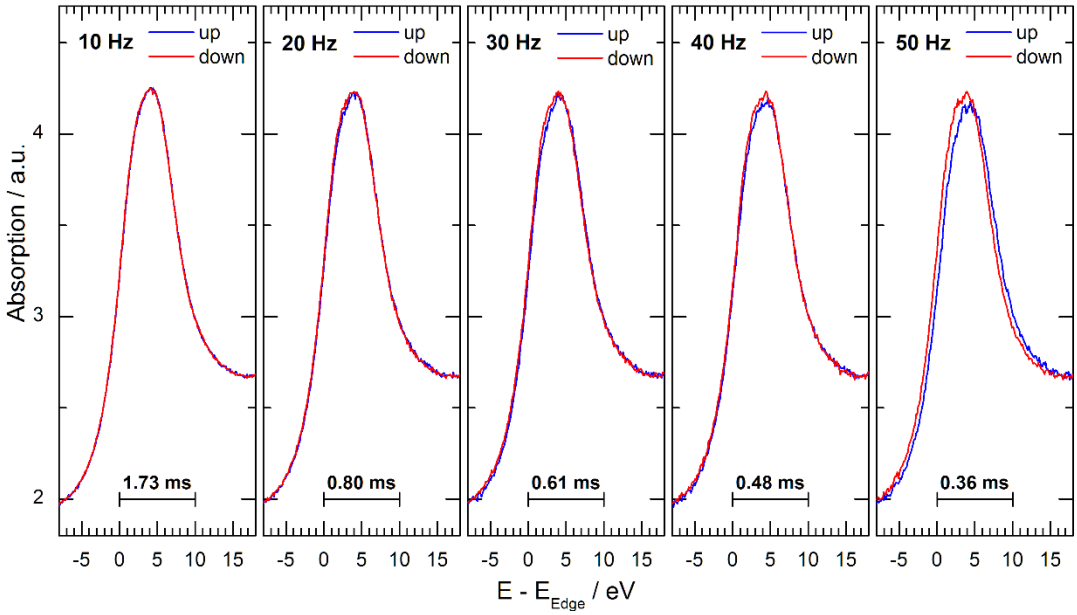

Figure 6.2: Close-up views of consecutive *up* and *down* spectra of Yb_2O_3 measured at the Yb L_{III}-edge with different oscillation frequencies between 10 Hz and 50 Hz. The uncropped spectra are shown in **Figure 6.1**.

6.1.2 Cu K-edge

The copper K-edge at 8979 eV exhibits a sharp distinct edge feature in form of a small edge peak. Due to its distinct shape a measurement is very sensitive to mechanical instabilities of the monochromator, its energy resolution and the bandwidth limitations of the detector system. It is therefore quite challenging to reproduce the near edge structure undisturbed at very high scan rates.

Quick-XANES and Quick-EXAFS spectra of copper have also been acquired at other QEXAFS beamlines to benchmark their capabilities [**3**,**20**]. These measurements, however, did not reach the herein presented time resolution or data quality.

Cu K-edge XANES

Absorption spectra of a copper metallic foil have been acquired with different acquisition rates ranging from 20 spectra per second to 100 spectra per second. Figure 6.3 shows single *down* spectra of the copper K-edge XANES. Again, the right plot gives a closer look of the edge region of the spectra. Without the vertical offset in the right plot it is visible, that all measured *down* spectra are in fact identical, which proves the excellent accuracy and reproducibility of the QEXAFS setup.

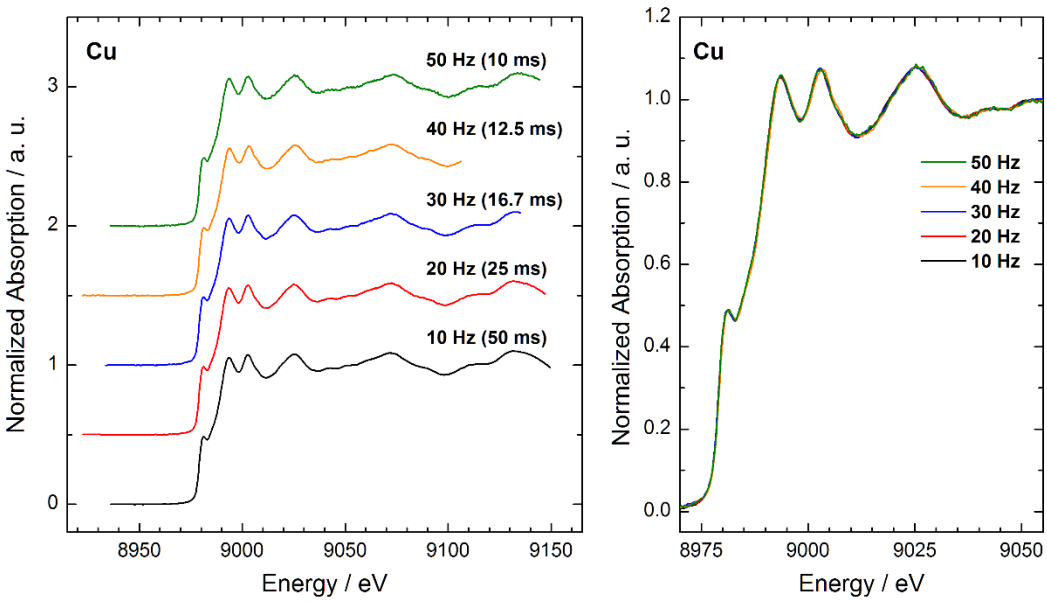

Figure 6.3: Single *down* XANES spectra of the Cu K-edge at various oscillation frequencies ranging from 10 Hz to 50 Hz.

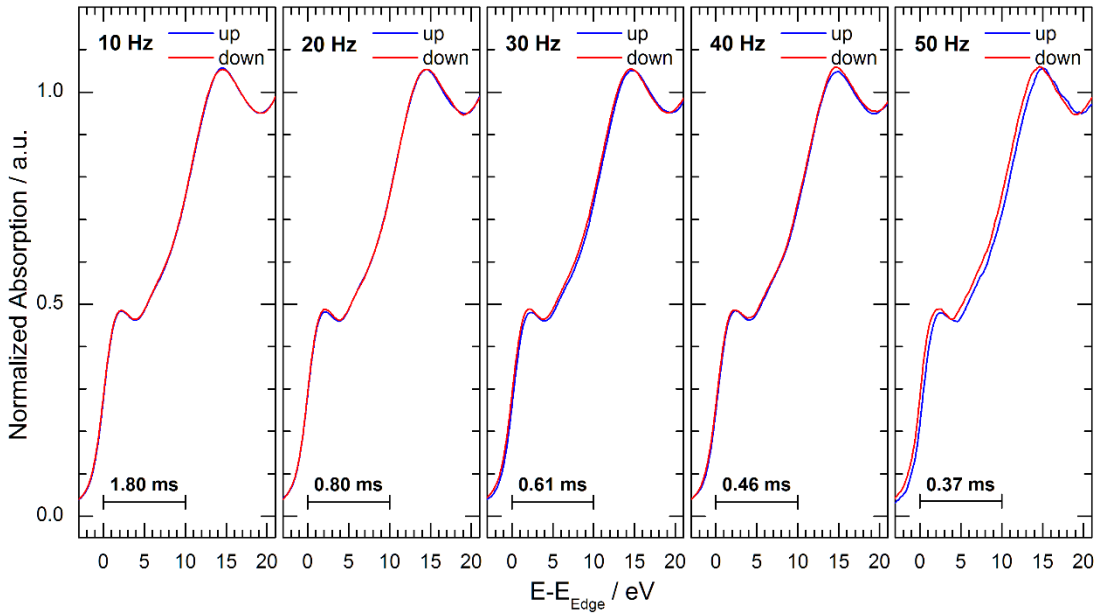

Figure 6.4: Consecutive *up* and *down* spectra of a Cu metal foil at the Cu K-edge measured at different oscillation frequencies. The uncropped spectra are shown in Figure 6.3.

Consecutive *up* and *down* spectra are compared in Figure 6.4. Consecutive spectra are plotted on top of each other to emphasize any possible deviations. Up to and including oscillation frequencies of 40 Hz no differences between the scan directions are noticeable and the acquired spectra are indistinguishable. At 50 Hz a small deviation appears. Similar to the previous observations at the Yb L_{III}-edge (see Figure 6.2) this shift-like deviation amounts to approximately 0.3 eV at the edge positon. Again, this shift is not constant throughout the spectrum but depends on the local rate of change of the spectrum. It is found that the observed deviation is in fact the same for every pair of consecutive spectra. Hence, spectra of both scan directions, i.e. *up* and *down*, can be reasonably used for proper data

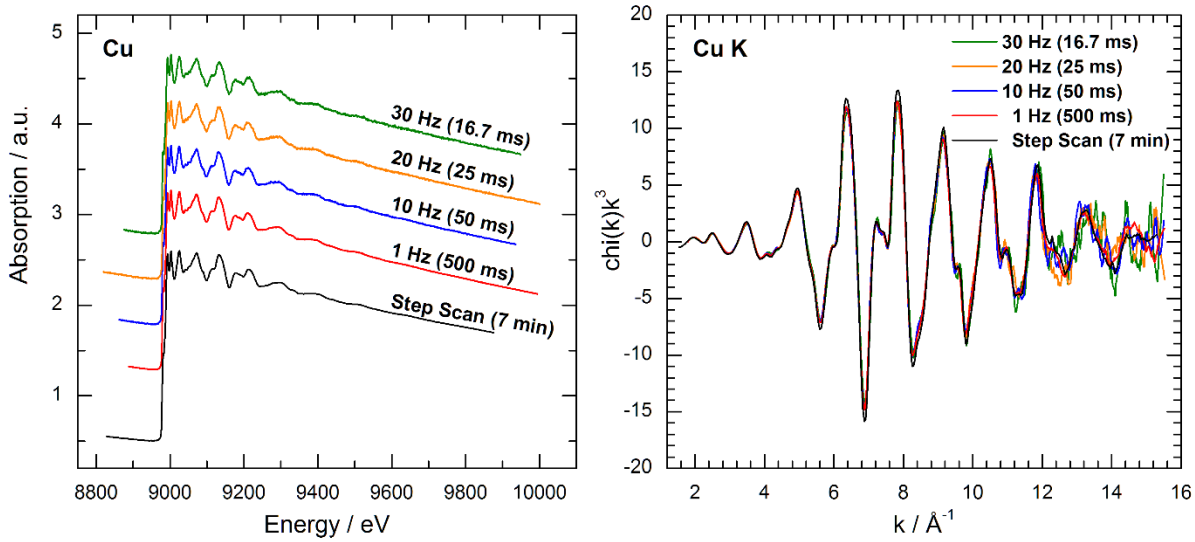

Figure 6.5: Single absorption spectra (left) and fine structure (right) of a copper metallic foil measured at the Cu K-edge with various oscillation frequencies.

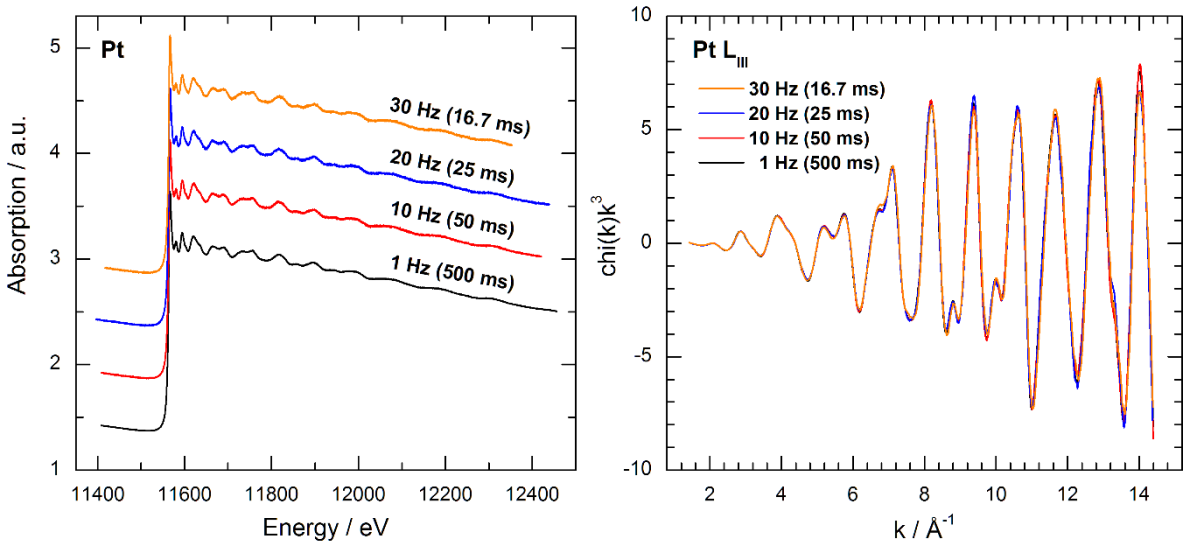

Figure 6.6: Single absorption spectra (left) and fine structure (right) of a platinum metallic foil measured at the Pt L_{III}-edge with various acquisition rates.

evaluation. This implies that a true temporal resolution of $1/2f_{Osc}$ at oscillation frequencies up to 50 Hz can be reached for XANES measurements.

Cu K-edge EXAFS

The K-edge EXAFS of a copper metallic foil has been measured as well at different oscillation frequencies. The acquisition rate has been varied between 2 spectra per second and 60 spectra per second. In addition a conventional step scan covering the same energy range within seven minutes was performed too. The absorption spectra and the extracted k^3-weighted fine structure are shown in the plots of Figure 6.5. The measurements demonstrate that, although the noise increases with higher acquisition frequencies, meaningful EXAFS up to 14 $Å^{-1}$ can be obtained at 30 Hz oscillation frequency.

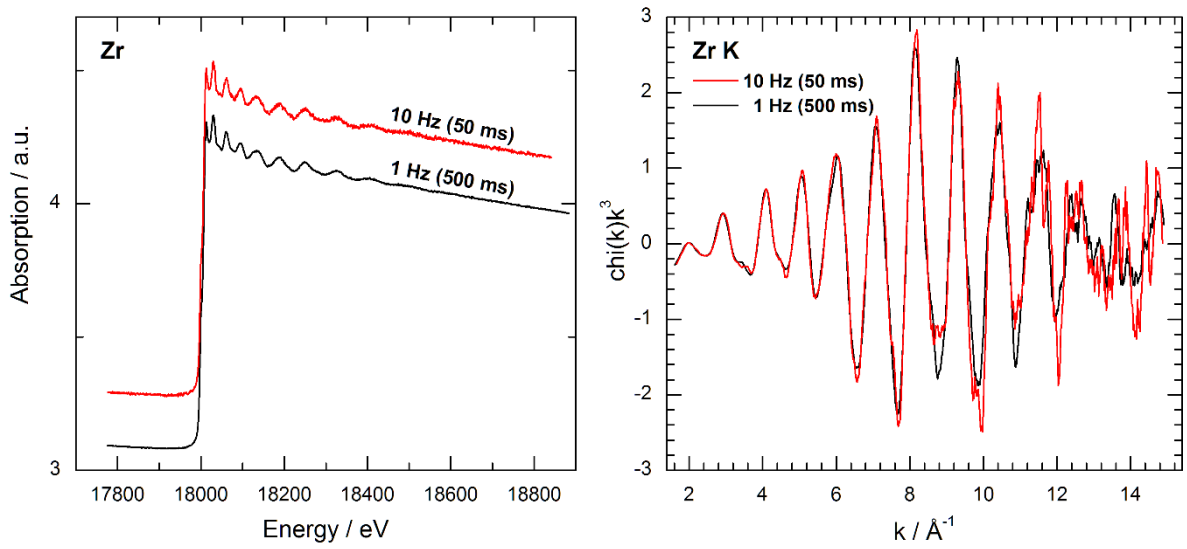

Figure 6.7: Single absorption spectra (left) and fine structure (right) of a zirconium metallic foil measured at the Zr K-edge. The spectra have been acquired with 1 Hz and 10 Hz oscillation frequency using the Si(311) channel cut crystal.

6.1.3 Pt L_{III}-edge

The EXAFS of a metallic platinum foil at the L_{III}-edge at 11564 eV was measured with oscillation frequencies between 1 Hz and 30 Hz. Platinum was chosen due to its importance in catalysis and to enable comparison with published measurements performed at other QEXAFS beamlines [**134**] [**3**,**19**,**134**,**135**]. The QEXAFS measurements are shown in Figure 6.6. The extracted fine structures of these measurements are shown in the right plot of this figure on top of each other. It clearly shows that deviations are only minor and the achieved data quality is excellent for all acquisition rates over the entire acquisition range of up to 14.4 $Å^{-1}$.

6.1.4 Zr K-edge

The zirconium K-edge at 17.998 keV is accessible with the Si(311) crystal of the monochromator. Besides the lower photon flux at these X-ray energies, the narrow Darwin width of the (311) cut further reduces the available flux on the sample. Compared to the previous measurements of the Pt L_{III}-edge, which is located near the critical energy of the source, the usable flux is diminished by a factor of around 20. This requires increased gains of the current-to-voltage amplifiers, which in turn inevitable decreases their bandwidth. As a consequence the highest acquisition rates may not be suitable to obtain absorption spectra of high quality. The EXAFS measurements of the Zr K-edge shown in Figure 6.7 were performed with an amplifier gain of 10^7 V/A at 1 Hz and 10 Hz oscillation frequency. The right plot displays the extracted and k^3-weighted fine structure. Both spectra match well up to 8 $Å^{-1}$ before an increasing noise level becomes prominent.

6.2 QEXAFS Measurements of Dynamic Samples

The Chapters 3 to 5 discussed all requirements to facilitate fast QEXAFS measurements on the sub second time regime. The previous section 6 showed that the system is in fact capable of achieving acquisition rates of up to 100 spectra per second. The accessible time resolution of real-world dynamic systems however is dependent on further parameters. In particular the sample cell and the trigger mechanism, which is applied to force the sample to transform, affect the observable dynamics as well.

The measurable response of a system is limited due to the time convolution of the actual systems response with the duration of the trigger. Therefore, to observe fast kinetics the system needs to be excited on a time scale which is shorter than the desired time resolution. Although, there are various types of triggers, a specific type is usually predetermined by the experiment and an optimization with respect to its duration and efficiency is often challenging. In many practical scenarios heat transport or fluid dynamics govern the duration of the trigger mechanism. Furthermore the trigger should excite the entire probed volume uniformly. This may be difficult to realize, in particular if gases or liquids are involved. Often these systems are therefore limited by diffusion processes. Minimizing the volume of the sample cell and the sample itself improves the situation. An interesting and promising approach, which follows this trend, is the utilization of microreactors [**136**,**137**,**138**,**139**].

The following example shows a liquid reaction which is triggered by combining two liquid reactants. To meet the requirements of a fast trigger, a specialized injection system was developed by Just [**140**].

6.2.1 Real Time observation of Cu_2ZnSnS_4 nanocrystal formation at the Cu and Zn K-edges

CZTS (Cu_2ZnSnS_4) is a p-type semiconductor material and a potential candidate for photon absorber layers in thin-film solar cells [**141**].[iv] This material can be synthesized in nano-crystalline form by hot-injection one-pot synthesis [**142**]. Uniform functional thin films can then be obtained by various deposition and recrystallization methods [**143**,**144**]. Since this approach is scalable and cost-efficient, it is a promising alternative in contrast to other more expensive vacuum based deposition processes. Of particular interest during formation of the CZTS nanocrystals are the incorporation kinetics of the different atomic species, which have been found to be integrated subsequently [**145**]. Therefore crystallization and growth have been investigated in real time by means of the QEXAFS technique. This material and its synthesis was studied in-depth by Justus Just. His findings are well covered in his doctoral thesis [**140**]. Here the analysis of a particular interesting reaction based on linear combination fitting with JAQ is presented.

[iv] More details on the in-situ reactor and CZTS material in thin film solar cells are covered in the doctoral thesis by Justus Just [**127**].

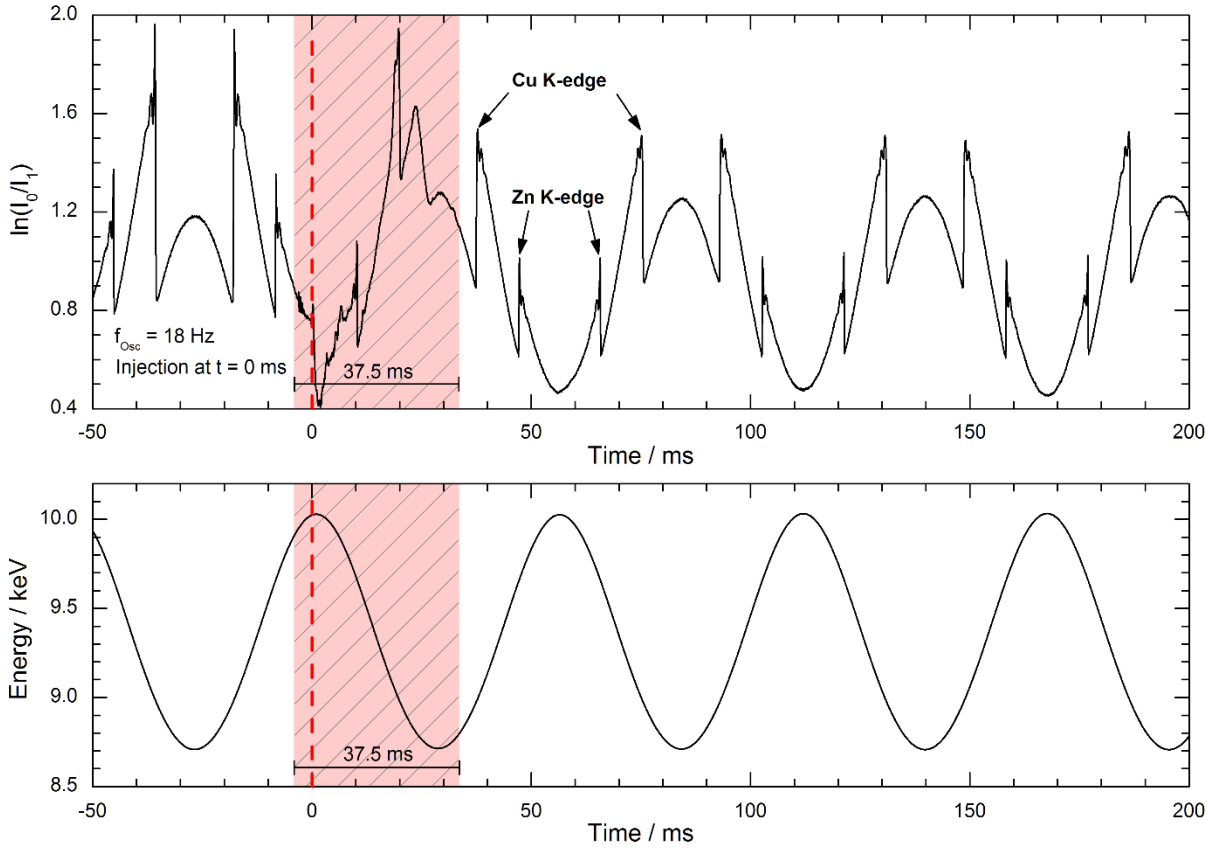

Figure 6.8: Raw time dependent QEXAFS signals of the investigated chemical reaction around the point of injection at t = 0 ms. The signals I_0 and I_1 refer to the measurements of the first and second ionization chamber. The shown signal is therefore proportional to the absorption of the sample. The light red shaded area indicates the dead time caused by the injection and the subsequent turbulences.

Experimental Description and Observations

The nanocrystal formation from solved metal salts of copper, zinc and tin was investigated using a specialized in-situ liquid chemical reactor, which was designed by Justus Just [**140**]. The reactor facilitates QEXAFS measurements in transmission geometry and was specifically constructed to enable highly time resolved measurements of the nucleation process close to its ignition point. During the measurement the reactor is heated with a controlled temperature ramp of 10 $Kmin^{-1}$ up to 250 °C where the temperature is finally kept constant. At 155 °C the nucleation is triggered by a fast combustion driven injection of a sulfur source, which produces an instantaneous oversaturation to exceed the nucleation threshold. An immediate quick and complete mixing of the reactants within a few milliseconds is forced by the impact of the injection. X-ray absorption spectra have been acquired at the Cu and Zn K-edges quasi simultaneously with an monochromator oscillation frequency of 18 Hz.

A close view of the acquired QEXAFS signal around the injection point is given in Figure 6.8. The ignition spark of the explosion produces a strong electronic pulse (< 1 µs) which is unintentionally picked up by the detection system at t = -4.6 ms. At t = 0 ms the reactant is injected into the reactor causing the X-ray absorption to drop abruptly. This point in time can be defined with an uncertainty of ±2 ms and is referenced as the origin of the measurement. Shortly after the injection, strong turbulences

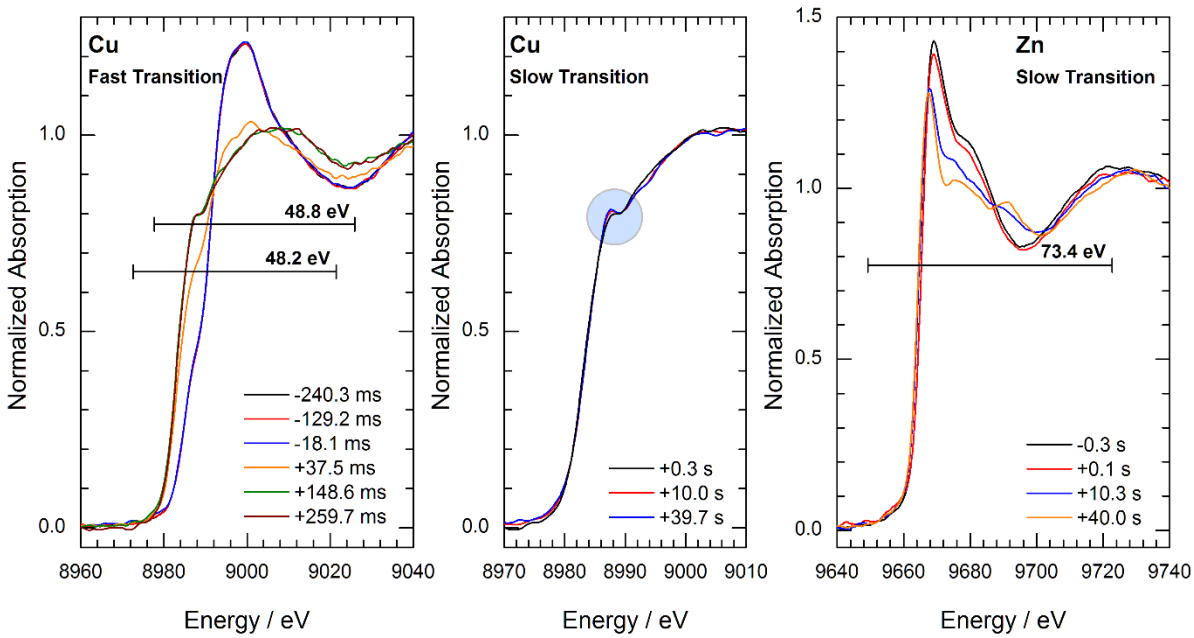

Figure 6.9: The plots show normalized Cu and Zn K-edge XANES spectra extracted at different times during the reaction. The slow transition at the Cu K-edge, shown in the center plot, is not well pronounced. The blue circle highlights one of the most distinctive changes of this transition. The horizontal bars in the outer plots indicate the energy range used in the LCA.

within the liquid are visible and render the data mostly impractical to be evaluated. The total dead time amounts to about 38 ms. From then on the measurement remains mostly undisturbed.

In Figure 6.9 single K-edge XANES spectra of Cu and Zn extracted at different times, before and after the injection, are shown. All spectra before injection match each other, which confirms stability and reproducibility of the measurements. Immediately after injection XANES spectra of the Cu K-edge show substantial changes over a period of a few hundred milliseconds. In contrast to this very fast response, changes of the Zn K-edge XANES occur on a much larger time scale of several seconds. Thus, based on this very brief observation it already can be deduced that Cu is built into the nanocrystals before Zn is integrated. Since both edges have been measured quasi simultaneously and Zn is assumed to be embedded in Cu containing nanocrystals a further modification of the Cu XANES on the same time scale is expected as well. This transition however is not very well pronounced and therefore difficult to identify.

In the following these transitions at the Cu and Zn K-edges are evaluated by means of the LCA tool available in JAQ (see section 4.3.3). The spectral range used in the evaluation is restricted to about 50 eV to 70 eV near the absorption edge and around the most dominant changes of the XANES. This energy range is measured within less than 1.5 ms. The individual regions of the measurement are therefore assumed to be quasi static.

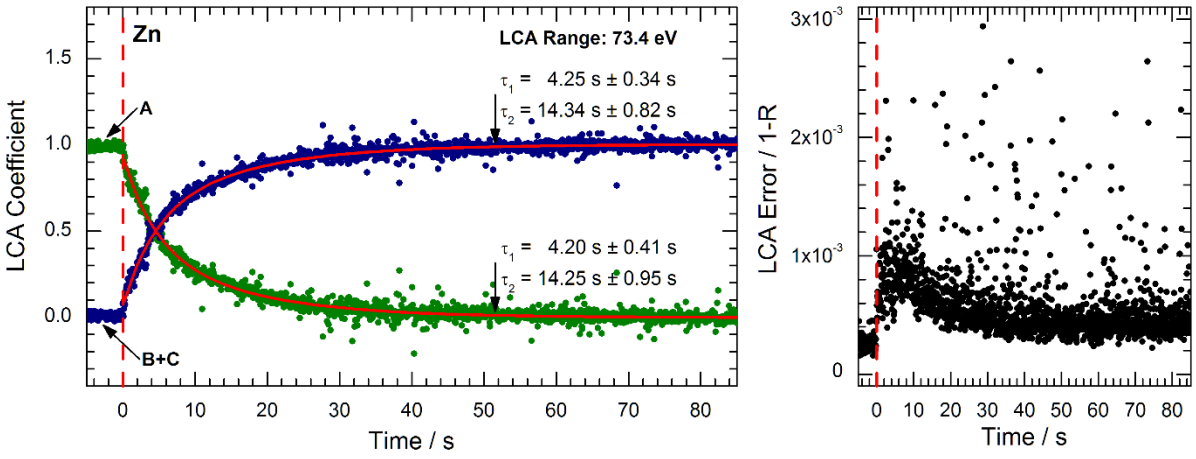

Figure 6.10: LC coefficients and LCA error of *down* spectra at the Zn K-edge. Two term exponential functions fitted to the data are given by the red curves.

Transitions at the Zinc K-Edge

The XANES at the Zn K-edge shows a comparatively slow transition over several seconds. The high acquisition rate, compared to the relevant time scale of this transitions, allows to skip every second spectrum and thus allows to restrict the data evaluation to the *down* scan direction only. This doesn't affect the underlying transient but can improve the quality of the LCA. In particular in the present case, with an oscillation frequency of 18 Hz and a spectral range of about 1.3 keV the measurements are close to the limit of the bandwidth of the detection system (see sections 4.1 and 5.2). Accordingly, small deviations between *up* and *down* spectra might be present, especially in the XANES region, and could deteriorate the significance of the LCA.

The transition is fitted with three references. A single reference taken around -7 s (A) before injection and two additional references extracted around +52 s (B) and +118 s (C) after injection are used to model the initial and final states. The LCA coefficients of the latter spectra are summed to give a measure of the final state and to compensate for the temperature drift of the heating ramp. The LCA results and the error estimate (see equation (4.17)) are shown in the plots of Figure 6.10. Expect for a few runaway points the LCA error is reasonably small and doesn't show a distinct trend, thus fortifying the chosen reference spectra. In the region after injection, a two term exponential function is fitted to the progression of the LCA coefficients. Both fits exhibit very similar time constants of averaged 4.2 s ± 0.5 s and 14.3 s ± 1.3 s. This together with the low LCA error over the fitting range, shows that there is no significant competition between the references, which validates the 3 spectra reference approach. The physical interpretation of a two term exponential transition remains however unclear. The incorporation of Zn could follow two different reaction paths which give rise to two different time constants.

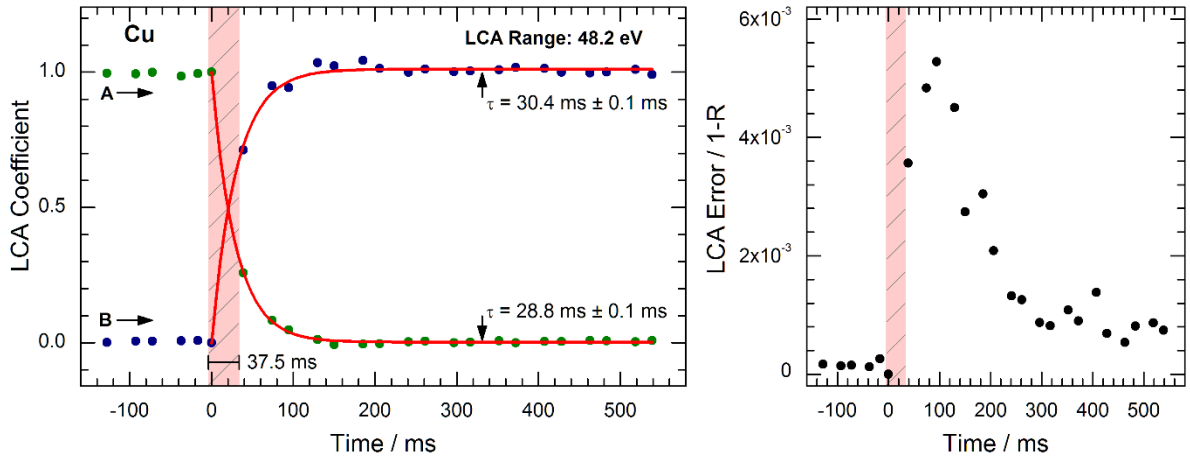

Figure 6.11: LC coefficients and error of *up* and *down* spectra at the Cu K-edge. The data points at t = 0 ms are added by manually. The red solid lines represent a fit of an exponential function. The light red shaded area indicates the dead time caused by the injection.

Transitions at the Copper K-Edge

According to the measurements shown in Figure 6.9, a very fast transition at the Cu K-edge, immediately after injection, can be clearly observed. Within only a few acquired spectra the entire transition completes. Due to the coarse spectra density within the relevant time frame both scan directions have to be evaluated. To cope with small deviations between *up* and *down* spectra, the LC fits of each spectrum is performed with a set of reference spectra of the same scan direction. Two references (A, B) are used to describe the initial and final states. These haven been extracted at -0.3 s (A) and +2.3 s (B). Results of the LCA are shown in the plots of Figure 6.11. The data points at t = 0 ms within the dead time have been added to enable proper fitting of the data. The progression of the LC coefficients can be well described by means of a single term exponential function. Corresponding fits are shown by the red solid curves. With regard to the quality of these fits a time constant of 30 ms ± 2 ms can be attributed to this transition.

Based on various complementary measurements and previous characterization of the reactor and injection system by Just, a slow mixing or failed injection can be ruled out with great certainty. The determined time constant is thus, in fact given by the dynamics of the nucleation of Cu based nano crystals [**140**]. Furthermore, this measurement is presumably the fastest reaction which has ever been observed with the QEXAFS technique.

Besides this fast transition, the observation at the Zn K-edge suggests a second transition at the Cu K-edge. This is based on the assumption that the Zn atoms are incorporated into nano crystals which already contain Cu to eventually form CTZS. Within the timeframe of about 100 s after injection, the K-edge XANES of Cu shows only minor deviations from each other (see Figure 6.9). Merely a small change around the first local maximum is noticeable by eye. To increase the sensitivity of the LCA, only *down* spectra are considered and beforehand digitally filtered in the time domain (see section 4.3.1). The used filter window width covers 20 spectra or approximately 1.1 s. This dampens deviations which occur

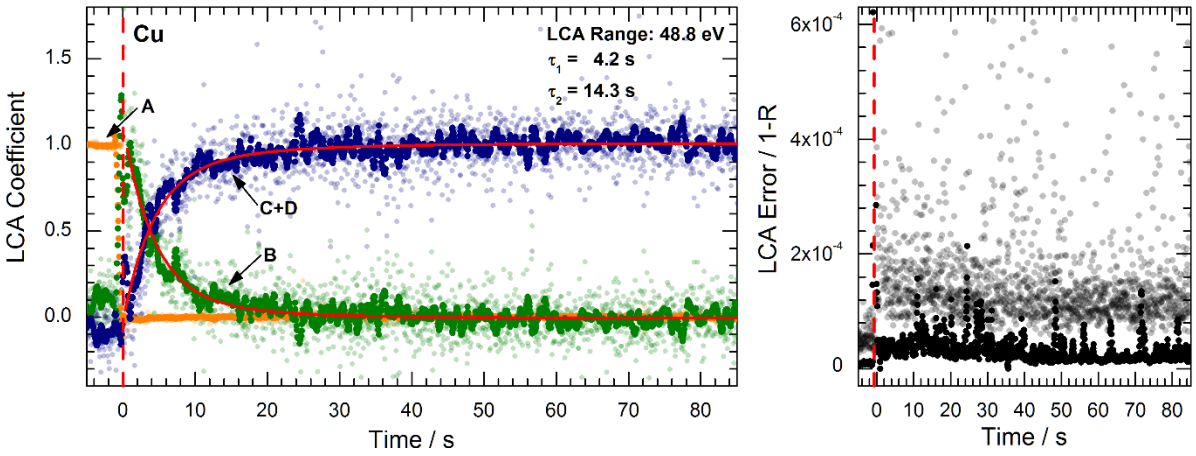

Figure 6.12: LC coefficients and error of raw (light points) and digital filtered (solid points) *down* spectra at the Cu K-edge. The red curves represent fits of two term exponential functions with fixed time constants τ_1 and τ_2 taken from the Zinc transition (see **Figure 6.10**).

on shorter time scales such as noise contributions. In Figure 6.12 LC fits of raw (light points) and filtered (solid points) spectra are shown. The spread of the LC coefficients and the LCA error are clearly reduced by means of the applied filter. Here, the LCA is based on four reference spectra (A-D). The initial state before injection is described by a spectrum extracted at -7.2 s (A). The final state of the fast transition is captured by a reference spectra extracted at +1.0 s (B). The final state of the slow transition is provided by two references, which have been extracted at +35.7 s (C) and +117.6 s (D). These are again summed to give a single measure of the final state.

Although deviations of the XANES spectra are hardly noticeable by eye, the LCA clearly reveals a transition of the expected shape and a two term exponential function can describe this transition satisfyingly. A fit with fixed time constants set to the LCA results of the Zn K-edge are shown by the red solid curves in the left plot of Figure 6.12.

Discussion

The nucleation and growth of nano-crystalline CTZS has been investigated by means of simultaneous measurement of Cu and Zn K-edges with 28 ms time resolution. A very fast transition of Cu could be observed immediately after hot injection of the reactant. Although the reaction speed is quite close to the time resolution of the measurement, the governing time constant could be determined with a good certainty to 30 ms ± 2 ms. This coincides with the typical progression expected by instantaneous crystallization from a hot-injection [**140**]. Within a time frame of a few 100 ms the entire amount of Cu has nucleated and transformed into the solid state. Since the Zn K-edge did not change substantially within this timeframe, it still has to be in its precursor form and the Cu atoms most likely built Copper-Sulfur or Cupper-Tin-Sulfur compounds. At the Zn K-edge a much slower transition on the second time scale was observed. By means of LCA, a correlated transition could also be found at the Cu K-edge. Thus, these transitions, which complete within about 50 s reveal the incorporation of Zn

atoms into the already existing crystals. It is yet unclear at which stage Sn comes into play. Thus, further investigations, in particular on the Sn K-edge, are required.

The observed nucleation of Cu is presumably the fastest reaction which has ever been captured with the QEXAFS technique. The fast gridded ionization chambers and current-to-voltage amplifiers are essential to reach the required time resolution, whereas the reactor and the injection system enabled a fast trigger of the investigated reaction. Without the coordinated interplay of all components the nucleation process could not have been resolved this detailed.

7 Summary and Outlook

The principles of time resolved hard X-ray absorption spectroscopy according to the QEXAFS method was comprehensively discussed. Based on the discussed important aspects of QEXAFS instrumentation an entirely new QEXAFS setup with millisecond time resolution has been developed [**16**]. The entire measurement chain was reviewed with respect to the frequency response of each component, followed by intensive studies of planar parallel plate and gridded ionization chambers. According to the developed concept two monochromators have been constructed assembled and installed at the synchrotron radiation facilities PETRA III (DESY, Germany) and SLS (PSI, Switzerland). While the P64 beamline at the PETRA III storage ring is still in the commissioning phase, the new QEXAFS monochromator at the SuperXAS beamline (SLS) is operational and available for the user community since January 2015 [**4**,**13**].

Based on a direct drive torque motor a new driving scheme and monochromator concept was developed (see Chapter 3). The novel open-loop drive proved to be ideally suited for dedicated QEXAFS monochromators. The rotor, which connects the Bragg axis of the crystals, oscillates in a magnetic potential minimum created by the stator of the drive. The implemented scheme allows remote control of the oscillation frequency and spectral range by altering and periodically perturbing the magnetic potential. Since no control feedback loop is required the achievable oscillation frequencies are only limited by the maximum torque of the drive. This allows to reach high oscillation frequencies, which in turn define the time resolution of the experiment. Oscillation frequencies of up to 50 Hz, yielding 100 spectra per second, have been realize with this setup. The crystal motion was investigated under various operating conditions and showed always a near sinusoidal trajectory, which reduces vibrations and unnecessary load within the mechanics. This property in particular contributes to stability and reproducibility of the QEXAFS measurements.

To acquire absorption spectra with the new monochromator, a new data acquisition system (DAQ) was developed (see Chapter 4). It is capable of processing and visualizing the incoming data in real time. This allows measurements to run uninterrupted for hours. All relevant analog and digital signals originating from the detectors, i.e. ionization chambers, and the angular encoder, are sampled

synchronously with an adjustable sampling rate of up to 2 MHz. Synchronicity is critical for the accuracy of the energy scale of each spectrum and was successfully established and verified.

QEXAFS often yields the best results in transmission geometry using gaseous ionization chambers. These measure the X-ray flux without interfering strongly with the properties of the beam and their intrinsic absorption can be optimized to the relevant photon energy by adjusting the pressure and the type of the filling. Regarding QEXAFS the bandwidth of ionization chambers is of particular interest. Therefore planar parallel plate and gridded ionization chambers have been built and investigated with respect to their dynamic behavior (see Chapter 5). By means of step response measurements their specific convolution kernels were determined. The influence of the electric field strength, the relative beam position and the filling gas on the step response was investigated in detail. Based on the developed theoretical model the effective ion mobility was defined and used to describe the response behavior. Distinct differences between nitrogen and argon filled planar parallel plate ionization chambers were noticed. While in the nitrogen filled ionization chamber the created ion distribution showed to be constant over the drift time, it was observed that the ion distribution in the argon filled ionization chamber is not necessarily constant and can change during the ion drift. Moreover, the investigations showed that the response time of conventional ionization chambers is always dominated by the ion drift velocity and therefore severely limited. As a consequence, the achievable bandwidth with conventional ionization chambers is insufficient for fast QEXAFS measurements. Therefore, gridded ionization chambers were developed, which suppress the ionic contribution to the output ionization current. Step response measurements have been performed in the same way and showed that the bandwidth of the gridded ionization chambers is in fact significantly increased by about two orders of magnitude. The rise time was determined to be shorter than 3.5 µs. The high bandwidth of the gridded ionization chamber allows to exploit the capabilities of the new QEXAFS monochromator and DAQ. Furthermore, the dependency of the relative beam position on the rise time, which was observed with conventional ionization chambers, is no longer existent.

With the complete QEXAFS setup installed at the SuperXAS beamline, first XANES and EXAFS measurements of static samples have been performed to investigate the capabilities and reproducibility (see Chapter 6). In particular consecutive XANES spectra acquired with various scan rates were analyzed. Only at high scan rates minor differences appear, resembling a small energy shift-like deviation. At the maximum scan rate of 100 spectra per second this energy shift amounts to approximately 0.3 eV. At scan rates of 80 spectra per second and less no deviations were noticeable. High quality EXAFS spectra up to about $k = 14$ Å^{-1} have been acquired with various scan rates up to 60 spectra per second. Differences or an increase in noise at high wave numbers were hardly noticeable.

To demonstrate the capabilities of the QEXAFS system studying dynamic samples, the formation and growth of Cu_2ZnSnS_4 of nanocrystals were investigated in-situ. This material was synthesized with an in-situ liquid chemical reactor in an one-pot hot-injection synthesis. The QEXAFS

monochromator allowed to record X-ray absorption spectra at the copper and the zinc K-edges quasi simultaneously, covering about 1250 eV in total, with a repetition rate of 36 spectra per second. Multiple transitions involving both absorption edges were observed and analyzed by means of linear combination fitting (LCF). It was shown that copper transforms very quickly at the beginning of the reaction and nucleates completely within a few 100 ms, while the zinc K-edge remained unaltered at the beginning. A transition at the zinc K-edge was observed on a much large time scale and completed within about 50 seconds. Due to the direct temporal correlation between both edges and the high sensitivity of linear combination analysis a weak transition with the same characteristic progression could also be identified at the copper K-edge. It was deduced that zinc atoms are incorporated in the already existing copper based nanocrystals.

This reaction was evaluated solely with the software program JAQ, which was specifically developed to enable QEXAFS data evaluation. The implemented algorithms and the generic workflow were outlined in the text. JAQ enables access to each spectrum contained in the QEXAFS data set and provides tools to edit, process and analyze them. Besides conventional tools, such as LCA, JAQ also offers unique features such as Time Correction Interpolation and digital energy and time filters. These functions specifically exploit the inherent temporal correlation between individual spectra, which is not as easily feasible as with comparable software programs. The distribution and access of capable software programs, like JAQ, is important for the growing user community and needs to be addressed. By adding more analytical methods the significance can be further increased.

The example of the nanocrystal growth experiment showed the importance of specialized sample cells and trigger mechanisms to investigate very fast chemical reactions. The observed transition at the copper K-edge progressed with a characteristic time constant of about 30 ms and is presumably the fastest reaction which has ever been captured with the QEXAFS technique. From a metrological point of view especially the gridded ionization chambers and the fast current amplifiers enabled the acquisition. The observation was made possible due to the almost instant mixing of the chemicals on a low millisecond time scale. Specialized in-situ sample cells with a minimized dead volume and novel trigger mechanism are required to make full use of high speed QEXAFS setups.

Apart from currently available sub-second QEXAFS beamlines at synchrotron radiation facilities, including NSLS II (USA), SPring-8 (Japan), SOLEIL (France) and SLS (Switzerland) new dedicated beamlines are presently planned and built worldwide. The next QEXAFS beamlines expected to become operational are located at PETRA III (Germany), NSLS II (USA), TPS (TAIWAN), PLS II (South Korea), LNLS (Brazil), SSRL (USA) and MAX IV (Sweden). The discussed QEXAFS setup provides a solid foundation for dedicated hard X-ray spectroscopic beamlines and two of the four current and future QEXAFS Beamlines in Europe have been built accordingly during this work. The accessible photon energy with the presented monochromator ranges from about 4 keV to 40 keV allowing access to K- or L-edges of almost all relevant elements. The acquisition rate and the spectral range of X-ray

absorption measurements can be remotely adjusted, making it ideal for dedicated user experiments. Moreover, the mechanical complexity of the monochromator was reduced to increase durability and lessen maintenance and downtime. The developed unique drive concept allows millisecond QEXAFS measurements as well as conventional step scans. For the first time, this allows all applications in scope of hard X-ray spectroscopic beamlines to be covered with a single monochromator. Another crucial development is given with gridded ionization chambers, which feature extremely short response times and enable acquisition of high quality absorption spectra on shortest time scales. It was shown that with gridded ionization chambers *up* and *down* spectra of static samples are truly indistinguishable at high acquisition rates up to 80 spectra per second. This solves a problem which inevitably persists with conventional parallel plate ionization chambers and requires to treat the different scan directions separately or to even discard one scan direction completely. With the gridded ionization chambers and the fast data acquisition system both scan directions can now be evaluated without constrains.

Appendix A – Estimation of the Maximum Scan Rate in QEXAFS Measurements

In the following the inequality (4.2), which estimates the maximum energy scan rate in QEXAFS measurements, assuming a sinusoidal crystal deflection, is derived. In combination with the energy resolution of the monochromator, the result can be used to define the required sampling frequency of QEXAFS measurements.

The relevant energy scan rate is given by the absolute value of the first derivative of the energy-time function, $E(t)$, of the scan. Starting with Braggs equation,

$$E(t) = \frac{hc}{2d}\frac{1}{sin\left(\theta_B(t)\right)} \tag{A.1}$$

and assuming a sinusoidal crystal oscillation,

$$\theta_B(t) = \varepsilon \sin(2\pi f_{Osc} t) + \theta_0 \tag{A.2}$$

the first derivative yields equation (A.3).

$$\frac{d}{dt}E = -\frac{hc}{2d} 2\pi\varepsilon f_{Osc} \cos(2\pi f_{Osc} t) \frac{cos\left(\theta_B(t)\right)}{sin\left(\theta_B(t)\right)^2} \tag{A.3}$$

The Bragg angle θ_B, is always positive and never exceeds 90°, thus the fraction containing the trigonometric functions in equation (A.3) can be estimated upwards by inequality (A.4).

$$\frac{cos\left(\theta_B(t)\right)}{sin\left(\theta_B(t)\right)^2} = \frac{cos(\varepsilon \sin(2\pi f_{Osc} t) + \theta_0)}{sin(\varepsilon \sin(2\pi f_{Osc} t) + \theta_0)^2} < \frac{cos(\theta_0 - \varepsilon)}{sin(\theta_0 - \varepsilon)^2} \tag{A.4}$$

The cosine function, $\cos(2\pi f_{Osc} t)$, obviously oscillates between ± 1. Since in any case the absolute value of dE/dt is of interest and the right side term of inequality (A.4) is always positive for possible values of θ_0 and ε, the cosine function can be estimated in any direction. This finally leads to inequality (A.5.), which is used in equation (4.2).

$$\left|\frac{dE}{dt}\right|_{max} < \frac{hc}{2d} 2\pi\varepsilon f_{Osc} \frac{cos(\theta_0 - \varepsilon)}{sin(\theta_0 - \varepsilon)^2} \tag{A.5}$$

Appendix B – JAQ File Formats

The data acquisition software, which runs the DAQ (see Chapter 4) creates two files: [*Filename*].bin and [*Filename*]_Encoder.bin. These contain the QEXAFS raw signals and can be processed by JAQ (see Chapter 4). JAQ itself generates additional files which allow to retrieve the contained spectra: [*Filename*]_SplitPositions, [*Filename*]_Calibrations.bin and [Filename].qexafs. The latter contains precalculated absorption spectra and does not require access to the other files. In the following the structure of all relevant files are given.

[*Filename*].bin

		Type	Length	Offset	Description
Header		Int32	4 Bytes	0	Length of Header in Bytes
		Int32	4 Bytes	4	Version of DAQ Software
		Int64	8 Bytes	8	Date and Time of Acquisition
		Single	4 Bytes	16	Number of Analog Channels
		Single	4 Bytes	20	Sampling Frequency in Hz
Analog Data	1	Single	4 Bytes		1st Sample Analog Channel 0
		Single	4 Bytes		1st Sample Analog Channel 1
					…
	2	Single	4 Bytes		2nd Sample Analog Channel 0
		Single	4 Bytes		2nd Sample Analog Channel 1
					…
	3	Single	4 Bytes		3rd Sample Analog Channel 0
		Single	4 Bytes		3rd Sample Analog Channel 1
					…
	…				…

Table B.1: Data structure of the [*Filename*].bin file. This file is written during acquistion by the DAQ's software.

[*Filename*]_Encoder.bin

		Type	Length	Offset	Description
Header		Int32	4 Bytes	0	Length of Header in Bytes
		Int32	4 Bytes	4	Version of DAQ Software
		Int64	8 Bytes	8	Date and Time of Acquisition
		Single	4 Bytes	16	Number of Encoder Channels
		Single	4 Bytes	20	Sampling Frequency in Hz
Encoder Data	1	Single	4 Bytes		1st Sample Angular Encoder 0
					…
	2	Single	4 Bytes		2nd Sample Analog Channel 0
					…
	3	Single	4 Bytes		3rd Sample Analog Channel 0
					…
	…				…

Table B.2: Data stucture of the [*Filename*]_Encoder file. This file is written during acquisition by the DAQ's software.

[*Filename*]_SplitPositions.bin

		Type	Length	Offset	Description
Header		Int32	4 Bytes	0	Length of Header in Bytes
		Int32	4 Bytes	4	Version of DAQ Software
		Int64	8 Bytes	8	Date and Time of Acquisition
		Int64	8 Bytes	16	Reserved
		Double	8 Bytes	24	Encoder Min
		Double	8 Bytes	32	Encoder Max
		Int32	4 Bytes	40	Cropped Lentgh
		Double	8 Bytes	44	Oscillation Frequency of Monochromator in Hz
		Double	8 Bytes	52	Truncation
		Double	8 Bytes	60	TimeOffset
		Int32	4 Bytes	68	Reserved
SplitPositions	1	Int64	8 Bytes		1st SplitPosition
	2	Int64	8 Bytes		2nd SplitPosition
	3	Int64	8 Bytes		3rd SplitPosition
	…				…

Table B.3: Data structure of the [*Filename*]_SplitPositions file. This file is created by JAQ.

[*Filename*]_Calibration.bin

Type	Length	Offset	Description
Int32	4 Bytes	0	Length of Header in Bytes
Int32	4 Bytes	4	Version of DAQ Software
Int64	8 Bytes	8	Date and Time of Acquisition
Double	8 Bytes	16	Edge Energy in eV
Double	8 Bytes	24	Encoder Value at Edge
Double	8 Bytes	32	Encoder Constant
Double	8 Bytes	40	Crystal Lattice Spacing
Int64	8 Bytes	48	Shift

Table B.4: Data structure of the [*Filename*]_Calibration file. This file is created by JAQ.

[*Filename*].qexafs

	Type	Length	Offset	Description
Header	Int32	4 Bytes	0	Length of Header in Bytes
	Int32	4 Bytes	4	Version of JAQ
	Int64	8 Bytes	8	Date and Time of Acquisition
	Int64	8 Bytes	16	n, Number of Spectra
	Int32	4 Bytes	24	m, Number of Points per Spectrum
	Single	4 Bytes	28	Number of Files
	Double	8 Bytes	32	Edge Energy
	Single	4 Bytes	40	Sampling Frequency in Hz
	Double	8 Bytes	48	Oscillation Frequency of Monochromator in Hz
		16 Bytes	54	Reserved
Energy m Entries	Single	4 Bytes		1^{st} Energy in eV
	Single	4 Bytes		2^{nd} Energy in eV
				…
	Single	4 Bytes		m^{th} Energy in eV
Time n Entries	Single	4 Bytes		1^{st} Time in ms
	Single	4 Bytes		2^{nd} Time in ms
				…
	Single	4 Bytes		n^{th} Time in ms
Spectra n x m Entries	Single	4 Bytes		$\mu(E_1, t_1)$
	Single	4 Bytes		$\mu(E_2, t_1)$
				…
	Single	4 Bytes		$\mu(E_m, t_1)$
	Single	4 Bytes		$\mu(E_1, t_2)$
	Single	4 Bytes		$\mu(E_2, t_2)$
				…
	Single	4 Bytes		$\mu(E_m, t_2)$
				…
	Single	4 Bytes		$\mu(E_1, t_n)$
	Single	4 Bytes		$\mu(E_2, t_n)$
				…
	Single	4 Bytes		$\mu(E_m, t_n)$
Spectra m x n Entries	Single	4 Bytes		$\mu(E_1, t_1)$
	Single	4 Bytes		$\mu(E_1, t_2)$
				…
	Single	4 Bytes		$\mu(E_1, t_n)$
	Single	4 Bytes		$\mu(E_2, t_1)$
	Single	4 Bytes		$\mu(E_2, t_2)$
				…
	Single	4 Bytes		$\mu(E_2, t_n)$
				…
	Single	4 Bytes		$\mu(E_m, t_1)$
	Single	4 Bytes		$\mu(E_m, t_2)$
				…
	Single	4 Bytes		$\mu(E_m, t_n)$

Table B.5: Data structure of the [*Filename*].qexafs file. This file is create by JAQ. It is in particlarly used for the digital filtering moduel in JAQ.

Appendix C – Generalized Time Base of QEXAFS measurements

Often QEXAFS measurements require a time base, which attributes a specific point in time to each spectrum. For instance, this is important if transients are to be investigated or if acquired spectra are to be correlated with other measurements, which have been performed synchronously. Implying a nearly constant oscillation frequency with only small variations, i.e. jitter, a reasonable time base can be defined by equation (C.1).

$$\langle t_c \rangle_i = \frac{2i+1}{4\langle f_{Osc} \rangle} + \langle t_0 \rangle \tag{C.1}$$

Accordingly, to compute the center time $\langle t_c \rangle_i$ of the ith spectrum only the mean frequency $\langle f_{Osc} \rangle$, which is given by equation (4.11) or (C.2), and an arbitrary time offset $\langle t_0 \rangle$ needs to be known.

$$\langle f_{Osc} \rangle = \frac{1}{2}\frac{m-1}{s_{m-1} - s_0} \tag{C.2}$$

In the following, equation (4.13), which determines $\langle t_0 \rangle$ based on the *split positions* s_i (see section 4.2.1) is derived. The s_i count from 0 to $m-1$ and refer to the time index of the reversal points of the of monochromator crystal's oscillation. Without any jitter and without any uncertainties in the determination of the *split positions*, the mean time offset $\langle t_0 \rangle$ would be equal to s_0. The *exact* center time of the ith spectrum is given by equation (C.3).

$$t_{c,i} = \frac{s_i + s_{i+1}}{2} \tag{C.3}$$

Following the idea of equation (C.1), this *exact* center time can also be defined by equation (C.4) with the mean oscillation frequency and a yet unknown time offset $t_{0,i}$.

$$t_{c,i} = \frac{2i+1}{4\langle f_{Osc} \rangle} + t_{0,i} \tag{C.4}$$

Putting equations (C.2) to (C.4) together the specific time offset of the ith spectrum can be determined by equation (C.5).

$$t_{0,i} = \frac{s_i + s_{i+1}}{2} - (2i+1)\frac{s_{m-1} - s_0}{2(m-1)} \tag{C.5}$$

Averaging this center time over all $m-1$ spectra finally yields equation (C.8), which is the claimed result.

$$\langle t_0 \rangle = \frac{1}{m-1}\sum_{i=0}^{m-2} t_{0,i} \tag{C.6}$$

$$= \frac{1}{2(m-1)}\sum_{i=0}^{m-2}(s_i + s_{i+1}) - \frac{s_{m-1} - s_0}{2(m-1)^2}\sum_{i=0}^{m-2}(2i+1) \tag{C.7}$$

$$= \frac{1}{2(m-1)}(s_0 + s_{m-1}) + \frac{1}{2(m-1)}\sum_{i=1}^{m-2} 2s_i - \frac{1}{2}(s_{m-1} - s_0) \tag{C.8}$$

Appendix D – Pulse Creation by Charge Induction

In section 5.1.2 the pulse and step response of planar parallel plate ionization chambers is derived by considering the time dependent surface charges caused by the electron and ion drift between the plates. The induced surface charge which is caused by a static point charge can be determined by means of Greens reciprocity theorem as given in equation (D.1).

$$\int_V \rho\varphi' dV + \oint_{\partial V} \sigma\varphi' da = \int_V \rho'\varphi dV + \oint_{\partial V} \sigma'\varphi da \tag{D.1}$$

Here φ is the electric potential which is caused by a space charge ρ within the Volume V and a surface charge σ at the boundary ∂V. Analogous the potential φ' is caused by a space charge ρ' and a surface charge σ' within the same volume and boundary.

In the following two infinitely large planar parallel electrodes are assumed and the Green reciprocity theorem is applied for two different electrostatic configurations. These are schematically shown in figure D.1. In the first configuration, the two electrodes are grounded. A space charge ρ between the electrodes causes the electric potential φ and the surface charges σ on these electrodes. In the second configuration, voltages U_I and U_{II} are applied to the electrodes causing the electric potential φ' and surface charges σ'. There shall be no space charge in this configuration.

The integration volume is chosen to be congruent with the cuboid bounded by the two electrodes. In this way both integrals on the right side of equation (D.1) vanish. The right volume integral is zero since no space charge is present, thus $\rho = 0$, and the right surface integral is zero because the electric potential φ is zero on the only surfaces (which are the grounded electrodes) at which the surface charge σ' is different from zero. The left side of equation (D.1) behaves differently. The left surface integral can be reduced to equation (D.4), since the surface charge σ can only exist on the electrodes and the electric potential has to be constant there.

(D.2)

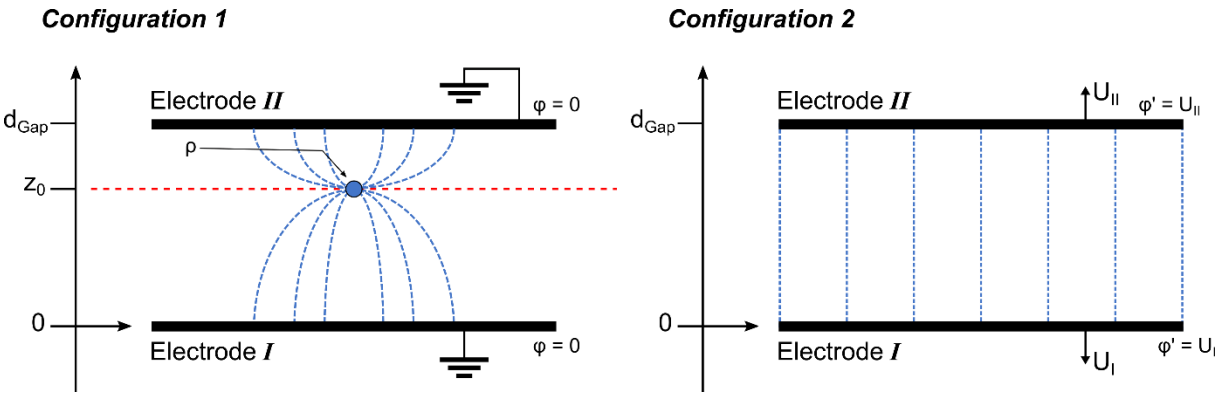

Figure D.1: Shown are two different electrostatic configurations which are used with Greens reciprocity theorem, equation (D.1), to determine the induced surface charges, which are caused by a point charge at z_0.

$$\oint_{\partial V} \sigma\varphi' da = \oint_{I} \sigma\varphi' da + \oint_{II} \sigma\varphi' da \tag{D.3}$$

$$= U_I \oint_{I} \sigma da + U_{II} \oint_{II} \sigma da$$
$$= q_I U_I + q_{II} U_{II} \tag{D.4}$$

The charges q_I and q_{II} are the induced charges on the corresponding electrodes. The left volume integral depends on the space charge ρ and the potential φ'. To obtain the induced charge as a result of a single point charge, such as an ion or electron, the space charge ρ can be written with a delta function as given in equation (D.5).

$$\rho(\boldsymbol{x}) = q\delta(\boldsymbol{x} - \boldsymbol{x}_0) \tag{D.5}$$

The electric potential φ' is known from electrostatics and is given by equation (D.6) where z is the perpendicular coordinate on the electrodes and d_{Gap} is the distance between them.

$$\varphi'(z) = (U_{II} - U_I)\frac{z}{d_{Gap}} + U_I \tag{D.6}$$

Thus equation (D.1) gives

$$\frac{qz_0}{d_{Gap}}(U_{II} - U_I) + qU_I + q_I U_I + q_{II} U_{II} = 0 \tag{D.7}$$

and taking into account that $q + q_I + q_{II} = 0$ finally yields equations (D.8) and (D.9).

$$q_I = -q\left(1 - \frac{z_0}{d_{Gap}}\right) \tag{D.8}$$

$$q_{II} = -q\frac{z_0}{d_{Gap}} \tag{D.9}$$

These equations determine the induced charges q_I and q_{II} on the corresponding electrodes as a result of a static point charge at z_0 between the electrodes.

Appendix E – Electron Momentum Transfer Cross Sections

In section 5.1.1 the drift velocity and the mean energy of electrons, which are subject to an external homogenous electric field, in gaseous environment are calculated by means of the MAGBOLTZ 2 code [**116**]. The following figures show the momentum transfer cross sections used in the calculations. Further or updated cross sections can be found in the LXcat database of the Plasma Data Exchange Project at *http://www.lxcat.net/*.

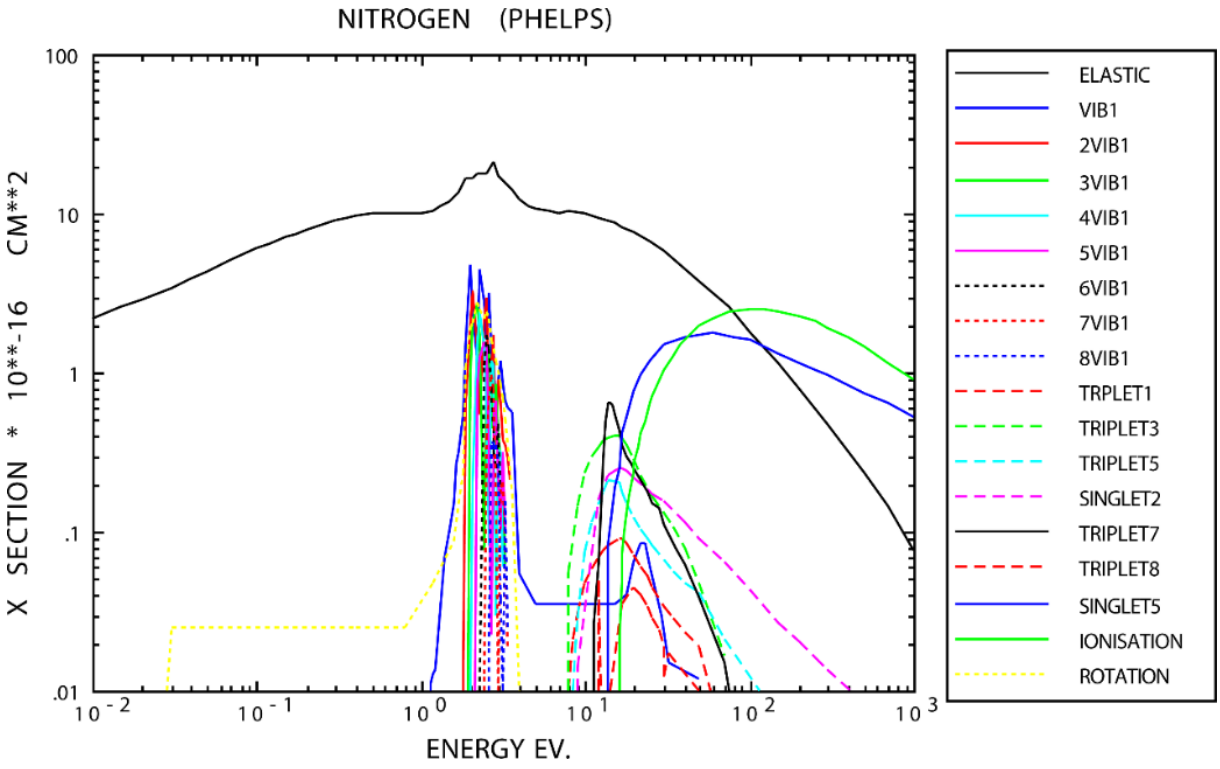

Figure E.1: Electron momentum transfer cross section of of nitrogen

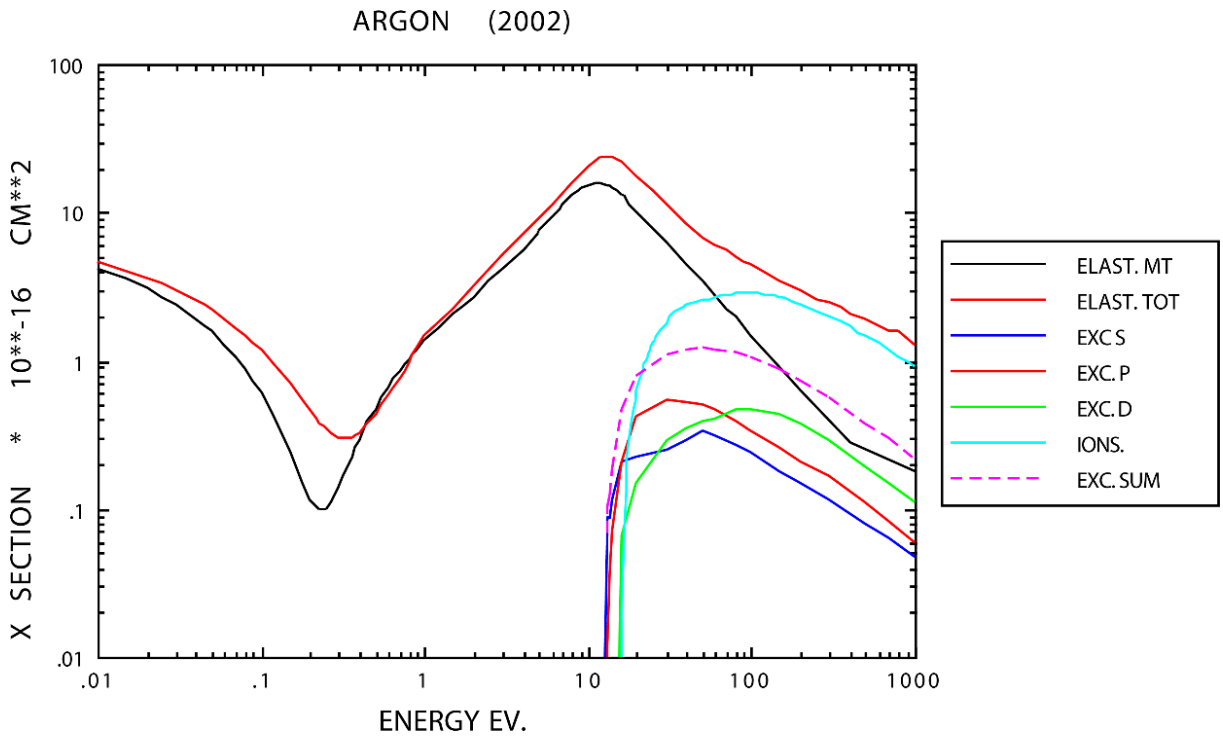

Figure E.2: Electron momentum transfer cross section of of argon.

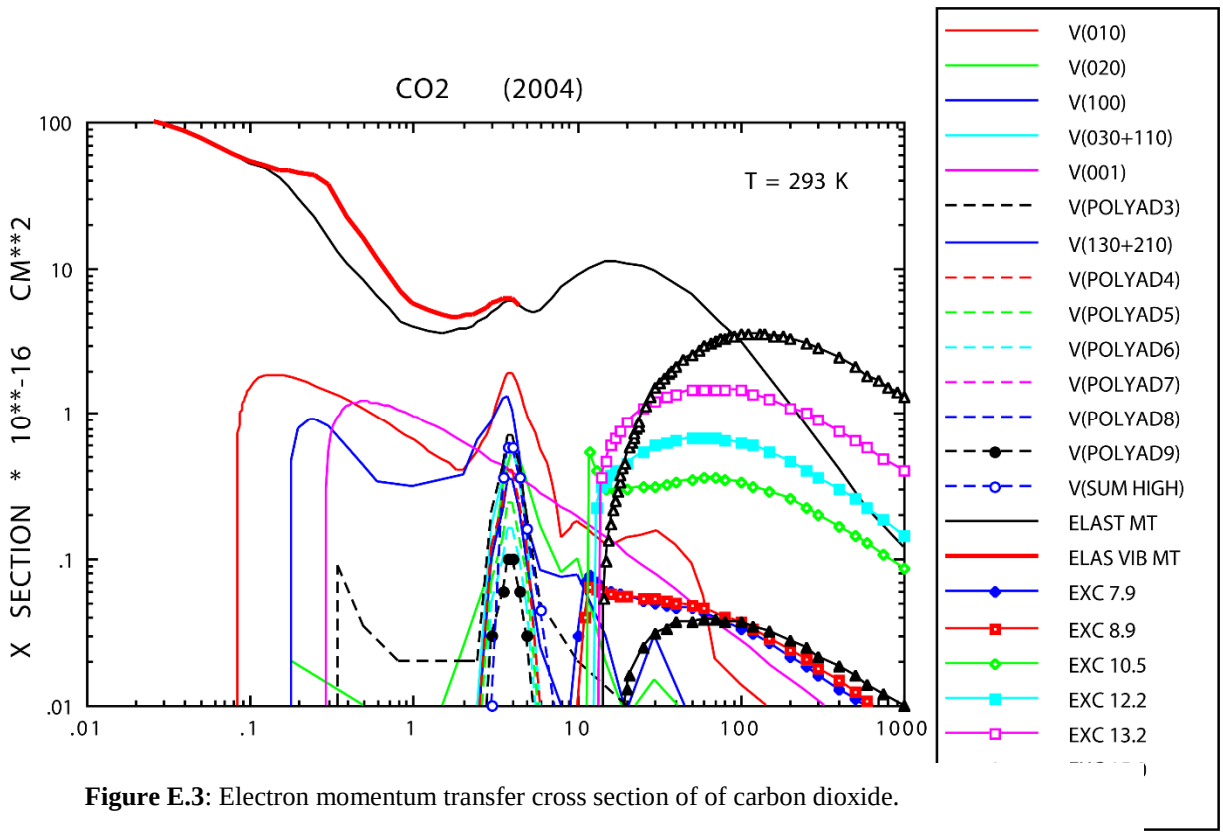

Figure E.3: Electron momentum transfer cross section of of carbon dioxide.

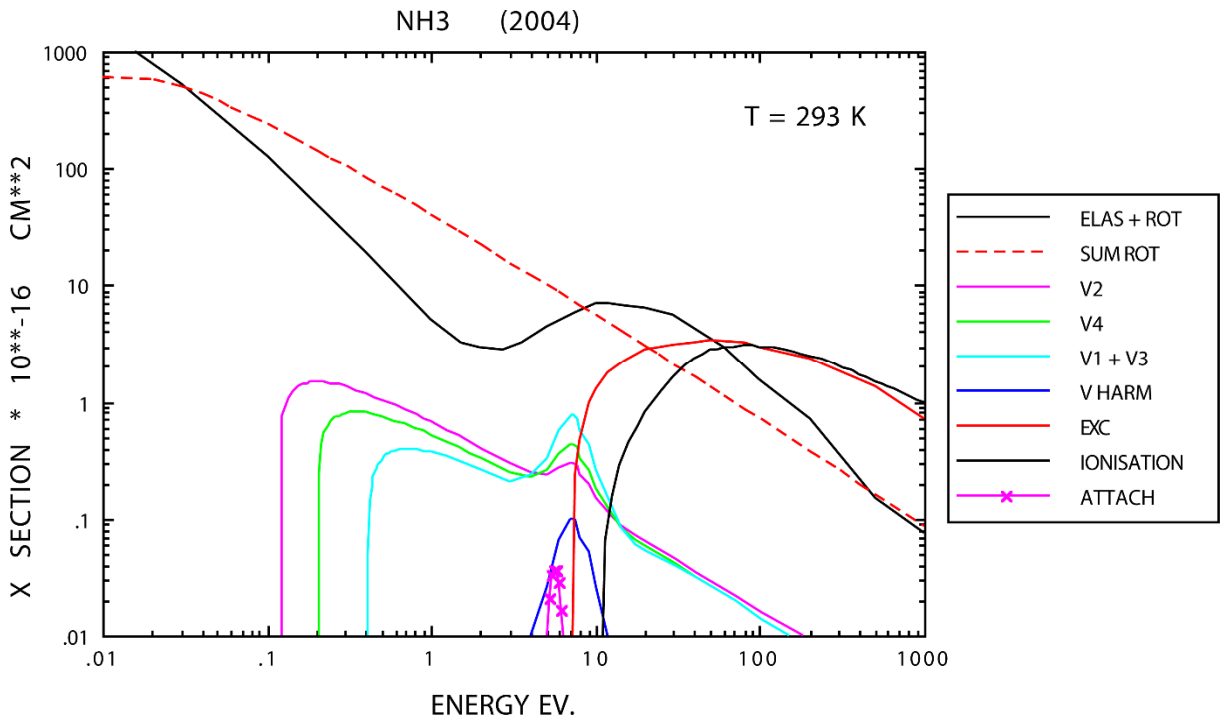

E.4: Electron momentum transfer cross section of of ammonia.

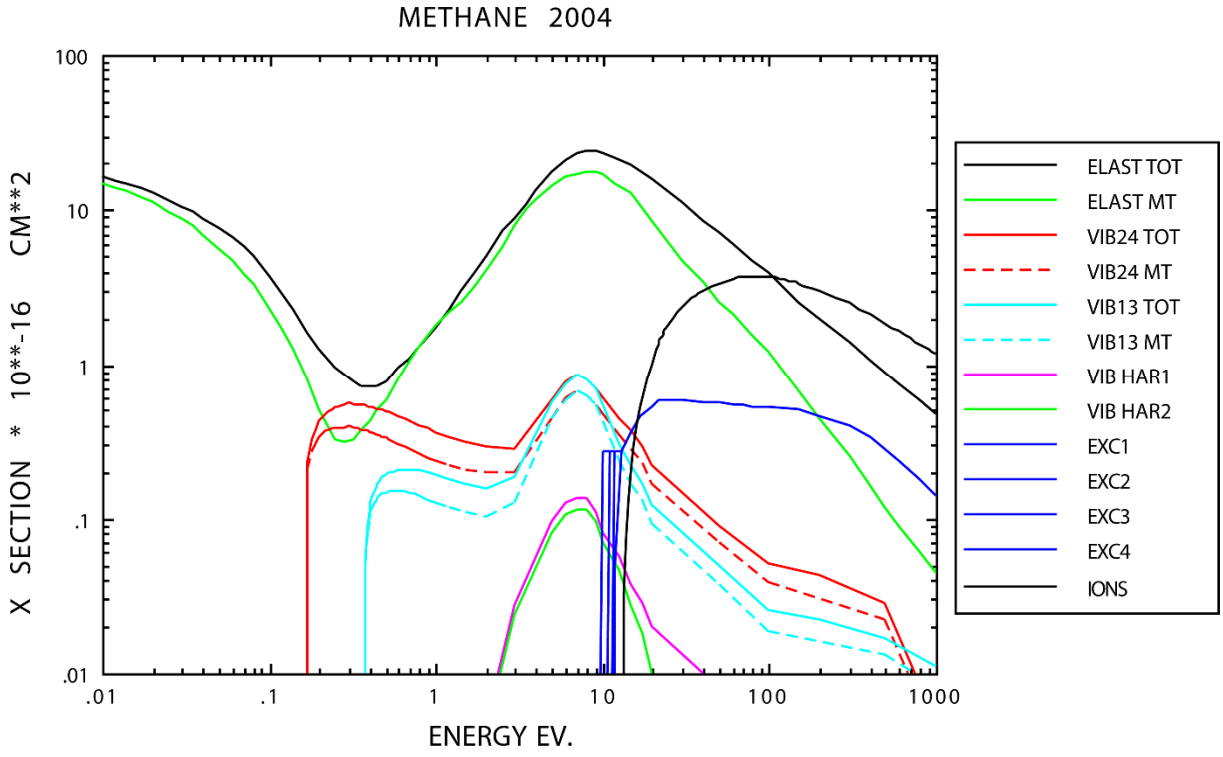

Figure E.5: Electron momentum transfer cross section of of methane.

Appendix F – Effective Ion Mobility

In section 5.1.2 the pulse and step response of planar parallel plate ionization chambers is derived by considering the time dependent surface charges caused by the electron and ion drift between the plates. Here this approach is followed to investigate the correlation between the ion mobility μ^+ and the first derivative of the step response within the slope region.

The induced surface charge q_I caused by an ion of charge q, at the position z between two planar parallel electrodes, d_{Gap} apart, was derived in the Appendix D and is given by equations (5.3), (D.8) or (F.1).

$$q_I(z) = -q\left(1 - \frac{z}{d_{Gap}}\right) \tag{F.1}$$

In the following this equation is generalized for multiple ions. To begin with only identical ions are considered. All ions of this species carry the same electrical charge q and have the same mobility μ^+. Superposition of all n ions yields the total induced surface charge $\bar{q_I}$ and result in equation (F.6).

$$\bar{q_I}(z_c) = \delta_q^+(z_1) + \cdots + \delta_q^+(z_n) \tag{F.2}$$

$$= -q\left(1 - \frac{z_1}{d_{Gap}}\right) - \cdots - q\left(1 - \frac{z_n}{d_{Gap}}\right) \tag{F.3}$$

$$= -q\left(1 - \cdots - 1 - \frac{z_1}{d_{Gap}} - \cdots - \frac{z_n}{d_{Gap}}\right) \tag{F.4}$$

$$= -nq\left(1 - \frac{z_c}{d_{Gap}}\right) \tag{F.5}$$

$$= -\bar{q}\left(1 - \frac{z_c}{d_{Gap}}\right) \tag{F.6}$$

Here z_c refers to the center of mass of the ions and $\bar{q}$ denotes the total charge. The drift motion of the center of gravity with the electric field $\mathcal{E}$ present, is given by equation (F.7).

$$z_c = z_0 + \frac{1}{2}\mu^+\mathcal{E}t \tag{F.7}$$

The factor $1/2$ originates from the continuous creation of new ions at z_0. Consequently the total charge also increases linearly with time. Given a constant ion creation rate η, which may also include the multiplicity of the charge state of the considered ion species, the total charge is given by equation (F.8).

$$\bar{q} = \eta e t \tag{F.8}$$

Combining equations (F.6) to (F.8) leads to the total time dependent surface charge $\bar{q}_I(t)$. Its result is given in equation (F.9).

$$\bar{q}_I(t) = -\eta e t \left(1 - \frac{z_0}{d_{Gap}} - \frac{\mu^+ \mathcal{E}}{2 d_{Gap}} t\right) \tag{F.9}$$

This equation is valid until the first ion reaches the electrode. From that moment on the center of mass and the total charge become constant and $\bar{q}_I$ independent of time. The time derivate of $\bar{q}_I(t)$ yields the electrical current caused (only) by the considered ion species during the step response. Hence, the second derivative, given in equation (F.11), reflects the slope of the step response.

$$\frac{d^2}{dt^2}\bar{q}_I(t) = \frac{d}{dt} I(t) \tag{F.10}$$

$$= \frac{\eta e \mu^+ \mathcal{E}}{d_{Gap}} \tag{F.11}$$

If the considered ion species is the only one, which is continuously created during operation of the ionization chamber, the equilibrium current I_{eq}, which settles when the output current becomes stable, is equal to ηe and equation (F.11) can be expressed as stated in (F.12).

$$\frac{d}{dt} I(t) = \frac{\mu^+ \mathcal{E}}{d_{Gap}} I_{eq} \tag{F.12}$$

Thus the actual ion mobility can be determine by equation (F.13).

$$\mu^+ = \frac{d_{Gap}}{I_{eq} \mathcal{E}} \frac{d}{dt} I(t) \tag{F.13}$$

Multiple Ion Species

If different species of ions are created or are transformed into each other during the drift, equation (F.13) no longer holds and needs to be modified. For each possible ion species a mobility μ_i^+ and a creation rate η_i need to be taken into account. Following the approach from above and superimposing the contributions of all ion species leads to equation (F.14).

$$\frac{d^2}{dt^2}\bar{q}_I(t) = \frac{e\mathcal{E}}{d_{Gap}} \sum\nolimits_i \eta_i \mu_i^+ \tag{F.14}$$

The sum goes over all ion species, whose drift path is not yet fully developed. If an ion of one species reaches the electrode this species is no longer part of the sum. From equation (F.14) finally follows

$$\hat{\mu}^+ := \frac{e}{I_{eq}} \sum\nolimits_i \eta_i \mu_i^+ = \frac{d_{Gap}}{I_{eq} \mathcal{E}} \frac{d}{dt} I(t) \tag{F.15}$$

which is used in section 5.2.3 to analyze the step response functions of planar parallel plate ionization chambers. The quantity $\hat{\mu}^+$ will be called the *effective ion mobility*.

References

[1] R. Frahm, New method for time dependent x-ray absorption studies, *Rev. Sci. Instrum.* **60**, 2515-2518 (1989).

[2] R. Frahm, QEXAFS: X-Ray Absorption Studies in Seconds, *Physica B* **158**, 342-343 (1989).

[3] J. Stötzel, D. Lützenkirchen-Hecht and R. Frahm, A new flexible monochromator setup for quick scanning x-ray absorption spectroscopy, *Rev. Sci. Instrum.* **81**, 073109 (2010).

[4] O. Müller, M. Nachtegaal, J. Just, D. Lützenkirchen-Hecht and R. Frahm, Quick-EXAFS setup at the SuperXAS beamline for in situ X-ray absorption spectroscopy with 10 ms time resolution, *J. Synchrotron Rad.* **23**, 260-266 (2016).

[5] C. G. Schroer, M. Kuhlmann, T. F. Günzler, B. Lengeler, M. Richwin, B. Griesebock, D. Lützenkirchen-Hecht, R. Frahm, E. Ziegler, A. Mashayekhi et al., Mapping the chemical states of an element inside a sample using tomographic x-ray absoprtion spectroscopy, *Appl. Phys. Lett.* **82**, 3360-3362 (2003).

[6] C. G. Schroer, M. Kuhlmann, T. F. Günzler, B. Lengeler, M. Richwin, B. Griesebock, D. Lützenkirchen-Hecht, D. Frahm, A. Mashayekhi, D. R. Haeffner et al., Tomographic X-Ray Absorption Spectroscopy, *Physica Scripta* **T115**, 1026-1028 (2005).

[7] J. Yano and V. K. Yachandra, X-ray absorption spectroscopy, *Photosynth Res* **102**, 241-254 (2009).

[8] J. Stötzel, D. Lützenkirchen-Hecht, R. Frahm, C. V. Santilli, S. H. Pulcinelli, R. Kaminski, E. Fonda, F. Villain and V. Briois, QEXAFS and UV/VIs Simultaneous Monitoring of the TiO_2-Nanoparticles Formation by Hydrolytic Sol-Gel Route, *J. Phys. Chem. C* **114**, 6228-6236 (2010).

[9] K. Föttinger, J. A. van Bokhoven, M. Nachtegaal and G. Rupprechter, Dynamic Structures of a Working Methanol Steam Reforming Catalyst: In Situ Quick-EXAFS on Pd/ZnO Nanoparticles, *J. Phys. Chem. Lett.* **2**, 428-433 (2011).

[10] Y. Nagai, K. Dohmae, Y. F. Nishimura, H. Kato, H. Hirata and N. Takahashi, Operando XAFS study of catalytic NO reduction over Cu/CeO_2: the effect of copper-ceria interaction under periodic operation, *Phys. Chem. Chem. Phys.* **15**, 8461-8465 (2013).

[11] D. E. Doronkin, M. Casapu, T. Günter, O. Müller, R. Frahm and J.-D. Grunwaldt, Operando Spatially- and Time-Resolved XAS Study on Zeolite Catalysts for Selective Catalytic Reduction of NO_x by NH_2, *J. Phys. Chem. C* **118**, 10204-10212 (2014).

[12] A. M. Gänzler, M. Casapu, A. Boubnov, O. Müller, S. Conrad, H. Lichtenberg, R. Frahm and J.-D. Grunwaldt, Operando spatially and time-resolved X-ray absorption spectroscopy and infrared thermography during oscillatory CO oxidation, *J. Catal.* **328**, 216-224 (2015).

[13] M. A. Newton, D. Ferri, G. Smolentsev, V. Marchionni and M. Nachtegaal, Room-temperatur carbon monoxide oxidation by oxygen over Pt/Al_2O_3 mediated by reactive platinum carbonates, *Nat. Commun.* 6:8675 (2016).

[14] J. Stötzel, D. Lützenkirchen-Hecht, E. Fonda, N. De Oliveira, V. Briois and R. Frahm, Novel angular encoder for a quick-extended x-ray absorption fine structure monochromator, *Rev. Sci. Instrum.* **79**, 083107 (2008).

[15] M. Nachtegaal, O. Müller, C. König and R. Frahm, QEXAFS: Techniques and Scientific Applications for Time-Resolved XAS, in *X-Ray Absorption and X-Ray Emission Spectroscopy: Theory and Applications* (eds. J. A. van Bokhoven and C. Lamberti), John Wiley and Sons, Ltd., New York (2016).

[16] O. Müller, D. Lützenkirchen-Hecht and R. Frahm, Quick scanning monochromator for millisecond in situ and in operando X-ray absorption spectroscopy, *Rev. Sci. Instrum.* **86**, 093905 (2015).

[17] O. Müller, J. Stötzel, D. Lützenkirchen-Hecht and R. Frahm, Gridded Ionization Chambers for Time Resolved X-Ray Absorption Spectroscopy, *J. Phys.: Conf. Ser.* **425**, 092010 (2013).

[18] J. J. Rehr and R. C. Albers, Theoretical approaches to x-ray absorption fine structure, *Rev. Mod. Phys.* **72**, 621-654 (2000).

[19] E. Fonda, A. Rochet, M. Ribbens, L. Barthe, S. Belin and V. Briois, The SAMBA quick-EXAFS monochromator: XAS with edge jumping, *J. Synchrotron Rad.* **19**, 417-424 (2012).

[20] T. Nonaka, K. Dohmae, T. Araki, Y. Hayashi, Y. Hirose, T. Uruga, H. Yamazaki, T. Mochizuki, H. Tanida and S. Goto, Quick-scanning x-ray absorption spectroscopy system with a servo-motor-driven channel-cut monochromator with a temporal resolution of 10 ms, *Rev. Sci. Instrum.* **83**, 083112 (2012).

[21] P. A. Lee, P. H. Citrin, P. Eisenberger and B. M. Kincaid, Extended x-ray absorption fine structure - its strenghts and limitations as a structural tool, *Rev. Mod. Phys.* **53**, 769-806 (1981).

[22] A. Bianconi, L. Incoccia and S. Stipcich, EXAFS and Near Edge Structure, Springer-Verlag, Berlin (1983).

[23] B. K. Teo, EXAFS: Basic Principles and Data Analysis, Springer-Verlag, Berlin (1986).

[24] D. C. Koningsberger and R. Prins, X-Ray Absorption: Principles, Applications, Techniques of EXAFS, SEXAFS and XANES, John Wiley & Sons, Inc., New York (1988).

[25] J. Als-Nielsen and D. McMorrow, Elements of Modern X-ray Physics, 2nd Edition, John Wiley & Sons, Ltd., (2011).

[26] E. B. Saloman and J. H. Hubbell, X-Ray Attenuation Cross Sections for Energies 100 eV to 100 keV and Elements Z = 1 to Z = 92, *Atom. Data and Nucl. Data Tab.* **38**, 1-197 (1988).

[27] M. J. Berger, J. H. Hubbell, S. M. Seltzer, J. Chang, J. S. Coursey, R. Sukumar, D. S. Zucker and K. Olsen, XCOM: Photon Cross Sections Database (version 1.5), *National Institute of Standards and Technology* [Online] http://physics.nist.gov/xcom/ (2010).

[28] J. Stümpel, P. Becker, S. Joksch, R. Frahm and G. Metrlik, Measurement of the Energy of X-Ray Absorption Edges, *Phys. Stat. Sol. A* **124**, 565-570 (1991).

[29] J. A. Victoreen, The Absorption of Incident Quanta by Atoms as Defined by the Mass Photoelectric Absorption Coefficient and the Mass Scattering Coefficient, *J. Appl. Phys.* **19**, 855-860 (1948).

[30] H. Fricke, The K-Characteristic Absorption Frequencies for the Chemical Elements Magnesium to Chromium, *Phys. Rev.* **16**, 202-215 (1920).

[31] G. Hertz, Über die Absorptionsgrenzen in der L-Serie, *Z. Phys.* **3**, 19-25 (1920).

[32] E. A. Stern, D. E. Sayers and F. W. Lytle, Extended x-ray-absorption fine-structure technique. III. Determination of physical parameters, *Phys. Rev. B.* **11**, 4836-4846 (1975).

[33] F. W. Lytle, D. E. Sayers and E. A. Stern, Extended x-ray-absorption fine-structure technique. II. Experimental practice and selected results, *Phys. Rev. B* **11**, 4825-4835 (1975).

[34] J. J. Rehr, C. H. Booth, F. Bridges and S. I. Zabinsky, X-ray-absorption fine structure in embedded atoms, *Phys. Rev. B.* **49**, 12347-12350 (1994).

[35] J. J. Rehr, S. I. Zabinsky, A. Ankudinov and R. C. Albers, Atomic-XAFS and XANES, *Phys. B* **208**, 23-26 (1995).

[36] Y. Nishihata, J. Mizuki, S. Emura and T. Uruga, EXAFS spectra above Pb and Pt K edges observed at low temperature, *J. Synchrotron Rad.* **8**, 294-296 (2001).

[37] D. E. Sayers, E. A. Stern and F. W. Lytle, New Technique for Investigating Noncrystalline Structures: Fourier Analysis of the Extended X-Ray Absorption Fine Structure, *Phys. Rev. Lett.* **27**, 1204-1207 (1971).

[38] A. L. Ankudinov, J. J. Rher, J. J. Low and S. R. Bare, Sensitivity of Pt x-ray absorption near edge structure to the morphology of small Pt clusters, *J. Chem. Phys.* **116**, 1911-1919 (2002).

[39] C. Paßlick, O. Müller, D. Lützenkirchen-Hecht, R. Frahm, J. A. Johnson and S. Schweizer, Structural properties of fluorozirconate-based glass ceramics doped with multivalent europium, *J. Appl. Phys.* **110**, 113527 (2011).

[40] F. Farges, G. E. Brown, Jr. and J. J. Rehr, Ti K-edge XANES studies of Ti coordination and disorder in oxide compounds: Comparison between theory and experiment, *Phys. Rev. B* **56**, 1809-1819 (1997).

[41] L. G. Parratt, Electronic Band Structure of Solids by X-Ray Spectroscopy, *Rev. Mod. Phys.* **31**, 616-645 (1959).

[42] A. L. Ankudinov, B. Ravel, J. J. Rehr and S. D. Conradson, Real-space multiple-scattering calculation and interpretation of x-ray-absorption near-edge structure, *Phys. Rev. B* **58**, 7565-7576 (1998).

[43] J. J. Rehr, J. J. Kas, M. P. Prange, A. P. Sorini, Y. Takimoto and F. Vila, Ab initio theory and calculations of X-ray spectra, *C. R. Physique* **10**, 548-559 (2009).

[44] M. O. Krause and J. H. Oliver, Natrual widths of atomic K and L levels, Kα Xray lines and several K L L Auger lines, *J. Phys. Chem. Ref. Data* **8**, 329-338 (1979).

[45] D. M. Mills, Third-Generation Hard X-ray Synchrotron Radiation Sources, John Wiley & Sons, Inc., New York (2002).

[46] J. Falta and T. Möller, Forschung mit Synchrotronstrahlung, Vieweg + Teubner Verlag, (2010).

[47] H. Onuki and P. Elleaume, Wiggler, Undulators and Their Applications, Taylor & Francus, Ltd., London (2002).

[48] J. A. Clarke, The Science and Technology of Undulators and Wigglers, OUP Oxford, (2004).

[49] E. Welter, Design considerations for a new beamline for standard EXAFS at a high-energy low-emittance storage ring, *J. Synchrotron Rad.* **19**, 905-910 (2012).

[50] O. Müller, D. Lützenkirchen-Hecht and R. Frahm, Hard disk drive based microsecond x-ray chopper for characterization of ionization chambers and photodiodes, *Rev. Sci. Instrum.* **86**, 035105 (2015).

[51] B. E. Warren, X-Ray Diffraction, Dover Publications, New York (1991).

[52] A. Authier, Dynamical Theory of X-Ray Diffraction, IUCr Monographs on Crystallography 11, Oxford University Press Inc., New York (2004).

[53] C. S. Rogers and L. Assoufid, Design and thermal stress analysis of high-power x-ray monochromators cooled with liquid nitrogen, *Rev. Sci. Instrum.* **66**, 2200-2202 (1995).

[54] D. H. Bilderback, K. Freund, G. S. Knapp and D. M. Mills, The historical deelopment of cryogenically cooled monochromators for third-generation synchrotron radiation sources, *J. Synchrotron Rad.* **7**, 53-60 (2000).

[55] W.-K. Lee, P. Fernandez and D. M. Mills, Performance limits of direct cryogenically cooled silicon monochromators - expreimental results at the APS, *J. Synchrotron Rad.* **7**, 12-17 (2000).

[56] W.-K. Lee, K. Fezzaa, P. Fernandez, G. Tajiri and D. Mills, Performance limits of indirectly cryogenically cooled silicon monochromators - experimental results at the APS, *J. Synchrotron Rad.* **8**, 22-25 (2001).

[57] K. Wille, Physik der Teilchenbeschleuniger und Synchrotronstrahlungsquellen, 2nd Edition, B. G. Teubner, Stuttgart (1996).

[58] R. Frahm, M. Nachtegaal, J. Stötzel, M. Harfouche, J. A. von Bokhoven and J.-D. Grunwaldt, The dedicated QEXAFS facility at the SLS: Performance and Scientific Opportunities, *AIP Conf. Proc.* **1234**, 251-255 (2010).

[59] O. von Polheim, O. Müller, D. Lützenkirchen-Hecht and R. Frahm, Design of Weak Link Channel-Cut Crystals for Fast QEXAFS Monochromators, *J. Phys.: Conf. Ser.* submitted (2015).

[60] S. Khalid, W. Caliebe, P. Siddons, I. So, B. Clay, T. Lenhard, J. Hanson, Q. Wang, A. I. Frenkel, N. Marinkovic et al., Quick extended x-ray absorption fine structure instrument with millisecond time scale, optimized for in situ applications, *Rev. Sci. Instrum.* **81**, 015105 (2010).

[61] R. Frahm, M. Richwin and D. Lützenkirchen-Hecht, Recent Advances and New Applications of Time-Resolved X-ray Abosrption Spectroscopy, *Physica Scripta* **T115**, 974-976 (2005).

[62] H. Bornebusch, B. S. Clausen, G. Steffensen, D. Lützenkirchen-Hecht and R. Frahm, A new approach for QEXAFS data acquisition, *J. Synchrotron Rad.* **6**, 209-211 (1999).

[63] D. Lützenkirchen-Hecht, S. Grundmann and R. Frahm, Piezo-QEXAFS with fluorescence detection: fast time-resolved investigations of dilute specimes, *J. Synchrotron Rad.* **8**, 6-9 (2001).

[64] M. Richwin, R. Zaeper, D. Lützenkirchen-Hecht and R. Frahm, Piezo-QEXAFS: advances in time-resolved X-ray absorption spectroscopy, *J. Synchrotron Rad.* **8**, 354-356 (2001).

[65] M. Richwin, R. Zaeper, D. Lützenkirchen-Hecht and R. Frahm, Piezo-XAFS - time-resolved x-ray absorption spectroscopy, *Rev. Sci. Instrum.* **73**, 1668-1670 (2002).

[66] J. Szlachetko, M. Nachtegaal, J. Sá, J.-C. Dousse, J. Hoszowska, E. Kleymenov, M. Janousch, O. V. Safonova, C. König and J. A. van Bokhoven, High energy resolution off-resonant spectroscopy at sub-second time resolution: ($Pt(acac)_2$) decomposition, *Chem. Commun.* **48**, 10898-10900 (2012).

[67] W. Blachuki, J. Szlachetko, J. Hoszowska, J.-C. Dousse, Y. Kayser, M. Nachtegaal and J. Sá, High Energy Resolution Off-Resonant Spectroscopy for X-Ray Absorption Spectra Free of Self-Absorption Effects, *Phys. Rev. Lett.* **112**, 173003 (2014).

[68] R. G. Lyons, Understanding Digital Signal Processing 3rd Edition, Pearson Eduaction, Inc., Prentice Hall, Upper Saddle River, NJ, et al. (2011).

[69] T. Ressler, WinXAS: a Program for X-ray Absorption Spectroscioy Data Analysis under MS-Windows, *J. Synchrotron Rad.* **5**, 118-122 (1998).

[70] M. Newville, IFEFFIT: interactive EXAFS analysis and FEFF fitting, *J. Synchrotron Rad.* **8**, 322-324 (2001).

[71] B. Ravel and M. Newville, ATHENA, ARTEMIS, HEPHAESTUS: data analysis for X-ray absorption spectroscopy using IFEFFIT, *J. Synchrotron Rad.* **12**, 537-541 (2005).

[72] K. V. Klementiev, Extraction of the fine structre from x-ray absorption spectra, *J. Phys. D: Appl. Phys.* **34**, 209-217 (2001).

[73] W. H. Press, S. A. Teukolsky, W. T. Vetterling and B. P. Flannery, Numerical Recipies 3rd Edition: The Art of Scientific Computing, Cambridge University Press, Cambridge et al. (2007).

[74] C. Champion, J. Champion and R. O. Sullivan, ZedGraph, *sourceforge.net* https://sourceforge.net/projects/zedgraph/ (2012).

[75] M. Frigeo and S. G. Johnson, The Design and Implementation of FFTW3, *Proc. IEEE* **93**, 216-231 (2005).

[76] P. Becker, Automatisierte Bestimmung von atomaren Strukturparametern aus QEXAFS-Daten, Master Thesis, Bergische Universität Wuppertal, Wuppertal (2014).

[77] A. Savitzky and M. J. E. Golay, Smoothing and Differentation of Data by Simplified Least Squares Procedures, *Anal. Chem.* **36**, 1627-1639 (1964).

[78] R. W. Schafer, What is a Savitzky-Golay Filter, *IEEE Sig. Proc. Mag.* **28**, 111-117 (2011).

[79] W. R. Dillon and M. Goldstein, Multivariate Analysis: Methods and Applications, John Wiley & Sons, New York (1984).

[80] M. Fernández-García, C. Márquez Alvarez and G. L. Haller, XANES-TPR Study of Cu-Pb Bimetallic Catalysts: Application of Factor Analysis, *J. Phys, Chem.* **99**, 12565-12569 (1995).

[81] P. Conti, S. Zamponi, M. Giorgetti, M. Berrettoni and W. H. Smyrl, Multivariate Curve Resolution Analysis for Interpretation of Dynamic Cu K-Edge X-ray Absorption Spectroscopy Spectra for Cu Doped V_2O_5 Lithium Battery, *Anal. Chem.* **82**, 3629-3635 (210).

[82] W. H. Cassinelli, L. Martins, A. R. Passos, S. H. Pulcinelli, C. V. Santilli, A. Rochet and V. Briois, Multivariate curve resolution analyis applied to time-resolved synchrotron X-ray Absorption Spectroscopy monitoring of the activation of copper alumina caralyst, *Catal. Today* **229**, 114-122 (2014).

[83] O. R. Frisch, Isotope analysis or uranium samples by measn of their α-ray groups, *British Atomic Energy Project* unpublished report.

[84] O. Bunemann, T. E. Cranshaw and J. A. Harvey, Design of Grid Ionization Chambers, *Can. J. Research, Sect. A* **27**, 191-206 (1949).

[85] D. H. Wilkinson, Ionization Chambers and Counters, Cambridge University Press, Cambridge (1950).

[86] B. B. Rossi and H. H. Staub, Ionization Chambers and Counters, McGraw-Hill Book Company Inc., New York et al. (1949).

[87] J. Sharpe, Nuclear Radiation Detectors, 2nd Edition, Methuen & Co Ltd, John Wiley & Sons Inc., London et al. (1964).

[88] G. F. Knoll, Radiation Detection and Measurement, 3rd Edition, John Wiley & Sons, Inc., New York (2000).

[89] E. B. Saloman, J. H. Hubbell and J. H. Scofield, X-Ray Attenuation Cross Sections for Energies 100 eV to 100 keV and Elements Z = 1 to Z = 92, *Atom. Data and Nucl. Data Tab.* **38**, 1-197 (1988).

[90] B. Sitar, G. I. Merson, V. A. Chechin and Y. A. Budagov, Ionization Measurements in High Energy Physics, Springer-Verlag, Berlin et al. (1993).

[91] H. W. Ellis, R. Y. Pai, E. W. McDaniel, E. A. Mason and L. A. Viehland, Transport Properties of Gasesous Ions Over a Wide Range, *Atom. Data Nucl. Data Tab.* **17**, 177-210 (1976).

[92] H. W. Ellis, E. W. McDaniel, D. L. Albritton, L. A. Viehland, S. L. Lin and E. A. Mason, Transport Properties of Gaseous Ions Over a Wide Energy Range. Part II, *Atom. Data Nucl. Data Tab.* **22**, 179-217 (1978).

[93] H. W. Ellis, M. G. Thackston, E. W. McDaniel and E. A. Mason, Transport Properties of Gaseous Ions Over a Wide Energy Range. Part III, *Atom. Data Nucl. Tab.* **31**, 113-151 (1984).

[94] L. A. Viehland and E. A. Mason, Transport Properties of Gaseous Ions Over a Wide Energy Range. IV, *Atom. Data Nucl. Tab.* **60**, 37-95 (1995).

[95] M. Tabrizchi and F. Rouholahnejad, Comparing the effect of pressure and temperature on ion mobilities, *J. Phys. D: Appl. Phys.* **38**, 857-862 (2005).

[96] J. A. R. Samson, Mobilities of Oxygen and Nitrogen Ions, *Phys. Rev.* **137**, 381-383 (1965).

[97] G. E. Keller, D. W. Martin and E. W. McDaniel, General Consideration Concerning Apparent Mobilities in Mixed Ion Population: Drift Velocities of Mass-Identified N^+, N_2^+, N_3^+, and N_4^+ Ions in Nitrogen, *Phys. Rev.* **140**, 1535-1546 (1965).

[98] M. Saporoschenko, Mobility of Mass-Analyzed N^+, N_2^+, N_3^+ and N_4^+ Ions in Nitrogen Gas, *Phys. Rev.* **139**, 352-356 (1965).

[99] J. T. Moseley, R. M. Snuggs, D. W. Martin and E. W. McDaniel, Mobilities, Diffusion Coefficients, and Reaction Rates of Mass-Indentified Nitrogen ions in Nitrogen, *Phys. Rev.* **178**, 240-248 (1969).

[100] A. N. C. Garcia, P. N. B. Neves, A. M. F. Trindade, F. P. Santos and C. A. N. Conde, A new contribution to the experimental measurement of the N^+_4 ion mobility in N_2 at 298 K, *J. Inst.* **7**, 1-7 (2012).

[101] J. A. Hornbeck, Charge transfer and the mobilizy of rare gas ions, *J. Phys. Chem.* **56**, 829-831 (1952).

[102] M. A. Biondi and L. M. Chanin, Mobilities of Atomic and Molecular Ions in the Noble Gases, *Phys. Rev.* **94**, 910-916 (1954).

[103] H. J. Oskam and V. R. Mittelstadt, Ion Mobilitites in Helium, Neon, and Argon, *Phys. Rev.* **132**, 1435-14444 (1963).

[104] J. M. Madson and H. J. Oskam, Mobility of Argon Ions in Argon, *Phys. Lett.* **25A**, 407-408 (1967).

[105] K. B. McAfee, D. Sipler and D. Edelson, Mobilities and Reactions of Ions in Argon, *Phys. Rev.* **160**, 130-135 (1967).

[106] I. Popescu and R. von der Heide, Beweglichkeit von Einfach. und Cluster-Ionen in Argon bei hohen Drücken, *Z. Physik* **220**, 337-348 (1969).

[107] R. von der Heide, Beweglichkeit und Bildung von Cluster-Ionen im eigenen Gas in He, Ne, und Ar unter hohen Drücken, *Z. Naturforsch.* **30a**, 868-870 (1975).

[108] R. Johnsen and M. A. Biondi, Mobilities of doubly charged rare-gas ions in their parent gases, *Phys. Rev. A* **18**, 989-995 (1978).

[109] H. Helm and M. T. Elford, Mobilities and ractions of diatomic rare-gas ions in their parent gases, helium, neaon, argon and krypton, *J. Phys. B: Arom. Molec. Phys.* **11**, 3939-3950 (1978).

[110] P. N. B. Neves, C. A. N. Conde and L. M. N. Távora, Experimental measurement of the mobilities of atomic and dimer Ar, Kr, and Xe ions in their parent gases, *J. Chem. Phys.* **133**, 124316 (2010).

[111] P. N. B. Neves, A. N. C. Garcia, A. M. F. Trindade, J. A. S. Barata, L. M. N. Távora and C. A. N. Conde, Experimental Measurements of the Ne^+ and Ne^+_2 Mobilities in Ne and the Reaction Rate Coefficient for $Ne^+ + 2Ne \rightarrow Ne_2^+ + Ne$, *IEEE Trans. Nucl. Sci.* **58**, 2060-2063 (2011).

[112] V. Palladino and B. Sadoulet, Application of Classical Theory of Electrons in Gases to Drift Proportional Chambers, *Nucl. Instrum. and Meth.* **128**, 323-335 (1975).

[113] R. Veenhof, Numerical methods in the simulation of gas-based detectors, *JINST* **4**, P12017 (2009).

[114] T. Zhao, Y. Chen, S. Hand and J. Hersch, A study of electron drift velocity in Ar-Co_2 and Ar-CO_2-CF_4 gas mixtures, *Nucl. Instr. and Meth in Phys. Res. A* **340**, 485-490 (1994).

[115] A. A. Sebastian and J. M. Wadehra, Time-dependent behaviour of electron transport in methane-argon mixtures, *J. Phys. D: Appl. Phys.* **38**, 1577-1587 (2005).

[116] S. F. Biagi, Monte Carlo simulation of electron drfit and diffusion in counting gases under the influence of electric and magnetic fields, *Nucl. Instr. and Meth. in Phys. Res. A* **421**, 234-240 (1999).

[117] G. J. M. Hagelaar and L. C. Pitchford, Solving the Boltzmann equation to obtain electron transport coefficients and rate coefficients for fluid models, *Plasma Sources Sci. Technol.* **14**, 722-733 (2005).

[118] J. Lucas and H. T. Saelee, A comparison of a Monte Carlo simulation and the Boltzmann solution for electrons swarm motion in gases, *J. Phys. D: Appl. Phys. 8* **8**, 640-650 (1975).

[119] P. J. Chantry and R. E. Wootton, A critique of methods for calculating the dielectric strength of gas mixtures, *J. Appl. Phys.* **52**, 2731-2739 (1981).

[120] D. Maric, O. Sasic, J. Jovanovic, M. Radmilovic-Radenovic and Z. L. Petrovic, Ionization coefficients in gas mixtures, *Rad. Phys. Chem.* **76**, 551-555 (2007).

[121] C. Ramsauer, Über den Wirkungsquerschnitt der Gasmoleküle gegenüber langsamen Elektronen, *Ann. Phys.* **369**, 513-540 (1921).

[122] C. Ramsauer, Über den Wirkungsquerschnitt der Gasmoleküle gegenüber langsamen Elektronen. II. Fortsetzung und Schluß, *Ann. Phys.* **377**, 345-352 (1923).

[123] C. S. Chua, S. P. A. Higgins and A. Fouras, An asynchronous high-speed synchrtron shutter, *J. Synchrotron Rad.* **17**, 624-630 (2010).

[124] M. Cammarata, L. Eybert, F. Ewald, W. Reichenbach, M. Wulff, P. Anfinrud, F. Schotte, A. Plech, Q. Kong, M. Lorenc et al., Chopper system for time resolved experiments with synchrotron radiation, *Rev. Sci. Instrum.* **80**, 015101 (2009).

[125] L. Orozcop, Programmable-Gain Transimpendance Amplifiers Maximize Dynamic Range in Spectroscopy Systems, *Analog Dialogue* **47**, 11-15 (2013).

[126] R. F. Pettifer, M. Borowski and P. W. Loeffen, The physics of ionization chambers - or how to improve your signal-to-noise ratio for transmission EXAFS measurements, *J. Synchrotron Rad.* **6**, 217-219 (1999).

[127] A. W. Castleman, Jr. and R. G. Keesee, Ionic Clusters, *Chem. Rev.* **86**, 589-618 (1986).

[128] N. E. Levinger, D. R. Ray, M. L. Alexander and W. C. Lineberger, Photoabsorption and photofragmentation studies of Ar^{+}_{n} cluster ions, *J. Chem. Phys.* **89**, 5654-5662 (1988).

[129] W. Miehle, O. Kandler, T. Leisner and O. Echt, Mass spectrometric evidence for icosahedral structure in large rare gas clusters: Ar, Kr, Xe, *J. Chem. Phys.* **91**, 5940-5952 (1989).

[130] E. Rühl, C. Schmale, H. W. Jochims, E. Biller, M. Simon and H. Baumgärtel, Charge separation in core excited argon clusters, *J. Chem. Phys.* **95**, 6544-6550 (1991).

[131] S. Kakar, O. Björneholm, J. Weigelt, A. R. de Castro, L. Tröger, R. Frahm, T. Möller, A. Knop and E. Rühl, Size-dependent K-Edge EXAFS study of the structure of free Ar clusters, *Phys. Rev. Let.* **78**, 1675-1678 (1997).

[132] A. B. Kanu, P. Dwivedi, M. Tam, L. Matz and H. H. Hill Jr., Ion mobility - mass spectrometry, *J. Mass Spectrom* **43**, 1-22 (2008).

[133] H. Murakami, H. Iwayama, K. Nagaya and M. Yao, Fragemntation channels of K -shell excited rare-gas clusters studied by multiple ion coincidence momentum imaging, *J. Chem. Phys.* **128**, 054303 (2008).

[134] T. Uruga, H. Tanida, K. Inoue, H. Yamazaki and T. Irie, Quick XAFS System using Quasimonochromatic Undulator Radiation at SPring-8, *AIP Conf. Proc.* **882**, 914-916 (2007).

[135] J. Stötzel, D. Lützenkirchen-Hecht and R. Frahm, A new stand-alone QEXAFS data acquisition system for in situ studies, *J. Synchrotron Rad.* **18**, 165-175 (2011).

[136] K. F. Jensen, Microreaction engineering - is small better?, *Chem. Eng. Sci.* **56**, 293-303 (2001).

[137] K. Jähnisch, V. Hessel, H. Löwe and M. Baerns, Chemistry in Microstructured Reactors, *Angew. Chem. Int. Ed.* **43**, 406-446 (2004).

[138] W. Wibel, A. Wenka, J. Brandner and R. Dittmeyer, Measuring and modeling the residence time distribution of gas flows in multichannel reactors, *Chem. Eng. J.* **215-216**, 449-460 (2013).

[139] S. Baier, A. Rochet, G. Hofmann, M. Kraut and J.-D. Grunwaldr, Lithographically fabricated silicon microreactor for in situ characterization of heterogeneous catalysts - Enabling correlative characterization techniques, *Rev. Sci. Instrum.* **86**, 065101 (2013).

[140] J. Just, Korrelation struktureller und elektronischer Eigenschaften in Kesterit-Dünnschichten, -Nanokristallen und -Solarzellen, Dissertation, Bergische Universität Wuppertal, Wuppertal (2015).

[141] A. Polizzotti, I. L. Repins, R. Noufi, S.-H. Wei and D. B. Mitzi, The state and future prospects of kesterite photovoltaics, *Energy Environ. Sci.* **6**, 3171-3182 (2013).

[142] C. B. Murray, D. J. Norris and M. G. Bawendi, Synthesis and Characterization of Nearly Monodisperse CdE (E = S, Se, Te) Semiconductor Nanocrystallites, *J. Am. Chem. Soc.* **115**, 8706-8715 (1993).

[143] Q. Guo, G. M. Ford, W.-C. Yang, B. C. Walker, E. A. Stach, H. W. Hillhouse and R. Agrawal, Fabrication of 7.2% Efficient CZTSSe Solar Cells Using CZTS Nanocrystals, *J. Am. Chem. Soc.* **132**, 17384-17386 (2010).

[144] R. Mainz, A. Singh, S. Levcenko, M. Klaus, C. Genzel, K. M. Ryan and T. Unold, Phase-transition-driven growth of compound semiconductor crystals from ordered metastable nanorods, *Nat. Commun.* **5**, 3133 (2014).

[145] C. Coughlan and K. M. Ryan, Complete study of the composition and shape evolution in the synthesis of Cu_2ZnSnS_4 (CZTS) semiconductor nanocrystals, *CrystEngComm* **17**, 6914-6922 (2015).

[146] J. A. Bearden and A. F. Burr, Reevaluation of X-Ray Atomic Energy Levels, *Rev. Mod. Phys.* **39**, 125-142 (1967).

Own Publications

Papers and Book Chapters

- O. von Polheim, O. Müller, D. Lützenkirchen-Hecht and R. Frahm, Design of weak link channel-cut crystals for fast QEXAFS monochromators , *AIP Conf. Proc.* **1741**, 040041 (2016).
- O. Müller, M. Nachtegaal, J. Just, D. Lützenkirchen-Hecht and R. Frahm, Quick EXAFS setup at the SuperXAS beamline for in-situ X-ray absorption spectroscopy with 10 ms time resolution, *J. Synchrotron Rad.* **23**, 260-266 (2016).
- O. Müller, D. Lützenkirchen-Hecht and R. Frahm, Quick scanning EXAFS monochromator for millisecond in-situ and in-operando X-ray absorption spectroscopy, *Rev. Sci. Instrum.* **86**, 093905 (2015).
- M. Nachtegaal, O. Müller, C. König and R. Frahm, QEXAFS: Techniques and scientific applications for time resolved XAS, in *X-Ray Absorption and X-Ray Emission Spectroscopy: Theory and Application* (eds. J. A. van Bokhoven and C. Lamberti), John Wiley and Sons, Ltd., New York (2016).
- O. Müller, D. Lützenkirchen-Hecht and R. Frahm, Hard disk drive based microsecond x-ray chopper for characterization of ionization chambers and photodiodes, *Rev. Sci. Instrum.* **86**, 035105 (2015).
- A. M. Gänzler, M. Casapu, A. Boubnov, O. Müller, S. Conrad, H. Lichtenberg, R. Frahm and J.-D. Grunwaldt, Operando spatially and time-resolved X-ray absorption spectroscopy and infrared thermography during oscillatory CO oxidation, *J. Catal.* **328**, 216-224 (2015).
- D. E. Doronkin, M. Casapu, T. Günter, O. Müller, R. Frahm and J.-D. Grunwaldt, Operando Spatially- and Time-Resolved XAS Study on Zeolite Catalysts for Selective Catalytic Reduction of NO_x by NH_3, *J. Phys. Chem. C* **118**, 10204-10212 (2014).
- O. Müller, J. Stötzel, D. Lützenkirchen-Hecht and R. Frahm, Gridded Ionization Chambers for Time Resolved X-Ray Absorption Spectroscopy, *J. Phys.: Conf. Ser.* **425**, 092010 (2013).
- D. Lützenkirchen-Hecht, J. Stötzel, O. Müller and R. Frahm, Surface science in sub-seconds by a combination of grazing incidence geometry and QEXAFS, *J. Phys.: Conf. Ser.* **425**, 092001 (2013).

- D. Lützenkirchen-Hecht, J. Stötzel, O. Müller, J. Just and R. Frahm, Quick-Scanning QEXAFS in grazing incidence: Surface science in sub-seconds, *J. Phys.: Conf. Ser.* **430**, 012124 (2013).
- C. Paßlick, O. Müller, D. Lützenkirchen-Hecht, R. Frahm, J. A. Johnson and S. Schweizer, Structural properties of fluorozirconate-based glass ceramics doped with multivalent europium, *J. Appl. Phys.* **110**, 113527 (2011).

Talks at International Conferences

- O. Müller, M. Nachtegaal, D. Lützenkirchen-Hecht and R. Frahm, The new QEXAFS monochromator, detection and data acquisition system at the SuperXAS beamline (SLS) for EXAFS spectroscopy with 15 ms time resolution, *16th International Conference on X-ray Absorption Fine Structure (XAFS 16)*, Karlsruhe, Germany, (2015).
- O. Müller, J. Stötzel, D. Lützenkirchen-Hecht and R. Frahm, Instrumentation for QEXAFS Spectroscopy at PETRA III, *15th International Conference on X-ray Absorption Fine Structure (XAFS 15)*, Beijing, China, (2012).

Poster Presentations at International Conferences

- O. Müller, P. Becker, D. Lützenkirchen-Hecht and R. Frahm, JAQ – JAQ Analyzes QEXAFS: Software for processing and analyzing time resolved XAS data, *16th International Conference on X-ray Absorption Fine Structure (XAFS 16)*, Karlsruhe, Germany (2015).
- O. Müller, D. Lützenkirchen-Hecht and R. Frahm, Fast Gridded Ionization Chambers with Microsecond Response Time, *12th International Conference on Synchrotron Instrumentation (SRI 2015)*, New York, USA (2015).
- O. Müller, M. Nachtegaal, D. Lützenkirchen-Hecht and R. Frahm, QEXAFS monochromator, Detectors and Data Acquisition System at the SuperXAS (SLS) Beamline for 15 ms EXAFS, *12th International Conference on Synchrotron Instrumentation (SRI 2015)*, New York, USA (2015).
- O. Müller, P. Becker, D. Lützenkirchen-Hecht and R. Frahm, Time Resolved XAS Instrumentation for PETRA III Extension Beamline P64, *22nd International Congress on X-ray Optics and Microanalysis (ICXOM 22)*, Hamburg, Germany (2013).
- O. Müller, J. Stötzel, D. Lützenkirchen-Hecht and R. Frahm, Gridded Ionization Chambers for Time Resolved X-Ray Absorption Spectroscopy, 11th International Conference on Synchrotron Radiation Instrumentation (SRI 2012), Lyon, France (2012).

Acknowledgements

I would like to thank Prof. Dr. Ronald Frahm for entrusting me with this particularly interesting and multifaceted topic. His confidence in my work and the granted freedom, which allowed me to pursue my own research priorities, led to the success of this work and was very much appreciated. I am also very grateful to Dr. Dirk Lützenkirchen-Hecht for his encouragement and professional advice during my work at the University.

My sincere thanks go to Dr. Maarten Nachtegaal, not only for providing the unique opportunity to test and eventually install the new QEXAFS system at the SuperXAS beamline but also in particular for all fruitful discussions, constant feedback, and his ongoing motivation. In this respect I also appreciate the support of the engineers and technicians and infrastructure groups of the Paul-Scherrer Institute. Especially I want to thank Patrick Ascher and Lorenz Bäni for their extraordinary support during the installation of the QEXAFS monochromator at the beamline.

I also want to thank Prof. Dr. Jan-Dierk Grunwaldt and the members of his research group, in particular Dr. Maria Casapu, Dr. Dmitry Doronkin and Andreas Gänzler for the enjoyable collaboration and valuable discussions about in operando QEXAFS and catalysis research in general.

I want to thank my fellow colleagues and my student assistants at the university. Especially I would like to acknowledge Dr. Justus Just, Pascal Becker, Oliver von Polheim, Serena Schlottmann, Ralph Wagner, Jan Gasse, Dr. Benjamin Bornmann and Dr. Daniel Krämer for their great support in the laboratories and during our beamtimes at the synchrotron.

Furthermore, I want to thank Dr. Wolfgang Caliebe, Dr. Edmund Welter, Dr. Wolfgang Drube and Dr. Horst Schulte-Schrepping as well as the FS-BT Vacuum Group of DESY for technical advice and their support during the installation of the QEXAFS monochromator at the P64 beamline.

I would like to thank Federal Ministry of Education and Research (BMBF) for financial support of this work (Project Nos. 05K10PX1 and 05K13PX1).

Last but not least I thank my family: my parents, Frank and Rosi, my brother Tobias and my lovely wife Stephi whose support during my studies and especially this work decisively contributed to its success.

Declaration of Authorship

I hereby confirm that this thesis with the title "*Hard X-Ray Synchrotron Beamline Instrumentation for Millisecond Quick Extended X-ray Absorption Spectroscopy*" and the work presented in it are my own and is the result of my own original research. Any sources of authors are listed in the bibliography of this thesis.

Wuppertal,

_____

Oliver Müller